In-depth Investigation of Self-assembling Peptides for Functional Nanomaterials

Dissertation zur Erlangung des Doktorgrades Dr. rer. nat.
am Fachbereich Chemie der Fakultät für Naturwissenschaften
der Universität Ulm

Thomas Mack
geb. in Günzburg
Ulm, 2021

Dissertation der Universität Ulm

Amtierender Dekan: Prof. Dr. Thorsten Bernhardt

1. Gutachter: Prof. Dr. Tanja Weil

2. Gutachter: Prof. Dr. Mika Lindén

Tag der Promotion: 11.03.2022

Universität Ulm, Fakultät für Naturwissenschaften, 2021

For my wonderful parents

Abstract

For a long time, nature has inspired scientists all over the world. Peptides and proteins play key roles in many essential biological processes in living systems. In the past decades, functional nanomaterials based on peptides as small building blocks have increasingly become focus of materials research. Today, there is a great interest in understanding the design principles of peptide-based materials that govern their properties and mechanisms of formation.

Still, there is a huge gap of our understandings of natural processes involving self-assembled materials due to their high structural complexity. The formation of supramolecular peptide-based biomaterials, their properties, and applicability are often a result of trial and error. A deeper understanding of how structures and their resulting properties as well as their bioactivities affect each other is crucial to develop tailored biomaterials that are able to match natural systems and ideally even surpass them. For example, it is still a key challenge to predict secondary structure elements of proteins and even more challenging to predict their unique tertiary structure, i.e. the three-dimensional shape formed by folding and which is essential for its function. To develop peptide-based nanomaterials for various applications, it is therefore desirable to gain a more profound knowledge about how the primary sequence affects folding, which would be important to design new sequences and structures that accomplish a specific function.

Nanomaterials based on peptidic building blocks have recently emerged in a broad range of applications, and their design is based on interdisciplinary research from biology over material science to physics. They show promising potential in various fields, and a deeper understanding would open new avenues to entirely novel functions.

In this thesis, I prepared and investigated short peptide sequences and utilized them as small building blocks that formed supramolecular nanoscaled structures in a bottom-up approach. These self-assembling peptides (SAPs) were systematically altered in their primary sequence to elucidate the effects on self-assembly, morphology, structure, and resulting biological response. Through this study, a deeper understanding of the structure-property relationship of peptide assemblies within biological surroundings was obtained, and the respective nanostructures were tailored

towards different applications. First, the effect of those SAPs on neuronal regeneration was investigated and revealed a structure-activity relationship in an *in vitro* screening of a peptide library. Hereby, structural key elements and resulting physico-chemical properties of the peptide nanofibrils (PNFs) were identified, which have a high impact on bioactivity. Furthermore, the applicability of potential peptides as substrates for supporting nerve regeneration was investigated in an *in vivo* mouse model of peripheral nerve damage. Optimized peptide nanostructures provided a better functional outcome and recovery from the injury compared to controls (chapter 3.1).

Next, functionalization of PNFs was presented by auto-oxidative polymerization of dopamine on the fibril surface. This idea was inspired by the nanofibril-mediated synthesis of melanin inside certain cells. The coated nanofibrils revealed similar bioactivity in supporting neuronal cell growth as the nanofibrils without polydopamine coating. However, polydopamine offers reactive groups such as catechols. In a proof-of-concept study, functionalization of fibrils' surface was performed using the known dynamic covalent chemistry of boronic acids and catechols, which presents a novel approach to attach and release functionalities in a pH-responsive fashion without compromising bioactivity (chapter 3.2).

PNFs are also known to be potent enhancers of retroviral transduction. However, the structural features that are crucial for bioactivity are also elusive here. We observed that high β-sheet content and physico-chemical properties like positive net charges had a high impact on their ability to bind virions, colocalize them at cellular membranes, and enhance retroviral gene transduction (chapter 3.3).

Our studies show that ordered structural elements such as cross-β-sheet structures as well as charges are important parameters for bioactivity. Based on these results, smaller and potent peptide sequences have been designed that quantitatively formed bioactive nanofibrils. In this way, the principles discovered in this thesis could facilitate the formation of entirely new peptide nanomaterials by rational design.

Index

I Introduction ... **1**

1.1 Nanotechnology and -materials ... 1

1.1.1 Natural supramolecular nanomaterials ... 2

1.2 Peptide-based nanomaterials ... 3

1.2.1 Peptides as small building blocks ... 3

1.2.2 Amyloid fibrils ... 7

1.2.2.1 Amyloids and diseases ... 9

1.2.2.2 Amyloid fibrils as building blocks for natural and functional materials ... 10

1.2.3 Peptide amphiphiles ... 12

1.2.4 Short aromatic self-assembling peptides ... 17

1.3 Potential applications for peptide-based nanomaterials ... 19

1.3.1 Peripheral nerve injuries ... 19

1.3.2 Retroviral gene transfer ... 23

II Motivation and Goal ... **25**

III Results and Discussion ... **29**

3.1 Introduction to "Sequenced-Optimized Peptide Nanofibers as Growth Stimulators for Regeneration of Peripheral Neurons" ... 29

3.2 Introduction to "Water-Dispersible Polydopamine-Coated Nanofibers for Stimulation of Neuronal Cell Growth" ... 34

3.3 Introduction to "Supramolecular Peptide Nanofibrils with Optimized Sequences and Molecular Structures for Efficient Retroviral Transduction" ... 38

IV Summary and Outlook ... **45**

V Publications ... **49**

5.1 Sequence-Optimized Peptide Nanofibers as Growth Stimulators for Regeneration of Peripheral Neurons ... 50

5.2 Water-Dispersible Polydopamine-Coated Nanofibers for Stimulation of Neuronal Growth and Adhesion ... 120

5.3 Supramolecular Peptide Nanofibrils with Optimized Sequences and Molecular Structures for Efficient Retroviral Transduction ... 145

References ... **193**

List of abbreviations ... **203**

List of amino acids ... **205**

List of publications ... **207**

Curriculum vitae ... **209**

List of conferences 211

Statutory declaration 213

Acknowledgements 215

I Introduction

1.1 Nanotechnology and -materials

Materials with nanoscale dimensions (1-100 nm) often combine unique material, biological, electronic, and optical properties. Therefore, research in this area expanded significantly in the past decades, and many researchers claimed that nanomaterials would play a key role in future materials science.[1] The field was initially inspired by the Nobel laureate Richard Feynman in 1959 in his famous talk "there's plenty of room at the bottom".[2] Today, nanomaterials show potential in several fields like medicine, electronics, or information technology, as shown in figure 1.[3] In general, the preparation of nanomaterials can be classified into two categories: the top-down and the bottom-up approaches. The top-down approach usually starts with larger bulk materials, and the micro- or nanoscale is reached by, for example, cutting or etching.[4] This approach is mainly used in industry, for example, to manufacture metal oxide semiconductors on silicon wafers through photolithography.[5] An alternative route is the bottom-up approach, which is based on small building blocks like atoms or molecules that can assemble into the desired structures. It is used when top-down approaches are limited.[4]

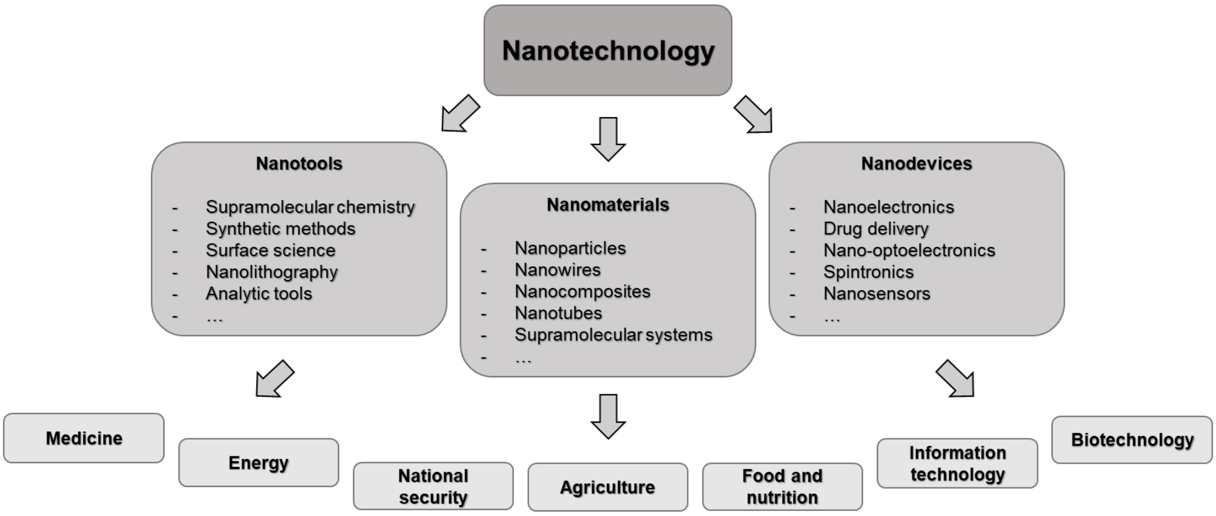

Figure 1. *Schematic illustration of the fields impacted by nanotechnology, its tools, materials, devices, and possible applications.*[3]

1.1.1 Natural supramolecular nanomaterials

Several components in nature and in living systems have sizes in the nanometer range (figure 2). For example, proteins fold into their unique, functional tertiary structure and are also able to self-assemble into nanoscaled quaternary structures with sizes of a few nanometers.[6] The DNA (desoxyribonucleic acid) double helix is another nanoscaled material with a diameter of a few nanometers and an average persistence length of around 50 nanometers in an aqueous solution formed by hydrogen bonds of complementary nucleic acids of single-stranded DNAs.[6,7] Viruses, like the tobacco mosaic virus, are formed from different components such as proteins and RNAs (ribonucleic acids) that are assembled in a controlled fashion forming the distinct three-dimensional structure.[6] Typically, a virus consists of an outer shell of assembled proteins (capsid) and an inner region consisting of the viral genome. The most common viruses have icosahedral or helical symmetries.[6,8]

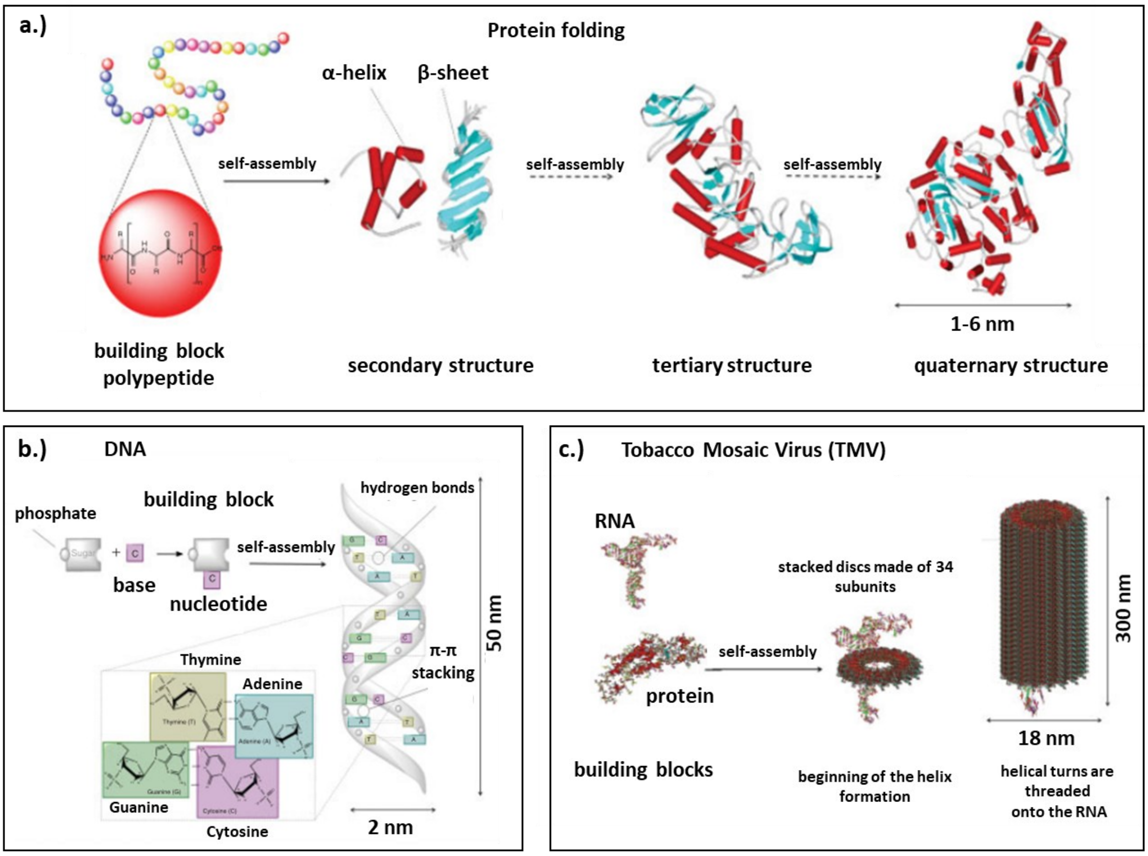

Figure 2. Examples for supramolecular assemblies with sizes in the nanometer range occurring in nature. (a) Protein folding, (b) double-stranded DNA, and (c) tobacco mosaic virus.[6] Figure adapted from [6], with permission from John Wiley & Sons, Inc.

These natural materials are formed in a bottom-up process by the self-assembly of smaller building blocks, such as polypeptides, into defined supramolecular structures by non-covalent interactions. A single supramolecular attraction is weak (2-250 kJ/mol) compared to a single covalent bond (100-400 kJ/mol). Still, it allows the stable and dynamic assembly if these interactions act collectively.[6] For the self-assembly of nanostructures, non-covalent bonds such as hydrogen bonds, aromatic interactions via π-π-stacking, van der Waals interactions, and electrostatic interactions play important roles.

Nature's ambitions to create functional systems on the nanoscale serve as an inspiration for nanomaterials research. Therefore, it is not surprising that nanoscaled materials are of high interest for various applications, such as in medicine.[9] Influencing cellular processes on the nanoscale could be beneficial for future treatment of diseases i.e. in regenerative medicine. Peptides are ideal for the fabrication of nanomaterials as they are relatively simple and easy to prepare and offer good biocompatibility and -degradability.

1.2 Peptide-based nanomaterials

1.2.1 Peptides as small building blocks

Peptides are relatively small molecules composed of amino acids. In organisms, peptides and proteins consist of typically 22 different proteinogenic amino acids that are recognized by the cellular machinery and used for the build-up of proteins. A summary of these 22 amino acids and a categorization into different groups due to their properties is given in figure 3.

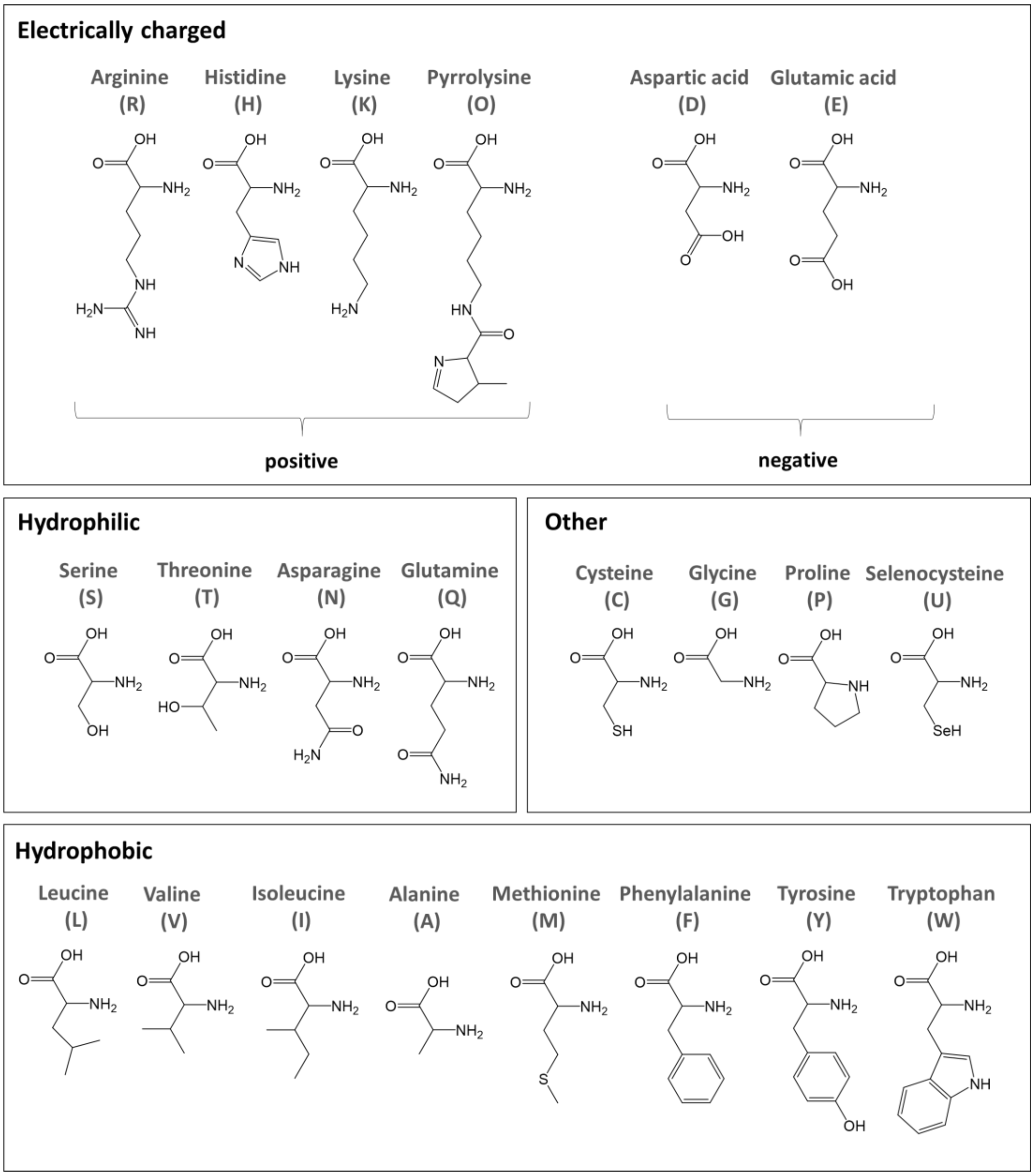

Figure 3. *Categorization of the 22 proteinogenic amino acids as molecules for peptide synthesis.*[10]

Peptide-based nanomaterials are mainly formed by self-assembly via non-covalent interactions. They represent ideal building blocks for creating nanomaterials due to their accessibility, tunability, and their easy and scalable synthesis since the development of solid-phase peptide synthesis by Merrifield.[11]

Even small peptides like dimers were shown to self-assemble into high-ordered structures.[12] Theoretically, the 22 proteinogenic amino acids allow 22^6 possibilities (~113 million) of different peptide sequences for a 6-mer, which can be expanded even further by using artificial building blocks like chemical modified amino acids.[13] Due to the almost endless number of possible combinations, there is a high potential for optimization. Still, it is also rather difficult to systematically investigate the relationship between primary sequences and properties of peptides and their assemblies.

Self-assembling peptides (SAPs) were shown to adopt several nanostructures like nanotubes, spherical particles, fibrils, discs, or ribbons, offering the potential for a wide variety of possible shapes.[14–16] In general, SAPs can be grouped into natural and artificial systems. Natural peptide nanostructures adopt conformations, which can be found in proteins like α-helices, β-sheets, and random coils (figure 4). Non-natural systems, for example, use amino acids linked to fatty acids (peptide amphiphiles) or to aromatic groups to introduce π-π-interactions that assemble into nanoscaled structures with different shapes.[17] Peptides can assemble based on different supramolecular interactions of the peptide backbone or the different side-chains. These interactions can occur both intermolecularly and intramolecularly. The primary sequence can adopt different structural elements. These structures are called secondary structures. A common secondary structure that a peptide or protein can adopt in nature is an α-helical conformation (figure 4a). It is a spiral-like conformation that is stabilized by a hydrogen bond between the N-H of one amino acid and the C=O of another amino acid four positions further. Side-chains can also influence self-assembly behavior through additional non-covalent forces or steric effects.[10,18] If three peptide chains form a higher-ordered structure with the same axis, the resulting construct is called a triple helix, which is found in collagen (figure 4b).[19] Another common motif found in nature is a β-sheet (figure 4c). It is formed by several β-strands, which can be oriented either parallel or antiparallel and is stabilized by hydrogen bonds in the backbone.[10] Several disease-related amyloid fibrils consist mainly of β-sheets.[20]

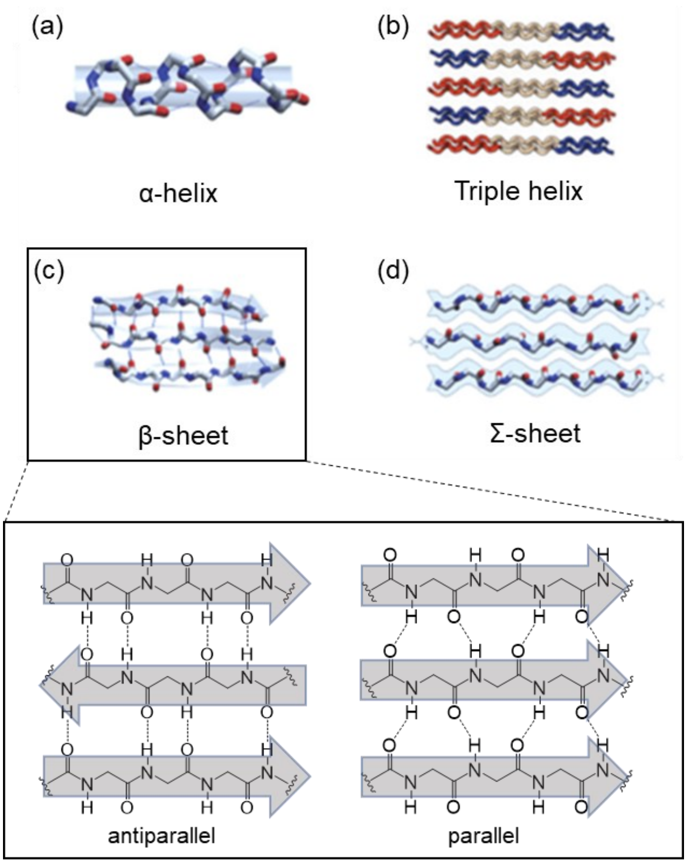

Figure 4. *Different possible secondary structures, which peptides can adopt.*[10,21,22] *(a, c, d) Adapted from [22], with permission from Springer Nature. (b) Adapted from [21], with permission from American Chemical Society (ACS).*

If two linked β-strands are oriented antiparallel, a β-turn is formed. β-Turns are very similar to β-sheets with an intramolecular folding. Recently, a new secondary structure was found for peptoids called Σ-strand (figure 4d). These peptoids carry the specific side group at the nitrogen atom instead of at the α-carbon. The structure of Σ-strands is based on β-strands with a rotational-state motif.[10] There are several other possible secondary structures, which occur in lower frequency compared to the ones described herein.[10,23] In the following chapter, amyloid fibrils as unique nanostructures occurring in nature are discussed. Furthermore, some examples of well-investigated and widely used artificial nanomaterials based on SAPs are introduced in chapters 1.2.3 and 1.2.4. Since the peptides investigated in this work highly tend to form β-sheets, relevant related systems in literature are discussed only. There are also many peptides, which tend to form different secondary structures like α-helices as a key structural element in their assemblies, which is not part of this work.[24]

1.2.2 Amyloid fibrils

Amyloid fibrils are unique peptide nanostructures based on the self-assembly of peptides or proteins, forming nanostructures with high β-sheet content. They occur in living systems as both a functional and a pathogenic material linked to several human diseases. Amyloid nanostructures revealed several unique features, and they served as a natural inspiration for artificial SAP-systems.

The term amyloid is derived from the Greek word amylon (“starch”) and was initially used by Matthias Scheiden to describe amylaceous parts in plants.[25] In 1854, Virchow first reported the term “amyloid” in a medicinal context to describe pathogenic deposits, which could be stained by iodine.[26] Later, those amyloids were found not to be “starch-like”, but to be proteinaceous.[25,27]

Amyloids were mainly linked to a group of systemic diseases in the past termed “amyloidosis”. Amyloid fibrils are the main component of amyloid deposits. Today, the term “amyloid” seems to be more challenging to use, since the research area expanded from an earlier only pathogenic phenomenon to a broader field. The nomenclature committee of the International Society of Amyloidosis suggested defining amyloids as “extracellular depositions of protein fibrils with characteristic appearance in electron microscope, typical X-ray diffraction pattern, and affinity for Congo red with concomitant green birefringence”.[28] In the following, several important characteristics of amyloids are discussed. Other fibrillar systems are referred to as peptide nanofibrils with amyloid characteristics to differentiate from the more pathogenic materials.

Amyloid fibrils are polypeptides, which generally exhibit a cross-β-sheet conformation as a structural key feature. Such fibrils are rich in β-sheets, where the β-strands are oriented perpendicular to the fibril axis. Those β-strands are stabilized by hydrogen bonds. The cross-β-sheet structure was first shown by X-ray studies of amyloid fibrils in 1961 and revealed a 4.7 Å repeating unit.[29] Today, it is known that many amyloid fibrils have a 4.6 to 4.8 Å spacing between the β-strands and a more variable spacing between two β-sheets with 5 to 12 Å in its diffraction pattern by X-ray analysis, where the more variable equatorial spacing is also caused by various side-chains of different amino acids.[30–33] Mature fibrils typically consist of so-called protofilaments or protofibrils, which are intermediates and can be twisted together (figure 5).[34,35]

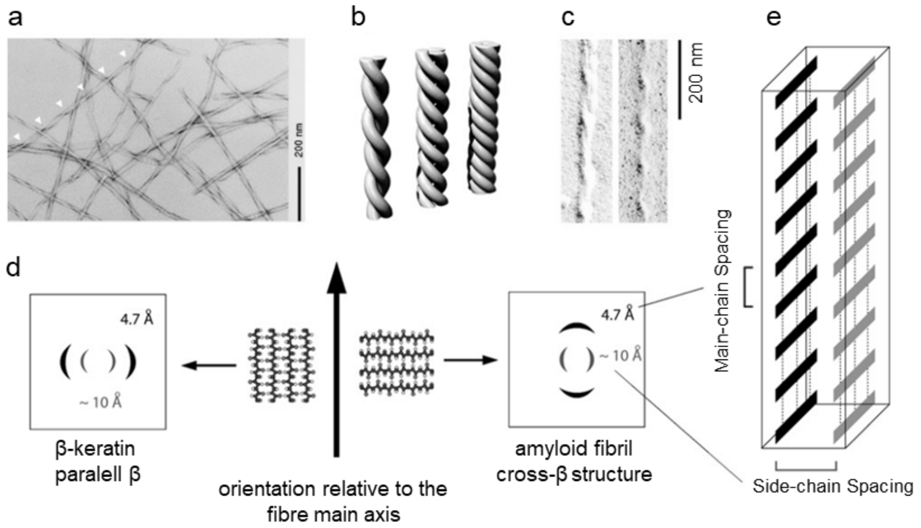

Figure 5. *Structural features of amyloid fibrils. (a) Transmission electron micrograph of Aβ (1-40) amyloid fibrils. (b) Schematic of fibrils formed by 2, 3, and 4 protofilaments. (c) Transmission electron micrograph of Aβ (1-40) amyloid fibrils after platinum side shadowing with a left-handed chirality. (d) Schematic X-ray diffraction pattern of parallel β and cross-β structures. (e) X-ray diffraction-based protofilament structure.*[36] *Figure adapted from [36], with permission from Springer Nature.*

Different models are describing the mechanism of amyloid fibril formation. Generally, amyloid fibrils follow a nucleated-growth mechanism. Aggregation into amyloid fibrils is highly dependent on environmental factors.[37] Furthermore, the kinetics of these aggregation processes were shown to be dependent on protein concentration.[38] Aggregation occurs over a broader time window with multiple pathways and involves several conformations.[37] The nucleation-elongation polymerization can be categorized into three steps: (i) the lag or nucleation phase, (ii) the elongation or growth phase, and (iii) the saturation phase.[37,39,40] In the nucleation phase, critical nuclei are formed. These nuclei represent the smallest stable, aggregated species, where monomer addition is faster than dissociation.[41] Nuclei have the highest free energy in the whole process.[41] The nucleation phase can be modified by adding pre-formed nuclei or aggregates, which is called seeding.[41,42] For amyloids, it was shown that both primary nucleation and secondary nucleation occur. Primary nucleation involves monomers of one species only to grow in solution (figure 6a) or on a foreign surface (figure 6b), while in secondary nucleation also aggregates of this species play a key role (figure 6c).[43,44] In an elongation step, monomers add to a fibril’s end (figure 6d). This phase proceeds rapidly due to the formation of thermodynamically more favored protofibrils.[37] In the saturation phase, the concentration of monomers is constant and protofibrils assemble into matured fibrils.[37]

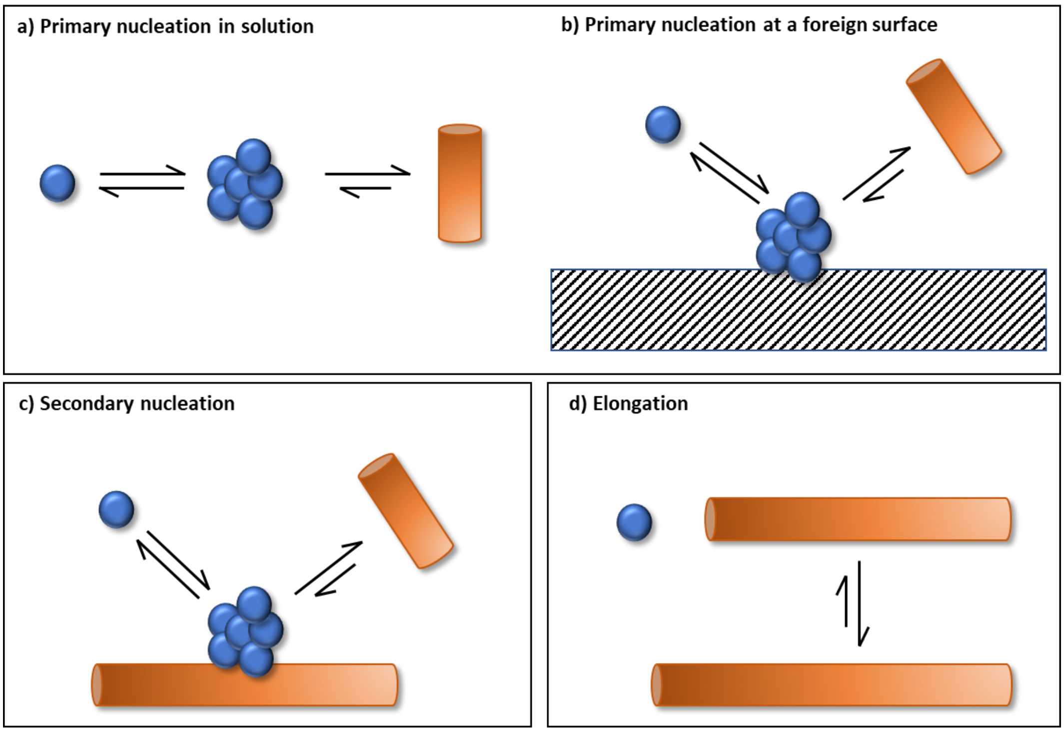

Figure 6. Schematic of primary nucleation, secondary nucleation, and elongation. Primary nucleation can occur (a) in solution and (b) at a foreign surface and only involves monomers of one species. (c) Secondary nucleation can occur on existing aggregates of the same substance. (d) Elongation occurs by adding monomers to a fibril's end. Blue spheres represent monomers, whereas orange cylinders represent fibrils.[43]

1.2.2.1 Amyloids and diseases

As mentioned above, amyloids were initially associated with several systemic diseases. The first amylogenic disease, the so-called Alzheimer's disease, was reported in 1901 by Alois Alzheimer.[45] In his work, Alzheimer investigated post-mortem amyloid plaques, including positive staining with Congo red. Today, more than 50 diseases related to *in vivo* amyloid formation are known, including several neurodegenerative ones like Alzheimer's or Huntington's disease.[46] The following table gives an overview of some amyloid-related diseases and their involved proteins or peptides (table 1).

***Table 1**: Some examples of amyloidosis and their in aggregation involved proteins or peptides.*[46]

Disease	**Aggregated protein or peptide**	**Amino acids**
Alzheimer	Amyloid-β peptide	40 or 42
Parkinson	α-synuclein	140
Huntington	Huntingtin with polyQ expansion	3144
Type II diabetes	Amylin	37
Cataract	γ-crystallins	various
Familial British dementia	Abri	23
Spinocerebbelar ataxias	Ataxins with polyQ expansion	816

Besides those neurodegenerative diseases, others were also found, like diabetes type II, which are linked to amyloid formation. In type II diabetes, the peptide amylin forms amyloid plaques.[47] Amyloidosis can occur in several tissues and organs. Alzheimer amyloid plaques, for example, occur in the brain. In AL amyloidosis, amyloid deposits were found in the kidney and heart formed by antibody light chains.[48] In general, amyloidosis becomes more prevalent with age. The increased number of patients in today's society can also be linked to increased life expectancy due to better life standards and modern medicine. The majority of amyloidosis is linked to misfolding of native proteins, and it is still a major challenge to identify the exact mechanism of toxicity for better treatment of amyloidosis. Early reports suggested that the amyloid plaques themselves correlate with harmful behavior, but recent studies have shown that already the existence of pre-amyloids can cause damage. Several studies showed that amyloid oligomers are able to bind to cellular membranes and cause, for example, harmful Ca^{2+} dysregulation.[49,50]

1.2.2.2 Amyloid fibrils as building blocks for natural and functional materials

For a long time, amyloid fibrils were mainly associated with diseases. However, in recent years, it was shown in several examples that amyloid fibrils can also fulfill useful functions in living systems, like in bacteria or even in humans.[51–55] Table 2 summarizes several organisms using protein-based amyloid fibrils as a functional material.

***Table 2:** Overview about functional amyloid-like fibrils in nature, their involved proteins, and their function.*[54]

organism	protein	function
bacteria		
Escherichia coli	Curli	biofilm formation, adhesion
Bacillus subtilis	TasA	biofilm formation
Streptomyces coelicolor	Chaplin	modulation of water-surface tension
fungi		
Neurospora crassa + other	Hydrophobins	fungal coating
Podospora anserina	HET-s	heterokaryon regulation
Saccharomyces cerevisiae	Ure2P	nitrogen regulation
animals		
silk moth	Chorion proteins	protective function
humans		
	Pmel17	melanin biosynthesis support
	various peptide hormones	storage and controlled release
	PAP	quality control of semen

For example, amyloid fibrils were found in bacteria biofilms like in Escherichia coli.[56] The so-called curli fibers promote adhesion and enable surface colonization of bacteria.[55] Furthermore, curli were also shown to mediate internalization by eukaryotic cells.[57] Analogous fibrillar systems were shown for other bacteria like Bacillus subtilis, where TasA fibrils support the structural integrity of biofilms or in Streptomyces coelicolor, where chaplin fibrils lower the water-surface tension.[58,59] Besides bacteria, amyloid fibrils were also found in some fungi species.[60] In several fungi like Neurospora crassa, amyloid fibrils formed by hydrophobic proteins play a crucial role in fungal coatings, which support surface adhesion.[61,62] HET-s amyloid state of Podospora anserine is involved in heterokaryon regulation.[63] In Saccharomyces cerevisiae, amyloids formed by Ure2P are involved in nitrogen regulation.[64] Besides being used as a functional material in lower organisms, amyloids from chorion proteins were also shown to support the protection of silk moth oocyte and embryos.[65] In humans, functional amyloids also exist, playing important roles in melanin biosynthesis. Herein, amyloids are formed by the melanosomal protein pmel17 under physiological conditions.[53,66] Melanin is a pigment and occurs in two types, the brown to black colored (eumalin) and the yellow to red colored (pheomelanin), which both are derived in a complex synthesis by L-tyrosine in melanosomes with support of tyrosinase.[67]

Melanin plays a crucial role in protecting the skin from UV radiation. Pmel17 fibrils are suggested to act as a scaffold for melanin synthesis and concentrate reactive intermediates, including toxic precursor molecules, and prevent their diffusion, thereby accelerating polymerization. Pmel17 fibril formation is a complex intracellular process, and it is well-controlled to prevent cytotoxicity.[53] Furthermore, peptide hormones were found to be stored in secretory granules in an amyloid state with controlled release of monomeric hormones, underlining amyloid's dynamic behavior.[68] In human semen, amyloids formed by fragments of the prostatic acid phosphatase were found.[69] Deeper investigations revealed that these fibrils not only increase viral uptake but also play a functional role participating in quality control of sperm such as promoting sperm selection by macrophages, but they also play a key role in clearing the lower reproductive tract.[69–71]

1.2.3 Peptide amphiphiles

Peptide amphiphiles (PAs) are another class of peptide molecules that undergo β-sheet interactions. They are non-natural, rationally designed building blocks for the self-assembly into high-ordered structures. In general, they consist of a hydrophobic and a hydrophilic segment. One of the first and best-studied PA-systems was developed by Jeffrey Hartgerink in the laboratory of S. Stupp.[72] These rationally designed PAs consist of up to four domains. The first segment is a hydrophobic alkyl tail. The second domain consists of an oligopeptide providing intermolecular hydrogen bonds to support β-sheet formation. The third segment consists of charged amino acids to increase solubility in aqueous solvents and offer responsiveness to changes in ionic strength and pH of the solution (figure 7). Furthermore, there is the possibility to add a fourth domain at the hydrophilic end with functional groups, e.g. bioactive epitopes, which should assemble at the fibril surface.[72,73]

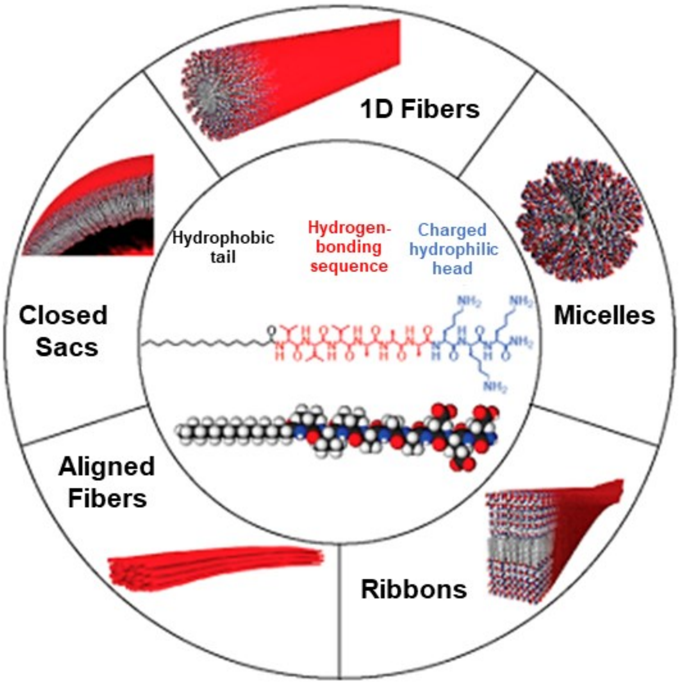

Figure 7. *Design of PAs and selection of possible nanostructures which can be adopted.*[74] *Figure adapted from [74], with permission from American Chemical Society (ACS).*

These PAs were shown to self-assemble into various nanostructures like fibrils, micelles, or ribbons. In the following, especially PAs forming fibrils are discussed. Due to the design principles, self-assembly is driven by the collapse of the hydrophobic alkyl segment in aqueous media, the hydrogen bonds and side-chain interactions of the second peptidic pattern, and electrostatic repulsion between charged amino acids in the third domain.[73] In-depth structure analysis with different techniques revealed the formation of β-sheets with parallel orientation in respect to the fibril axis with altered internal order dependent on the molecular structure of the PA.[75] Those SAPs furthermore revealed interesting dynamic behavior. Mixing, for example, of complementary charged PAs resulted in the formation of co-assemblies. This allows the generation of tailored fibrils based on different monomers to incorporate different functionalities into a single fibril.[76,77] FRET technique and stochastic optical reconstruction microscopy (STORM) revealed a dynamic exchange between different individual fibrils. Therefore, PAs were functionalized with the fluorescent dyes Cy5 and Cy3 and fibrils of each functionalized PA were formed. After mixing, two-color STORM experiments showed the exchange of both monomers and small clusters.[78] Interestingly, this behavior was not found in all areas of the fibrils, implicating a structural diversity.[78] Beyond the molecular design and its resulting nanostructures, the behavior of these fibrils to create materials in the macroscale was investigated. Stupp et al. showed that these PA nanostructures are able to form gels in aqueous media under charge-screening conditions by the addition of metal salts. Furthermore, the gelation kinetics were adjustable by altering the PA's molecular structure, and these gels are promising injectable biomaterials.[73,79,80] Thermal annealing followed by slow cooling can yield long fibrils that can be aligned into centimeter-scale strands by drawing them from a pipette into an aqueous salt solution.[73,74,81]

The nanostructures formed by PAs are highly tunable and offer an exciting tool box, especially for medical applications.[73] Stupp et al. investigated PA-derived nanostructures for several applications. PA-derived nanofibrils can serve as a template for mineralization reactions. Such PAs were designed with a phosphoserine functionality and serve for the nucleation of cadmium sulfide crystals.[82] Furthermore, these PAs were used to serve for enzymatic harvesting of phosphate ions to nucleate hydroxyapatite on the fibrils' surface for biomimetic mineralization.[83] PA-derived fibrils are also very suitable for drug delivery. For example, PAs were used to encapsulate the anticancer drug camptothecin, which is normally poorly soluble and whose solubility was increased 50-fold in its encapsulated form.[84,85] Increased anticancer activity was observed *in vitro* and in an *in vivo* mouse model for breast cancer.[85] In another approach, PAs were covalently conjugated to drugs using a hydrazone linker, which is hydrolyzable in aqueous media to release the drug in a controlled fashion.[86] Gels of such modified PAs revealed drug release over a period of several weeks due to hydrolysis.[87] Another study described the usage of a PA nanofiber gel for delivery of carbon monoxide (CO). Ruthenium glycinate, a well-known compound for spontaneous release of CO in aqueous media, was linked to PAs, and gels were formed and injected into the desired area. Cardiomyocytes, which were under oxidative stress had significantly improved viability.[88] PAs were also shown to improve neural regeneration.[73,89–92] To track PAs *in vivo* in a non-invasive approach, PAs were synthesized with covalently linked 1,4,7,10-tetraazacyclododecane1,4,7,10 tetraacetic acid (DOTA). DOTA is a chelate ligand and allows the complexation with Gd(III), which can be tracked via magnetic resonance imaging (MRI). The DOTA modified PAs were still suitable to self-assemble into nanostructures and could be imaged by MRI.[93] PAs also revealed increased regeneration of bone tissue. Therefore, a porous titanium scaffold was filled with PAs, which is suitable for implants.[94] Furthermore, these hybrid materials increased attachment and migration of pre-osteoblasts.[95]

To summarize, rationally designed PAs offer a great toolbox for the fabrication of fibrillar nanostructures with diverse functions. Those fibrils can mimic the extracellular matrix and have been applied successfully in various applications, such as in regenerative medicine. Further functionalization of PAs with, for example, bioactive groups or fluorescent markers allow the fabrication of tailored nanomaterials with various functionalities. Additionally, PA-based systems offer the possibility to create gels as a 3D-scaffold.

Another exciting peptide-based system is RADA-16 and its derivatives. These peptides are comparable to PAs, but they only consist of amino acids with an amphiphilic pattern. Such hydrogel-forming peptides based on short self-assembling peptide sequences were first reported in 1993 by Zhang et al. inspired by the EAK16-II sequence, a fragment of the Z-DNA binding protein in yeast.[96] Until today, many studies were published on this family of SAPs. The most common one is the well-studied polypeptide RADA-16 with the sequence RADARADARADARADA, which combines positively charged arginines (R), hydrophobic alanines (A), and negatively charged aspartic acids (D). This alternating motif promotes the formation of β-strand nanostructures.[96,97] RADA-16 forms fibrils in aqueous media with a diameter of 6-10 nm.[98] In-depth investigations of such fibrils revealed the formation of parallel β-sheets.[97] Those fibrils can arrange to form a hydrogel scaffold mimicking the ECM with pore sizes in a range of 5-200 nm.[98] RADA-16 systems revealed several features like high biocompatibility, the possibility to degrade into its biocompatible building blocks, or low immunogenicity, which makes them attractive for biomedical applications.[98]

Therefore, these fibrils and hydrogels were used in various medical and regenerative applications. The following figure 8 gives an overview of tissue engineering applications for RADA-16.[98]

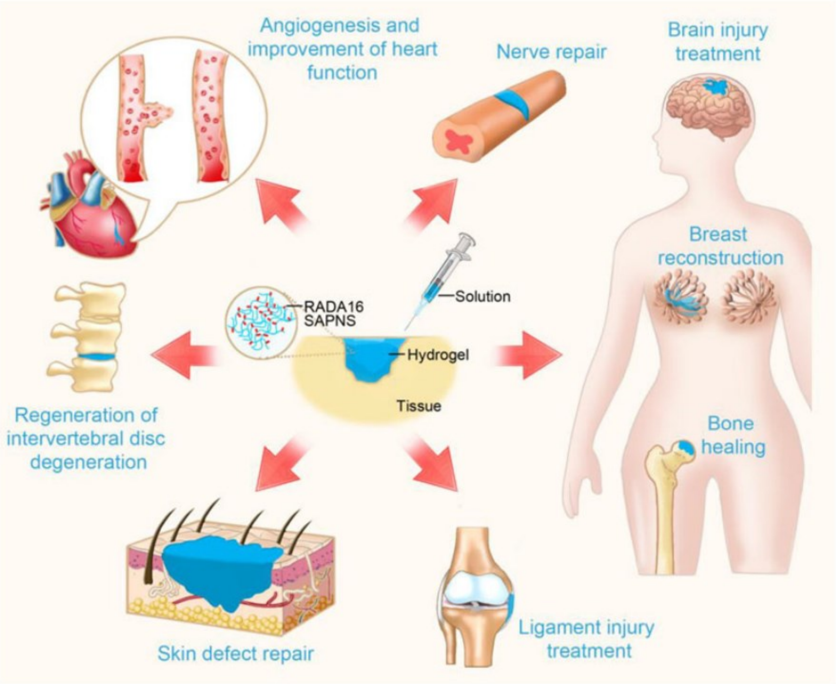

Figure 8. *RADA-16 and modified derivatives as a peptide hydrogel for tissue engineering. RADA-16 allows the formation of gels, which can be injected into various damaged tissues like nerves, skins, or bones to support regeneration locally.*[98] *Figure reprinted from [98], with permission from Taylor & Francis (www.tandfonline.com).*

RADA-16 systems were shown in several studies to support neural regeneration. [99,100] RADA-16 also revealed its potential, for example, in bone regeneration. A study described a multifunctional RADA-16-based system using three functional motifs. Osteogenic growth peptide ALK, osteopontin cell adhesion motif DGR, and the RGD binding motif PGR were linked to the peptide.[101,102] These multifunctional scaffolds enhanced mouse pre-osteoblast cell proliferation and differentiation in an efficient fashion.[103] In another approach, RADA-16 was used to successfully support skin repair as shown by the improved proliferation of skin-derived precursors.[104] RADA-16 was furthermore used for breast reconstruction.[105] Herein, RADA-16 hydrogels were loaded with the antitumor substrate tamoxifen and human mesenchymal stem cells.[105] Additionally, RADA-16 was also suitable for drug delivery. One study, for example, described the controlled release of lipophilic drugs from a RADA-16 hydrogel.[106] In another study, modified RADA-16 hydrogels were used for the controlled release of the anti-cancer drug 5-fluorouracil.[107]

All in all, the RADA-16 system is a well-studied toolbox for the fabrication of gels consisting of self-assembled nanofibrils. RADA-16 offers many possibilities to functionalize its side chains or its termini with various groups without harming self-assembly behavior by co-assembly of RADA-16 and modified RADA-16.[99] Until today, RADA-16 is mainly used in biomedical applications, especially as a 3D cell culture scaffold, and has beneficial effects on the differentiation of several cell types.[98] However, synthesis of RADA-16 is comparable difficult in high yields and purities, as some studies revealed.[108]

1.2.4 Short aromatic self-assembling peptides

Short aromatic peptides offer another class of promising building blocks for creating nanosized structures and materials. Diphenylalanine (FF) is one of the best-studied peptides in this class and has broad applicability (figure 9).[14] It is inspired by nature's amyloid fibrils. For example, in β-amyloid, FF is part of the core sequence.[14,109] FF-based building blocks can form a broad range of supramolecular nanostructures like nanofibrils or nanotubes.[14]

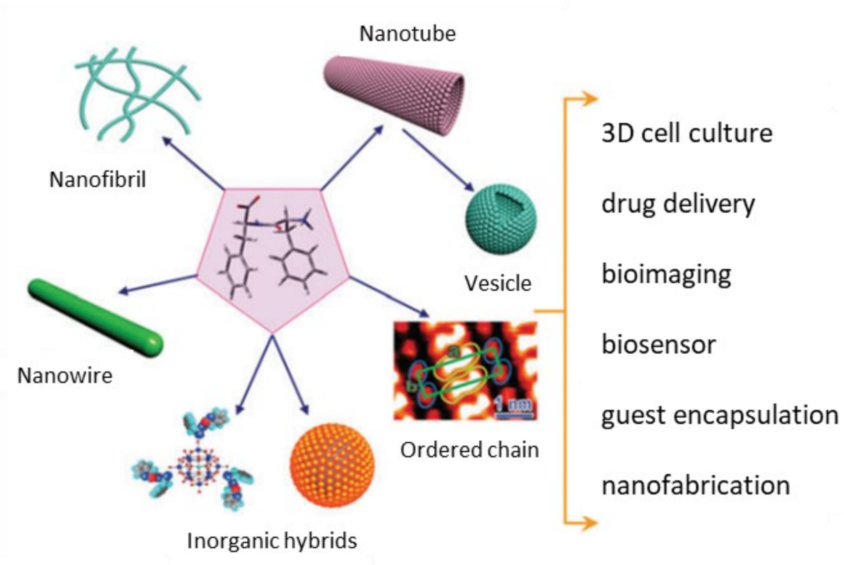

Figure 9. *Variety of nanostructures based on the self-assembling of the FF dimer and its range of applications.*[14] *Figure adapted from [14], with permission from Royal Society of Chemistry.*

FF is one of the simplest self-assembling peptidic building blocks. It can self-assemble into highly-ordered nanotubes through a combination of hydrogen bondings of the peptide backbone and π-π stacking due to the aromatic side-groups. Those well-ordered tubes are very stable against heat treatment.[109,110] Further investigations of these tubes revealed a very high rigidity with a Young's modulus of around 19 GPa compared to, for example, natural microtubules of the cytoskeleton with a Young's modulus of 1 GPa.[111,112] The resulting morphology of FF-assemblies as well as their formation kinetics are highly dependent on the solvent.[113] Furthermore, FF nanotubes are suitable building blocks for macroscaled materials. For example, they were shown to vertically align by controlled film growth in a dense order, and a spatial horizontal alignment could be reached by using a magnetic field.[114–116] Addition of small functionalities at the N-terminus was further reported to affect self-assembly and its resulting morphology.[117] Fmoc-FF was shown to self-assemble into nanofibrils in water, and it can also form gels.[118] These hydrogels are remarkably stiff and rigid with ordered peptide chains in an antiparallel β-sheet structure.[119] Another study revealed that the substitution of phenyl alanines with derivatives modified by various lengths between the α-carbon and the side-chain phenyl ring affected self-assembly behavior.[120] Functionalization of the phenyl ring with, for example, halogen substituents also revealed altered self-assembly behavior.[12] In addition, FF can co-assemble with other small aromatic peptides. A study reported the co-assembly of FF and FFF at different ratios and revealed changes in morphology that can be advantageous for controlling self-assembly and resulting structure.[121] It was also reported that functionalization with boronic acids resulted in a pH-dependent self-assembly behavior, which can be used for the functionalization with polyols.[122]

Such FF-based nanomaterials have a high potential for several applications. For example, FF-based nanofibril hydrogels can mimic the extracellular matrix and are suitable for 3D cell culturing and several biomedical applications.[118] They were also used for drug delivery, for example, to transport oligonucleotides.[123] Combination of FF nanotubes with quantum dots allows the usage in bio-imaging methods.[124] Additionally, Fmoc-FF was mixed with Fmoc-RGD to incorporate another functional motif, and 3D-gels were fabricated, where RGD-groups are presented on the fibrils' surface.[125] The combination of such functionalities makes this system a promising material for cell studies.

FF-nanotubes were also used in more technological fields, for example, for the fabrication of nanowires. Silver ions were reduced in FF-nanotubes and the peptide backbone can be enzymatically degraded resulting in silver nanowires with high persistence lengths.[109] With a similar approach, even co-axial metal nanowires can be fabricated.[126] Electrodes modified by FF-peptide nanoforests showed promising results as a biosensor with enhanced sensitivity compared to uncoated electrodes.[127]

FF-based nanomaterials offer a variable toolbox for several material science and biomedical applications. Functionalization affects the self-assembly behavior in several studies and has the potential to control the self-assembly process and its resulting structures. FF and its derivatives can adopt various nanostructures from tubes to fibrils and can be even aligned and used as tailored nanomaterials. FF can also co-assemble with other aromatic, short peptides, allowing the control of its structure and the incorporation of additional functionalities.

All in all, peptide-based nanomaterials offer a highly versatile and promising tool for several applications, especially for medicine. In chapter 1.3, an introduction to peripheral nerve injuries and gene therapy is given. Peptides used in this thesis were applied in both models to investigate their behavior in different cellular environments.

1.3 Potential applications for peptide-based nanomaterials

1.3.1 Peripheral nerve injuries

The human nervous system consists of two parts, the peripheral and the central nervous system. The central nervous system primarily consists of the brain and the spinal cord. In contrast, the peripheral nervous system (PNS) consists of the nerves outside this area, such as the spinal nerves connected to the spinal cord. The primary function of the PNS is to combine the peripheral nerves in the body with the more protected central nervous system.

Peripheral nerve injuries (PNI) are relatively common and impact many individuals. In the USA, for example, 350,000 people suffer from PNIs per year.[128] PNI is caused by several reasons, including different kinds of accidents, such as with knives, during sports, at work, and also with vehicles.[129,130] The body’s own potential for nerve regeneration and full recovery is often limited. Thus, the development of suitable methods for treating peripheral nerve injuries is of high interest, also because of the high complexity of such injuries, which can occur at different levels throughout the body.

Several approaches have been developed to treat PNI. The most common method to treat PNIs is nerve surgery, which dates back to 1608 when Ferrara performed the first reconstruction of a cut.[131] Although progress has been made in recent decades, is a full recovery often limited. Several surgical approaches are used to treat injuries of the PNS. In general, successful repair and the kind of surgical approach depend on several factors like time of surgery after an injury and associated injuries, age, and health of a patient.[132]

The gold standard to treat PNI is microsuturing (figure 10a), where nerve stumps are sutured together. Like most surgical methods, it is important to proceed within a short period of time after injury to increase the chance of successful repair. Suturing is dependent on the kind of damage and location in the body as well as the individual ability of the surgeon. Furthermore, the correct guidance of axons, the nerve fibers responsible for transmitting information between neurons, is necessary.[129,132] If nerve gaps are larger or tissue is lost, suturing is not always the method of choice. The gold standard for treating large gaps between nerve endings is the usage of nerve grafts to bridge the gap (figure 10b). The first reported use of an allograft was in 1885 by Albert.[133] This technique uses tissue material or nerves from human cadavers and does not require harvesting of the body’s tissue, but it could cause undesirable immune responses.[134] Autologous nerve grafts can overcome these limitations of immune response by harvesting a nerve graft from the patient's body. Millesi initially demonstrated these benefits in 1967 in animal experiments.[134,135] The most commonly used autograft is derived from the sural nerve of the lower part of the knee.[129,136]

A further concept is the application of nerve guide conduits (NGC, figure 10c). This was first shown in 1881 by using a hollow bone to bridge a nerve gap in a dog model.[134] The idea behind a NGC is to bridge a nerve gap, guide regeneration, and protect this process from the outside.[134,137,138] NGCs should support axon regeneration but also speed it up.[134]

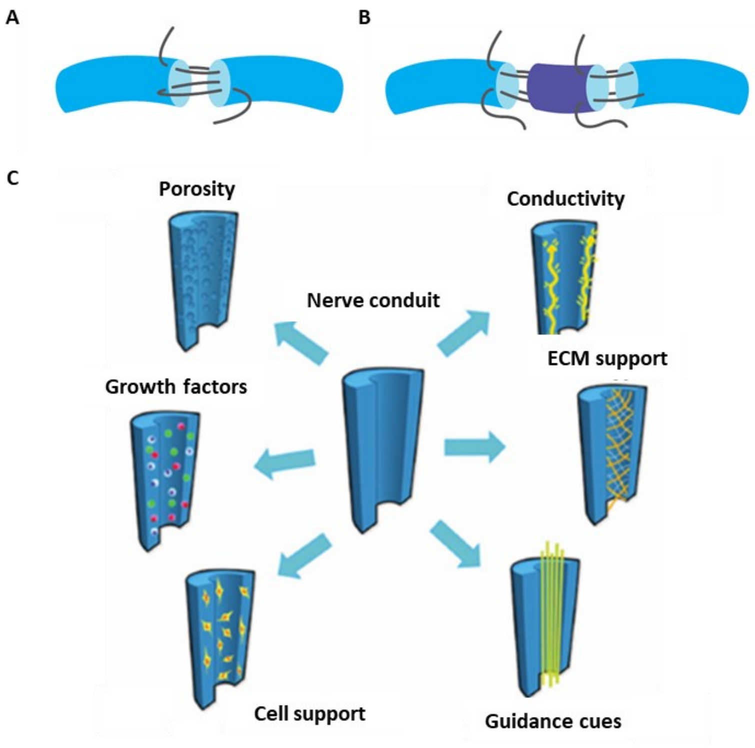

Figure 10. *Current approaches for the treatment of nerve injury. (A) Microsuturing, (B) usage of nerve grafts, and (C) usage of NGCs.*[139] *(C) Adapted from [139], published under CC-BY 4.0, https://creativecommons.org/licenses/by/4.0/.*

The first hollow NGCs provided only poor regeneration.[140] In the last decades, there have been several approaches to generate improved NGCs by incorporating permeability, multichannels, or conductive polymers. NGCs should provide biocompatibility but also biodegradability.[129,134] Recent NGCs are fabricated by natural as well as synthetic materials. Natural NGCs, for example, were produced with collagen[141] or chitosan[142]. Examples of synthetic polymers are PGA[143], PLGA[144], or PCL[145]. The addition of cells, especially Schwann cells, to such tubes can support regeneration.[146] Furthermore, also nerve growth factors were added to NGCs like nerve growth factor (NGF)[147], glial cell line-derived neurotrophic factor (GDNF)[148], or neurotrophin-3[149] to improve the healing process.

SAPs have shown beneficial effects in nerve regeneration in several studies and may offer an additional treatment option, also in combination with the use of NGCs. Such systems offer the advantages that they can also be used non-invasively, and the design can be modified as desired. For example, peptide amphiphiles (PAs) were shown to improve neural regeneration and recovery. Such PAs were functionalized with the laminin-derived sequence IKVAV, which promotes neurite growth. After modification, these PAs were still able to form peptide fibrils and even gel-like scaffolds. *In vitro* investigations with neural progenitor cells revealed enhanced differentiation into neurons.[150] In another study, PA properties were adjusted to understand their bioactive behavior better. Stiffness was varied and revealed an important role in using PA substrates with an altered molecular structure to cultivate hippocampal neurons.[73,89] In addition to these *in vitro* applications to investigate the suitability of PA systems, animal models have been established. IKVAV PA gels revealed beneficial effects in a mouse model. Furthermore, IKVAV PA gels were injected in a spinal cord injury and supported healing.[90] A multifunctional IKVAV PA gel containing the brain-derived neurotrophic factor (BDNF) was investigated in a rat model and revealed improved regeneration.[91] The use of aligned PA fibrils with encapsulated sonic hedgehog had beneficial effects in the regeneration of the cavernous nerve.[92] Furthermore, RADA-16 systems were used for the treatment of damaged nerves. RADA-16 was functionalized with the IKVAV motif, including a spacer to enhance the flexibility of the bioactive epitope. 3D-scaffolds formed by the self-assembling peptide enhanced proliferation and differentiation of neural stem cells into neurons in an *in vitro* approach.[99] Another study described the functionalization of RADA-16 with mimetics derived from BDNF as well as nerve growth factor (NGF), and different mono-functionalized RADA-16 derivatives were mixed to result in a multifunctional, adjustable hydrogel that was used to culture neurons.[100] Hydrogels obtained by mixing the different RADA-16 species resulted in improved bioactivity and revealed synergistic effects. Improved recovery was found in an *in vivo* model for a 10 mm long sciatic nerve defect in rats.[100]

So far, PNI is still mainly treated by surgery. NGCs are a promising alternative and the focus of recent research. However, the outcome is not comparable to surgery, and NGCs are very expensive. SAPs showed high potential to stimulate the intrinsic regeneration, but they are combined with supporting materials like NGCs or additional growth factors in most approaches. Biomaterial-based approaches without the necessity of further supporting materials, which can be applied directly and cost-efficient, are largely missing and could serve future opportunities to treat PNIs and are also of high interest for various further approaches like gene therapy as described in the following chapter.

1.3.2 Retroviral gene transfer

Besides the promising behavior of SAPs to support nerve regeneration, they also revealed beneficial behavior in other biomedical fields. Fibrillar systems for transporting retroviral particles into cells have recently been shown for treating genetic diseases by introducing genetic material into host cells.[151] Retroviral gene transfer allows the stable and safe introduction of genetic material *in vivo* into host cells.[152] Common retroviral vectors are derivatives of the human immunodeficiency virus 1 (HIV-1) or murine leukemia virus (MLV). MLV vectors can transduce only dividing cells, whereas HIV-1 vectors are also capable of transducing non-dividing cells.[152,153] Retroviral vectors can be generated in specific cells (packaging cells) that synthesize all necessary retroviral proteins and the retroviral particle in the absence of replication-competent viruses. In general, retroviral vectors consist of a transgene, glycoproteins, and structural proteins. Glycoproteins support fusion with host cells, where the transgene is reverse transcribed into double-stranded DNA and subsequently integrated into the host cell's genome.[154] However, retroviral gene transfer is still limited by poor transduction rates mainly due to low virus concentrations as well as inefficient cell attachment caused by electrostatic repulsion between negatively charged viral particles and cell membranes.[154–156] To overcome these limitations, several materials have been used in the past as transduction enhancers. The most common class of materials used for this approach are cationic polymers like polybrene[156]. Still, these substrates often lack biocompatibility. Therefore, there is still a need for other substrates that enhance gene delivery, like liposomes, which were shown to increase viral uptake efficiently.[157] Protamine sulfate, a nature-derived cationic substrate, was also shown to increase transduction rates efficiently.[158] Another commonly used transduction enhancer is the fibronectin-derived polypeptide retronectin.[159] All of these materials mediate the attachment of viral particles to host cells by overcoming electrostatic repulsion. Recently, fibrillar systems have been shown as alternative candidates, which especially offer good biocompatibilities.[154] In a study to investigate semen's role in HIV infection, a cationic amyloid-like fibril was discovered.[69,70] A fragment of the prostatic acid phosphatase, $PAP_{248-286}$, was shown to enhance viral uptake drastically. This peptide is able to form amyloid-like structures with β-sheet-rich composition, and the characteristic fibrils have dimensions of several micrometers in length and high sensitivity towards amyloid-specific dyes like Thioflavin

T or Congo red.[69] Another promising fibril-forming peptide is the so-called enhancing factor C (EF-C). EF-C was discovered by coincidence during investigations of the HIV glycoproteins to develop a peptide-based transduction inhibitor. The 12-mer QCKIKQIINMWQ self-assembled into cationic, β-sheet-rich peptide nanofibrils with amyloid-like characteristics that surprisingly drastically enhanced viral uptake.[151] Such SAPs offer a new class of future retroviral transduction enhancers, and they are more efficient than other materials (figure 11a). Due to the high amount of cross-β-sheet structures, these fibrils revealed a very high stiffness and rigidity than other polymer-based enhancers. The more flexible polymers tend to attach better to the surface of virions and shield negative net charge of the particles more efficiently, which causes reduced transduction rates compared to the rigid fibrils (figure 11b). After fibril-virus complexation, fibrils mediate cell interaction and viral uptake immediately by bridging electrostatic repulsion (figure 11c).

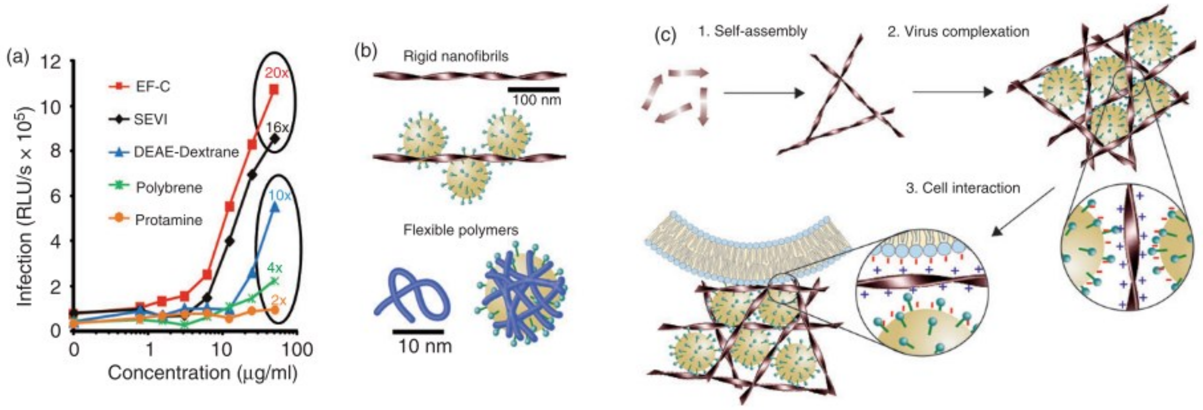

Figure 11. *Proposed mechanism of retroviral transduction. (a) SEVI and EF-C transduction rates compared to other substrates. (b) Schematic description of nanofibrils and their binding to retroviral particles compared to flexible polymers. (c) Schematic description of the virus complexation of nanofibrils and further attachment to cell membranes based on electrostatic attractions.*[151,154] *(a) Adapted from [151], with permission from Springer Nature. (b, c) Reprinted from [154], with permission from John Wiley and Sons, Inc.*

However, even though basic principles for enhanced transduction rates were discovered, there is still less systematic research on how the primary sequence affects self-assembly behavior, nano-structuring, properties, and biological impact. Such SAPs already offer a promising alternative to retronectin *ex vivo* and *in vitro,* especially regarding the simplicity of manufacturing and the lower costs. First studies from mice showed promising results *ex vivo*[151], but for *in vivo* applications, it is still necessary to investigate the fibrils' effects in a living system and their fate.

II Motivation and Goal

Peptides occur in nature in many biological systems and cellular environments in several functions and are essential for many biological processes. Nature perfectly realized the bottom-up approach of small building blocks to create nanoscaled materials and processes. Self-assembling peptides are supposed to offer good biocompatibility and have great potential for the fabrication of programmable, artificial materials that can mimic natural structures, systems, and processes on the nanoscale in a dynamic fashion. Next to these attributes, peptides also offer easily scalable synthesis and high suitability in modification by, for example, functionalization of the terminus or the side chains to extend their applicability. Therefore, they have attracted great interest in the past decades due to their remarkable properties in several technological and biomedical applications.

Many different peptide systems have been described in literature, investigated in great detail, and their sequences have been optimized for specific applications. While research in this area could generate general design rules for SAPs, a systematic understanding of how the primary sequence affects downstream processes like self-assembly behavior, resulting structure and morphology, and final properties is still largely missing. Several approaches are still based on trial and error.

Considering all common 22 natural amino acids without extending to artificial building blocks, nearly endless possibilities are available already for small peptides. Single substitutions of amino acids within small peptides can alter their self-assembly behavior and change the resulting properties dramatically. For a systematic investigation, it is necessary to create a peptide library to gain significant results on the relationship between primary sequence and resulting attributes up to their biological behavior. This could be highly beneficial to obtain a more exact and predictable outcome (figure 12).

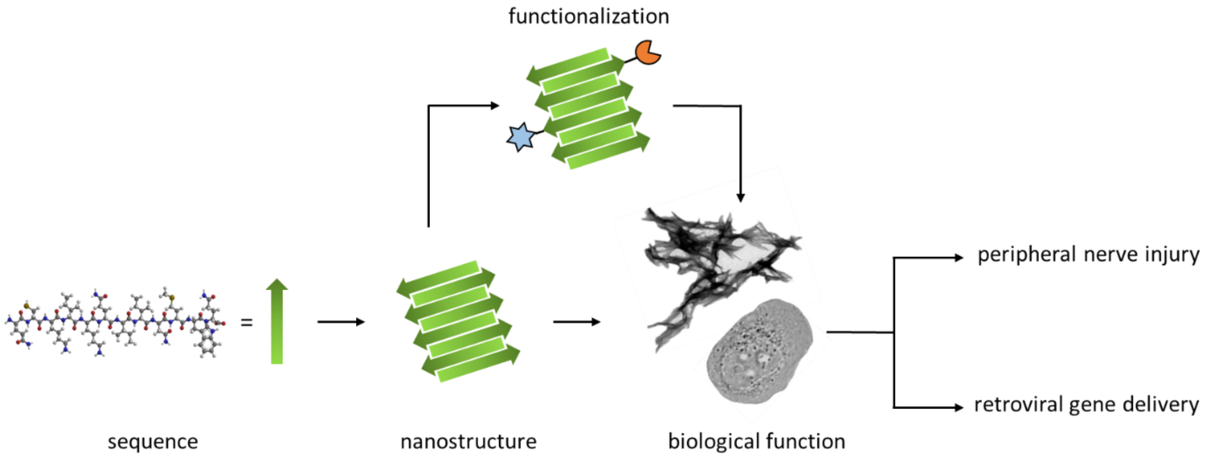

Figure 12. *Schematic representation of the process for obtaining structure-activity relationships in three steps: First, a peptide library is synthesized. Subsequently, the self-assembled structure and corresponding physico-chemical properties are studied. Finally, these nanomaterials are tested in the presence of cellular systems to evaluate the biological response, thus completing the SAR process. Furthermore, functional groups can be attached to the fibril surface to expand their usability.*

Starting from a known peptide sequence, EF-C, which has a strong tendency to form fibrillar amyloidal aggregates and shows intrinsic bioactivity, this thesis aims to generate an in-depth understanding of structure-activity relationships (SAR) in peptide assemblies. Therefore, the primary sequence was altered rationally, creating a library of β-sheet forming compounds. The self-assembly behavior of these peptides as well as the properties of the resulting nanostructures were studied, and bioactivity in models for PNI and gene therapy were investigated. Such findings could be very beneficial for designing tailored peptide-based materials for biomedical applications.

Here, I chose two systems to test the biological response to the peptide library. First, due to the strong similarity of the EF-C fibrils to fibril-forming proteins of the extracellular matrix, the SAPs obtained from the peptide library were tested as growth substrates for neural cells both *in vitro* and *in vivo*. With a better understanding of the underlying SAR, therapeutic improvements in the regeneration of damaged neurons may be achieved. Furthermore, auto-oxidative polymerization of dopamine was performed on the fibril surface. Therefore, functionalization was performed on preformed nanofibrils to not affect the self-assembly process and retain their properties while expanding their usability with additional functionalities in, for example, a pH-responsive fashion. This could give insights into the potential for attaching additional functionalities. This part of my thesis was done in collaboration with the group of Prof. Bernd Knöll at Ulm University.

Second, together with the group of Prof. Jan Münch, the EF-C derived SAP library was tested as viral transduction enhancers, following the serendipitous discovery of the EF-C sequence as a potent candidate. This study aims to better understand the contributions of structural features to the overall bioactivity and result in even more efficient transduction enhancers.

Taken together, the two biological systems may provide insights into general design rules for highly active peptide assemblies from EF-C-derived SAPs as an example of bio-functional nanomaterials.

III Results and Discussion

3.1 Introduction to “Sequenced-Optimized Peptide Nanofibers as Growth Stimulators for Regeneration of Peripheral Neurons”

Self-assembling peptides (SAPs) are exciting building blocks for the formation of nanomaterials. They have great potential to mimic natural cell scaffolds and could serve as an exciting artificial material in tissue engineering and regeneration.[160] Still, it is difficult to predict which sequences and structures affect a particular cellular response. In this article, we investigated the structural key elements of peptidic nanomaterials and how they affect cellular behavior. Therefore, we have established a peptide library consisting of 27 short SAPs with systematic variations in the primary structure. Table 1 describes some representative SAPs.

Table 3*. Characteristics of a selection of SAPs: SAP name and one letter code amino acid sequence. Qualitative fibril formation (fibril form.) based on transmission electron microscopy studies (“+” for fibrils, “0” for aggregates and “-“ for no fibrils or aggregates). Zetapotential based on electrophoretic mobility measurements. FT-IR bands in the amide I range. Conversion rates (conver. rate) as the amount of peptide monomers participating in fibril formation. Proteostat® binding (prot. bind., “-“ for < 10 n-fold fluorescence enhancement and “+” ≥ 10 n-fold fluorescence enhancement). Table adapted from “Schilling et al. Sequence-Optimized Peptide Nanofibers as Growth Stimulators for Regeneration of Peripheral Neurons, Adv. Funct. Mater. 2019, 29”, with permission from John Wiley and Sons, Inc.*

SAP name	sequence	fibril form.	Zetapotential (mV)	FT-IR (cm^{-1})	conver. rate (%)	prot. bind.
SAP^{1d}	KIKIQI	-	n.d.	1630	5	-
SAP^{1e} (H_2O)	Fmoc-KIKIQI	+	54.7 ± 2.1	1628	94	+
SAP^{2b}	KFKFQF	-	n.d.	1626	83	-
SAP^{2e}	CKFKFQF	+	22.3 ± 1.4	1627	95	+
SAP^{5c}	RGDKIKIQIC	+	21.7 ± 1.2	1627	80	+
SAP^{6a}	KIKIQIRGD	+	-10.1 ± 1.3	1626	n.d.	+
SAP^{7a}	HHHHKIKIKIKIWWWW	0	18.1 ± 0.5	1628	96	+
SAP^{7b}	KIKIKIKIWW	0	21.0 ± 0-3	1627	92	-
SAP^{8a}	EIEIQINM	+	-36.0 ± 3.5	1630	77	+

All peptides are derived from the previously developed transduction enhancer EF-C, and most of the SAPs contain the core pattern KIKIQI or KFKFQF.[151] The majority of the new SAPs in the library were shown to spontaneously self-assemble into peptide nanofibrils in phosphate buffered saline (H_2O for SAP^{1e}) as investigated with transmission electron microscopy (TEM). The peptide nanofibrils have lengths of up to a few micrometers and diameters of up to several nanometers. They can form 2D networks, which could to a certain extent mimic the extracellular matrix. Additionally, we also determined the amount of peptide monomers converting into a fibril with a fluorescence-based assay previously established in our group.[161] We found a wide range of conversion rates (CR) for the peptides with values ranging from 5% (SAP1d, KIKIQI) up to 96% (SAP7a, HHHHKIKIKIKIWWWW), often corresponding to significant differences in self-assembly behavior. Most peptides with medium to high conversion rates also formed fibrillar nanostructures. However, in some cases, only aggregates or soluble material could be detected via TEM, such as for SAP^{1a} (KIKIKIQI) or SAP^{2c} (KFKFKFQF).

Furthermore, we also investigated the zeta potential of the peptide assemblies by determining the electrophoretic mobility as a measure for the fibrils' surface charge. We expected a net positive surface charge to be more prone for interactions with net negatively charged cellular membranes. Most of our peptides were net positively charged. However, we could demonstrate that tuning the surface charge through the choice of amino acids is possible. For example, the substitution of lysines with glutamic acids resulted in net negatively charged peptide nanofibrils (SAP^{8a}, EIEIQINM). Nevertheless, a few lysine-containing sequences like SAP^{6a} (KIKIQIRGD) revealed net negatively charged surfaces.

Next, we investigated the ability of all SAPs to promote cell adhesion as well as cell growth and survival. In a medium throughput screening assay, we found that several SAPs, when applied as surface coatings, could enhance cell adhesion and growth of neurons from the adult mouse dorsal root ganglia (DRG) without the need for additional growth factors. We grouped neurons regarding their co-localized DAPI and βIII tubulin signals into small neurons (908-1994 μm^2), medium neurons (1994-4161 μm^2), and large neurons (4161-18721 μm^2). The following figure 13 shows all SAPs and their ability to adhere and grow neurons in a ranking related to the number of large neurons.

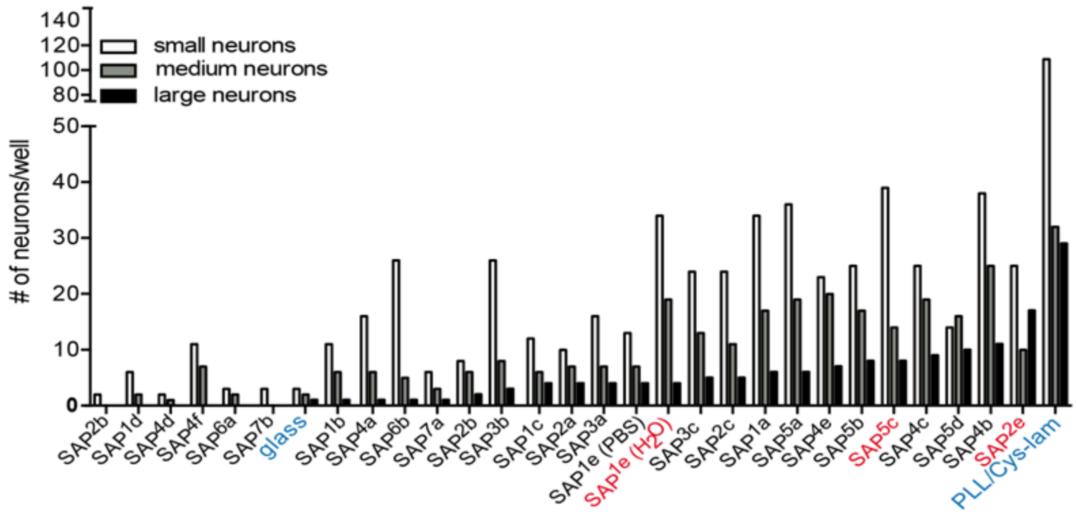

***Figure 13**. Quantification of neurons. Neurons were grouped into small (908-1994 μm²), medium (1994-4161 μm²), and large ones (4161-18721 μm²). All SAPs were ranked according to the number of large neurons. PLL (poly-L-lysine) served as a positive control, whereas glass served as a negative control. Figure adapted from "Schilling et al. Sequence-Optimized Peptide Nanofibers as Growth Stimulators for Regeneration of Peripheral Neurons, Adv. Funct. Mater. 2019, 29", with permission from John Wiley and Sons, Inc.*

SAP^{5c} (RGD-KIKIQIC), SAP^{1e} (Fmoc-KIKIQI), and SAP^{2e} (CKFKFQF) showed the best performance. Interestingly, their primary sequences are significantly different. The biological performance was analyzed with the following parameters: i) impact of the SAP in enhancing the number of neurons attaching to the SAP coating; ii) the number of branches, and iii) the potential to elevate the neuronal area and average length of the longest neurite. Still, there were significant differences in bioactive behavior in some peptides when only minor changes were made to their sequence. For example, the sequence KFKFQF (SAP^{2b}) turned into a highly bioactive SAP with the single addition of a cysteine (CKFKFQF, SAP^{2e}). Therefore, we elucidated the structural features of the SAPs that are necessary for inducing high neuron outgrowth. One necessary feature of the SAPs seems to be a strong propensity to form fibrils.

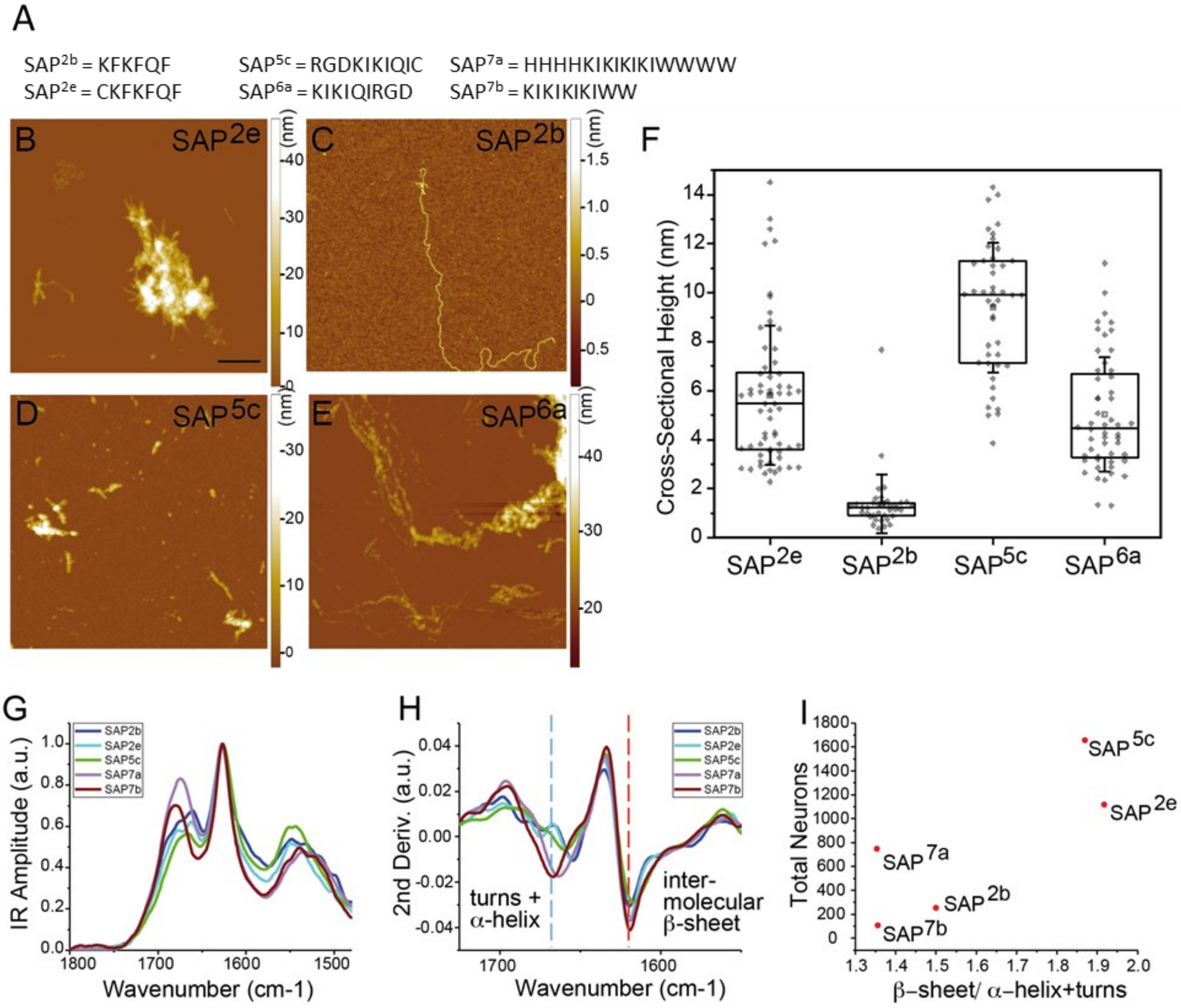

Figure 14. (A) SAP labels and sequences. (B–F) Analysis of PNF morphology via AFM of 4 SAPs. Scale-bar = 500 nm. (F) Cross-sectional height investigated of several individual fibrils. (G-I) Secondary structure analysis. (G) FT-IR spectra normalized to the maximum in the amide I range. (H) Second derivative of IR spectra. (I) Ratio of intermolecular β-sheets to α-helices and turns versus number of total neurons. Figure adapted from “Schilling et al. Sequence-Optimized Peptide Nanofibers as Growth Stimulators for Regeneration of Peripheral Neurons, Adv. Funct. Mater. 2019, 29”, with permission from John Wiley and Sons, Inc.

All highly bioactive SAPs revealed fibril formation as investigated with TEM and conversion rate assay. Nevertheless, good self-assembly properties alone did not explain the high biological activity without considering further aspects. For example, the peptide SAP^{6a} showed decent nanofibril formation in TEM but almost no bioactivity. Therefore, we expanded our characterization with a more detailed structure analysis. We investigated the cross-sectional height with atomic force microscopy (AFM, figure 14B-F). SAP^{2e} (CKFKFQF) showed significantly enhanced bioactive behavior and higher diameters compared to SAP^{2b} (KFKFQF). The same tendency was found for SAP^{5c} (RGDKIKIQIC) and SAP^{6a} (KIKIQIRGD).

Furthermore, we used FT-IR for secondary structure analysis (figure 14G-I). All SAPs showed signals in the amide I band in the region of 1625-1635 cm^{-1}, corresponding to β-sheets, and in the region of 1650-1685 cm^{-1}, corresponding to α-helices and turns. Quantification of the different secondary structure elements revealed an increasing bioactivity with increasing β-sheet content (figure 16I). Fibrils with higher diameter correlated with higher β-sheet content and higher bioactivity, which could be explained by the higher stiffness and persistence length or the change of the fibrils' surface and therefore better performance in neuronal outgrowth. In addition, all bioactive SAPs were positively charged, as shown by measurements of the electrophoretic mobility, while negatively charged fibrils did not enhance biological activity. This could be explained by the increased cell adhesion due to electrostatic interactions between negatively charged cell membranes and positively charged fibrils. A positive net charge is crucial, but increased bioactivity can only be achieved by combining all described structural key features and physico-chemical properties.

In the next step, we have chosen SAP^{5c}, as one of the best performing PNFs from the *in vitro* screening experiment, for first investigations in an *in vivo* PNS lesion model of the facial nerve in mice. Fluorescently labeled SAP^{5c} fibrils remained at the lesion site up to several weeks after direct injection and promoted faster regeneration as well as functional recovery compared to a negative control group.

To sum up, we investigated a library consisting of 27 SAPs forming peptide nanofibrils. We were able to identify sequences with increased biological activity for neuronal cell growth, and we were able to correlate structural key features for high biological impact like the ability to form fibrils, positive net charge, increased cross-sectional heights, and higher β-sheet content. Good candidates showed increased cell adhesion, neuronal outgrowth, and even faster functional recovery in an *in vivo* mouse model without the addition of growth factors. Furthermore, our SAPs could be injected directly into an *in vivo* mouse model and offer an excellent toolbox for regenerative medicine without the necessity to embed them into hydrogels or nerve conduits.

These results are presented comprehensively in the manuscript in chapter 5.1.

3.2 Introduction to “Water-Dispersible Polydopamine-Coated Nanofibers for Stimulation of Neuronal Cell Growth”

We have previously shown the great potential of SAPs as substrates to adhere and enhance neuronal cell growth. In the next step, chemical modification of preformed nanofibrils was accomplished to diversify the functionality of fibrils.

Inspired by the amyloid fibril catalyzed polymerization of melanin, we tested if PNFs could act as a scaffold for synthesizing polydopamine (pDA) coated fibrils, thereby combining the fibrils’ morphology and bioactive properties with the pDA’s versatile chemical functions.[53] We envisioned the pDA as a thin coating for further introduction of functional groups while retaining the bioactive behavior of the fibrils (figure 15a).

We have chosen the peptide with the sequence KIKIQIII and first investigated its self-assembly behavior via TEM. The peptide formed nanofibrils in aqueous media with several micrometers in length (figure 15b). FT-IR investigations revealed a signal in the amide I band region at 1631 cm^{-1} indicating β-sheets as a secondary structure element. In the next step, we added DA to preformed fibrils, and polymerization occurred by auto-oxidation. Absorbance spectroscopy was used at 300 nm to verify the presence of dopaminochrome and dopamine-*o*-quinone as known intermediates of the DA polymerization (figure 15d). Furthermore, TEM investigations revealed changes in the fibril morphology from fibrous aggregates to a denser packing with less visible fibrillar bundles, which is likely a result of the strong adhesive properties of the pDA coating (figure 15c). In addition, we used the amyloid-specific fluorescence dye Proteostat®, which has shown a strong enhancement of fluorescence for the fibrils only and decreased in the presence of pDA hybrid fibrils. This could indicate failed incorporation caused by the pDA coating.

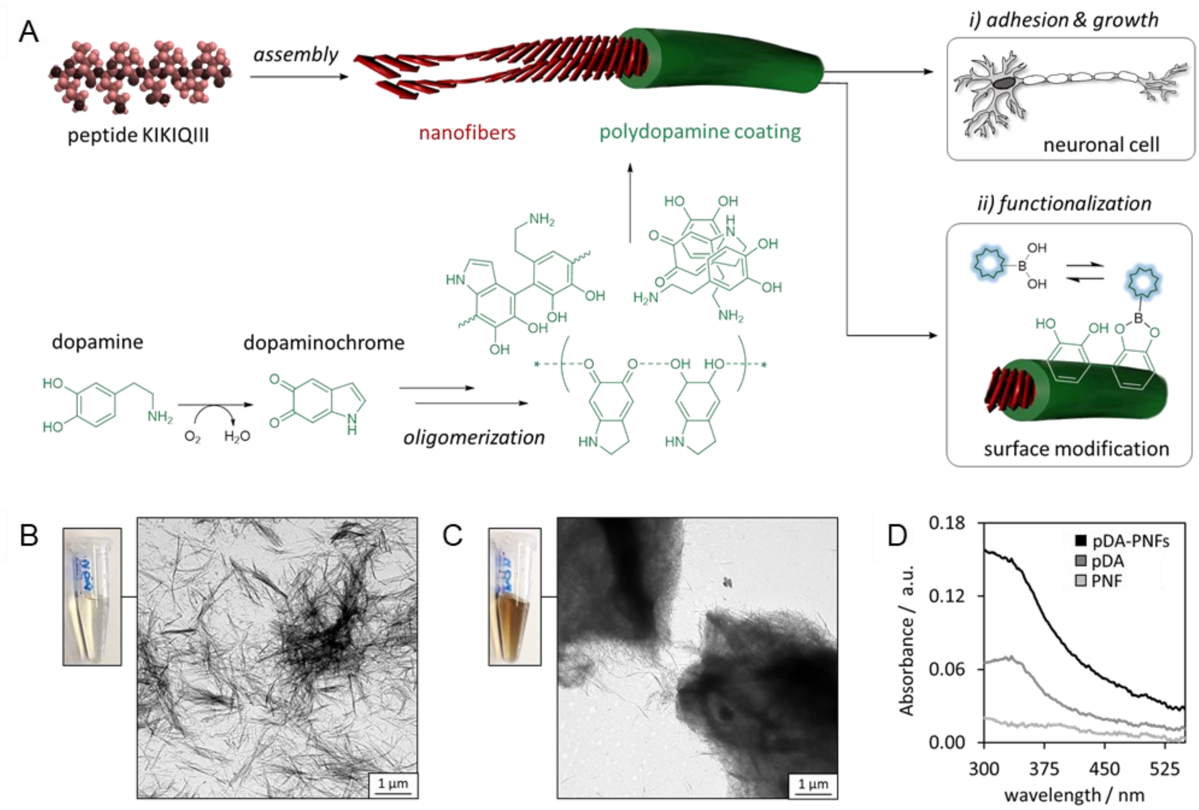

Figure 15. (A) Illustration of DA polymerization in the presence of preformed KIKIQIII fibrils and the following investigations on adhesion and growth of neuronal cells as well as the pH-dependent functionalization of catechols on the pDA surface with boronic acid modified Rhodamine B. (B-C) TEM micrograph of KIKIQIII fibrils (B) before coating and (C) after coating. (D) Absorption spectra of PNF, pDA, and pDA-PNF solutions (PNF and DA concentrations: 0.5 × 10^{-3} and 0.08 × 10^{-3} M). Figure adapted from "Sieste et al. Water-Dispersible Polydopamine-Coated Nanofibers for Stimulation of Neuronal Growth and Adhesion, Adv. Healthc. Mater. 2018, 7", with permission from John Wiley and Sons, Inc.

AFM was used to investigate the cross-sectional height. We found an increased thickness of 0.41 nm ± 0.08 nm indicating an ultrathin pDA coating, thus confirming the possibility to use PNFs as scaffolds for the synthesis of pDA coated hybrid materials.

Next, we investigated the accessibility of the well-known catechol functionality on the pDA's surface. Catechols are able to react with boronic acids in a pH-responsive, reversible covalent reaction. Therefore, we used a boronic acid modified Rhodamine B dye for a proof of concept. We were able to successfully bind the dye to hybrid fibrils at pH = 7.4, as shown with fluorescent microscopy. After incubating at pH = 3.0, no fluorescence was detectable on the pDA-fibril deposits, indicating the successful release of the dye.

Finally, we wanted to show the potential of such hybrid fibrils in neural cell growth. Primary postnatal mouse cerebellar neurons were cultivated on glass coverslips coated with pDA-fibrils. Compared to negative controls of coated pDA only and glass, there was an increased cell and neuron attachment and growth (figure 16A+B) as well as neurite length (figure 16C). The average neurite length was even comparable to a positive control containing a coating with pLL and laminin. The biological impact was equal before and after pDA-coating of peptide nanofibrils. Furthermore, we investigated the stimulatory behavior of coated nanofibrils on the morphology of cones, the sensory tips of nerve fibers, derived from the mouse hippocampal neurons and found a stimulating effect (figure 16D-J).

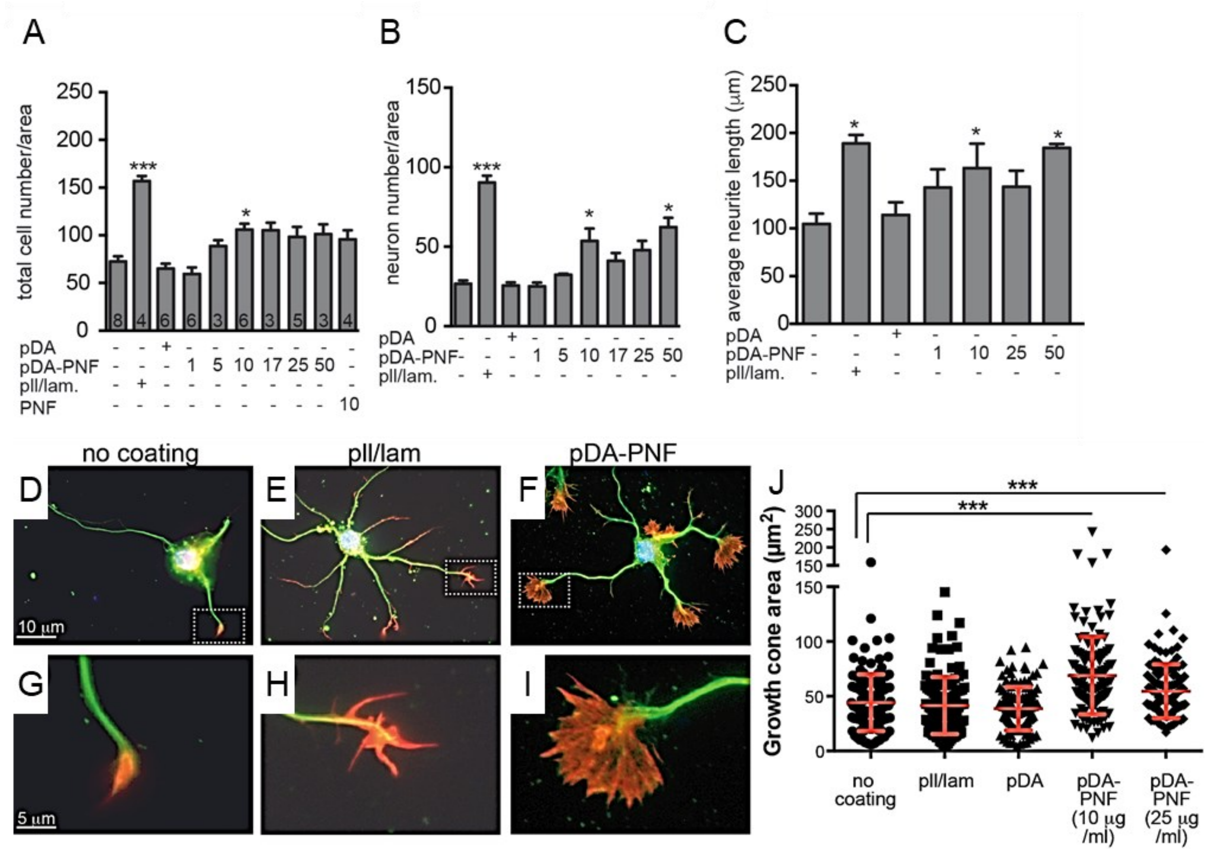

Figure 16. *(A-C) Primary neuron attachment of mice and nerve fiber growth on unmodified glass coverslips and coatings of pll/lam, pDA, and pDA-PNF. Quantification of (A) total cell number, (B) number of neurons per area, and (C) average neurite length based on optical microscopy images (not shown here). (D-I) Cultivation of mouse primary hippocampal neurons plated on the indicated substrates. Labeling of microtubules (green) and F-actin indicating growth cones (red). (D+G) Growth cone area on glass only, (E+H) on pll/lam, and (F+I) on pDA-PNF. (G-I) represent higher magnifications of certain areas. (J) Quantification of the growth cone area for different conditions in at least three independent experiments. Each circle, square, or triangle indicates to a single growth cone. **: p ≤ 0.01; ***: p ≤ 0.001. Figure adapted from "Sieste et al. Water-Dispersible Polydopamine-Coated Nanofibers for Stimulation of Neuronal Growth and Adhesion, Adv. Healthc. Mater. 2018, 7", with permission from John Wiley and Sons, Inc.*

Overall, we demonstrated the successful auto-oxidative polymerization of DA into pDA in the presence of peptide nanofibrils spontaneously formed by the sequence KIKIQIII in an aqueous solution. AFM investigations revealed an increased thickness of hybrid fibrils, indicating an ultrathin layer of pDA. Using a boronic acid functionalized fluorescent dye verified the presence of catechol groups on the surface of pDA-coatings in a pH-responsive reaction. We suggest those hybrid fibrils as a tool for further functionalization with cell receptor-specific groups or neuronal cell growth factors and thus also a promising biomaterial for nerve regeneration, since the bioactivity of hybrid fibrils was not altered compared to non-coated fibrils.

These results are presented comprehensively in the manuscript in chapter 5.2.

3.3 Introduction to “Supramolecular Peptide Nanofibrils with Optimized Sequences and Molecular Structures for Efficient Retroviral Transduction”

In chapter 3.1, a peptide library of several SAPs was investigated. Certain structural features and physico-chemical properties of PNFs were shown to critically determine the corresponding bioactivity regarding neuronal cell growth.

EF-C was previously shown to be a promising enhancer of retroviral transduction. Therefore, we were curious whether these SAPs were also suitable for such cellular systems and applications and show a structure-activity relationship for enhancing transduction.

In a similar approach to chapter 3.1, we investigated a peptide library consisting of 30 derivatives. The EF-C-derived peptide library was established via multi-parameter and multi-scale optimization.

The EF-C sequence QCKIKQIINMWQ was categorized into three domains: (i) the short N-terminal QC fragment; (ii) the amphiphilic KIKQII domain consisting of three isoleucines (I), which could drive the self-assembly and two positively charged lysines (K), which could support the solubility as well as the stability in aqueous media and also could play a crucial role in adhesion with both cells and negatively charged virions, and finally (iii) the C-terminal NMWQ fragment, which may play an important role in cell binding with CD4 receptors. Thus, the primary sequence may be important for self-assembly behavior into fibrils and for bioactivity. The SAPs have to serve mainly two crucial functions: (i) the binding and up-concentration of virions and (ii) mediating cell fusion (figure 17).

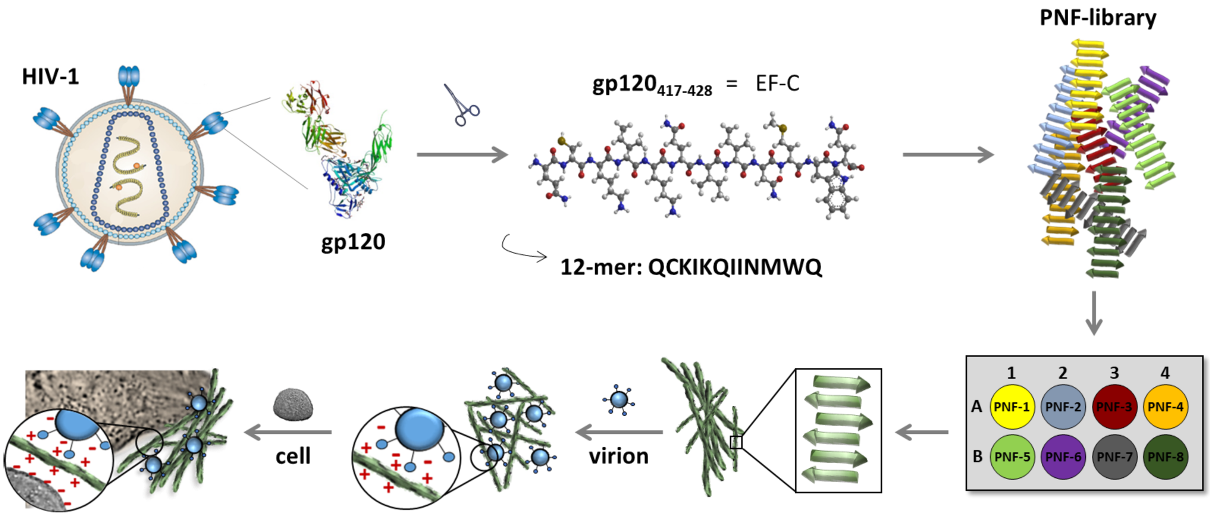

Figure 17. Schematic illustration of the structure-activity study of a novel peptide library. All peptides are derived by the bioactive fragment of the HIV-1 glycoprotein gp120 named EF-C in a multi-parameter and multi-scale optimization. This peptide library was investigated systematically for fibril formation, structural parameters, virion-PNF, and PNF-cell attraction, and finally transduction enhancement. Figure adapted from "Sieste et al. Supramolecular Peptide Nanofibrils with Optimized Sequences and Molecular Structures for Efficient Retroviral Transduction, Adv. Funct. Mater. 2021, 2009382", published under CC-BY 4.0, https://creativecommons.org/licenses/by/4.0/.

The self-assembly behavior of all SAPs was investigated with TEM and supported by determination of CR and incorporation of Proteostat®. Furthermore, we also determined zeta potential as a mass for the fibrils' surface charge, which could play a crucial role for binding negatively charged virions and adhering to negatively charged cell membranes. FT-IR was used to analyze secondary structures of all SAPs in the range of the amide I band. We used HIV-1 as a retroviral vector and TZM-bl as a model cell line to determine transduction enhancement. Transduction enhancement was determined with a chemiluminescence-based assay. HIV-1 vectors were able to integrate a β-galactosidase gene into cells and infected cells produced β-galactosidase, which was directly quantified and correlated to the viral uptake.

We have systematically truncated our sequences compared to EF-C at the N-terminus and the C-terminus. Furthermore, we have conducted a rearrangement of the amino acids to correct a structural defect in EF-C resulting in facially amphiphilic peptides. The rearrangement from PNF-1 (CKIKQIINMWQ) to PNF-7 (CKIKIQINMWQ) and PNF-3 (CKIKQII) to PNF-9 (CKIKIQI) revealed a drastic increase in bioactivity, and all sequences still showed self-assembly behavior. Cutting the N-terminal cysteine (C) resulted in a total loss of transduction enhancement exemplary shown here for PNF-12 and a significant decrease for all other PNFs compared to their cysteine (C) containing derivatives. The shortest peptide PNF-12 showed no self-assembly behavior anymore and therefore no biological impact. This behavior was observed for all peptide sequences with six amino acids, which could be the minimum length necessary to form fibrils. Cysteine seems to play a crucial role in both self-assembly behavior and resulting biological impact (figure 18). To underline this result, we substituted cysteine (C) with methionine (M) and saw a significant decrease in viral uptake again.

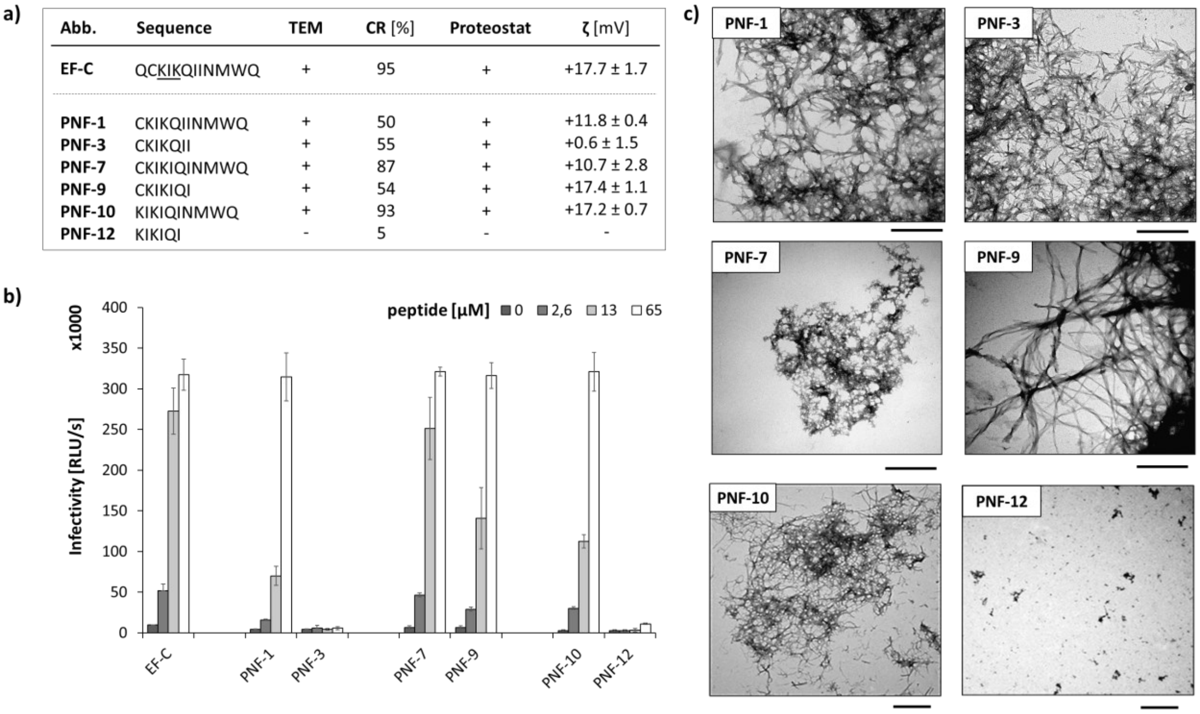

a)

Abb.	Sequence	TEM	CR [%]	Proteostat	ζ [mV]
EF-C	QCKIKQIINMWQ	+	95	+	+17.7 ± 1.7
PNF-1	CKIKQIINMWQ	+	50	+	+11.8 ± 0.4
PNF-3	CKIKQII	+	55	+	+0.6 ± 1.5
PNF-7	CKIKIQINMWQ	+	87	+	+10.7 ± 2.8
PNF-9	CKIKIQI	+	54	+	+17.4 ± 1.1
PNF-10	KIKIQINMWQ	+	93	+	+17.2 ± 0.7
PNF-12	KIKIQI	-	5	-	-

Figure 18. (a) List of synthesized peptide derivatives with varied sequences including the ability to form PNFs as obtained in TEM measurements ("+" = fibrils and "-" = no aggregate). CR for monomer-to-fibril conversion rate. Ability to bind Proteostat ("+" for ≥10 n-fold fluorescence enhancement and "−" for ≤10 n-fold fluorescence enhancement). Zeta potential (ζ) values as a mass of charge. (b) β-Galactosidase assay showing HIV-1 infection rates of TZM-bl cells observed in the presence of different concentrations of PNF. Values above the columns depict the change from baseline (0 µM). Shown are mean values derived from triplicate infections ± standard deviation in relative light units per s (RLU/s). (c) Representative TEM micrographs to investigate self-assembly behavior (scale bars = 500 nm). Figure adapted from "Sieste et al. Supramolecular Peptide Nanofibrils with Optimized Sequences and Molecular Structures for Efficient Retroviral Transduction, Adv. Funct. Mater. 2021, 2009382", published under CC-BY 4.0, https://creativecommons.org/licenses/by/4.0/.

Next, we substituted isoleucines (I) with other hydrophobic amino acids like the less hydrophobic alanine (A) and the sterically more demanding phenylalanine (F), which could influence packing of the PNFs (figure 19a). All shown peptides were able to form fibrils with moderate to high CR (figure 19a+b). Interestingly, fibrils, where isoleucines (I) were substituted with alanines (A), did not enhance viral uptake, which could be explained by altered packing of fibrils or surface changes. PNF-3 and PNF-15 revealed self-assembly behavior, but were not able to increase viral uptake. Strikingly, PNF-3 and PNF-15 fibrils were the only ones that exhibited a neutral or negative charge. Therefore, lysines (K) were exchanged with glutamic acid (E), which could result in negatively charged fibrils for additional proof. As expected, (E)-containing peptides all formed negatively charged nanofibrils and revealed mostly no transduction enhancement. To investigate this behavior in more detail, we used Proteostat® labeled PNFs (red) and YFP-labelled virions (green) to investigate virion attachment on fibrils by fluorescence scanning laser microscopy (LSM) and fibril attachment to labeled cells (figure 19d). Interestingly, negatively charged PNFs were still able to bind virions, but did not attach to cells to mediate cellular uptake, as shown here for PNF-19 (CEIEIQINMWQ). Overall, the formation of positively charged peptide nanofibrils is an absolute necessity to enhance viral uptake.

In chapter 3.1, we have shown that secondary structure composition could play a crucial role in bioactivity. Here, we investigated all PNFs with FT-IR, and all derivatives revealed bands in the amide I range indicating β-sheet formation. FT-IR investigations for those compounds revealed furthermore that net positively and net negatively charged fibrils both show comparable contents of β-sheets (figure 19e).

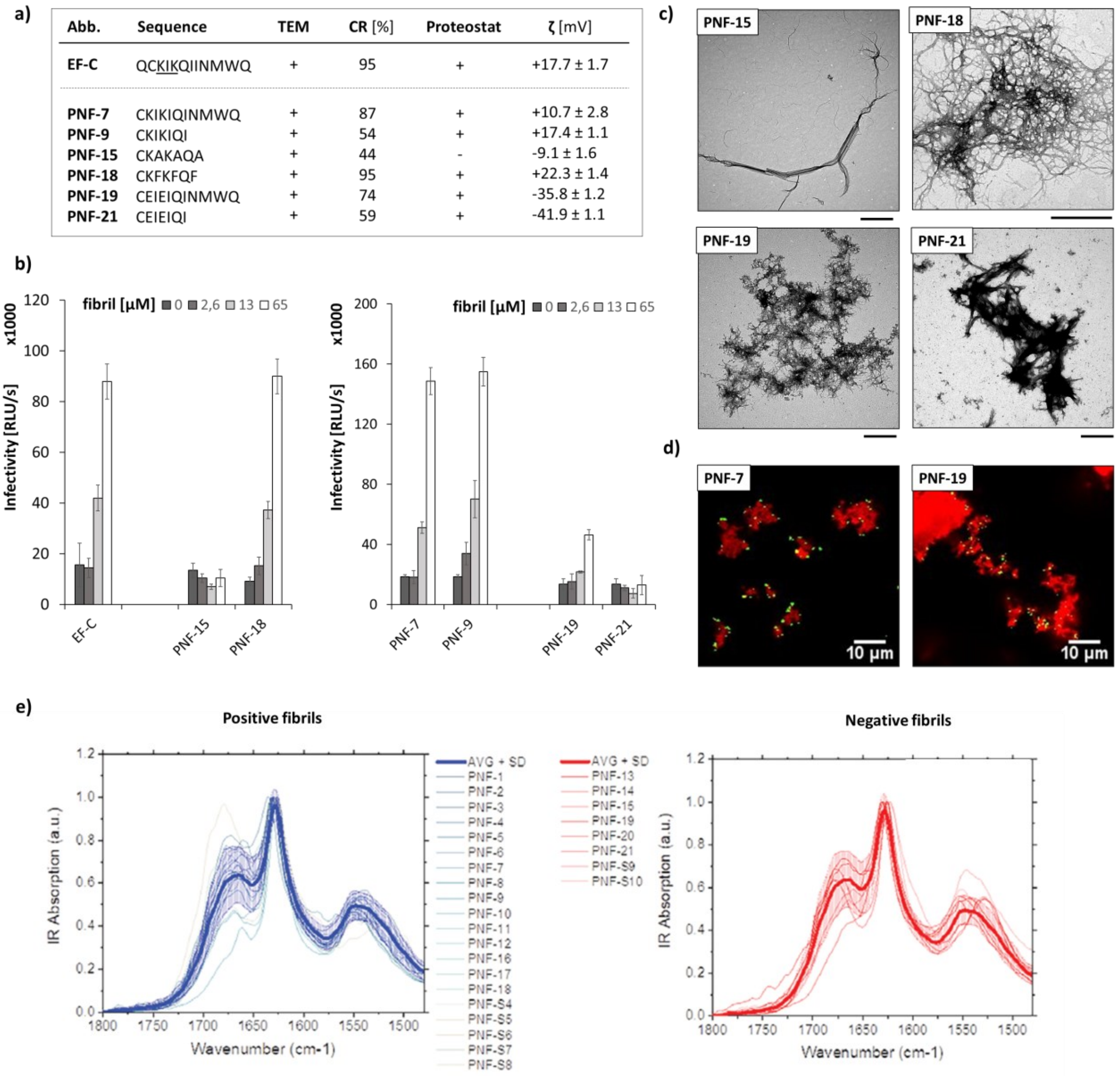

Abb.	Sequence	TEM	CR [%]	Proteostat	ζ [mV]
EF-C	QCKIKQIINMWQ	+	95	+	+17.7 ± 1.7
PNF-7	CKIKIQINMWQ	+	87	+	+10.7 ± 2.8
PNF-9	CKIKIQI	+	54	+	+17.4 ± 1.1
PNF-15	CKAKAQA	+	44	-	-9.1 ± 1.6
PNF-18	CKFKFQF	+	95	+	+22.3 ± 1.4
PNF-19	CEIEIQINMWQ	+	74	+	-35.8 ± 1.2
PNF-21	CEIEIQI	+	59	+	-41.9 ± 1.1

Figure 19. *(a) List of synthesized peptide derivatives with varied sequences including the ability to form PNFs as obtained in TEM measurements ("+" = fibrils and "-" = no aggregate). CR for monomer-to-fibril conversion rate. Ability to bind Proteostat ("+" for ≥10 n-fold fluorescence enhancement and "−" for ≤10 n-fold fluorescence enhancement). Zeta potential (ζ) values as a mass for charge. (b) β-galactosidase assay showing HIV-1 infection rates of TZM-bl cells observed in the presence of different concentrations of PNF. Values above the columns depict the change from baseline (0 µM). Shown are mean values derived from triplicate infections ± standard deviation in relative light units per s (RLU/s). (c) Representative TEM micrographs to investigate self-assembly behavior (scale bars = 500 nm). (d) Laser scanning micrographs to investigate virus-PNF clusters. Red indicates Proteostat® labeled PNFs and green YFP labeled virions. (e) FT-IR spectra of several net positively charged PNF (blue) and net negatively charged PNF (red) in the amide I range. Figure adapted from "Sieste et al. Supramolecular Peptide Nanofibrils with Optimized Sequences and Molecular Structures for Efficient Retroviral Transduction, Adv. Funct. Mater. 2021, 2009382", published under CC-BY 4.0, https://creativecommons.org/licenses/by/4.0/.*

We quantified secondary structure elements and correlated them to transduction rates under consideration of conversion rates and surface charges. Again, we found PNFs with high intermolecular β-sheet content like PNF-18 to correlate with high bioactivities (figure 20).

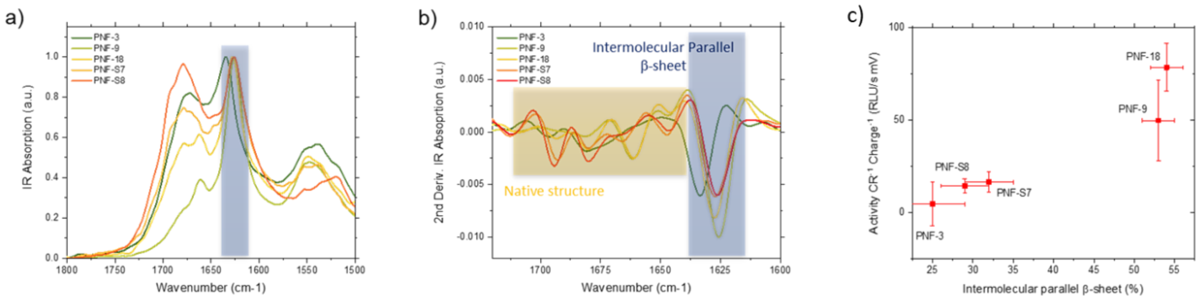

Figure 20. *(a) IR spectra of selected PNFs normalized to the maximum in the amide I band range. (b) Second derivative of IR spectra for secondary structure analysis. (c) Secondary structure elements correlated with transduction rates under consideration of conversion rates and surface charges of several PNFs. Figure adapted from “Sieste et al. Supramolecular Peptide Nanofibrils with Optimized Sequences and Molecular Structures for Efficient Retroviral Transduction, Adv. Funct. Mater. 2021, 2009382”, published under CC-BY 4.0, https://creativecommons.org/licenses/by/4.0/.*

To sum up, we optimized peptides derived from the previously described transduction enhancer EF-C. Our studies revealed a deeper understanding of the PNFs’ self-assembly, ability to bind virions and to cells and therefore enhance gene transfer. We were able to show that the NMWQ domain is not necessary for bioactivity. The minimum sequence length was determined to be seven amino acids, as demonstrated with CKIKIQI and CKFKFQF. The self-assembly into positively charged PNFs was a key requirement for increased transduction rates, since negatively charged PNFs could bind virions but did not mediate viral uptake with cells. N-terminal cysteines had a high impact on self-assembly as well as on bioactivity. As shown in the previous study, increasing β-sheet content again led to increased bioactivity. The study resulted in PNF-18 (CKFKFQF), which had a 40% reduced sequence length compared to EF-C with still better bioactivity. Therefore, it is also very attractive regarding economic aspects.

These results are presented comprehensively in the manuscript in chapter 5.3.

IV Summary and Outlook

In the last decades, peptides have gained an increasing focus for the bottom-up fabrication of nanomaterials in several medical and technological fields. During this time, general design principles for SAPs and resulting materials were achieved. Still, it is impossible to create artificial materials that can rival those produced by nature in terms of structural complexity, precision, and resulting performance in a particular task. This is mainly due to the high complexity of these systems. Overall, there is no systematic study on SAPs and their resulting properties yet.

This creates a huge gap in knowledge for the rational design of tailored peptide-based nanomaterials. The majority of the recently published studies are based on phenomenological observations and often trial and error. Even a single truncation, addition, or substitution of an amino acid in a short peptide sequence can drastically alter self-assembly behavior and properties. Therefore, studying this issue is of high interest for the specific development of application-oriented peptide-based nanomaterials.

During my work, I have investigated a library consisting of novel short peptides. The design of these peptides was derived from the previously published transduction enhancer EF-C. The peptides within the library were rationally altered in their primary sequence to investigate the resulting behavior more systematically.

In cooperation with the Institute of Physiological Chemistry at Ulm University, we investigated those peptides as substrates for the cultivation of neuronal cells. The results obtained in this study revealed beneficial effects of SAPs on the adhesion and growth of neurons *in vitro* (DRGs, hippocampal neurons) as well as in an *in vivo* mouse model for peripheral nerve injury. Most of these SAPs were shown to self-assemble into fibrils or aggregates. Interestingly, there were big differences between these SAPs in their biological performance. To investigate this in a more detailed way, various techniques were applied to determine their physico-chemical properties and elucidate structural key features that determine high bioactivity. The studies revealed that the formation of net positively charged nanofibrils is a key requirement for increased cell adhesion and growth. This can be simply related to attractive interactions between positively charged nanofibrils and negatively charged cell membranes. Nevertheless, features such as the formation of net positively charged fibrils were not able to explain large differences for various primary sequences without further investigations. Together with the Centre for Misfolding Diseases at the University of Cambridge, the peptide fibrils were thoroughly investigated regarding their internal structure. FT-IR was applied to elucidate the secondary structure, and AFM was used to determine cross-sectional heights of individual fibrils. These studies revealed that peptide nanofibrils with increased β-sheet content led to fibrils with higher cross-sectional heights and could be directly linked to an increased potential for neuronal cell adhesion and growth. Furthermore, promising candidates were applied in an *in vivo* mouse model for a peripheral nerve injury. Those nanofibrils were injected directly to the lesion site without the necessity for further components like nerve guide conduits or additional growth factors and remained up to three weeks at the lesion site and showed a faster functional recovery than controls. Overall, novel peptide-based nanomaterials could be established in these studies with beneficial effects on neuronal regeneration and key structural features as well as physico-chemical properties were determined in a structure-activity relationship.

I was interested in if such a relation could also be found in a second approach in a similar fashion. Certain nanofibrils, especially EF-C, have been previously shown as very effective transduction enhancers. Therefore, we investigated the peptide library in cooperation with the Institute of Molecular Virology at Ulm University for its potential to enhance viral transduction. This study again revealed the necessity for the formation of net positively charged nanofibrils, which seems to be a key requirement for the interaction with cells. Interestingly, net negatively charged virions were still able to bind to net negatively charged peptide nanofibrils, but viral uptake was not mediated anymore, most likely due to failed attachment to net negatively charged cell membranes caused by repulsive forces.

N-terminal cysteines were very beneficial on both self-assembly behavior and increasing transduction rates. Again, FT-IR was performed to investigate the structural key elements. SAPs forming assemblies with high β-sheet content were found to increase transduction rates more efficiently than their counterparts with lower β-sheet content. Those results are in line with previously obtained data in neuronal cell environments. Combining both studies, especially the sequence CKFKFQF could be a promising and efficient candidate for further biomedical applications.

It was demonstrated that SAPs are beneficial for neuronal regeneration and increased transduction rates for gene therapy approaches. In both studies, it was found that certain structural key features and resulting physico-chemical properties for good biological performance correlate and that there could be general attributes for the interaction of cells and nanofibrils.

These novel SAPs are an ideal platform for biomedical applications due to their high efficiency, low costs and scalable synthesis, their high potential for further functionalization and tuning, and their promising biological performance.

During my thesis, we also investigated peptide nanofibrils as a scaffold for dopamine polymerization inspired by the amyloid fibril-driven synthesis of the chemically comparable melanin to show their potential to further modify them and increase their applicability. Those hybrid fibrils revealed a similar biological impact compared to non-coated fibrils. At the same time, polydopamine offers several functionalities on its surface, which allow attachment of functional groups even in a pH-dependent fashion, as shown in a proof of concept.

Due to the variety of different amino acids with varying functionalities, there are several possibilities to chemically modify SAPs and fibrils for tailored nanomaterials with labels and dyes for monitoring *in vitro* and *in vivo*, cell targeting moieties, or bioactive groups such as nerve growth factors. Furthermore, the incorporation of breaking points can support and trigger their dis-assembly.

Nevertheless, several key questions remain and need to be investigated in future studies. In this thesis, key structural features were investigated that are responsible for high activity, but a more mechanistic-driven study would be beneficial to determine the interaction of nanofibrils and cells on a molecular level. Furthermore, even though there was no harmful behavior of those novel SAPs in cellular environments and living systems, the fate of fibrils needs to be clarified in long-term studies, also concerning their structural relation to toxic amyloid fibrils. It is not clear yet, if a living system degrades those nanofibrils or if they deposit in certain parts of the body and cause long-term harmful effects.

V Publications

In the following are the reprints of manuscripts. The reprints were made with the permission of the respective journal. Furthermore, the copyrights are given on the covers, and the contributions of the individual authors are listed.

5.1 Sequence-Optimized Peptide Nanofibers as Growth Stimulators for Regeneration of Peripheral Neurons

Corinna Schilling,# Thomas Mack,# Selene Lickfett, Stefanie Sieste, Francesco S. Ruggeri, Tomas Sneideris, Arghya Dutta, Tristan Bereau, Ramin Naraghi, Daniela Sinske, Tuomas P. J. Knowles, Christopher V. Synatschke, Tanja Weil,* and Bernd Knöll*

shared first authorship, * corresponding author

Published in Adv. Funct. Mater. 2019, 29, 1809112. DOI: 10.1002/adfm.201809112

Abstract:

There is an urgent need for biomaterials that support tissue healing, particularly neuronal regeneration. In a medium throughput screen novel self-assembling peptide (SAP) sequences that form fibrils and stimulated nerve fiber growth of peripheral nervous system (PNS)-derived neurons are identified. Based on the peptide sequences and fibril morphologies and by applying rational data-mining, important structural parameters stimulating neuronal activity are elucidated. Three SAPs (SAP^{1e}, SAP^{2e}, and SAP^{5c}) enhance adhesion and growth of PNS neurons. These SAPs form 2D and 3D matrices that serve as bioactive scaffolds stimulating cell adhesion and growth. The newly discovered SAPs also support the growth of CNS neurons and glia cells. Subsequently, the potential of SAPs to enhance PNS regeneration *in vivo* is analyzed. For this, the facial nerve driving whisker movement in mice is injured. Notably, SAPs persist for up to 3 weeks in the injury site indicating highly adhesive properties and stability. After SAP administration, more motor neurons incorporating markers for successive regeneration are observed. Recovery of whisker movement is elevated in SAP-injected mice. In summary, short peptides that form fibrils are identified and the adhesion, growth, and regeneration of neurons have been efficiently enhanced without the necessity to attach hormones or growth factors.

Contribution of the respective authors:

Corinna Schilling: Conduction of biological relevant assays including assays in mice. Design and discussion of the concept and results. Correcting the manuscript.

Thomas Mack: Design, synthesis and characterization of peptide nanofibrils. Design and discussion of the concept and results. Correcting the manuscript.

Selene Lickfett: Performing experiments with primary neurons.

Stefanie Sieste: Design, synthesis and characterization of peptide nanofibrils. Design and discussion of the concept and results. Correcting the manuscript.

Francesco S. Ruggeri: Design and discussion of the concept and results. Conducting of AFM measurements. Discussion of FT-IR and AFM results. Writing and correcting the manuscript.
Tomas Sneideris: Conduction of AFM measurements.
Arghya Dutta: Conduction and discussion of data-mining approach.
Tristan Bereau: Conduction and discussion of data-mining approach.
Ramin Naraghi: Contributing intellectual input and acquiring funding for the project.
Daniela Sinske: Performing experiments with primary neurons.
Tuomas P. J. Knowles: Acquiring funding for the project, correcting the manuscript.
Christopher V. Synatschke: Discussion of the concept and results. Writing and correcting the manuscript.
Tanja Weil: Acquiring funding for the project, design and discussion of the concept and results, writing and correcting the manuscript.
Bernd Knöll: Acquiring funding for the project, design and discussion of the concept and results, writing and correcting the manuscript.

FULL PAPER

Peripheral Nerve Regeneration

ADVANCED FUNCTIONAL MATERIALS

www.afm-journal.d

Sequence-Optimized Peptide Nanofibers as Growth Stimulators for Regeneration of Peripheral Neurons

Corinna Schilling, Thomas Mack, Selene Lickfett, Stefanie Sieste, Francesco S. Ruggeri, Tomas Sneideris, Arghya Dutta, Tristan Bereau, Ramin Naraghi, Daniela Sinske, Tuomas P. J. Knowles, Christopher V. Synatschke, Tanja Weil, and Bernd Knöll**

There is an urgent need for biomaterials that support tissue healing, particularly neuronal regeneration. In a medium throughput screen novel self-assembling peptide (SAP) sequences that form fibrils and stimulated nerve fiber growth of peripheral nervous system (PNS)-derived neurons are identified. Based on the peptide sequences and fibril morphologies and by applying rational data-mining, important structural parameters stimulating neuronal activity are elucidated. Three SAPs (SAP^{1e}, SAP^{2e}, and SAP^{5c}) enhance adhesion and growth of PNS neurons. These SAPs form 2D and 3D matrices that serve as bioactive scaffolds stimulating cell adhesion and growth. The newly discovered SAPs also support the growth of CNS neurons and glia cells. Subsequently, the potential of SAPs to enhance PNS regeneration in vivo is analyzed. For this, the facial nerve driving whisker movement in mice is injured. Notably, SAPs persist for up to 3 weeks in the injury site indicating highly adhesive properties and stability. After SAP administration, more motor neurons incorporating markers for successive regeneration are observed. Recovery of whisker movement is elevated in SAP-injected mice. In summary, short peptides that form fibrils are identified and the adhesion, growth, and regeneration of neurons have been efficiently enhanced without the necessity to attach hormones or growth factors.

1. Introduction

Tissue damage results in cavity formation thereby disrupting cell–cell interactions. Several strategies in tissue engineering aim at filling these lesions with biomaterials facilitating cellular reconnection and functional recovery.[1] In the peripheral nervous system (PNS) injuries split the nerves into two nerve stumps separated by a gap ranging between millimeters to centimeters. The current therapeutic gold standard is surgical end-to-end suturing of disconnected nerves.[2] However, for larger gaps, nerve interponates so-called autografts from the same patient bridge the gap between both stumps.[3] The intrinsic regenerative potential of transected PNS nerves is superior to injured central nervous system (CNS) axons.[4] Still, in the PNS, complete axon regeneration and full functional recovery often cannot be achieved. One drawback in using autologous nerves and blood vessels as donor tissues is the fact that this approach requires further surgery and may induce ectopic pain sensation.[1] These limitations have encouraged new biomaterial-based therapeutic strategies to bridge disconnected nerve stumps and enhance nerve reconnection and functional recovery in a non-invasive fashion.[1]

Self-assembling peptides (SAPs) have emerged as a promising biomaterial in regenerative medicine.[1a,5] These peptides undergo spontaneous self-assembly and depending on the peptide sequence, various nanostructures such as fibers, rods, and tubes have been formed.[5b] Peptide nanofibers (PNFs) can form networks resembling the extracellular matrix in key aspects that could serve as an artificial scaffold structure promoting cell adhesion and growth.[6] Certain PNFs revealed high biocompatibility and

---

C. Schilling, S. Lickfett, D. Sinske, Prof. B. Knöll
Institute of Physiological Chemistry
Ulm University
Albert-Einstein-Allee 11, 89081 Ulm, Germany
E-mail: bernd.knoell@uni-ulm.de

T. Mack, S. Sieste, Prof. T. Weil
Institute of Inorganic Chemistry I
Ulm University
Albert-Einstein-Allee 11, 89081 Ulm, Germany
E-mail: weil@mpip-mainz.mpg.de

The ORCID identification number(s) for the author(s) of this article can be found under https://doi.org/10.1002/adfm.201809112.

DOI: 10.1002/adfm.201809112

Dr. F. S. Ruggeri, Dr. T. Sneideris, Prof. T. P. J. Knowles
Department of Chemistry
University of Cambridge
Cambridge CB2 1EW, UK

Dr. A. Dutta, Dr. T. Bereau
Max Planck Institute for Polymer Research
Ackermannweg 10, 55128 Mainz, Germany

Dr. R. Naraghi
Department of Neurosurgery
German Armed Forces Hospital Ulm
Oberer Eselsberg 40, 89081 Ulm, Germany

T. Mack, S. Sieste, Dr. C. V. Synatschke, Prof. T. Weil
Department Synthesis of Macromolecules
Max Planck Institute for Polymer Research
Ackermannweg 10, 55128 Mainz, Germany

did not promote tissue inflammation.[1a] Further functionalities have been attached either to the peptide sequences before assembly or to the already formed fibers, including epitopes of extracellular matrix proteins such as laminin or fibronectin,[7] polydopamine,[8] glycosaminoglycans,[9] or growth factors[10] including BDNF.[11] These biomimetic SAPs increased focal adhesion assembly, which is attractive for processes such as axonal regeneration.[12] In addition, enhanced nerve fiber growth from primary rodent neurons has been demonstrated on SAP matrices.[8,13] In these cell culture experiments, SAPs enhanced axon regrowth and regeneration. So far, SAPs have mainly been used in CNS injury models such as spinal cord lesions. These SAPs reduced glial scarring and neuroinflammation while simultaneously promoting outgrowth and functional recovery of severed axons.[7b,c,14] In contrast, there are only a few studies of PNFs in PNS regeneration. So far, two model systems of PNS regeneration, that is, facial[15] or sciatic nerve regeneration,[16] were mainly employed. For those studies, different PNFs were used including nanofibers composed of C16VVVAAAEEE[15] or RADA 16-I derived SAPs with two functional motifs IKVAV and RGD.[16a,b] These nanofibers were incorporated into collagen tubes,[15] poly lactic-co-glycolic acid (PLGA) tubes,[16b,c] or hydrogels.[16a] This is one of the first studies applying "free" nanofibers without any filling into conduits. The preparation of such conduits is labor- and cost-intensive and it would be advantageous to instead simply inject biomaterials such as PNFs into the injury site.

A direct comparison of the results in these studies is difficult for several reasons. The reported animal studies used different parameters to assess functional regeneration such as histology, gene expression, and functional tests. For instance, nanofiber-filled neurografts were comparable to the gold standard (i.e., a nerve autograft) in enhancing nerve action potential propagation after a facial nerve injury.[15] In a different histological parameter, the nanofiber-filled neurograft was even superior to the autograft and restored the axon diameter of injured axons almost completely to pre-injury levels.[15] However, most available studies could only demonstrate a limited increase in individual regeneration parameters, which did not exceed effects observed with nerve autografts.

Herein, we have identified short SAPs that formed PNFs capable of enhancing PNS regeneration without additional bioactive peptides, growth factors, or hormones. Also, no filling into conduits was required. Bioactive SAPs were identified by screening a peptide library consisting of short peptide sequences with an average of nine amino acids per peptide that were stabilized by intermolecular β-sheet structures. We used the facial nerve in mice to study PNS regeneration. Facial motor neurons (MN) in the brain are connected by the facial nerve with several facial muscles to control, for example, whisker movement. This injury model has the advantage that regeneration success can be monitored by histological means (e.g., retrograde transport of fluorescent racer along axons) and also on the functional level. For the latter, recovery of whisker movement after injury is quantified by videotaping with a high-speed camera.

In other studies on nerve regeneration, SAPs were introduced into hydrogels or tubes, which can lead to heterogeneous distribution and aggregation of the material.[15,16] We have directly injected dispersed SAP nanofibers in solution at the lesion site, where the SAPs revealed highly adhesive behavior and persisted at the lesion site for several weeks. The SAPs identified from our library enhanced axon regeneration and they augmented adhesion and growth of primary PNS neurons. The most bioactive SAP^{5c} was tested in vivo in a mouse model resulting in enhanced facial nerve regeneration as well as functional recovery of whisker movement.

Overall, this is one of the first studies on the identification of SAPs based on the correlation of structural parameters and bioactivity yielding bioactive fibrils that supported neuronal growth and nerve regeneration without the necessity of additional components such as growth factors, extracellular matrix domains, or hormones. We believe that the newly discovered SAPs form a bioactive and convenient to use nanomaterial with high potential for regenerative medicine.

2. Results

2.1. Design and Synthesis of the SAP Fibril Library

A peptide library was prepared consisting of about 27 different peptide sequences via Fmoc solid phase peptide synthesis (**Table 1**; Table S1, Supporting Information). The sequences were designed based on the peptide sequence QCKIKQIINMWQ originating from the glycoprotein GP120$_{417-428}$ of human immunodeficiency virus (HIV) that enhanced the cellular uptake of virions.[17] Most of the sequences comprised the amphiphilic six amino acid sequences KIKIQI or KFKFQF (Table 1). Almost all SAPs had an overall positive net charge thus being more likely to interact with negatively charged cell membranes. In accordance, the negatively charged SAP^{8a} (Table 1) failed to enhance cell adhesion and growth (Figure S1, Supporting Information). In some cases, functionalities such as an Fmoc protection group (SAP^{1e}) or the RGD sequence (SAP^{5a} to SAP^{6b}) were added at the N- or C-terminus to further enhance self-assembly and possibly cell adhesion (Table 1).[18] The peptides listed in Table 1 were purified with high performance liquid chromatography (HPLC) and characterized by mass spectrometry and the corresponding spectra are given in Table S1 and Figure S2, Supporting Information.

To induce fibril formation, SAPs were dissolved in dimethylsulfoxid at 10 mg mL^{-1} as a non-selective solvent, followed by tenfold dilution in PBS (phosphate buffered saline or double-distilled water, ddH$_2$O, for SAP^{1e}) to induce self-assembly (**Figure 1**A). The conversion rate of the SAPs to PNFs was determined using an assay developed in our group.[19] Here, the conversion rate measures the amount of peptide monomers that form fibers in solution. High conversion rates were indicated by 70–100% (e.g., SAP^{2e}, SAP^{5c}) whereas moderate and low fibril formation was obtained for SAP^{5d} and SAP^{1d}, respectively (Table 1). Transmission electron microscopy (TEM) was used to acquire 2D micrographs and analyze the SAP aggregation state. High aspect ratio PNFs were found for most SAPs (Figure 1B; Figure S3, Supporting Information) with a variety of morphologies like sheet-like aggregates (SAP^{4e}), twisted fibrils (SAP^{1b}), or amyloid-like fibrils (SAP^{1e}; Figure 2B; Figure S3, Supporting Information). A summary of the observed morphologies ("+" = fibers, "0" = aggregates, "–" = no assembly) is given in Table 1.

Table 1. Characteristics of the SAP library: SAP #, SAP name, and one-letter code of amino acid sequence.

#	SAP name	Sequence	PNF form.	Zetapotential [mV]	FT-IR [cm^{-1}]	Conver. rate [%]	PROT bind.
1	SAP^{1a}	KIKIKIQI	–	10.5 ± 0.8	1626	80	+
2	SAP^{1b}	KLKLKLQL	+	–0.8 ± 1.3	1626	n.d.	–
3	SAP^{1c}	KIKIQIII	+	19.5 ± 2.9	1629	87	+
4	SAP^{1d}	KIKIQI	–	n.d.	1630	5.2	–
5	SAP^{1e} (H_2O)	Fmoc-KIKIQI	+	54.7 ± 2.1	1628	94	+
	SAP^{1e} (PBS)	Fmoc-KIKIQI	+	3.0 ± 6.6	1628	31	+
6	SAP^{2a}	KFKFQFFF	+	19.3 ± 0.6	1635	99	+
7	SAP^{2b}	KFKFQF	–	n.d.	1626	83	–
8	SAP^{2c}	KFKFKFQF	0	22.5 ± 0.8	1630	94	+
9	SAP^{2d}	KFKFQFNM	+	20.2 ± 1.9	1628	94	–
10	SAP^{2e}	CKFKFQF	+	22.3 ± 1.4	1627	95	+
11	SAP^{3a}	KIKIQINMWQ	+	11.4 ± 5.9	1629	93	+
12	SAP^{3b}	CKIKIQINMWQ	+	10.7 ± 2.8	1632	87	+
13	SAP^{3c}	KIKIQINM	+	41.9 ± 1.1	1627	64	+
14	SAP^{4a}	CKIKQIINM	+	11.5 ± 6.6	1630	45	+
15	SAP^{4b}	CKIKIQIII	+	19.0 ± 0.3	1630	n.d.	+
16	SAP^{4c}	CKIKIQINM	+	22.3 ± 0.6	1628	72	+
17	SAP^{4d}	CKIKQII	+	n.d.	1635	55	–
18	SAP^{4e}	CKIKIQI	+	17.4 ± 1.1	1626	54	+
19	SAP^{4f}	CKIKQIINMWQ	+	9.7 ± 2.0	1631	n.d.	+
20	SAP^{5a}	RGDKIKIQINMC	+	9.1 ± 2.2	1627	60	+
21	SAP^{5b}	RGDKIKIQINM	+	24.0 ± 0.5	1627	48	+
22	SAP^{5c}	RGDKIKIQIC	+	21.7 ± 1.2	1627	80	+
23	SAP^{5d}	RGDKIKIQINMWQ	+	8.7 ± 2.3	1627	66	+
24	SAP^{6a}	KIKIQIRGD	+	–10.1 ± 1.3	1626	n.d.	+
25	SAP^{6b}	CKIKIQIRGD	0	3.1 ± 0.1	1627	91	–
26	SAP^{7a}	HHHHKIKIKIKI WWWW	0	18.1 ± 0.5	1628	96	+
27	SAP^{7b}	KIKIKIKIWW	0	21.0 ± 0.3	1627	92	–
28	SAP^{8a}	EIEIQINM	+	–36.0 ± 3.5	1630	77	+

Qualitative fibril formation determined via transmission electron microscopy ("+" for fibrils, "0" for aggregates, and "–" for no fibrils/aggregates). PNF form. refers to PNF formation. Zetapotential calculated by electrophoretic mobility. FT-IR band in amide I range. Conversion rate ("Conver. rate") as the amount of SAPs forming PNFs. Ability to bind Proteostat ("PROT bind.," "+" for ≥10 *n*-fold fluorescence enhancement and "–" for ≤10 *n*-fold fluorescence enhancement).

2.2. Identification of Nerve Fiber Growth Stimulating SAPs by Automated Screening

All PNFs were then investigated regarding their potential to promote cell adhesion and growth. The SAPs were coated as 2D matrix on glass coverslips to assess their ability to interact with PNS neurons. Adult mouse dorsal root ganglion (DRG) neurons were used as well-established PNS neuron cell type.[20] In culture, neuronal cell bodies form several protrusions, so-called neurites that differentiate into either an axon or a dendrite. Interestingly, we observed that neurite tips, so-called growth cones, were frequently contacting SAP positive areas on the coverslip (Figure 1C). The spatial pattern of SAP localization on glass surfaces was further analyzed by scanning electron microscopy (Figure 1D–F). Typically, PNFs were arranged in networks (Figure 1F,G) forming plaques with areas up to 1 mm^2 (Figure 1D). Neurons localized on top of these plaques (Figure 1D) contacted the PNFs with several protrusions (arrows in Figure 1E,F).

In the next step, 27 different SAPs were screened for their ability to enhance adhesion and neurite growth using an automated Olympus ScanR microscope (**Figure 2**; Figure S4, Supporting Information). For this, glass dishes were coated with 25 µg mL^{-1} SAP solutions. As negative control, glass surfaces remained uncoated. The SAP activity on neurite growth was compared to a laminin-derived peptide (Cys-lam) used as an established positive control (Figure 2B).[21] Cys-laminin also forms nanofibers and was added on top of poly-L-lysine (PLL) pre-coated glass (PLL/Cys-lam). DRG neurons were cultured in nerve growth factor (NGF) supplemented medium for 24 h.

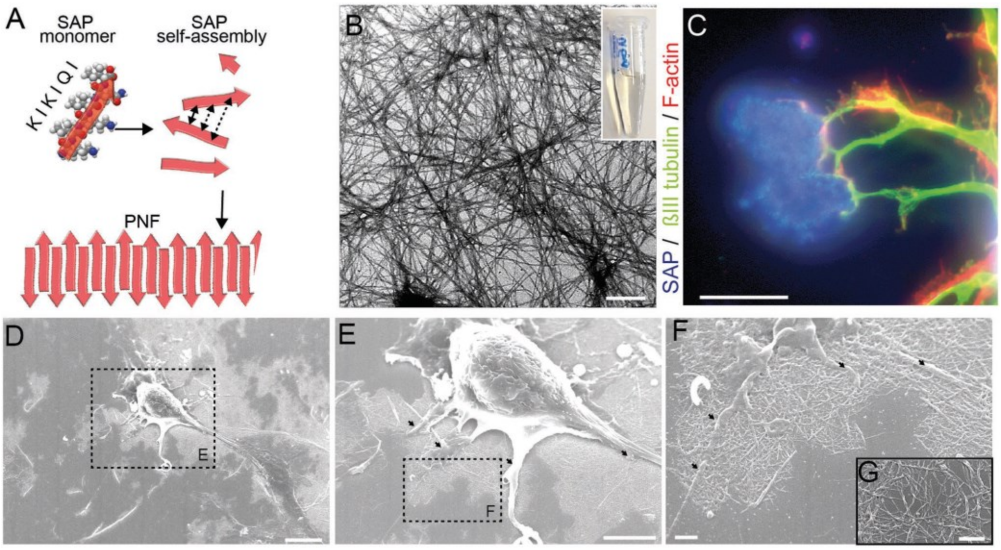

Figure 1. SAPs form PNFs that arrange in networks that can serve as scaffold for neuronal cell adhesion. A) Schematic illustration of SAP assembly forming PNFs. A SAP monomer consisting of the amino acid sequence KIKIQI interacts with other monomers to form PNFs. B) TEM picture of PNFs based on SAP^{1e} in solution. PNFs are up to several 100 µm in length. C) PNFs form plaques (blue) on glass coverslips serving as adhesion points for nerve fibers (green). D–G) Scanning EM pictures of primary neurons plated on SAP^{1e} PNFs. Neurons contact PNFs with several cellular protrusions (arrows in E,F) and PNFs are arranged in networks (F,G). (B) = 600 nm; (C) = 20 µm; (D) = 100 µm; (E) = 50 µm; (F) = 10 µm; (G) = 5 µm.

In order to measure the activity of SAPs on neurons, we quantified three parameters (Figure 2 and Figure S4, Supporting Information). i) The number of attaching neurons was calculated by counting the number of DAPI and βIII tubulin double positive cells. ii) The neuronal area (revealed by the sum of all βIII tubulin signals/neuron) was automatically measured (see Materials and Methods provided in the Supporting Information). Here, each neuron was grouped into three categories according to the total βIII tubulin area determined (large, medium, and small neurons; see Materials and Methods). Neurons with the largest area are typically also those neurons with longest neurites. To directly estimate neurite length, we assessed the length of the longest neurite/neuron with Axiovision software (Figure S4B, Supporting Information). iii) The number of branches per neuron was quantified with a Sholl analysis (Figure S4, Supporting Information). SAPs with highest biological activity should also enhance the number of attaching neurons, induce a high number of branches and elevate the neuronal area strongest, thereby elevating the percentage of neurons classifying for "large neurons" in comparison to less active SAPs.

DRG neurons cultured on uncoated glass (Figure 2A,E) were not able to adhere or protrude neurites whereas PLL/Cys-lam (Figure 2B,F) coating enhanced both parameters. Inspection of the SAP library revealed that many but not all SAPs improved adhesion of non-neuronal and neuronal cells and promoted nerve fiber growth (Figure 2I; Figure S4, Supporting Information). The number of neurons grown on SAP^{5c} or SAP^{2e} was almost identical to our positive control PLL/Cys-lam (Figure S4, Supporting Information). In addition, coating with SAP^{5c} or SAP^{2e} had a strong impact on neurite growth since many neurons were grouped into "medium" or "large" neurons (Figure 2I) and they also enhanced the number of branches/neuron (Figure S4C, Supporting Information). Both SAP^{5c} and SAP^{2e} revealed a much stronger activity on neurite growth than the negative control glass and many other SAPs and they reached approximately 50–60% of the values obtained for the PLL/Cys-lam positive control (Figure 2I).

Interestingly, attachment of an Fmoc-protection group in SAP^{1e} enhanced neuronal growth (Figure 2I; Figure S4, Supporting Information) compared to the unprotected backbone (SAP^{1d}), a finding in agreement with a previous report using different Fmoc-protected SAPs.[22] We noted that RGD functionalization at the SAP N-terminus (e.g., SAP^{5b}, SAP^{5c}, SAP^{5d}) also showed a positive effect and further enhanced SAP activity compared to the backbone alone. Interestingly, however, a C-terminal RGD (e.g., SAP^{6a}) revealed the opposite effect and reduced neuron outgrowth (Figure 2I; Figure S4, Supporting Information).

SAP^{5c}, SAP^{1e}, and SAP^{2e} showed the most promising activity as revealed by three parameters i) the impact of the SAP in enhancing numbers of neurons adhering to the SAP coated coverslip (Figure S4A, Supporting Information), ii) the number of branches (Figure S4C, Supporting Information), and iii) the potential to elevate the neuronal area (Figure 2I) and average length of the longest neurite (Figure S4B, Supporting Information) as an indication for their potential to stimulate neuronal

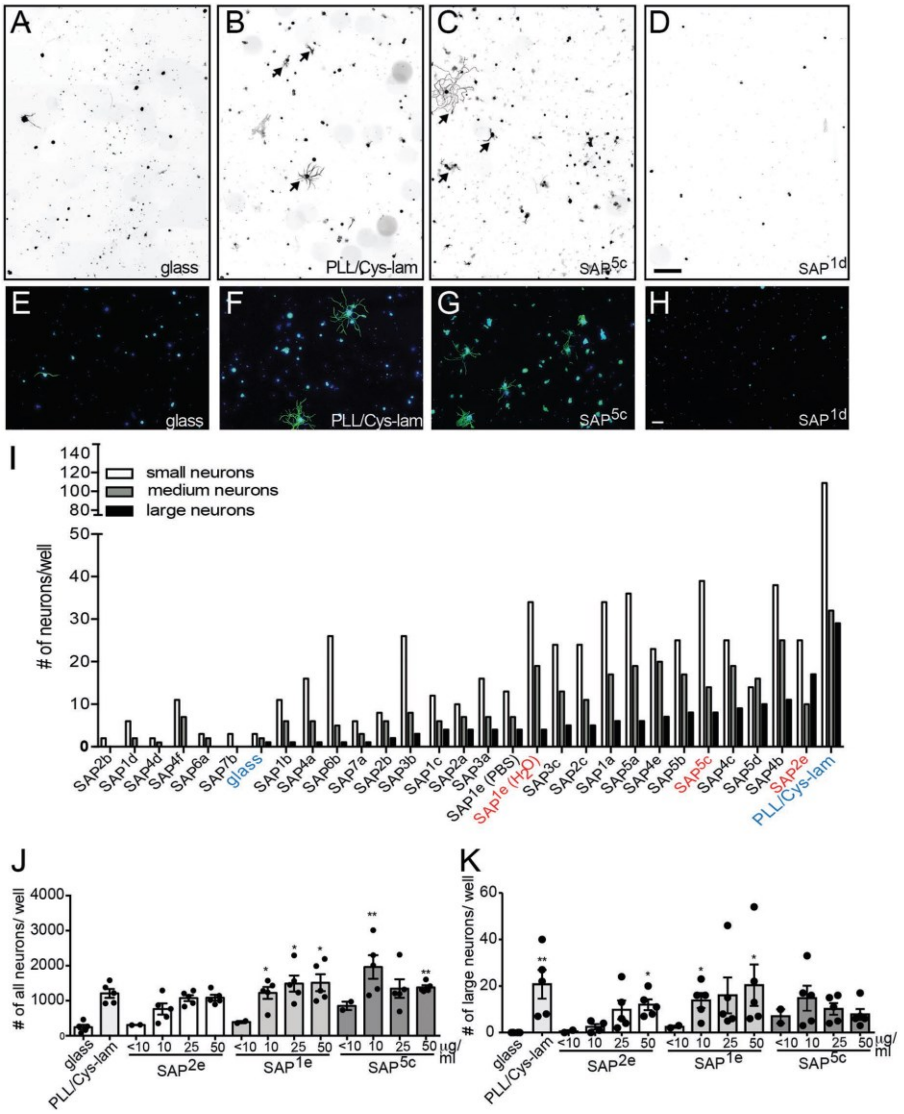

Figure 2. SAPs stimulate adhesion and outgrowth of PNS neurons. A–H) DRG neurons were plated on coverslips without coating (A,E), or coated with PLL/Cys-lam (B, F), SAP^{5c} (C, G) or SAP^{1d} (D,H). After 24 h in culture, neurons were stained with βIII tubulin (black in A–D; green in E–H) and DAPI to label cell nuclei (E–H). (E–H) show higher magnifications of individual neurons. SAP^{5c} stimulated neuronal adhesion and growth (C,G), in opposite to SAP^{1d} (D,H). I) Quantification by grouping neurons according to their total area into small, medium and large neurons. All SAPs were ranked with regard to the number of large neurons. The positive control PLL/Cys-lam was placed at the top, whereas the negative control glass was positioned at the bottom. Several SAPs, including SAP^{1e}, SAP^{5c}, and SAP^{2e} (in red), used for further analysis, stimulated cell adhesion and growth almost to the same extent as PLL/Cys-lam. J,K) Different concentrations of SAP^{2e}, SAP^{1e}, and SAP^{5c} were used to coat coverslips. Below 10 µg mL^{-1}, SAPs did not promote neuronal adhesion (J) and growth (K). Above 10 µg mL^{-1}, SAPs stimulated both parameters with no effect by further enhancing SAP concentration except for SAP^{2e}. For "<10 µg mL^{-1}" data from 1 and 5 µg mL^{-1} were pooled. Each circle represents one culture derived from one mouse. Statistical significance was calculated in relation to glass. Scale-bars (A–D) = 500 µm; (E–H) = 100 µm.

growth (Figure 2I). Thus, these three SAPs were selected for a more in-depth investigation in additional independent experiments (Figure 2J,K). The three selected SAPs were analyzed for a concentration-dependent effect (Figure 2J,K). We found that for all cases, concentrations of about 10 µg mL^{-1} were sufficient to induce bioactivity. Notably, only SAP^{2e} showed a strong concentration-dependent increase in activity on neuronal adhesion (Figure 2J) and outgrowth (Figure 2K), whereas SAP^{1e} and SAP^{5c} activity could not be further augmented above a concentration of 10 µg mL^{-1}.

So far, all SAPs were tested in the presence of NGF. Notably, when omitting NGF, SAP^{1e} and SAP^{5c} were as efficient or even better in stimulating neurite growth compared to PLL/Cyslam (Figure S4, Supporting Information). Finally, we assessed whether SAPs also promoted CNS neuron growth (Figure S5, Supporting Information). For this, mouse primary cerebellar neurons were plated on SAPs. Indeed, as observed for PNS neurons (Figure 2), some SAPs also enhanced outgrowth of CNS neurons as well (Figure S5, Supporting Information). The in vitro screen of our original SAP library allowed the identification of novel SAPs that formed PNFs with high conversions that stimulated cell growth and adhesion in general and in particular of primary mouse PNS and CNS neurons.

2.3. Correlation of SAP Sequences and PNF Morphologies with Neuronal Activity

To gain insights into the various structural features of the identified SAPs that could be responsible for high neuron outgrowth, a structure–property relationship analysis was accomplished. First, we related the SAP amino acid sequences to their neuronal activity in a data-mining approach (**Figure 3**A).[23] Then, the resulting PNFs were studied to assess their physicochemical properties such as PNF morphology, surface charge, intermolecular β-sheet content, persistence length, and stiffness and correlate these parameters to their neuronal activity.

The data-mining approach was accomplished based on the identification of recurring patterns of amino acid sequences that are present in high-activity SAPs and, simultaneously, are absent in low or medium active SAPs. However, this search was challenging for the following reasons. First, it is not feasible to experimentally test the activity of all possible sequence combinations, or even a sizable subset thereof, which relates mainly to the problem of dimensionality. Second, already minor changes to an SAP sequence can lead to a major change in their activity. For example, by extending the sequence of SAP^{2b} (KFKFQF) with a single cysteine residue (SAP^{2e}, CKFKFQF), the neuronal activity was significantly enhanced (Figure 2).

To render this high-dimensional problem tractable, we simplified the system by coarse-graining the amino acids into four basic features according to their hydrophobicity and charge, namely hydrophobic (H^0), hydrophilic (P^0), positively charged (P^+), and negatively charged (P^-) (Table S2, Supporting Information). This simplification drastically reduced the number of possible sequences, while keeping the essential chemical features intact. With these coarse-grained SAP features, we then built a library of amino acid patterns. We composed sequence units of length 3 to 5 considering all possible combinations of the four features at each sequence position. Further repetitions of these units provided us with a comprehensive library of polypeptide patterns (1344 in total, see Figure S6 and surrounding text, Supporting Information). These patterns were subsequently compared to the SAPs using an overlap index "I" (Equation (S2), Supporting Information). We then ranked patterns by means of a score (Equation (S3), Supporting Information) that favors features present in high-activity SAPs and penalizes those found in the low- and medium-activity sequences. Polypeptide patterns with high scores represent potential candidates for high neuronal activity. In a final step, these high-score candidates were further analyzed for the variability of the amino acid features along the peptide sequence (Figure S7, Supporting Information). We found that some features, particularly those at positions 1, 2, 4, and 5, were highly conserved in the patterns predicted for high neuronal activity, while the feature at position 3 has a higher variability. The most likely pattern to yield high activity SAPs was identified as the sequence $H^0P^+H^0P^+H^0$, shown in Figure 3, with alternating hydrophobic and positively charged amino acids along the peptide chain. The predicted pattern is robust as it consistently occurred in an out-of-sample analysis (Figure S8 and surrounding text, Supporting Information). In addition, we compared the predicted pattern to peptide sequences with high neuronal activity that were reported in the literature (Table S3 and Figure S9, Supporting Information). We observed a broad range of overlap values. However, other SAPs belonging to the peptide amphiphile and RADA families only showed moderate to low overlap. This result is conceivable as these SAPs belong to very different regions of the sequence space and they have quite different structural properties.

Table 1 gives an overview of the morphologies of all PNFs that were obtained by 2D TEM micrographs as discussed above. It is known that intermolecular β-sheet structures, stabilized by hydrogen bonding, within the PNF have an important impact on their persistence lengths and stiffness. Therefore, the β-sheet structures in PNFs were first characterized by the blue-shifted emission of Proteostat (Figure S10, Supporting Information).[24] Most SAPs, which formed PNFs or aggregates in TEM investigations, also showed a fluorescence enhancement in the presence of Proteostat. However, some PNFs did not incorporate the dye (e.g., SAP^{2d}, SAP^{4d}). SAP^{3b} revealed a significant fluorescent enhancement, but no PNFs in TEM investigations (Figures S3 and S10, Supporting Information). The 3D morphology of two pairs of SAPs with similar sequences was then analyzed with sub-nanometer resolution by phase-controlled atomic force microscopy (AFM).[25] We performed a single PNF statistical analysis by AFM to determine the cross-sectional fiber height[26] (Figure 3B–F; Figure S11, Supporting Information). The fibrous morphology found in TEM images was confirmed (Figure 3B–F). Interestingly, the cross-sectional height of PNFs formed from SAP^{2b} (KFKFQF) and SAP^{2e} (CKFKFQF) differed significantly. This was an unexpected observation as both SAPs had a similar sequence with a terminal cysteine as the only difference. SAP^{2b} (1.4 ± 0.4 nm) without the cysteine showed a significantly lower cross-sectional height than SAP^{2e} (5.8 ± 0.5 nm; Figure 1L). The same trend was found for SAP^{5c} compared to SAP^{6a} (9.4 ± 0.5 nm vs 5 ± 0.5 nm; Figure 3F).

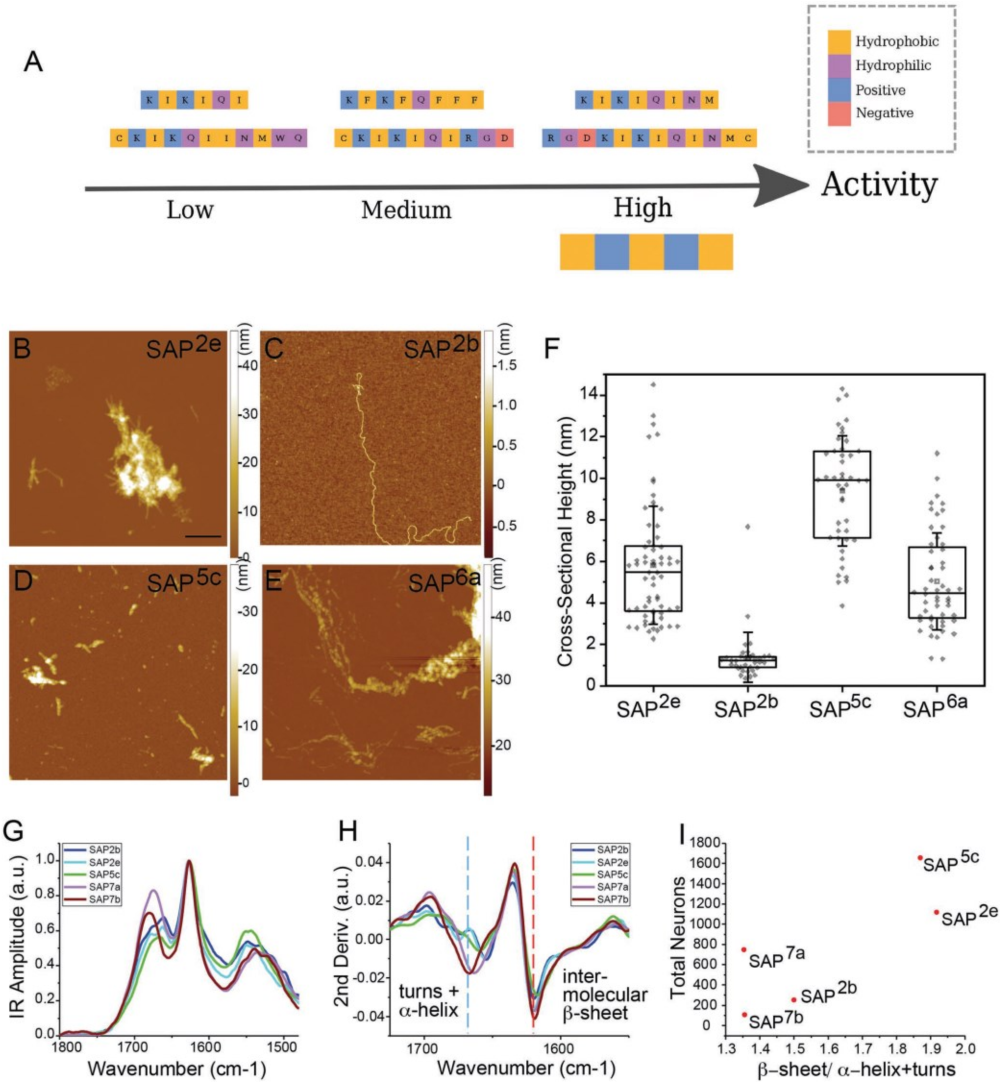

Figure 3. Rational analysis of SAP and PNF features to elucidate the important factors for neural activity. A) The structural motif of "active" SAP sequences essential for high neuronal activity was identified using a statistical analysis and is shown in the figure in coarse-grained representation. B–F) AFM analysis of PNF morphologies. Examples of individual PNFs from different SAPs are depicted in (B–E). Measurement of cross-sectional height of several PNFs (F). Scale-bars (B–E) = 500 nm. G–I) Analysis of PNF structure by FT-IR spectroscopy. G) IR spectra of selected SAPs normalized to the maximum of the amide I band. H) Second derivative of IR spectra for secondary structure analysis. I) The total number of neurons correlates with the ratio of intermolecular β-sheets to α-helix and turns.

To determine secondary structural elements in a more quantitative fashion,[27] FTIR spectroscopy of lyophilized PNFs was performed and signals in the amide I band region in the range of 1625–1635 cm^{-1} (Table 1; Figure S12, Supporting Information) corresponding to intermolecular parallel β-sheet conformation as well as signals between 1650–1685 cm^{-1}, corresponding to α-helices and turns were analyzed. Obviously, the β-sheet content within the PNFs varied and we could clearly observe from the FT-IR spectra an increase of the β-sheet content for highly active SAP^{2e} and SAP^{5c}.

By combining the structural and physico-chemical information of the PNFs with the data on neuronal activity obtained from the automated screen, critical parameters that define the biological activity of the SAPs were identified (summarized in Table S4, Supporting Information). 1) PNF morphology and high conversion rates were essential for bioactivity. SAP^{1d}, for example, showed a low conversion rate of ≈5%, indicating its poor ability to form assemblies, consequently preventing the formation of PNFs that could interact with cells. 2) Positive surface charges appear essential for interactions with neurons. SAP^{8a} and SAP^{6a} form fibers with negative zeta potentials that did not show high neuronal activity. 3) A significant intermolecular β-sheet signal in FT-IR, such as for SAP^{2e} and SAP^{5c} (Figure 3G–I) was clearly correlated with increased cross-sectional height of the fibrils and high neuronal activity. Positively charged PNFs that did not exhibit strong content of intermolecular β-sheet structure only revealed moderate to low neuronal activity (see for example SAP^{2b}, SAP^{7a}, and SAP^{7b}). Interestingly, the intermolecular β-sheet coincides with a higher fiber diameter, as measured by AFM, indicating that the thicker fibers likely provide higher stiffness and persistence length compared to their non-mature counterparts (compare SAP^{2e} and SAP^{2b}).[24,25] However, the change in the cross-sectional geometry of the fiber may also change the surface of the fibers, which could also contribute to their biological performance.

2.4. SAP-Derived Nanofibers Enhanced Neuronal Adhesion in the Stripe Assay and Schwann Cell Adhesion and Growth

In order to further test SAPs as substrates for neuronal growth, we employed the so-called stripe assay (Figure S13, Supporting Information).[28] Here, bona fide growth promoting substrates are arranged in alternating stripes interspersed by control lanes. We prepared alternating stripes consisting of RITC (Rhodamine B isothiocyanate)-conjugated SAP^{5c} and glass (Figure S13A, Supporting Information). Indeed, DRG neurites preferred to grow on stripes containing SAP^{5c} (Figure S13A, Supporting Information). In fact, some neurites were crossing an SAP^{5c}-free stripe to connect to the next available SAP^{5c} stripe. In addition to neurites that preferentially adhered to SAP^{5c}-positive stripes, neuronal cell bodies (arrows Figure S13A, Supporting Information) and non-neuronal DAPI positive cells also showed a strong tendency to grow on SAP^{5c} stripes (blue in Figure S13A, Supporting Information).

As control, we used assays with both stripes containing SAP^{5c} (Figure S13B,D, Supporting Information). Here, we observed a randomized outgrowth of DRG neurites (Figure S13B,D, Supporting Information). The stripe assay results show that DRGs neurons prefer to grow on SAP substrates with high bioactivity.

So far, the impact of SAPs was primarily tested on neurons (Figure 2 and Figure S13, Supporting Information). However, Schwann cells, the PNS myelinating cells, also influence outcome of axon regeneration.[29] Thus, the impact of SAPs on Schwann cell function was analyzed since SAPs may exert a positive influence on both neurons and Schwann cells, leading to a synergistic effect in axon regeneration (Figure S14, Supporting Information).

Primary S100-positive Schwann cells derived from DRGs interacted with RITC-conjugated SAP^{2e} positive plaques (Figure S14A, Supporting Information) similarly to neurons (see Figure 1). All three selected SAPs, SAP^{2e}, SAP^{1e}, and SAP^{5c} elevated Schwann cell adhesion (Figure S14G, Supporting Information) and size (Figure S14H, Supporting Information) compared to uncoated glass. Notably, all three SAPs provided a growth scaffold for this glial cell type, which was about as potent as laminin (Figure S14G,H, Supporting Information). Thus, SAPs increased adhesion and growth in several cell types including neurons and glia cells.

2.5. SAPs Stick in the Lesion Center of Lesioned Peripheral Nerves

In previous experiments, selected SAPs stimulated outgrowth of primary neurons. In the next step, we assessed the potential of these SAPs to potentiate axon regeneration in vivo. We employed a mouse PNS lesion model where the facial nerve branches that connect motor neurons in the brainstem with several facial muscles responsible for triggering, for example, whisker movement, are surgically injured (**Figure 4**A).[30]

In the first set of experiments, we tested the time-window of SAPs to remain in the lesion site and determined the precise SAP localization with regard to the severed nerve stumps. This was important, since rapid diffusion away from the injury site and random localization of any biomaterial would not support stimulation of axon regeneration. Therefore, RITC-conjugated SAP^{5c} (SAP^{5c}-RITC) was injected into the lesioned buccal and marginal nerve branch (Figure 4A). Subsequently, whole amount preparations of the nerve and underlying muscle were analyzed at 7 (Figure 4B–D), 14 (Figure 4E), and 21 (Figure 4F) days after injury. We observed perseverance of fluorescence signal originating from SAP^{5c}-RITC located precisely at the injury site at several time-points along the entire 3-week period after injury (Figure 4B–F). The ability of the SAPs to remain at the injection site in vivo is further supported by SAP^{5c}-fibers persisting in the presence of proteinase K (Figure S15, Supporting Information). We further inspected PNF localization on histological sections through the two nerve stumps (Figure 4G–I). PNFs were found exactly in the gap between two nerve stumps and also in the facial nerve (arrows Figure 4I). Quantification of the staining intensity of SAP^{5c}-RITC confirmed enrichment of the PNFs in the lesion center (Figure 4J). We wondered whether the highly adhesive properties of SAP^{5c} were due to their potential to form fibrils. As a control experiment, we injected RITC alone and almost no signal was detectable (Figure 4L) arguing again for a role of the SAP part in mediating tissue interaction. SAP^{1d}-RITC with a weak tendency to form PNFs (Figure 4K; Figure S3, Supporting Information) was added and resulted in only weak signals (Figure 4K) indicating that PNF formation contributed to high tissue adhesiveness of SAPs. Most likely, the positive charge of the PNFs was responsible for their stickiness. In summary, we succeeded in administering the SAPs to a precise localization

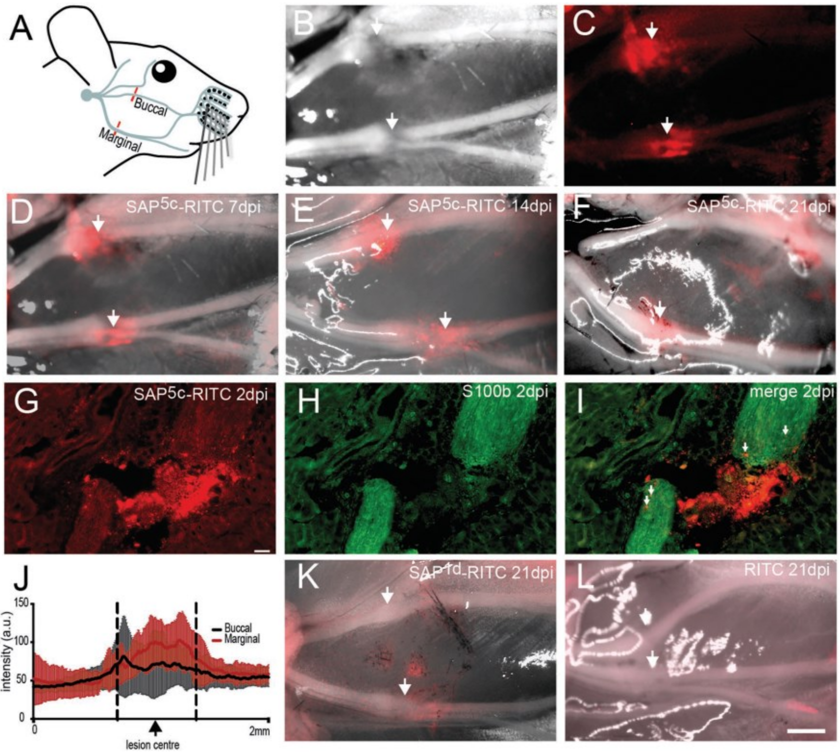

Figure 4. SAPs stick to injured nerves for up to 3 weeks. A) Overview of the mouse facial nerve (blue) with lesion sites (red lines) at the buccal and marginal branch. B–F) SAP^{5c}-RITC was injected into the lesion site and nerve preparations were analyzed at one (B–D), 2 (E) or 3 (F) weeks after injury. (B–D) shows light microscopical picture of the nerve (B), the same nerve with RITC fluorescence alone (C), and the composite picture (D). Arrows indicate the lesion and SAP injection site. G–I) Section through the nerve stumps at 2 dpi stained for SAP^{5c}-RITC (G) and S100b to label Schwann cells in the nerve (H) and the merged picture (I). SAP^{5c}-RITC was found between the nerve stumps but also inside the nerve (arrows in I). J) Quantification of SAP^{5c}-RITC intensity at the buccal and marginal branch in the lesion center and the surrounding nerve. Strongest signals were observed in the lesion center. K) SAP^{1d}-RITC, an SAP only weakly producing nanofibers, resulted in faint signals around the two lesion sites (arrows). L) RITC not conjugated to an SAP did not adhere to the facial nerve. Scale-bars (B–F,K,L) = 1 mm; (G–I) = 50 µm.

and—importantly—the SAPs persisted at the injection site for prolonged periods of time, indicating good stability during axon regeneration.

2.6. The SAP^{5c} Enhances Peripheral Nerve Regeneration

Since SAPs used in this study showed strong adherence to nerve tissue (Figure 4), next we assessed their potential to augment facial nerve regeneration (Figures 5 and 6). For this, we again performed unilateral lesion to the mouse facial nerve and injected SAP^{5c}-RITC or—as control—PBS in the lesion site (**Figure 5**). We also used SAP^{1d}, a SAP previously shown to have no neurite growth propagating potential and a weak tendency to form nanofibers (Figure 2; Figure S4, Supporting Information). Here, axon regeneration was similar to the negative control PBS (data not shown). After injection, the extent of nerve regeneration was analyzed by several histological parameters at 7, 14, or 21 days post injury (dpi).

First, we analyzed retrograde transport of a fluorescent tracer (FG) injected into the whisker pads (Figure 5A–D,Q). Upon successful axonal regeneration, FG is retrogradely transported from the whisker pad via the reconnected nerves to the facial motor neurons.[20,31] FG-positive neurons were counted and normalized to numbers obtained on the intact facial nucleus presenting maximal FG transport along axons. At 7 days post injury, approximately 30% of all MNs were FG-positive indicative of successful regeneration, however, without any difference between experimental groups (Figure 5Q). One week later, this percentage doubled and SAP^{5c}-injected animals already showed a tendency toward higher numbers of FG-positive MNs (Figure 5Q). After 3 weeks of injury, we obtained a statistically significant increase in facial nerve regeneration in the SAP^{5c} group compared to PBS-treated animals

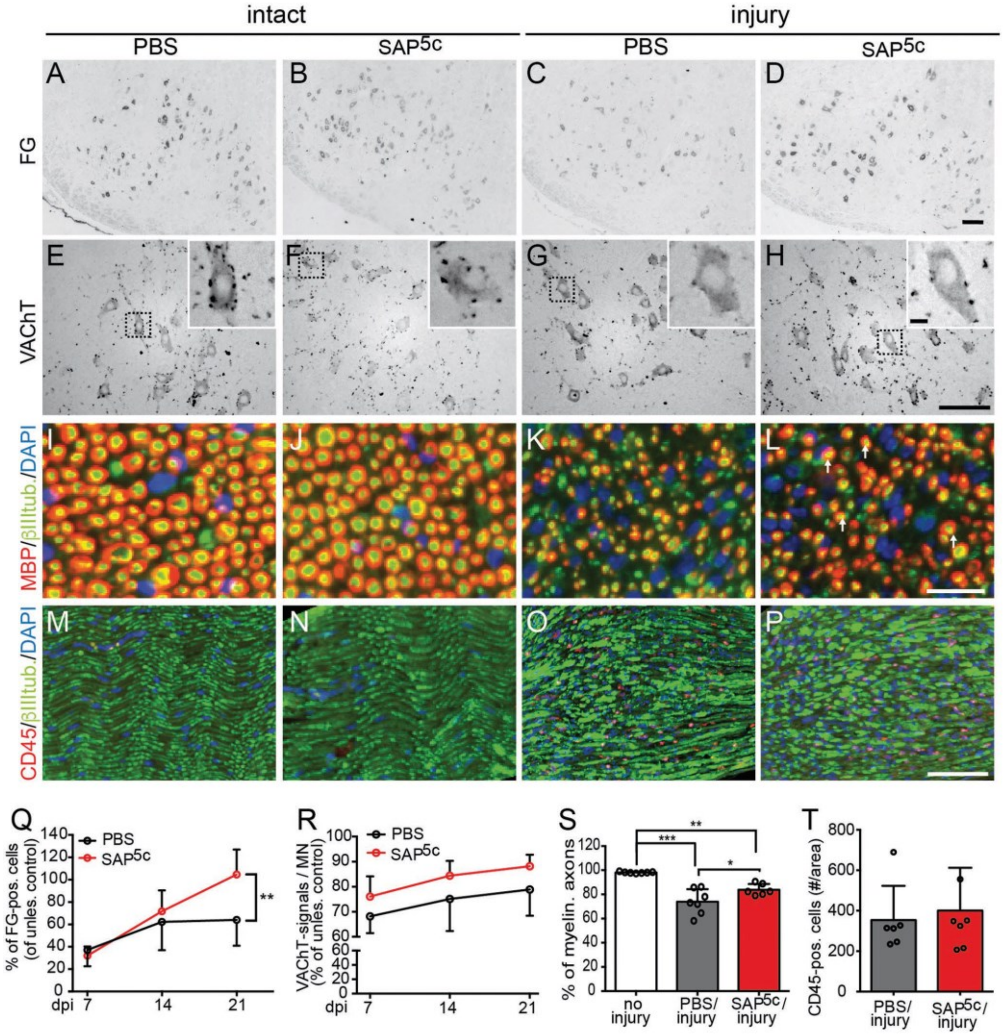

Figure 5. SAP5c improves several histological parameters of facial nerve regeneration. A–D) Number of tracer (FG) positive neurons are depicted at 21 dpi. In the intact facial nucleus, numbers of FG-positive MNs are identical in PBS-injected (A) and SAP^{5c}-injected (B) animals. After injury, more FG-positive MNs are present in SAP^{5c}-treated animals (D) compared to PBS-treated animals (C). B–H) The number of VAChT positive axonal sprouts was higher upon SAP^{5c} injection (H) in comparison to PBS (G) at 21 dpi. Insets show higher magnification of MNs marked with dashed lines. I–L) Axons and myelin of facial nerves were stained with βIII tubulin and MBP, respectively. At 21 dpi, the number of myelinated axons was higher in SAP^{5c}-treated animals (arrows in L) compared to PBS-treated animals (K). M–P) Peripheral CD45-positive immune cells were present in the facial nerve at 7 dpi to a comparable extent in PBS-injected animals (O) and SAP^{5c}-injected animals (P). Without injury, no CD45-positive cells are present (M, N). Q) Quantification of FG-positive MNs at three time-points post injury. Data are normalized to the non-injured condition (set to 100%). R) Quantification of VAChT signals/MN at three time-points post injury. Data are normalized to the non-injured condition (set to 100%). S) Quantification of myelinated axons after injury. Intact nerves were set to 100%. Each circle reflects one animal. T) Quantification of CD45-positive cells in the facial nerve. No differences between groups were observed. Each circle reflects one animal. Scale-bars (A–D; E–H; M–P) = 100 µm; (E–H insets) = 10 µm; (I–L) = 20 µm.

(Figure 5C,D,Q). Now, SAP^{5c}-treated animals showed approximately 30–40% more FG-positive MNs than animals treated with PBS (Figure 5Q). The total MN number staining positive for Nissl was comparable between conditions (data not shown) thus indicating that SAP^{5c} effects are not due to altered neuron death or survival.

Next, we tested the abundance of vesicular acetylcholine transporter (VAChT; Figure 5E–H,R) whose abundance is downregulated during motor neuron degeneration and increasing once axons start to regenerate.[32] We analyzed VAChT abundance at all three time-points after injury and normalized numbers to intact facial nuclei of PBS-(Figure 5E) or SAP^{5c}-treated (Figure 5F) animals. In line with previous reports,[32] VAChT was distributed mainly at the periphery of cell bodies (Figure 5E–H). At 7 dpi VAChT numbers were reduced by approximately 30–35% compared to intact MNs and numbers gradually increased up to 90% at 21 dpi (Figure 5R). Importantly, at all three time-points, SAP^{5c}-treated animals (Figure 5H) showed on average 10% more VAChT positive sprouts compared to the PBS-injected animals (Figure 5G,R).

In the nerve injury, so-called Wallerian degeneration triggers nerve degeneration and removal of myelin resulting in un-myelinated axons.[33] Indeed, numbers of myelinated axons decreased 21 dpi (Figure 5K,L) by about 30% compared to intact nerves in either experimental group (Figure 5I,J). Facial nerves injected with SAP^{5c}-RITC (arrows Figure 5L) had 10% more myelinated axons compared to nerves receiving PBS (Figure 5K) suggesting that SAP^{5c} can enhance re-formation of myelinated axons (Figure 5S).

Finally, we analyzed infiltration of peripheral CD45-positive immune cells into the facial nerves to control for a potential augmented immune response elicited by the SAPs (Figure 5M–P,T). We observed entry of immune cells specifically in the injured (Figure 5O,P) and not control (Figure 5M,N) nerve at 7 dpi. However, quantification revealed no additional immune cell infiltration by the SAP injection (Figure 5T). Thus, as also observed in previous reports,[7c] SAPs do not appear to trigger an immune response in the host tissue. In summary, several histological parameters of PNS regeneration showed enhanced facial nerve regeneration in animals injected with SAP^{5c}.

2.7. SAP^{5c} Enhanced Physiological Recovery of Whisker Movement After Injury

Histological inspection already suggested enhanced motor neuron recovery after injury by SAP injection (Figure 5). However, this does not automatically result in the recovery of physiological function of injured nerves. In order to analyze whether nerve regeneration also enhanced function of the neuromuscular unit controlling whisker movement, we performed timelapse-videomicroscopy as reported by others[34] and us[35] before (**Figure 6**). Here, individual vibrissae of both sides of the animals were recorded before and at several timepoints after injury (Figure 6A). Typically, whisker movement of both sides is synchronized as shown by our quantification (Figure 6D). One day after injury, whisker movement is impaired on the injured side (see video trace in Figure 6E) and vibrissae engage a stiff position pointing toward one direction (arrows Figure 6B). At 18 dpi whisker movement is partially restored (Figure 6C) and the injured whiskers (black line in Figure 6F) start to rotate again.

When comparing PBS- and SAP^{5c}-injected animals (N = 7 each), we observed in both groups an identical drop in whisker movement at 1 dpi for two parameters, sum of all angles rotated (Figure 6G) and maximal amplitude (Figure 6H). Within the next 18 days, whisker movement increased in both groups. However, we noted that recovery in SAP^{5c}-treated compared to PBS-treated animals was enhanced (Figure 6G,H). This was evident with the angular range (Figure 6H) and even more pronounced when inspecting the angular sum (Figure 6G) at several time-points post injury showing that SAP^{5c} enhanced regeneration in comparison to the PBS-treated animals. However, statistical significance was not reached between PBS- and SAP-treated groups and would require more animals to be included. As control, we again employed SAP^{1d}, an SAP with no obvious biological activity (Figure 2). PBS- and SAP^{1d}-injected animals were indistinguishable with regard to whisker recovery (data not shown). We also tested SAP^{2e} as a second active SAP that also enhanced whisker movement compared to PBS-treated animals although weaker compared to SAP^{5c} (data not shown). These first results are very promising and show that SAPs have the potential to not only enhance histological parameters of nerve regeneration (Figure 5) but also functional recovery of motor functions (Figure 6). We believe that additional experiments, for example, for dose finding, will be required to further boost the in vivo effectiveness.

3. Discussion

3.1. Structural Features of SAPs for the Modulation of Cellular Adhesion and Growth

We have shown that SAPs are a promising and versatile biomaterial in neuronal regeneration. In our studies, several unmodified and also RGD-functionalized SAPs stimulated adhesion and growth of nerve cells (Figure 2; Figure S4, Supporting Information). Fibril formation was a prerequisite for cell growth stimulation as SAP^{1d} with moderate fibril formation and conversion rate only weakly promoted neurite growth (Figure 2). Only when fibril formation was induced in SAP^{1d} through Fmoc-functionalization (now called SAP^{1e}) strong neurite growth potential was observed (Figure 2). A data-mining approach allowed us to identify a general amino acid pattern that could propose high-activity peptide sequences (Figure 3) based on alternating hydrophobic and positively charged amino acids ($H^0P^+H^0P^+H^0$). The positive charges are essential as they provide “stickiness,” which seems essential for direct in vivo application.

Interestingly, we observed a strong correlation between the cross-sectional height of the fibers and their activity (Figures 2 and 3; Figure S11 and Table S4, Supporting Information). Materials such as SAP^{2e} and SAP^{5c} formed fibers of significantly larger diameter and revealed much higher activity on neuronal growth than their analogues without a terminal cysteine group (SAP^{2b} and SAP^{6a}). We attributed the change in cross-sectional

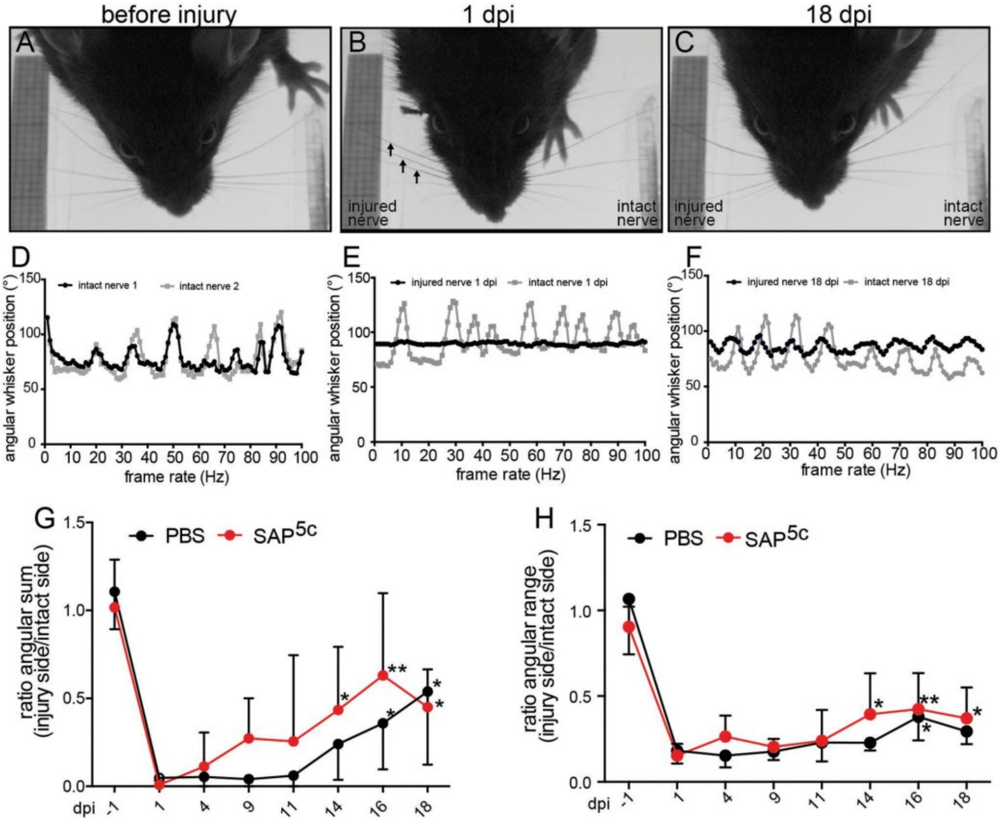

Figure 6. Recovery of whisker movement is enhanced by SAP5c-injection. A–C) Representative pictures of whisker position before injury (A), 1 (B), and 18 (C) dpi. One day after injury, vibrissae of the injured whisker pad (arrows) cannot move and point all toward the same position. D–F) Representative whisker traces from a 100 Hz sequence. Without injury, vibrissae from both sides rotate synchronously (D). At 1 dpi, whiskers do not move at the injured side (black line E) whereas movement is possible on the contralateral side (gray line in E). At 18 dpi, whisker movement at the injured side recovers to some extent (black line in F). G) All movements with angles ≥10° were summed up in a 100 Hz sequence. A ratio between the injured and un-injured side was calculated and plotted along several time-points of measurement. Whisker movement in SAP^{5c}-injected animals (red line) recovered quicker than in PBS-treated (black line) animals. H) The maximal amplitude of whisker movement is depicted. SAP^{5c}-treated animals had in general higher amplitude than the PBS control group.

height to a difference in the maturity of amyloid fibers and to a different surface structure consequently leading to a change of activity. In addition, the nanofiber diameter is correlated to an increased persistence length of the fibrils that is likely to be positively correlated with higher stiffness of the fibrils. It is known that substrate stiffness affects neuronal growth[36] and increased substrate stiffness enhances DRG growth in particular,[37] which is in agreement with our data (Figure 2).

We observed that the unmodified SAP backbone SAP^{1e}, SAP^{4e}, SAP^{2c}, and, for example, SAP^{4b} already provided a good growth substrate (Figure 2; Figures S4 and S5, Supporting Information). This adhesiveness might be mediated by electrostatic forces of negatively charged cell membranes interacting with positively charged nanofibers. This observation is further supported by the lack of cell adhesion on SAPs with a net negative charge (Figure S1, Supporting Information). Additional functional groups such as the RGD sequence in SAP^{5c}, SAP^{5b}, and SAP^{5d} further augmented the potential of SAPs to enhance neuronal growth (Figure 2). In fact, SAP^{5c}-derived nanofibrils gave best results in our in vivo PNS regeneration model (Figures 5 and 6). In addition to testing the linear RGD epitope, we also analyzed cyclic RGD, which did not further increase nerve fiber growth (data not shown). Interestingly, only N-terminal but not C-terminal RGD (e.g., SAP^{6a}, SAP^{6b}) SAP modifications provided a boost in activity (Figures 1 and 2). This points toward a potential sterical hindrance of the RGD epitope at the C-terminus preventing its surface exposure and possibly interaction with its cognate cellular integrin receptor.

3.2. Direct SAP Nanofibril Injection as Tool in Tissue Regeneration

The SAP activity was not limited to individual cell types but they exhibited a wide range of bioactivities including stimulation of cell adhesion and growth of glial and neuronal cells derived from both the PNS and CNS (Figure 2; Figures S4, S5, and S13, Supporting Information). Considering previous reports on SAP-mediated activity on muscle cells,[38] stem cells[39] and, for example, bone cells,[40] these results suggest that SAPs represent a versatile extracellular-matrix mimicking biomaterial providing adhesion and growth support to many different cell types in the CNS and PNS.

In this study, we used a novel approach to deliver SAP-derived PNFs to injured tissue in living animals. PNFs in solution were directly applied to the injury site without any additional incorporation into hydrogels or artificial nerve conduits (Figures 4–6). This was only possible since the newly discovered and optimized SAPs used in this study provided high adhesive properties to tissues (Figure 4). Importantly, this "stickiness" was not temporary but lasted for at least 3 weeks after injury (Figure 4). Such a time window is sufficient to induce enhanced regenerative cell processes during axonal regeneration as investigated in this mouse study (Figures 5 and 6) but also in other injured organs. For instance, PNFs could be used to fill cavities formed during bone fracture, CNS spinal cord lesions or traumatic brain injury. In support for the latter, we demonstrated already that selected SAPs identified in this study enhance outgrowth of CNS neuron types (Figure S5, Supporting Information).

In all parameters of axonal regeneration, the RGD-containing SAP^{5c} was superior to PBS control or other SAPs thereby highlighting the specificity of SAP^{5c} results obtained (Figures 5 and 6). It is rather challenging to directly compare our data with previously reported PNF approaches since often, different species (rat vs mouse), model systems (e.g., facial vs sciatic nerve), application routes (hydrogels, tubes conduits etc.), time-points after injury (3–8 weeks) were used. For instance, in mice, the application of nerve autografts[15] as positive control could not be used since an autograft of the mouse facial nerve is far too small to suture it to an injured nerve stump. Therefore, the regeneration outcome was compared to PBS injection in the lesion site as negative control. In addition, depending on the disease model, different regeneration parameters (histological, physiological, molecular) were employed, which also limits a direct one-to-one comparison.

We observed on the histological level, that SAPs used in our study elevated regeneration between 10–40% depending on histological read-out (Figure 4Q–S). This is in concordance with previously achieved results, for instance the effect of the RADA 16 nanofibers that elevated numbers of axons reinnervating target muscles by 10–20%.[16a,b] For functional regeneration, for example, recovery of limb movement or whisking in sciatic or facial nerve injury, respectively, data are in general more heterogenous which is often due to variability between injured animals. In our study, SAP^{5c} was able to enhance functional recovery of whisker movement to approximately 40–50% or pre-injury values at 14 days post injury (Figure 6). Similar to us, in the only other facial nerve injury study available using C16VVVAAAEEE nanofibers, the authors observed that the maximum nerve compound action potentials reached 40% of pre-injury levels. However, here, much longer time-points were required for regeneration (i.e., 8 weeks). In sciatic nerve injury, C16VVAAEE[16c] or the RADA 16 derived nanofibers[16a] enhanced functional recovery of limb motor function by 10–20%. Thus, with all the caution that should be taken into consideration when comparing regeneration data between different model systems and experimental set-ups, data obtained on nanofibers in this study reached levels at least comparable to previous reports. We would like to stress that the SAP material designed and used in this study achieved all effects without the need to additionally use tubes, hydrogels, or other conduits that were required in previous studies, which clearly simplifies their applications.

4. Conclusions

From a library of 27 short SAPs forming nanofibers with an intermolecular β-sheet structure, we identified peptide sequences that stimulated the growth and adhesion of primary mouse PNS and CNS neural cells. Highly active peptides 1) have a strong propensity to form fibers, 2) consist of an alternating pattern of hydrophobic and positively charged amino acids and positive net charge, 3) showed higher intermolecular β-sheet contents, and 4) a larger cross-sectional diameter in single-fiber AFM analysis. After direct injection of the sticky SAPs into the site of injury in an in vivo PNS lesion model of the facial nerve, the PNFs remained at the lesion site for several weeks. Furthermore, the SAPs promoted the regeneration of the facial nerve, leading to improved functional recovery of the whisker movement. These results indicate the potential of optimized SAP nanofibrils as a promising, cost-effective, and labor-saving material for tissue engineering, also applicable to other tissues including brain, bones, heart or muscle.

In preliminary results, we noted that SAPs can interact with proteins when mixed in solution (Figure S16, Supporting Information). Thus, we envision that the SAP-based PNFs could serve as versatile platform for further functionalization by binding other proteins upon mixing for attaching, for example, active growth factor domains of, for example, NGF or GDNF (glial derived neurotrophic factor),[41] which offers great potential to further boost PNS nerve fiber growth.

Supporting Information

Supporting Information is available from the Wiley Online Library or from the author.

Acknowledgements

C.S. and T.M. contributed equally to this work. The work by B.K. was supported by the Deutsche Forschungsgemeinschaft (DFG) through the Collaborative Research Center 1149 "Danger Response, Disturbance Factors and Regenerative Potential after Acute Trauma" and grant KN543/6. Further, B.K. was supported by the Paul und Marlene Hepp-Stiftung and an Ulm University and German Army Hospital research initiative (U2.1d E/U2AD/ED002/EF550). T.W. acknowledges funding by the Volkswagen Foundation (project 89943) as well as by the European Research Council for a Synergy Grant (319130-BioQ). The work was partially supported by BiGmax, the Max Planck Society's Research Network on Big-Data-Driven Materials-Science. T.B. was supported by the Emmy Noether program of the Deutsche Forschungsgemeinschaft (DFG). The authors thank Swiss National Foundation for Science (SNF) for the financial support (grant number P2ELP2_162116 and P300P2_171219) and the Darwin College. The authors also thank Aileen Jehle for her experimental support. All experiments in this study were reviewed and approved and were in accordance with regulations by the local veterinary authorities (Regierungspräsidium Tübingen, Germany). The Figure 1 caption, Table 1, Figure 3, and the supporting information were updated to correct mislabeled data points and missing information on June 13th, 2019 after initial online publication.

Conflict of Interest

The authors declare no conflict of interest.

Keywords

facial nerve, naofiber, neuron growth, regeneration, self-assembling peptide

Received: December 21, 2018
Revised: March 11, 2019
Published online: April 15, 2019

---

[1] a) K. M. Koss, L. D. Unsworth, *Materials* **2018**, *11*, 1539; b) M. D. Sarker, S. Naghieh, A. D. McInnes, D. J. Schreyer, X. Chen, *Prog. Neurobiol.* **2018**, *171*, 125.

[2] A. C. Pinho, A. C. Fonseca, A. C. Serra, J. D. Santos, J. F. Coelho, *Adv. Healthcare Mater.* **2016**, *5*, 2732.

[3] a) B. Jiang, P. Zhang, B. Jiang, *Artif. Cells, Blood Substitutes, Immobilization Biotechnol.* **2010**, *38*, 1; b) D. P. Kuffler, *Prog. Neurobiol.* **2014**, *116*, 1.

[4] N. D. Fagoe, J. van Heest, J. Verhaagen, *NeuroMol. Med.* **2014**, *16*, 799.

[5] a) Y. Loo, M. Goktas, A. B. Tekinay, M. O. Guler, C. A. Hauser, A. Mitraki, *Adv. Healthcare Mater.* **2015**, *4*, 2557; b) R. Pugliese, F. Gelain, *Trends Biotechnol.* **2017**, *35*, 145; c) C. M. Rubert Perez, N. Stephanopoulos, S. Sur, S. S. Lee, C. Newcomb, S. I. Stupp, *Ann. Biomed. Eng.* **2015**, *43*, 501.

[6] J. B. Matson, S. I. Stupp, *Chem. Commun.* **2012**, *48*, 26.

[7] a) S. S. Negah, A. Khooei, F. Samini, A. Gorji, *Cell Tissue Res.* **2018**, *371*, 379; b) V. M. Tysseling, V. Sahni, E. T. Pashuck, D. Birch, A. Hebert, C. Czeisler, S. I. Stupp, J. A. Kessler, *J. Neurosci. Res.* **2010**, *88*, 3161; c) V. M. Tysseling-Mattiace, V. Sahni, K. L. Niece, D. Birch, C. Czeisler, M. G. Fehlings, S. I. Stupp, J. A. Kessler, *J. Neurosci.* **2008**, *28*, 3814.

[8] S. Sieste, T. Mack, C. V. Synatschke, C. Schilling, C. Meyer zu Reckendorf, L. Pendi, S. Harvey, F. S. Ruggeri, T. P. J. Knowles, C. Meier, D. Y. W. Ng, T. Weil, B. Knoll, *Adv. Healthcare Mater.* **2018**, *7*, e1701485.

[9] B. Mammadov, M. Sever, M. Gecer, F. Zor, S. Ozturk, H. Akgun, U. H. Ulas, Z. Orhan, M. O. Guler, A. B. Tekinay, *RSC Adv.* **2016**, *6*, 110535.

[10] a) A. L. Rodriguez, K. F. Bruggeman, Y. Wang, T. Y. Wang, R. J. Williams, C. L. Parish, D. R. Nisbet, *J. Tissue Eng. Regener. Med.* **2018**, *12*, e1571; b) W. Shi, C. J. Huang, X. D. Xu, G. H. Jin, R. Q. Huang, J. F. Huang, Y. N. Chen, S. Q. Ju, Y. Wang, Y. W. Shi, J. B. Qin, Y. Q. Zhang, Q. Q. Liu, X. B. Wang, X. H. Zhang, J. Chen, *Acta Biomater.* **2016**, *45*, 247.

[11] C. Lu, Y. Wang, S. Yang, C. Wang, X. Sun, J. Lu, H. Yin, W. Jiang, H. Meng, F. Rao, X. Wang, J. Peng, *ACS Biomater.* **2018**, *4*, 2994.

[12] a) Z. Huang, C. J. Newcomb, Y. Lei, Y. Zhou, P. Bornstein, B. A. Amendt, S. I. Stupp, M. L. Snead, *Biomaterials* **2015**, *61*, 216; b) S. Sur, F. Tantakitti, J. B. Matson, S. I. Stupp, *Biomater. Sci.* **2015**, *3*, 520.

[13] a) E. J. Berns, S. Sur, L. Pan, J. E. Goldberger, S. Suresh, S. Zhang, J. A. Kessler, S. I. Stupp, *Biomaterials* **2014**, *35*, 185; b) T. C. Holmes, S. de Lacalle, X. Su, G. Liu, A. Rich, S. Zhang, *Proc. Natl. Acad. Sci. USA* **2000**, *97*, 6728; c) Z. Zou, Q. Zheng, Y. Wu, X. Guo, S. Yang, J. Li, H. Pan, *J. Biomed. Mater. Res., Part A* **2010**, *95*, 1125.

[14] a) F. Gelain, S. Panseri, S. Antonini, C. Cunha, M. Donega, J. Lowery, F. Taraballi, G. Cerri, M. Montagna, F. Baldissera, A. Vescovi, *ACS Nano* **2011**, *5*, 227; b) Y. Liu, H. Ye, K. Satkunendrarajah, G. S. Yao, Y. Bayon, M. G. Fehlings, *Acta Biomater.* **2013**, *9*, 8075.

[15] J. J. Greene, M. T. McClendon, N. Stephanopoulos, Z. Alvarez, S. I. Stupp, C. P. Richter, *J. Tissue Eng. Regener. Med.* **2018**, *12*, 1389.

[16] a) X. Wu, L. He, W. Li, H. Li, W. M. Wong, S. Ramakrishna, W. Wu, *Regener. Biomater.* **2017**, *4*, 21; b) X. Wang, M. Pan, J. Wen, Y. Tang, A. D. Hamilton, Y. Li, C. Qian, Z. Liu, W. Wu, J. Guo, *Neural Regener. Res.* **2014**, *9*, 2132; c) A. Li, A. Hokugo, A. Yalom, E. J. Berns, N. Stephanopoulos, M. T. McClendon, L. A. Segovia, I. Spigelman, S. I. Stupp, R. Jarrahy, *Biomaterials* **2014**, *35*, 8780.

[17] a) M. Yolamanova, C. Meier, A. K. Shaytan, V. Vas, C. W. Bertoncini, F. Arnold, O. Zirafi, S. M. Usmani, J. A. Muller, D. Sauter, C. Goffinet, D. Palesch, P. Walther, N. R. Roan, H. Geiger, O. Lunov, T. Simmet, J. Bohne, H. Schrezenmeier, K. Schwarz, L. Standker, W. G. Forssmann, X. Salvatella, P. G. Khalatur, A. R. Khokhlov, T. P. Knowles, T. Weil, F. Kirchhoff, J. Munch, *Nat. Nanotechnol.* **2013**, *8*, 130; b) C. Meier, T. Weil, F. Kirchhoff, J. Munch, *Wiley Interdiscip. Rev.: Nanomed. Nanobiotechnol.* **2014**, *6*, 438.

[18] a) A. Lampel, R. V. Ulijn, T. Tuttle, *Chem. Soc. Rev.* **2018**, *47*, 3737; b) S. Das, K. Zhou, D. HGhosh, N. N. Jha, P. K. Singh, R. S. Jacob, C. C. Bernard, D. I. Finkelstein, J. S. Forsythe, S. K. Maji, *NPG Asia Mater.* **2016**, *8*; c) E. V. Alakpa, V. Jayawarna, K. E. V. Burgess, C. C. West, B. Peault, R. V. Ulijn, M. J. Dalby, *Sci. Rep.* **2017**, *7*, 6895.

[19] J. Gac anin, J. Hedrich, S. Sieste, G. Glasser, I. Lieberwirth, C. Schilling, S. Fischer, H. Barth, B. Knoll, C. V. Synatschke, T. Weil, *Adv. Mater.* **2019**, *31*, e1805044.

[20] M. Gey, R. Wanner, C. Schilling, M. T. Pedro, D. Sinske, B. Knoll, *Open Biol.* **2016**, *6*, 160091.

[21] C. Meier, S. Anastasiadou, B. Knoll, *PLoS One* **2011**, *6*, e26089.

[22] R. S. Jacob, D. Ghosh, P. K. Singh, S. K. Basu, N. N. Jha, S. Das, P. K. Sukul, S. Patil, S. Sathaye, A. Kumar, A. Chowdhury, S. Malik, S. Sen, S. K. Maji, *Biomaterials* **2015**, *54*, 97.

[23] R. K. Das, R. V. Pappu, *Proc. Natl. Acad. Sci. USA* **2013**, *110*, 13392.

[24] F. S. Ruggeri, J. Adamcik, J. S. Jeong, H. A. Lashuel, R. Mezzenga, G. Dietler, *Angew. Chem.* **2015**, *54*, 2462.

[25] F. S. Ruggeri, S. Vieweg, U. Cendrowska, G. Longo, A. Chiki, H. A. Lashuel, G. Dietler, *Sci. Rep.* **2016**, *6*, 31155.

[26] F. S. Ruggeri, F. Benedetti, T. P. J. Knowles, H. A. Lashuel, S. Sekatskii, G. Dietler, *Proc. Natl. Acad. Sci. USA* **2018**, *115*, 7230.

[27] D. M. Byler, H. Susi, *Biopolymers* **1986**, *25*, 469.

[28] B. Knoll, C. Weinl, A. Nordheim, F. Bonhoeffer, *Nat. Protoc.* **2007**, *2*, 1216.

[29] K. R. Jessen, R. Mirsky, A. C. Lloyd, *Cold Spring Harbor Perspect. Biol.* **2015**, *7*, a020487.

[30] L. B. Moran, M. B. Graeber, *Brain Res. Rev.* **2004**, *44*, 154.

[31] a) S. Di Giovanni, C. D. Knights, M. Rao, A. Yakovlev, J. Beers, J. Catania, M. L. Avantaggiati, A. I. Faden, *EMBO J.* **2006**, *25*, 4084;

b) G. Raivich, M. Bohatschek, C. Da Costa, O. Iwata, M. Galiano, M. Hristova, A. S. Nateri, M. Makwana, L. Riera-Sans, D. P. Wolfer, H. P. Lipp, A. Aguzzi, E. F. Wagner, A. Behrens, *Neuron* **2004**, *43*, 57.

[32] a) T. Ichimiya, S. Yamamoto, Y. Honda, R. Kikuchi, S. Kohsaka, K. Nakajima, *Brain Res.* **2013**, *1507*, 35; b) M. Makwana, A. Werner, A. Acosta-Saltos, R. Gonitel, A. Pararajasingham, C. Ruff, P. Rumajogee, D. Cuthill, M. Galiano, M. Bohatschek, A. S. Wallace, P. N. Anderson, U. Mayer, A. Behrens, G. Raivich, *J. Comp. Neurol.* **2010**, *518*, 699.

[33] A. D. Gaudet, P. G. Popovich, M. S. Ramer, *J. Neuroinflammation* **2011**, *8*, 110.

[34] a) M. Grosheva, O. Guntinas-Lichius, S. Arnhold, E. Skouras, S. Kuerten, M. Streppel, S. K. Angelova, K. Wewetzer, C. Radtke, S. A. Dunlop, D. N. Angelov, *Biol. Chem.* **2008**, *389*, 873; b) O. Guntinas-Lichius, G. Hundeshagen, T. Paling, M. Streppel, M. Grosheva, A. Irintchev, E. Skouras, A. Alvanou, S. K. Angelova, S. Kuerten, N. Sinis, S. A. Dunlop, D. N. Angelov, *Neurobiol. Dis.* **2007**, *28*, 101.

[35] R. Wanner, M. Gey, A. Abaei, D. Warnecke, L. de Roy, L. Durselen, V. Rasche, B. Knoll, *NeuroMol. Med.* **2017**, *19*, 357.

[36] K. Franze, P. A. Janmey, J. Guck, *Annu. Rev. Biomed. Eng.* **2013**, *15*, 227.

[37] D. Koch, W. J. Rosoff, J. Jiang, H. M. Geller, J. S. Urbach, *Biophys. J.* **2012**, *102*, 452.

[38] D. A. Harrington, E. Y. Cheng, M. O. Guler, L. K. Lee, J. L. Donovan, R. C. Claussen, S. I. Stupp, *J. Biomed. Mater. Res., Part A* **2006**, *78*, 157.

[39] F. A. Somaa, T. Y. Wang, J. C. Niclis, K. F. Bruggeman, J. A. Kauhausen, H. Guo, S. McDougall, R. J. Williams, D. R. Nisbet, L. H. Thompson, C. L. Parish, *Cell Rep.* **2017**, *20*, 1964.

[40] L. Lu, N. Arizmendi, M. Kulka, L. D. Unsworth, *Adv. Healthcare Mater.* **2017**, *6*, 1700334.

[41] J. Nielsen, K. Gotfryd, S. Li, N. Kulahin, V. Soroka, K. K. Rasmussen, E. Bock, V. Berezin, *J. Neurosci.* **2009**, *29*, 11360.

ADVANCED FUNCTIONAL MATERIALS

Supporting Information

for *Adv. Funct. Mater.,* DOI: 10.1002/adfm.201809112

Sequence-Optimized Peptide Nanofibers as Growth Stimulators for Regeneration of Peripheral Neurons

Corinna Schilling, Thomas Mack, Selene Lickfett, Stefanie Sieste, Francesco S. Ruggeri, Tomas Sneideris, Arghya Dutta, Tristan Bereau, Ramin Naraghi, Daniela Sinske, Tuomas P. J. Knowles, Christopher V. Synatschke, Tanja Weil, and Bernd Knöll**

Sequence-Optimized Peptide Nanofibers as Growth Stimulators for Regeneration of Peripheral Neurons

Corinna Schilling[1,#], Thomas Mack[2,4 #,] Selene Lickfett[1], Stefanie Sieste[2,4], Francesco S. Ruggeri[3], Tomas Sneideris[3] Arghya Dutta[4], Tristan Bereau[4], Ramin Naraghi[5], Daniela Sinske[1], Tuomas P. J. Knowles[3], Christopher V. Synatschke[6], Tanja Weil[2, 6, *], Bernd Knöll[1,*]

[1] Institute of Physiological Chemistry
Ulm University
Albert-Einstein-Allee 11
89081 Ulm
Germany

[2] Institute of Inorganic Chemistry I
Ulm University
Albert-Einstein-Allee 11
89081 Ulm
Germany

[3] Department of Chemistry
University of Cambridge
Cambridge CB2 1EW
UK

[4] Max Planck Institute for Polymer Research
Ackermannweg 10
55128 Mainz
Germany

[5] Department of Neurosurgery
German Armed Forces Hospital Ulm
Oberer Eselsberg 40
89081 Ulm
Germany

[6] Department Synthesis of Macromolecules
Max Planck Institute for Polymer Research
Ackermannweg 10
55128 Mainz

*co-corresponding authors
# both authors contributed equally

Supplementary Materials & methods

Materials for peptide synthesis and characterization

PyBOP, Fmoc-Lys(Boc)-OH, Fmoc-Phe-OH, Fmoc-Gln(Trt)-OH, Fmoc-Ile-OH, Fmoc-Cys(Trt)-OH, Fmoc-Arg(Pbf)-OH, Fmoc-Gly-OH, Fmoc-Asp(OtBu)-OH, Fmoc-Trp(Boc)-OH, Fmoc-Asn(Trt)-OH, Fmoc-Met-OH, Fmoc-Leu-OH, Fmoc-Phe-Wang resin, Fmoc-Ile-Wang resin, Fmoc-Gln(Trt)-Wang resin, Fmoc-Asp(OtBu)-Wang resin, Fmoc-Trp(Boc)-Wang resin, Fmoc-Leu-Wang resin, Fmoc-Met-Wang resin and Fmoc-Cys(Trt)-Wang resin were purchased from Novabiochem®. N-ethyldiisopropylamine for synthesis (DIPEA), potassium chloride (KCl) and rhodamine B isothiocyanate (RITC) were obtained from Merck. Piperidine (≥ 99.5 % for peptide synthesis) and trifluoroacetic acid (TFA, ≥ 99.9 %) were obtained from Carl Roth. Dimethylformamide (DMF, peptide synthesis), diethyl ether and acetonitrile (HiPerSolv Chromanorm for HPLC-gradient grade) were purchased from VWR Chemicals Prolabo. Dimethylsulfoxid (DMSO, ACS reagent, ≥ 99.9 %) was purchased from Honeywell, Riedel-de Haën®. Vivaspin 500 tubes (3 kDa MWCO) were purchased from Sartorius. Syringe filters Chromafil®Xtra RC-20/13 (0.20 µm) were obtained from Machery-Nagel. Uranyl acetate was purchased from Merck. Fluorescamine was purchased from PanReac AppliChem. Proteinase K and α-Cyano-4-hydroxycinnamic acid were purchased from Sigma Aldrich. The peptide SAP[8a] was purchased from Cassie Peptides, China.

Methods

Solid-phase peptide synthesis

All peptides were synthesized according to standard microwave-assisted Fmoc solid-phase peptide synthesis with amino acid pre-loaded Wang resins from the *C* to *N* terminus on a 0.1 mM scale. Fmoc-deprotection was carried out with dimethylformamide (DMF) solutions containing 20% to 25% (v/v) piperidine. Coupling reactions were done with 5 eq of amino acid catalyzed by 5 eq hexafluorophosphate benzotriazole tetramethyl uronium (HBTU) or benzotriazol-1-yl-oxytripyrrolidinophosphonium hexafluorophosphate (PyBOP) and 10 eq *N,N*-diisopropylethylamine (DIPEA). Cleavage from the resin and side chain deprotection was carried out by addition of a mixture of trifluoroacetic acid (TFA), triisopropylsilane (TIS) and H_2O at a ratio of 95:2.5:2.5 by shaking at RT for 2 h. Cleaved peptides were precipitated in cold diethylether and lyophilized.

Purification of SAPs

All peptides were purified via HPLC using a binary gradient with an eluant mixture of 0.1 % TFA water-acetonitrile. For preparative scale a Shimadzu system was used (LC-20AP, CBM-20A, SPD-20A) with a reversed phase C18 column (LiChrospher, Merck). Analytical scale was performed onto an analytical ChroCART® 125-4 column (LiChrospher, Merck) with a 1260 Infinity Quarternary LC System (Agilent Technologies). All peptides were analyzed by matrix assisted laser desorption/ionization time of flight (MALDI-TOF, Bruker Reflex III) using 4-Hydroxy-α-cyanocinnaminic acid as matrix.

SAP fiber formation

Lyophilized peptide was dissolved in DMSO to yield a 10 mg/mL stock solution, which was stored at 4 °C prior to usage. The stock solution was diluted tenfold in freshly filtered PBS or ddH_2O (0.22 µm pore size) to initiate fiber formation. All peptides were incubated at a final concentration of 1 mg/mL for at least 16 h to ensure complete fiber formation at room temperature. Lower concentrations indicated in the text were achieved by dilution of preformed fibers.

Transmission electron microscopy (TEM)

5 µL of each SAP were deposited on copper grids, which were coated with a thin electron-transparent Formvar-layer and were freshly etched with oxygen plasma before use. After 5 min incubation time, excess sample solution was removed with filter paper and the copper grid was further incubated for 5 minutes in 2% uranyl acetate solution to enhance sample contrast. After staining, the samples were washed three times in MilliQ-water, dried in air and micrographs were taken in high vacuum with an EM 109 transmission electron microscope (Zeiss) at an acceleration voltage of 80 kV. Pictures were processed with the EM109 microscope software ImageSP V1.2.6.22.

Atomic Force Microscopy (AFM)

AFM samples were prepared on the freshly functionalized MICA surfaces by the deposition of a 10 µL drop of protein (2 µM) for 5 min. Salts were washed away with 1 ml of MilliQ water and the samples were stored in sealed containers until imaging.

High-resolution images (1024x1024 pixels) were collected using an NX10 Atomic Force Microscopy (Park Systems, South Korea) in ambient conditions and in non-contact Amplitude Modulation (NC-AM). We performed all the measurements using sharp cantilevers (PPP-NCHR, Park Systems, South Korea) with resonance frequency of 330 kHz and typical radius of curvature of 8 nm. Raw images were flattened with the XEI software (Park System, South Korea). In order to keep consistency in the further statistical analysis, all images were processed with the same parameters. Cross-sectional height of individual fibrillar aggregates was quantified as the maximum of the cross-sectional profile perpendicular to the main axis of symmetry of the fibril, by using SPIP (Image metrology, Denmark) software. Data were analyzed and histograms were created using OriginPro (OriginLab) software.

Zeta potential

The electrophoretic mobility of fibrils was measured to enable comparisons of surface charge. 50 µL of preformed fibrils were diluted in 950 µL of 1 mM freshly prepared and filtered (pore size 0.22 µm) KCl solution. The sample solutions were measured in 1 mL disposable folded capillary cells (Zetasizer Nano series, Malvern) on a Zetasizer Nano ZS (Malvern Instruments) at ambient temperature. The mobility was converted to corresponding ζ-potential values by processing the data with the Zetasizer Nano ZS Software (V7.12). The ζ-potential was calculated by the mean value achieved of at least three independent measurements à 20 runs.

Proteostat® Assay

Fluorescence spectra were recorded on an Infinite® M1000 PRO microplate reader (Tecan). 9 µL of sample aliquots were placed in black UV Star® 384 microliter well-plates (Greiner bio-one). A ProteoStat® solution was prepared according to manufacturers' protocol and diluted hundred-fold in PBS. After addition of 1 µL of Proteostat® solution to all samples and 10 min incubation time, the fluorescence emission was recorded at 603 nm upon excitation at 550 nm with multiple reads per well (3x3).

Conversion rate assay

To determine the amount of peptide monomer converting into fibers we established a fluorescence-based assay. Each peptide sample was incubated as previously described (200 µL). 100 µL per sample was centrifuged in a Vivaspin 500 tube (3kDa MWCO) to separate fibers from free peptide monomer (13 krpm, 4°C, 45 min). The filtrate and the other 100 µL of sample (original sample) were lyophilized and dissolved in 25 µL DMSO to suppress fiber formation. The amount of peptide was determined by adding the amine reactive dye fluorescamine and measuring fluorescence enhancement. In a black 384-well-plate (Greiner Bio-one) 10 µL of the DMSO samples (filtrate and original sample) were submitted and 3 µL of fluorescamine solution (10 mg/mL, DMSO) was added. After 20 min of incubation at RT, fluorescence was measured with an excitation wavelength of λ_{ex} = 365 nm and an emission wavelength of λ_{em} = 470 nm with multiple reads 3x3 (Infinite® M1000 PRO microplate reader). All values were calculated as n-fold fluorescence enhancement (DMSO only as a reference was set to 1). The conversion rate CR was defined according to the following equation:

$$CR = 100 - \frac{100 \cdot \text{Fluorescence Intensity (Filtrate)}}{\text{Fluorescence Intensity (Original)}} \; [\%] \quad (1)$$

ATR FT-IR

To determine secondary structure elements in peptide nanofibers ATR FT-IR was used. 50 µL of each peptide sample was lyophilized and spectra were recorded on a Bruker Tensor 27 spectrometer with a diamond crystal as ATR element (PIKE Miracle^{TM}, spectral resolution 4 cm^{-1}). Every sample was measured with 20 scans. Data were analyzed with OriginPro (OriginLab) software.

Primary neuronal cultures

Coatings

As positive control for neuronal and Schwann cell growth, a mixture of poly-L-lysine (PLL) and Cys-laminin (Cys-lam) was used. Cys-lam is part of the extracellular matrix protein laminin A chain (2091-2108) with an additional Cystein on its n-terminal end. For coating, the bottom of the wells were incubated with 100 µg/mL PLL in borate buffer for 1 h at 37° C. After incubation the PLL was removed and the well was washed 3 x with autoclaved ddH_2O. Following complete removal of ddH_2O, 20 µg/mL Cys-laminin in HBSS was coated on the glass bottom and incubated o/n at room temperature. SAP monomers were dissolved in DMSO (C = 10 mg/mL) to prevent fiber formation and stored at –20° C before usage. For fiber formation DMSO stocks were diluted in a polar solvent (1X PBS or ddH_2O for SAP^{1e}) to yield a final concentration of 1 mg/mL. After at least 18 h of incubation, the mature fiber solution was diluted in 10 mM Tris to get the desired concentrations ranging from 1 µg/ml to 50 µg/mL. 200 µL of SAP-solution were coated on the bottoms of the 24-well plates and dried o/n at RT. Directly before use, the wells were covered with 500 µL culture media.

Cell preparation

DRGs (dorsal root ganglia) of 7-9 weeks old C57BL/6 mice were isolated. As a first step, the spine with the rib cage of the mouse was removed and cleaned in ice cold PBS. Dissected DRGs were collected in Petri dishes with ice cold HBSS, dispensable tissue was removed and cleaned DRGs were stored on ice in 1 mL HBSS until further preparation. Following dissection, the DRGs were first centrifuged at 1000 rpm for 2 min at RT and the HBSS was replaced by 500 µL digestion solution (0.25% collagenase, 5% dispase dissolved in DMEM). For digestion, tubes containing DRGs and digest solution were incubated at 37° C for 1 h and flicked every 15 min. Afterwards the DRGs were spun down at 800 rpm for 2 min at RT and then washed with 1 mL pre-warmed DRG media (DMEM/NBM ratio 1:1, supplemented with 10% FCS, 2% B27 supplement, 0.1% L-glutamine), following another centrifugation step at 800 rpm for 2 min at RT. Again, DRGs were washed with 1 ml DRG media and then transferred into falcon tubes. The solution was triturated 30 times with glass pipettes with whole diameter following 15 times triturating with glass pipettes with half the diameter. Afterwards, to get rid of tissue clumps, the solution settled for approximately 30 seconds and the supernatant was transferred to a new falcon tube. This was repeated once before the supernatant was centrifuged at 800 rpm for 5 min at RT. The resulting cell pellet was resuspended in 500 µL DRG culture media without NGF.

For CNS cultures, hippocampus of mice at post natal day 1-2 (P1-P2) and cerebellum of mice (P2-P4) were used. Mice were sacrificed by decapitation and their heads were immediately transferred into ice cold PBS. The head was then transferred into a Petri dish and the brain was dissected using microscissors. After dissection, the brain was put in another Petri dish containing cold HBSS and by the use of a stereomicroscope the cerebellum or both hippocampi were dissected. Subsequently, the tissue was digested with 2-3 mL trypsin per mouse for 10 min at 37°C. Digestion was stopped by replacing the trypsin with 1 mL pre-warmed HBSS. This was done two times and then the HBSS was completely removed following incubation with 1 mL pre-warmed DMEM supplemented with 10% horse serum (HS). Glass pipettes with whole diameter were first used for 1 min triturating followed by 1 min triturating with glass pipettes with half the diameter. After the solution was homogenized, the cells were centrifuged for 5 min with 600 rpm at RT. The supernatant was discarded and the cell pellet was resuspended in pre-warmed NMEM/B27 with Gentamycin (1:2000). The cell number was determined by counting with a Neubauer improved hemocytometer. For analysis of cell growth a total of 16 x

10^3 were platted on each well (⃠ 15 mm). The cells were cultured for 24 h in the Olympus microscope for time lapse recordings at 37°C and 5% CO_2.

Live cell imaging and analysis

To analyze cell attachment and growth, 5 x 10^3 DRG cells per well were seeded and incubated at 37°C and 5% CO_2. After 1.5 h incubation, the medium was replaced with fresh DRG culture medium (± NGF at 50 ng/mL). Afterwards, time-lapse recordings were performed by the Olympus microscope and the Olympus ScanR acquisition software. Cells were recorded for approximately 23 h, with pictures taken every 30 min at 37°C and 5% CO_2. Six positions per well were recorded with the UPLFLN-PH 10X objective. After cell staining, the plate was scanned by the microscope again. Using the ScanR acquisition software, 520 positions per well were recorded with the UPSALPO 10X objective. On each position the microscope performed the hardware autofocus (AF hardware) and fine autofocus (AF fine). After the recording, the cells could be analyzed via threshold detection using the corresponding ScanR analysis software. Different gates were defined to categorize the cells. First, a "Neuron" was defined by a co-localized DAPI and βIII tubulin signal. The detected DRG neurons were grouped in "round neurons" (208-908 μm^2), "small neurons" (908-1994 μm^2), "medium neurons" (1994-4161 μm^2) and "large neurons" (4161-18721 μm^2). A similar approach was used for CNS neurons and Schwann cells.

For measuring the neurite length of the cells, 20 cells per condition were chosen randomly. Images were taken with the Zeiss Axiovert 200 M microscope with a 10 X magnification. The neurite length was measured by using AxioVision software. For analysis, always the longest neurite of the neuron was chosen and measured from one tip of the neurite across the cell body to the other tip.

To determine neurite branching an automatic Sholl analysis using the Fiji plugin was used developed by Ferreira et al., 2014. The starting radius was set to 30 µm and the step size was determined to 20 µm. Ten cells per condition were analyzed. If possible, only cells with a neurite length ≥ 50 µm were chosen for analysis, otherwise the number of intersections was set to zero.

Stripe assay

Stripe assays were performed according to a published protocol (Knoll et al., 2007). Silicon matrices (provided by M. Bastmeyer, KIT, Karlsruhe, Germany) were washed in boiling autoclaved ddH_2O with 2 % SDS and afterwards in autoclaved ddH_2O only for 10 min each. After boiling, matrices were dried o/n at RT and subsequently positioned on glass coverslips (⦸ 15 mm). For the first stripes, 200 µg/mL SAP^{5c}-RITC were mixed with 10 µg/mL Alexa546 (goat) labeled antibodies (Invitrogen) to enhance fluorescence. 20 µL were injected with a Hamilton syringe per silicon matrix to create a pattern of alternating red-labeled stripes. Without removing the matrices, the SAP stripes dried o/n at RT in the dark. On the following day, the matrices were gently removed and the coverslips were either directly transferred into Nunc® 4 well plates and covered with 500 µL DRG culture medium with NGF, or stripes were covered with 50 µL unlabeled SAP^{5c} (final conc. 25 µg/mL), which dried o/n at RT in the dark. 20 x 10^4 DRG cells per coverslip were seeded and incubated at 37°C and 5% CO_2. Stripe assays were analyzed automatically by using an ImageJ plugin (Yamagishi et al., 2011).

Immunocytochemistry

After washing with PBS, cells were fixed with 4 % PFA in PBS for 15 min. Following fixation, the cells were washed three times with PBS and permeabilized with 0.1 %

Triton-X-100/PBS for 5 min. Then, the cells were washed again with PBS two times and subsequently incubated in blocking solution (2 % BSA in PBS) for 30 min at RT. Primary antibodies were diluted as described below in blocking solution and applied to the cells o/n at 4°C. The next day, the primary antibody solution was removed and the cells were washed three times with PBS. Secondary antibodies were also diluted in blocking solution 1:1500 and applied for 1 h at RT (anti-βIII tubulin, 1:2000, Covance; anti-S100b, 1:250, Abcam; Texas Red conjugated Phalloidin; 1:100, Molecular Probes; DAPI, 1:5000, AppliChem). Following two times of washing with PBS, the cell nuclei were stained with DAPI. After 5 min incubation with DAPI, the cells were washed with PBS again and mounted with pre-warmed Mowiol on microscope slides. The slides were dried o/n at RT and stored at 4°C.

Facial nerve axotomy

Adult C57BL/6 mice (10-12 weeks old) were anesthetized with isoflurane and subcutaneously injected with 5 mg/kg of the analgesic carprofen (Rimadyl 50 mg/mL). After shaving the right side of the mouse face, the skin on the right masseter muscle was cut with scissors. Subsequently, the buccal and marginal branch was cut with scissors. Directly after cutting, 1 µL per branch of RITC-labeled SAP-solution (1 mg/mL) or PBS for the control group was applied with a Hamilton syringe (26g) into the lesion site. To make sure that the SAPs will stay in the lesion site, the skin was not directly sutured, but the injury was protected from light for approximately 1 min so the labeled SAPs could stick to the tissue. For quantification of RITC signals in the lesion site, we used Axiovision software. Subsequently, the skin was closed with an Ethicon K871H suture and successfully performed surgery was controlled by impaired whisker movement. The surgery was performed unilaterally, so that the uninjured contralateral side of the mouse could serve as internal control.

To asses axonal regeneration of the injured facial nerve the retrograde axonal tracer Fluoro-Gold (FG; Milipore) was used. A 4 % solution of FG in ddH_2O was injected in both whisker pads by using a Hamilton syringe. For each side, a total of 4 µL FG solution was used and injected at two positions in the upper part of the whisker pad and at two positions in the lower part. FG injection was performed one day prior to sacrificing the mice. All experiments in this study were reviewed and approved and were in accordance with regulations by the local veterinary authorities (Regierungspräsidium Tübingen, Germany).

Whisker movement

The whisking was recorded one day before facial nerve transection and on different time points during regeneration. Cohorts with a regeneration period of 21 days were recorded at 1, 4, 9, 11, 14, 16 and 18 days post injury (dpi). For recordings the mice were placed under a high-speed camera (Basler acA1300-60gc) on an illuminated plate. Video recordings lasted for 60 s with a frame rate of 100 Hz. For analyzing the recorded whisking of the mice, the videos were reviewed and a sequence of 1s duration was further processed with Templo Software (CONTEMPLAS GmbH, Germany). The selected video sequences were analyzed by Vicon Motus 2D software (CONTEMPLAS GmbH, Germany). Different parameters of whisker movement were measured by the Vicon Motus 2D software, including angular range, velocity and acceleration. The angular range was defined as the difference between minimum and maximum deflection of the vibrissae. The overall angular sum of whisker movement during 1 s was calculated with a custom MATLAB program, where all deflections above a threshold of 10° were summed up for lesion and control side.

Immunohistochemistry

Tissue was fixed in 4% formaldehyde (FA) for three days, followed by preparation of 5µm paraffin microtome slices. Immunohistochemistry was performed using Biotin (1:500; Vector Laboratories) or Alexa Fluor (1:500; Invitrogen) conjugated secondary antibodies and peroxidase-based detection systems using the ABC complex (Vector Laboratories) and DAB as substrate. Primary antibodies included anti-FG (rabbit, 1:5000, AB153; Millipore), anti-S100b (rabbit, 1:1000; Abcam), anti-VAChT (goat, 1:1000, Merck), anti-MBP (mouse, 1:1500, Covance), anti-βIII tubulin (rabbit, 1:1000, Covance), DAPI (1:5000, AppliChem)

Scanning Electron Microscopy

The SAPs were coated on glass slips as described above and dried overnight. Primary neuronal cells from adult mouse DRGs were dissected as described before. Neurons were cultivated for 3 DIV without additional NGF in the growth medium. The next steps were performed by the electron microscopy core facility at Ulm University and will only be described briefly. For a more detailed protocol see (Walther et al., 2010). First, the peptides were fixed for 1 h with a fixation solution containing glutaraldehyde. Then they were washed three times and fixed additionally with 4% osmiumtetroxyd. Any remaining water was removed by an increasing alcohol series. Afterwards, the alcohol was replaced by CO_2. The probes were dried by critical point drying. There, the probes were dried above the critical point of CO_2, where liquid and gas phase cannot be separated. By slowly decreasing the pressure while keeping the temperature constantly supercritical, the probes were dried without destroying the natural structure. To increase the electrical conductivity, the probes were vaporized with a platinum layer. Probes were analyzed with the Hitachi S-5200 Scanning Electron Microscope (Hitachi High Technologies Corporation).

Data Mining of Peptides

We modeled amino acids as building blocks with two important physical properties relevant for this problem: hydrophobicity and charge. An amino acid can be hydrophobic (H^0) or hydrophilic. The hydrophilic amino acids can be uncharged (P^0), positively charged (P^+) or negatively charged (P^-). This coarse-graining of amino acids provided us with four types of amino acids (see Table S2 for classification of amino acids into these categories).

To make the library of amino acid sequences, we noted that each position in a sequence of amino acids can be occupied by one of the four types of amino acids. Consequently, a 3-length sequence can be one of the 4x4x4=64 types. We made a library of all 3, 4, and 5 amino acid long sequence units to proceed systematically. Combinatorially, there are 1344 such sequence units. Longer polypeptide sequences were constructed by repeating the same-length units. This procedure allowed us to make a large number of sequences with a fixed and reproducible protocol. As an example, $H^0H^0P^+$ and $P^+P^+P^-P^+$ are one trimeric and one tetrameric unit, respectively, in our representation. The longer sequences they make are $H^0H^0P^+H^0H^0P^+$… and $P^+P^+P^-P^+P^+P^+P^-P^+$ … Note that each sequence unit can represent multiple amino acid sequences. We also used the fact that the cell membranes are negatively charged in the experiments and the overall positively charged SAPs have higher activity. In our library, the overall net charge of a constructed sequence was constrained to be positive to make accurate predictions. This reduced the number of considered sequences from 1344 to 501.

We then compared how similar each of these sequences are to SAPs. The similarity between an experimental SAP, denoted X, and a constructed sequence, denoted Y, was quantified by the overlap index(I) defined as

$$I(X,Y) = \frac{|X \cap Y|}{\min(|X|,\ |Y|)}. \quad (2)$$

The numerator in Eq. (2) is the number of position-matched amino acids between sequences X and Y. For example, there are 2 matches between the sequences $P^+P^+P^-P^+$ and $P^+P^+H^0P^-$. The denominator is the minimum among the lengths of $P^+P^+P^-P^+$ and $P^+P^+H^0P^-$, which is 4 as they are of the same length. Thus, $I = \frac{2}{4} = 0.5$ for these two sequences.

As mentioned before, the sequences that have high overlap index with SAPs with high activity and low overlap index with sequences with low or medium activity are the most promising sequences to show high activity in experiments. In Figure S6, these most promising sequences are represented by the points on the lower-right corner.

To rank the sequences, we formulated the index:

$$Q = I(X,Y_h)_{Av} - I(X,Y_l)_{Av} - I(X,Y_m)_{Av}. \quad (3)$$

In the above equation X represents a sequence from the library, Y_h is a high-activity sequence, Y_l is a low activity sequence and Y_m is a medium activity sequence. The averaging was done over the respective activity types. We conjecture that sequences with high values of Q has the potential to show higher activity in the experiments.

Once we ranked the constructed sequences, we found out relative occurrences of amino acid types present in each position of the sequences with high values of the index Q. The resulting histograms, drawn for sequences having the highest 5, 10, and 15 Q values, are shown in Figure S7. Based on this analysis, we found that in the top-ranking sequences the recurring pattern is $H^0P^+H^0P^+H^0$. The third position is a bit ambiguous as it varies when we consider the best 15 sequences. The observed variability stems from the limited dataset of SAP sequences. To get longer polypeptide sequences one needs to repeat the predicted unit like $H^0P^+H^0P^+H^0H^0P^+H^0P^+H^0$.

Next, we compared the predicted pattern, namely $H^0P^+H^0P^+H^0$, that we obtained from our own dataset with peptide sequences reported in the literature that were shown to support neuronal growth and determined how well the identified pattern matches with these sequences. We selected a total of 18 peptide-containing molecules from the literature that were used as coatings in neuronal cultures. We found that two classes of molecules, peptides belonging to the RADA family and peptide amphiphiles (PAs), were used most frequently in relevant literature studies. In order to be accessible to our data mining approach, molecules need to be represented as pure amino acid sequences. However, PA molecules feature an alkyl tail coupled to a peptide sequence. We chose to represent the palmityl group of PAs as 4 leucine units in the simplified sequence used for comparing with our dataset. Likewise, small chemical modifications such as the amidated *C*-terminus of certain peptides are not represented in the translated sequence. The *in vitro* data provided in the literature uses different culturing conditions and even different cell types, which prevents a direct evaluation of “neuronal activity” as defined in our work and we assigned medium or high activity after considering the presented data. Nevertheless, we believe that a comparison with our dataset can give valuable insight.

For comparison with the literature sequences, we first performed an out-of-sample analysis. We randomly split our SAP dataset into one larger set (training set) containing 75% and one smaller set (test set) containing 25% of the whole dataset using the scikit-learn package (Pedregosa et al., 2011). We then identified the most-occurring pattern by applying our algorithm only on the training set and measured its overlap with SAPs only from the test set. Repetition of this analysis allows us to: a) verify that, on average, $H^0P^+H^0P^+H^0$ is the most-occurring pattern - indicating the robustness of our predicted pattern - and b) find the average overlap of the predicted pattern with the experimental SAPs. After repeating the test-train splitting 2000 times and collecting the overlap data for each of them, we were able to obtain reliable statistics. Figure S8 shows that indeed, on average, $H^0P^+H^0P^+H^0$ is the most-occurring pattern in the high-activity SAPs and, thus, our prediction is robust. Figure S9 shows the overlap statistics. First, we note that $H^0P^+H^0P^+H^0$ has better overlap with high activity SAPs than low activity SAPs, which confirms that the predicted pattern works well when applied to a high-activity SAP from a randomly chosen test set from our data. However, when we compare the predicted pattern with the high-activity literature sequences, we obtain a broad range of overlap values. The best match is found for P7, reaching a value of 0.45, while some other sequences have a low overlap value of around 0.1. Interestingly, the PA molecules show moderate overlap with the predicted pattern (see P1, P6, P10, P14-P16 in Table S3), while peptides belonging to the RADA family generally show a low overlap (see P3, P4, P17, P18 in Table S3).

The observed moderate to low overlap of the predicted pattern with the peptides from PA family or RADA family is not unexpected since all of the SAPs that we used to train our data-mining model have a net positive charge and repeating coarse-grained amino acid units, while many of the peptides from these families are negative or neutral and have quite different structure and thus belong to very different regions of the sequence space than that we considered. For peptide P7, which falls in the broad structural class of the SAPs, the match is reasonable. We expect that augmenting the training of our proposed algorithm with a list of peptides having different structures but one unifying feature, namely high neuronal regeneration activity, will considerably enhance the predictive power of this data-mining approach for the current problem. This study thus motivates larger data-mining studies across peptide sequences.

Supplementary Tables

Table S1

Collected fractions of all peptides after purification with HPLC. Calculated mass and found m/z of all peaks with an intensity of at least 10 % in relation to the main peak.

#	SAP name	fraction collected [min]	calc. exact mass [g/mol]	*m/z* found
1	SAP^{1a}	10.17 to 10.72	982.69	983.70 $[M+H]^+$, 1005.68 $[M+Na]^+$
2	SAP^{1b}	10.40 to 10.93	982.69	983.70 $[M+H]^+$, 1005.68 $[M+Na]^+$
3	SAP^{1c}	11.06 to 11.30	967.68	968.69 $[M+H]^+$, 990.67 $[M+Na]^+$
4	SAP^{1d}	9.82 to 10.29	741.51	742.52 $[M+H]^+$, 764.50 $[M+Na]^+$
5	SAP^{1e}	12.81 to 13.66	963.58	964.59 $[M+H]^+$, 986.57 $[M+Na]^+$, 1002.54 $[M+Ka]^+$, 1008.55 [unknown]
6	SAP^{2a}	12.04 to 13.02	1137.60	1138.61 $[M+H]^+$, 1160.59 $[M+Na]^+$, 1176.56 $[M+K]^+$
7	SAP^{2b}	10.64 to 11.41	843.46	844.47 $[M+H]^+$, 866.45 $[M+Na]^+$
8	SAP^{2c}	10.95 to 11.90	1118.63	1119.63 $[M+H]^+$, 1141.62 $[M+Na]^+$
9	SAP^{2d}	10.09 to 11.08	1088.55	1089.55 $[M+H]^+$, 1105.55 $[M+O+H]^+$, 1111.54 $[M+Na]^+$
10	SAP^{2e}	10.78 to 11.38	946.47	947.48 $[M+H]^+$, 1136.52 $[M+O+H]^+$, 1892.94 $[2M-2H+H]^+$
11	SAP^{3a}	10.65 to 11.29	1300.73	1301.74 $[M+H]^+$, 1317.74 $[M+O+H]^+$, 1323.55 $[M+Na]^+$, 1349.73 [unknown]
12	SAP^{3b}	10.29 to 11.28	1403.74	1404.75 $[M+H]^+$, 1420.74 $[M+O+H]^+$, 1426.73 $[M+Na]^+$, 1436.74 [unknown], 1452.73 [unknown], 2807.47 $[2M-2H+H]^+$
13	SAP^{3c}	9.96 to 10.49	986.59	987.60 $[M+H]^+$, 1003.60 $[M+O+H]^+$
14	SAP^{4a}	9.81 to 10.79	1089.60	976.57 $[M-ASN+H]^+$, 1090.61 $[M+H]^+$, 1112.59 $[M+Na]^+$, 1196.65 $[M+Anisyl+H]^+$, 2065.15 [unknown], 2179.20 $[2M-2H+H]^+$ 2201.18 $[2M-2H+Na]^+$
15	SAP^{4b}	n.d.		n.d.
16	SAP^{4c}	10.25 to 10.67	1089.60	976.57 $[M-ASN+H]^+$, 1090.61 $[M+H]^+$, 1003.60 $[M+O+H]^+$, 2065.16 [unknown], 2179.20 $[2M-2H+H]^+$.
17	SAP^{4d}	9.63 to 10.05	844.52	845.53 $[M+H]^+$, 867.51 $[M+Na]^+$, 1034.57 [unknown], 1688.03 $[2M+H]^+$, 1710.01 $[2M+Na]^+$
18	SAP^{4e}	n.d.	844.52	845.53 $[M+H]^+$, 1688.03 $[2M+H]^+$
19	SAP^{4f}	n.d.	1403.74	n.d.
20	SAP^{5a}	10.00 to 10.59	1417.75	1418.76 $[M+H]^+$, 1451.85 [unknown], 1469.86 [unknown], 1485.85 [unknown]
21	SAP^{5b}	9.98 to 10.53	1314.74	1201.71 $[M-ASN+H]^+$, 1315.75 $[M+H]^+$, 1337.73 $[M+Na]^+$
22	SAP^{5c}	9.54 to 10.52	1172.67	1173.68 $[M+H]^+$, 1224.78 $[unknown]^+$, 1279.72 $[M+Anisyl+H]^+$, 2345.34 $[2M-2H+H]^+$
23	SAP^{5d}	10.14 to 11.12	1628.88	1515.85 [M-ASN+H], 1629.89 $[M+H]^+$, 1677.88 [unknown]
24	SAP^{6a}	9.07 to 9.57	1069.66	1070.67 $[M+H]^+$, 1092.65 $[M+Na]^+$
25	SAP^{6b}	10.06 to 10.42	1172.67	1173.68 $[M+H]^+$, 1279.72 $[M+Anisyl+H]^+$, 2345.33 $[2M-2H+H]^+$
26	SAP^{7a}	12.19 to 13.17	2275.28	2140.23 [unknown], 2277.29 $[M+H]^+$, 2299.27

				[M+Na]$^+$
27	SAP7[b]	11.36 to 12.35	1354.88	922.54 [unknown], 1227.80 [M-Lys+H]$^+$, 1355.89 [M+H]$^+$, 1387.88 [unknown]
28	SAP8[a]	n.d.	988.49	989.50 [M+H]$^+$, 1005.49 [M+O+H]$^+$, 1011.48 [M+Na]$^+$, 1027.48 [M+K]$^+$

Table S2

Classification of amino acids based on their hydrophobicity and side-chain charge (at pH 7.4)

Name	**Type**	**Kyte-Doolittle hydropathy index** (Kyte and Doolittle, 1982)	**Charge**	**Example**
H^0	Hydrophobic	Positive	0	Alanine, Cysteine, Phenylalanine, Isoleucine, Leucine, Methionine, Valine
P^+	Positively charged	Negative	+1	Histidine, Lysine, Arginine
P^-	Negatively charged	Negative	-1	Aspartic acid, Glutamic acid
P^0	Hydrophilic	Negative	0	Glycine, Asparagine, Proline, Glutamine, Serine, Threonine, Tryptophan, Tyrosine

Table S3

List of peptide sequences found in the literature with high or moderate neuronal activity for comparison with SAP dataset.

Name	Original Sequence	Simplified Sequence	Neuro Activity	Reference
P1	Palmitoyl-VVAAEE-NH2	LLLLVVAAEE	high	Angeloni et al., 2011; Berns et al., 2016; Choe et al., 2017; Berns et al., 2014
P2	RADARADARADARADA	RADARADARADARADA	high	Ellis-Behnke et al., 2006; Francis et al., 2016
P3	AcN-RARADADARARADADA-GG-RPKPQQFFGLM	RARADADARARADADA-GGRPKPQQFFGLM	high	Kim et al., 2013
P4	RARADADARARADADA	RARADADARARADADA	high	Kim et al., 2013
P5	RAEARAEARAEARAE	RAEARAEARAEARAE	medium	Liang et al., 2015
P6	Palmitoyl-VVVAAAEEE-NH2	LLLLVVVAAAEEE	high	Greene et al., 2018
P7	CCRRIKVAVWLC	CCRRIKVAVWLC	high	Li et al., 2014
P8	Palmitoyl-AAAGGGEIKVAV	LLLLAAAGGGEIKVAV	high	Zou et al., 2009
P9	KKQLQLQLQLQLQLKK	KKQLQLQLQLQLQLKK	high	Liu et al., 2013
P10	Palmitoyl-VVAAEE-ADEGVFDNFVLK	LLLLVVAAEEADEGVFDNFVLK	high	Berns et al., 2016
P11	RADARADARADARADA-GG-CQAASIKVAV	RADARADARADARADA-GGCQAASIKVAV	high	Tavakol et al., 2016, Tavakol et al., 2017
P12	RADARADARADARADA-RGIDKRHWNSQ	RADARADARADARADA-RGIDKRHWNSQ	high	Shi et al., 2016
P13	Palmitoyl-VVAAEEEEGIKVAV-COOH	LLLLVVAAEEEEGIKVAV	high	Berns et al., 2014
P14	Palmitoyl-VVAAEEEEGVVIAK-COOH	LLLLVVAAEEEEGVVIAK	medium	Berns et al., 2014
P15	Palmitoyl-VVAAEERGDS-NH2	LLLLVVAAEERGDS	medium	Berns et al., 2014
P16	Palmitoyl-VVAAEERSDG-NH2	LLLLVVAAEERSDG	medium	Berns et al., 2014
P17	RADARADARADARADA-GG-CTDIKGKCTGACDGKQC	RADARADARADARADA-GGCTDIKGKCTGACDGKQC	high	Lu et al., 2018
P18	RADARADARADARADA-GG-RGIDKPHWNSQ	RADARADARADARADA-GGRGIDKPHWNSQ	high	Lu et al., 2018

Table S4

Summary of several biophysical parameters along with SAP's potential to stimulate neuronal growth

SAP	Neuronal Activity	intermolecular b-content	Conversion Rate [%]	Diameter
SAP^{1d}	low	++	5	n/a
SAP^{1e} (PBS)	medium	++	30	n/a
SAP^{2b}	medium	--	83	-
SAP^{2e}	high	++	95	++
SAP^{5c}	high	++	80	++
SAP^{6a}	low	-	n/a	+
SAP^{7a}	medium	--	96	n/a
SAP^{7b}	low	---	92	n/a

Supplementary Figures

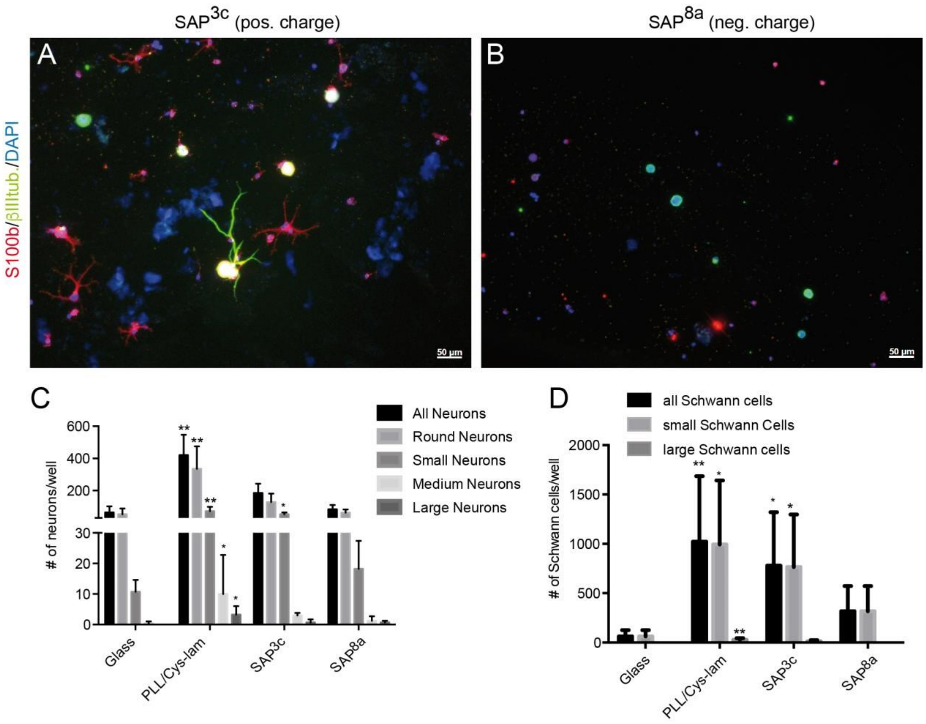

Figure S1

Negatively charged SAPs do not mediate cell adhesion or growth

(A, B) DRG neurons were cultivated on coverslips coated with SAP^{3c} (positively charged) or SAP^{8a} (negatively charged). Cells were stained with S100b and βIII tubulin to label Schwann cells and neurons, respectively. In contrast to SAP^{8a} (B), neurons adhered to and grew on SAP^{3c} (A).

(C, D) Quantification neuronal (C) or Schwann cell (D) growth on glass, PLL/Cys-lam, SAP^{3c} and SAP^{8a}. Data show mean ± SD of four independent cultures.

Scale-bar (A, B) = 50 µm

SAP^{1a}

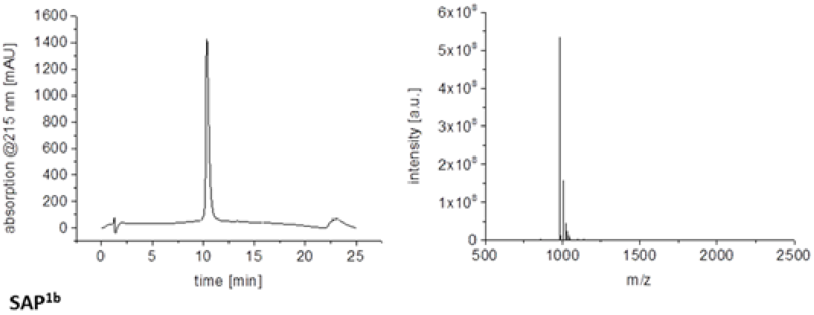

SAP^{1b}

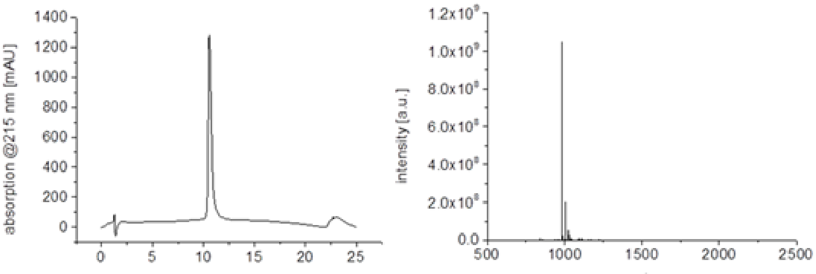

SAP^{1c}

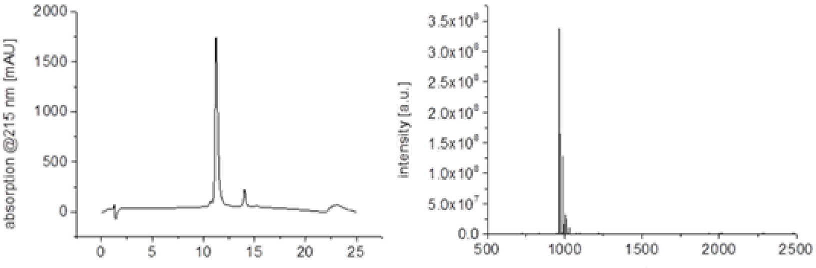

SAP^{1d}

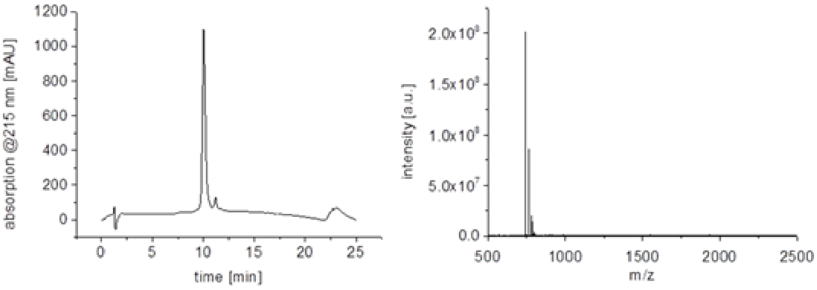

SAP^{1e}

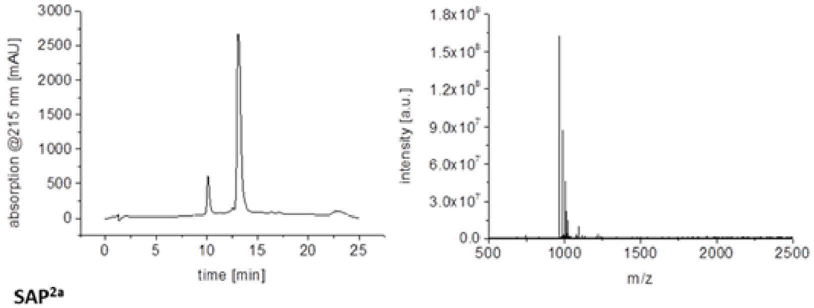

SAP^{2a}

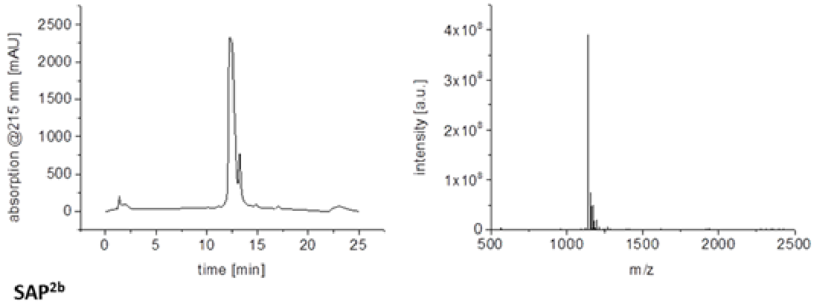

SAP^{2b}

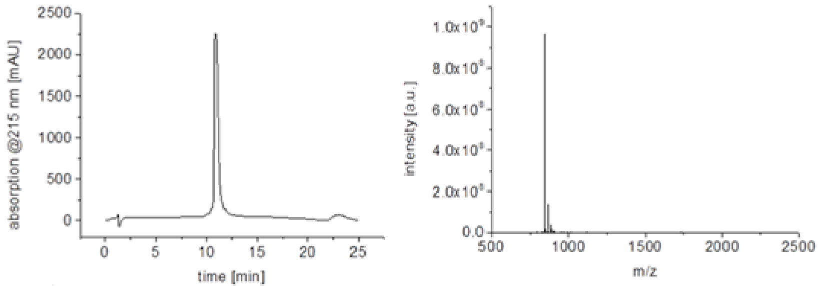

SAP^{2c}

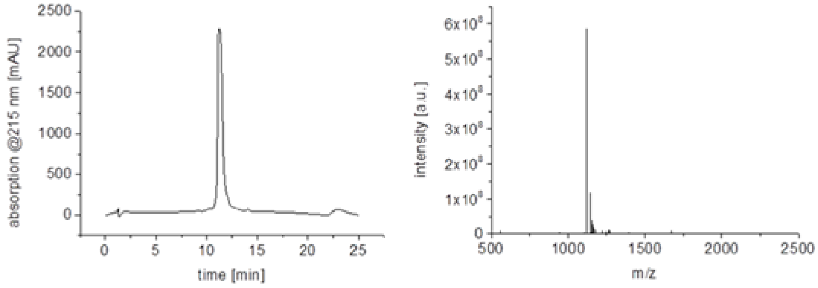

SAP^{2d}

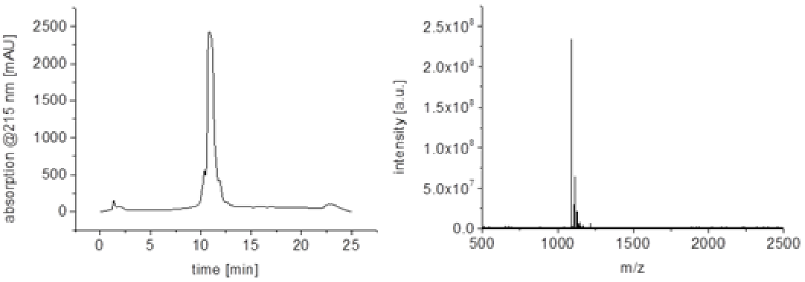

SAP^{2e}

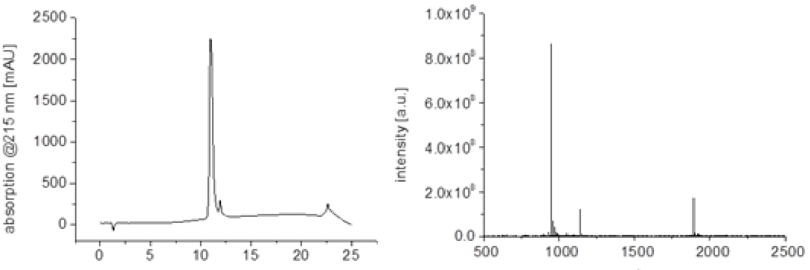

SAP^{3a}

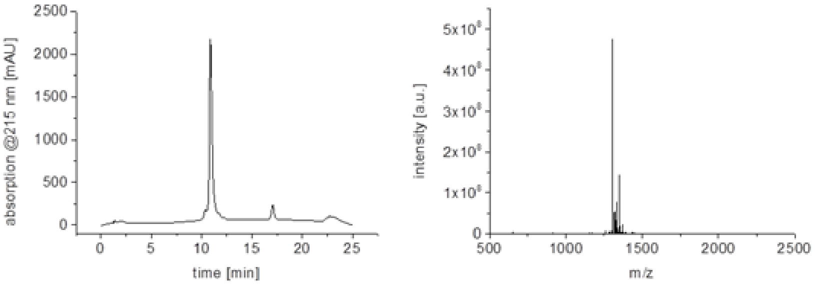

SAP^{3b}

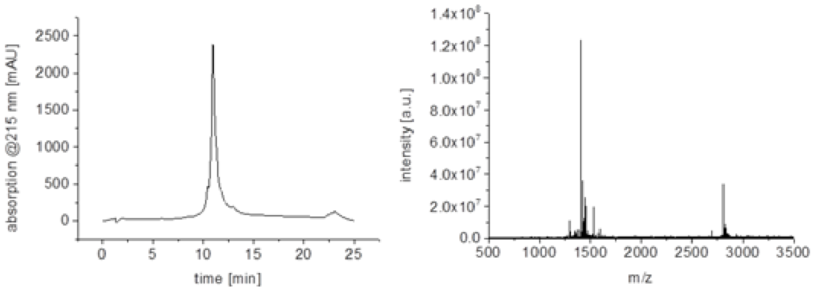

SAP^{3c}

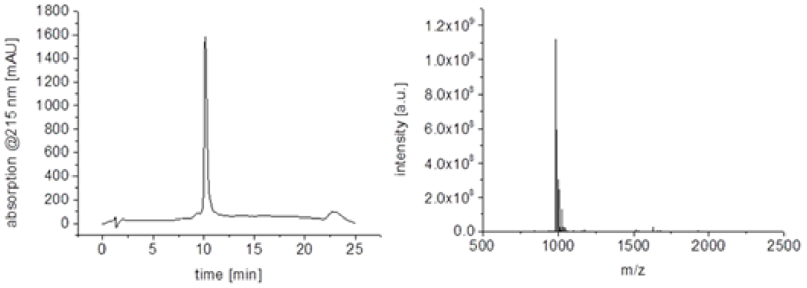

SAP^{4a}

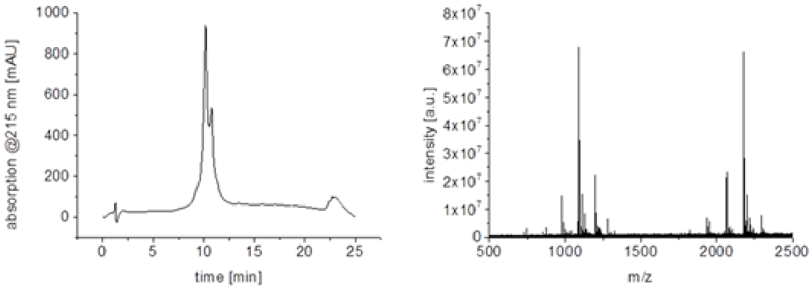

SAP^{4c}

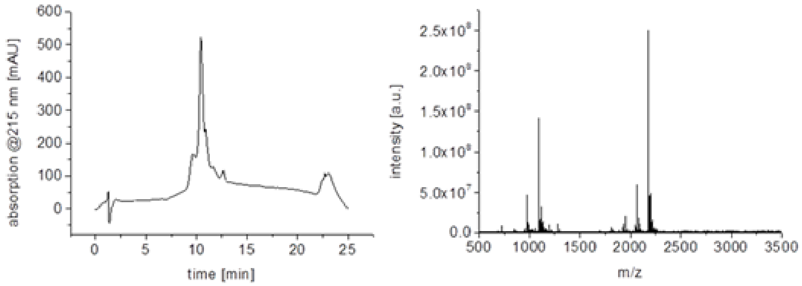

SAP^{4d}

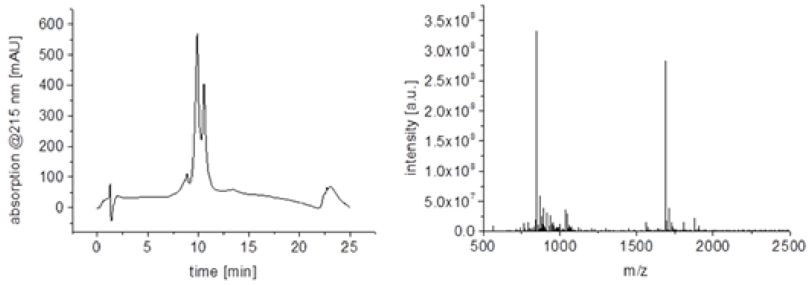

SAP^{4e}

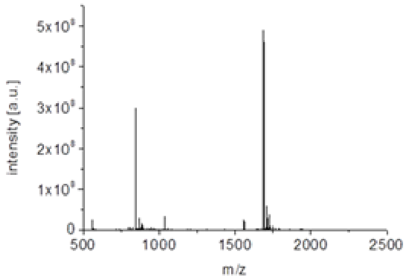

SAP^{5a}

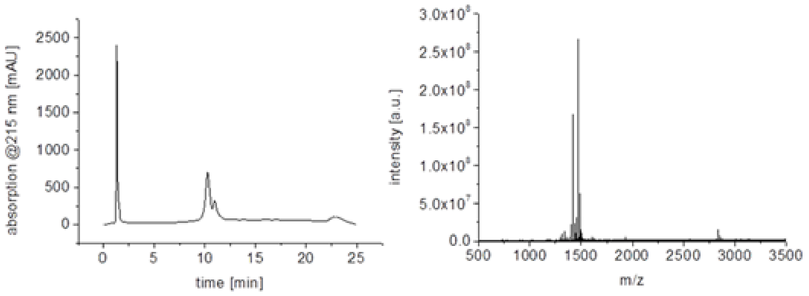

SAP^{5b}

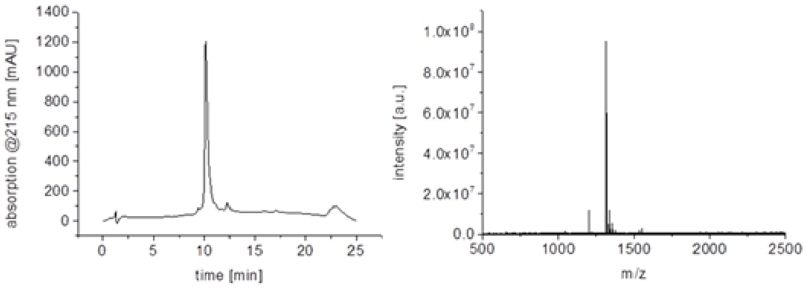

SAP^{5c}

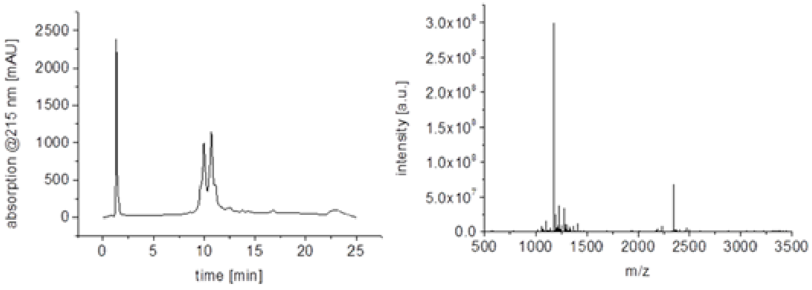

SAP^{5d}

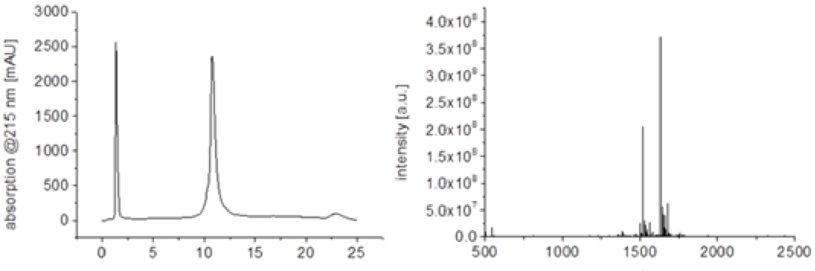

SAP^{6a}

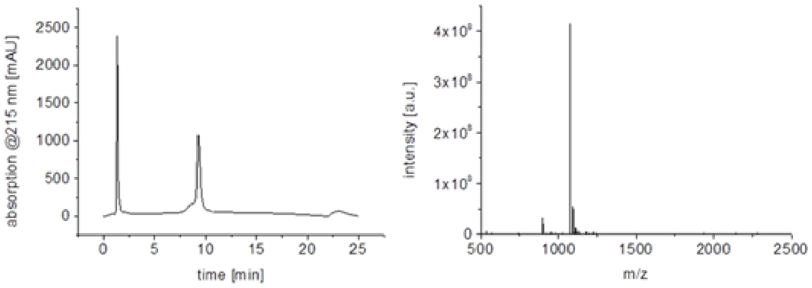

SAP^{6b}

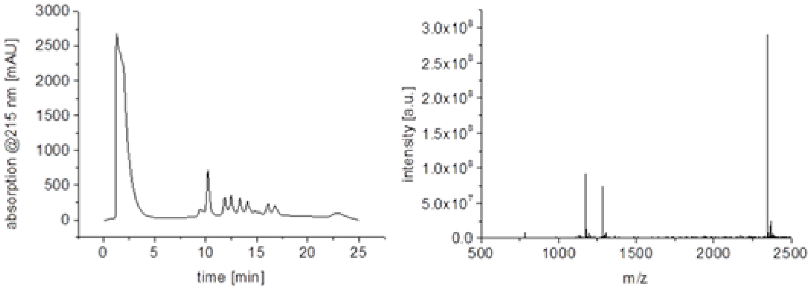

SAP^{7a}

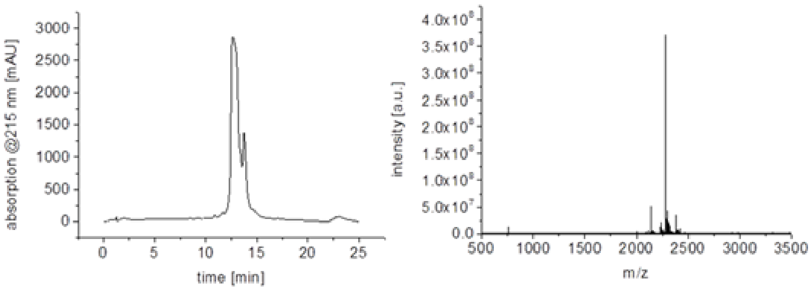

SAP^{7b}

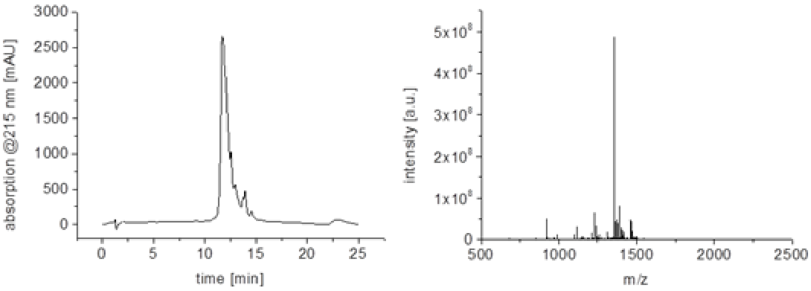

SAP^{8a}

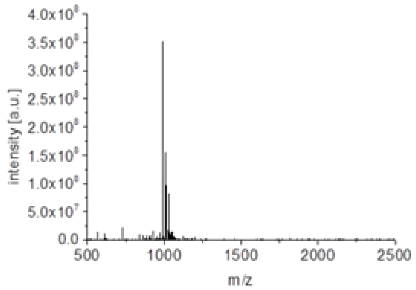

Figure S2

HPLC chromatograms of peptides (left side). MALDI-TOF mass spectra of peptides (right side). All data are summarized in Table S1.

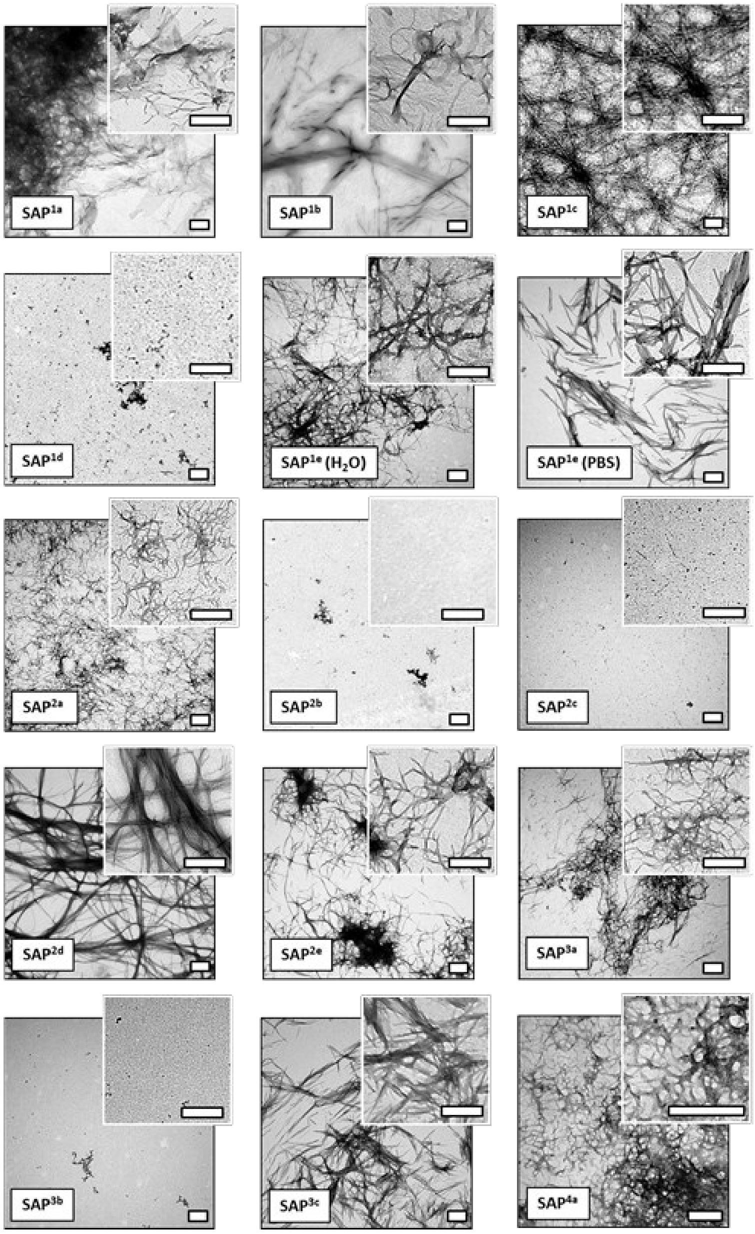
SAP1a
SAP1b
SAP1c
SAP1d
SAP1e (H2O)
SAP1e (PBS)
SAP2a
SAP2b
SAP2c
SAP2d
SAP2e
SAP3a
SAP3b
SAP3c
SAP4a

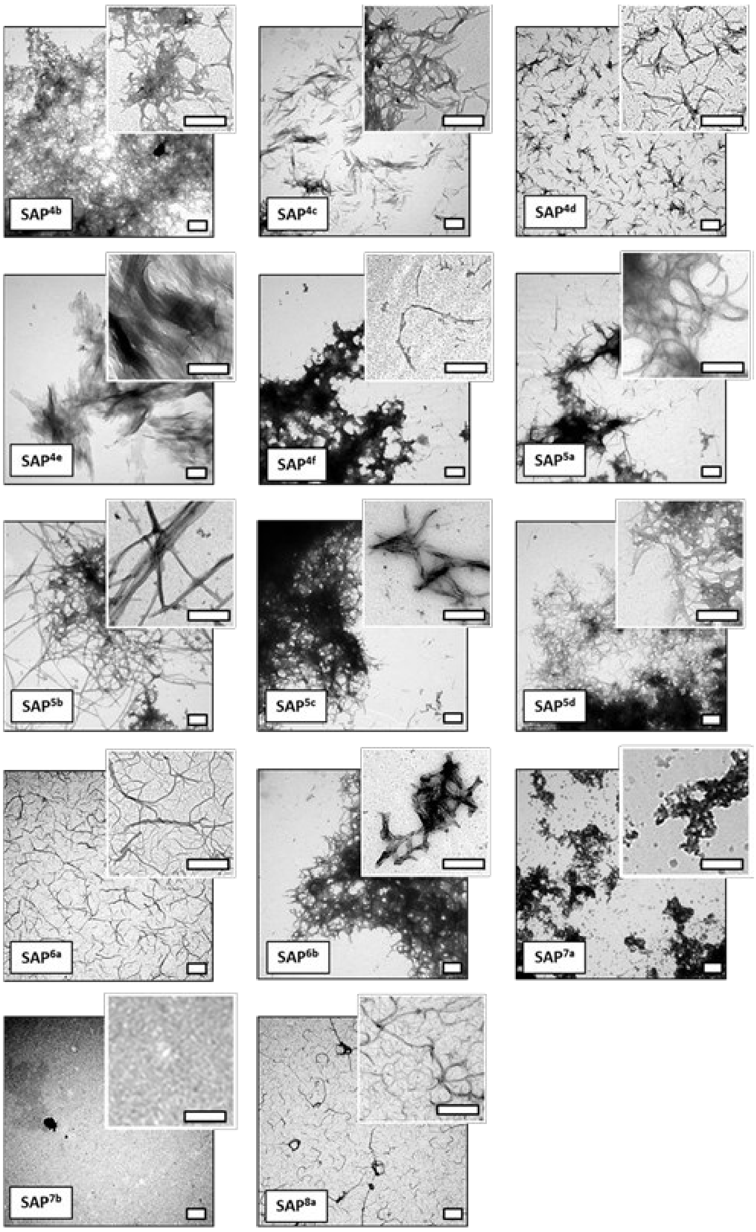

Figure S3

Transmission electron microscopy images of all peptides after 1 day of incubation in PBS (ddH$_2$O) with a final concentration of 1 mg/mL. Scale-bars = 250 nm.

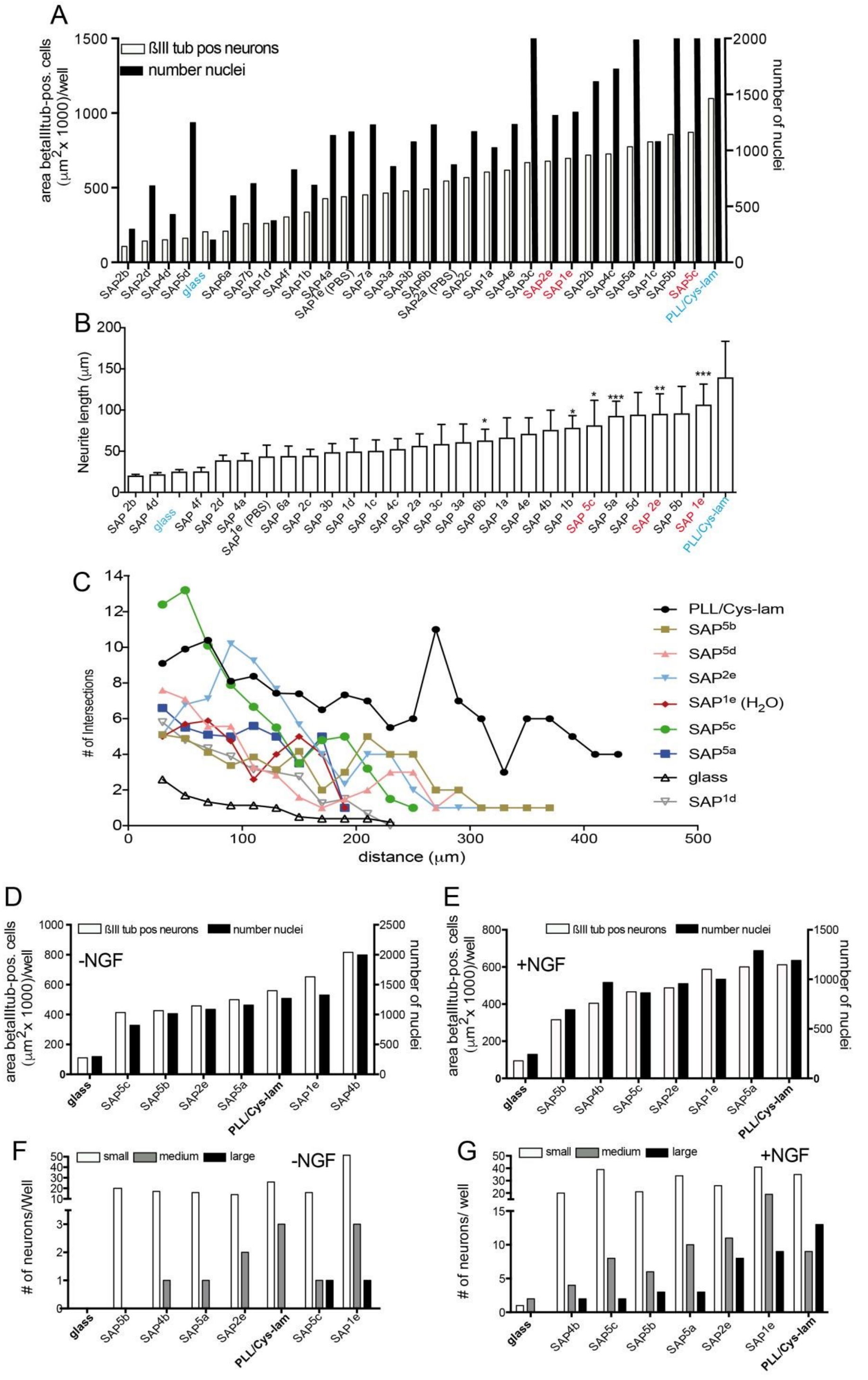
A
area betaIIItub-pos. cells (μm² x 1000)/well
ßIII tub pos neurons
number nuclei
number of nuclei
0
500
1000
1500
2000
SAP2b
SAP2d
SAP4d
SAP5d
glass
SAP6a
SAP7b
SAP1d
SAP4f
SAP1b
SAP4a
SAP1e (PBS)
SAP7a
SAP3a
SAP3b
SAP6b
SAP2a (PBS)
SAP2c
SAP1a
SAP4e
SAP3c
SAP2e
SAP1e
SAP2b
SAP4c
SAP5a
SAP1c
SAP5b
SAP5c
PLL/Cys-lam
B
Neurite length (μm)
0
50
100
150
200
SAP 2b
SAP 4d
glass
SAP 4f
SAP 2d
SAP 4a
SAP 1e (PBS)
SAP 6a
SAP 2c
SAP 3b
SAP 1d
SAP 1c
SAP 4c
SAP 2a
SAP 3c
SAP 3a
SAP 6b
SAP 1a
SAP 4e
SAP 4b
SAP 1b
SAP 5c
SAP 5a
SAP 5d
SAP 2e
SAP 5b
SAP 1e
PLL/Cys-lam
*
*
*
***
**
***
C
# of Intersections
distance (μm)
0
2
4
6
8
10
12
14
0
100
200
300
400
500
PLL/Cys-lam
SAP5b
SAP5d
SAP2e
SAP1e (H2O)
SAP5c
SAP5a
glass
SAP1d
D
-NGF
area betaIIItub-pos. cells (μm² x 1000)/well
ßIII tub pos neurons
number nuclei
number of nuclei
0
200
400
600
800
1000
500
1000
1500
2000
2500
glass
SAP5c
SAP5b
SAP2e
SAP5a
PLL/Cys-lam
SAP1e
SAP4b
E
+NGF
area betaIIItub-pos. cells (μm² x 1000)/well
ßIII tub pos neurons
number nuclei
number of nuclei
0
200
400
600
800
500
1000
1500
glass
SAP5b
SAP4b
SAP5c
SAP2e
SAP1e
SAP5a
PLL/Cys-lam
F
-NGF
# of neurons/Well
small
medium
large
0
1
2
3
10
20
30
40
50
glass
SAP5b
SAP4b
SAP5a
SAP2e
PLL/Cys-lam
SAP5c
SAP1e
G
+NGF
# of neurons/ well
small
medium
large
0
5
10
15
20
30
40
50
glass
SAP4b
SAP5c
SAP5b
SAP5a
SAP2e
SAP1e
PLL/Cys-lam

Figure S4 (previous page)

Quantification of total cell number and neuronal cells only for SAPs

(A) Quantification of total neuronal area (white bars) and number of neuronal nuclei (black bars) for DRG cell cultures grown on the different SAPs indicated.

(B) Quantification of average neurite length (in μm) of the longest neurite/neuron for all conditions. Data are depicted as mean ± SEM.

(C) Scholl analysis of the number of branches (“intersections”) in relation to the distance apart from the cell body. Neurons grown on PLL/Cys-lam had the highest number of branches whereas neurons grown on glass had the fewest branches. Neurons grown on SAP^{5c}, SAP^{1e} and SAP^{2e} also had a high number of branches.

(D, E) Selected SAPs were compared with glass (negative control) and the growth substrate PLL/Cys-laminin as positive control. Total neuronal area (white bars) and number of neuronal nuclei (black bars) were quantified (see A). Cells were either cultured without the growth factor NGF (D) or in its presence (E).

(F, G) Same experiment as in (D, E) but graphs depict quantification of neuronal size in the absence (F) or presence (G) of NGF.

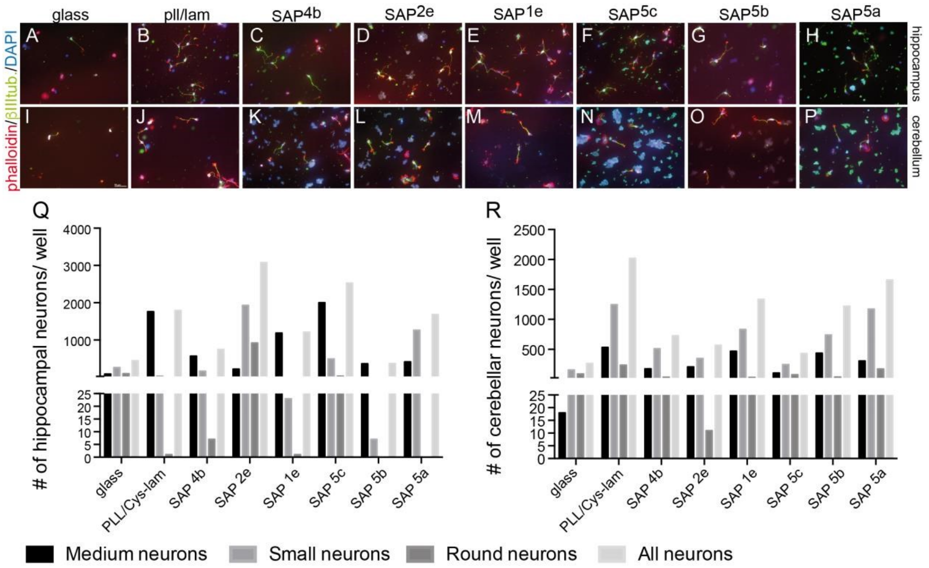

Figure S5

SAPs also stimulate adhesion and neurite growth of primary mouse CNS hippocampal and cerebellar neurons

(A-P) Mouse primary hippocampal (A-H) or cerebellar (I-P) neurons were cultured on the respective SAPs, glass or PLL/Cys-lam. Cells were stained with phalloidin to label F-actin and βIII tubulin to label neurons, respectively. DAPI was used to label nuclei. Please note that some SAPs (SAP^{4b}, SAP^{2e}, SAP^{5c}) were also positively stained for DAPI.

(Q, R) Quantification hippocampal (Q) and cerebellar (R) neuron growth by calculating number of all neurons and neurons with no neurites (”round neurons”) or small and medium size. Scale-bars (A-P) = 50 μm

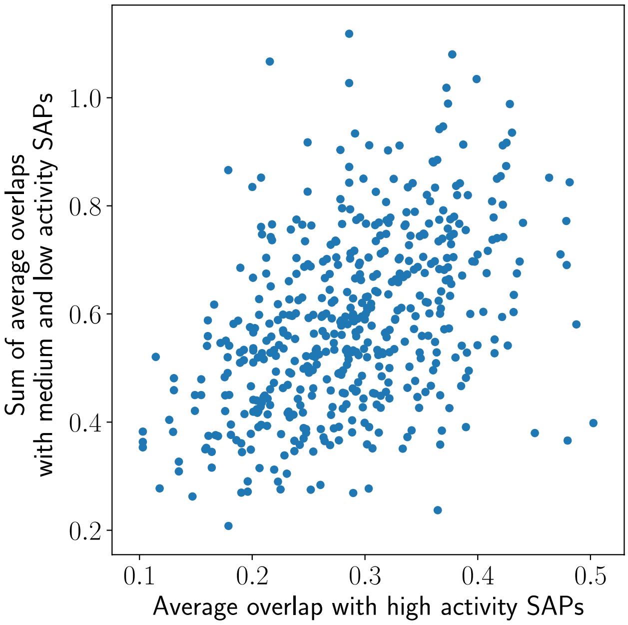

Figure S6

Overlap index I between constructed sequences from library and SAPs. Sequences represented by the points on the lower-right corner have high values of Q and predicted to have higher activity.

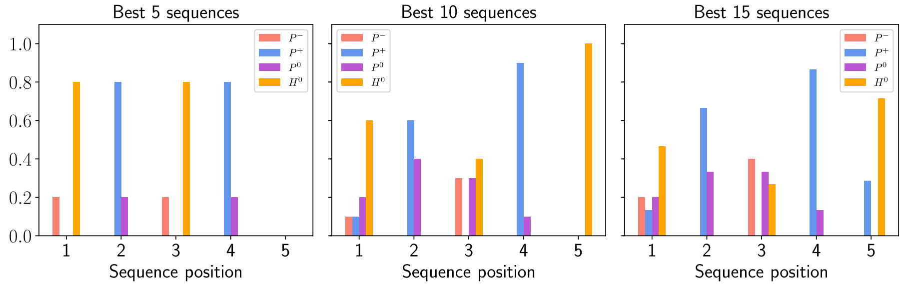

Figure S7

Histogram showing occurrences of amino acid types at different sequence positions. The recurring motif that emerges from the analysis is $H^0P^+H^0P^+H^0$. Note that the third position shows higher variability.

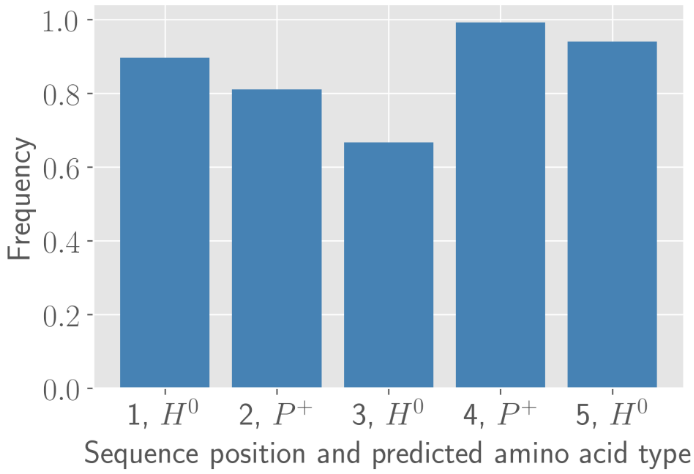

Figure S8

Results from the train-test splitting show that on average the most-occurring pattern found from only using the training sets is the same as the predicted pattern $H^0P^+H^0P^+H^0$ found using the whole dataset. This confirms that our predicted sequence is robust.

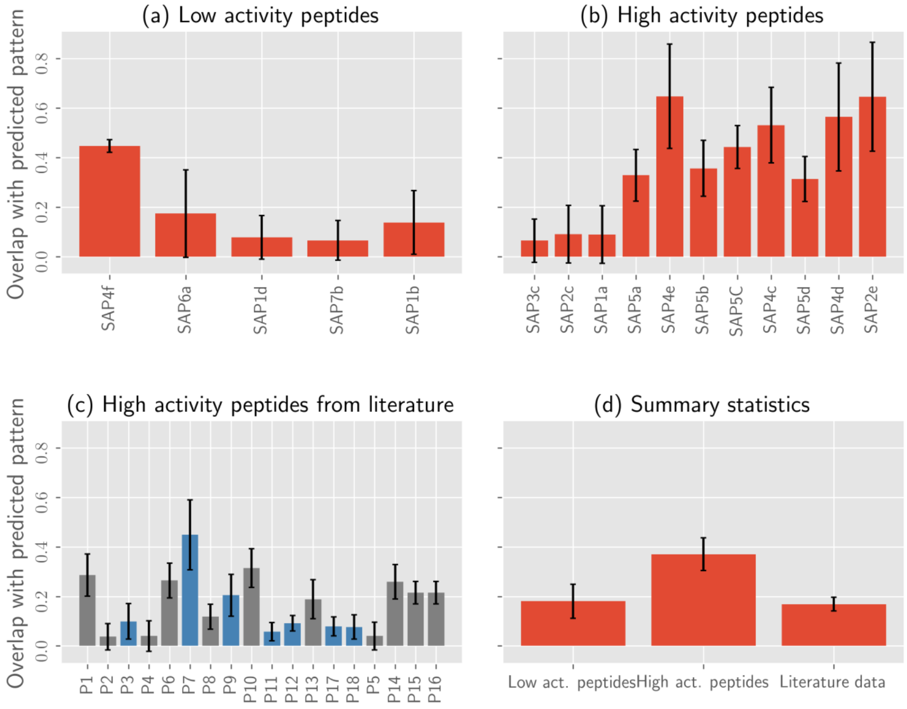

Figure S9

Plot shows the average overlap of the most-occurring pattern found using the training set with: a) Low activity SAPs from our data, b) High activity SAPs from our data, and c) High activity peptides collected from the literature. The peptides drawn with a grey bar in c) denote peptides with net neutral or negative charge and the blue bars denote peptides with net positive charge. Plot d) shows the mean overlap for each of low, high and literature data.

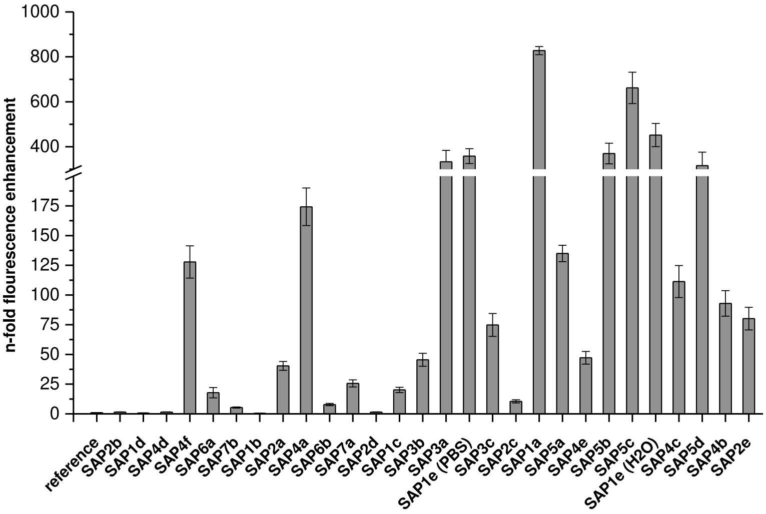

Figure S10

N-fold fluorescence enhancement of preformed fibers (1 day, PBS, 1 mg/mL) with Proteostat®.

SAP^{2b}

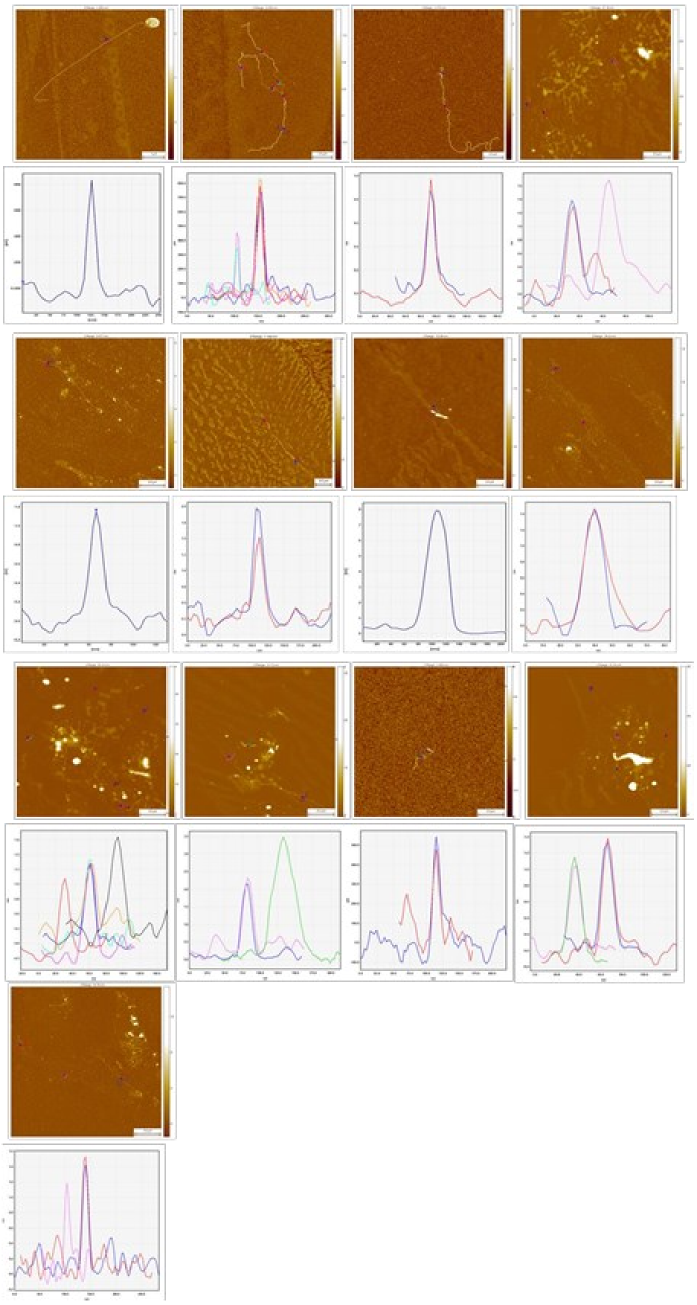

SAP^{2e}

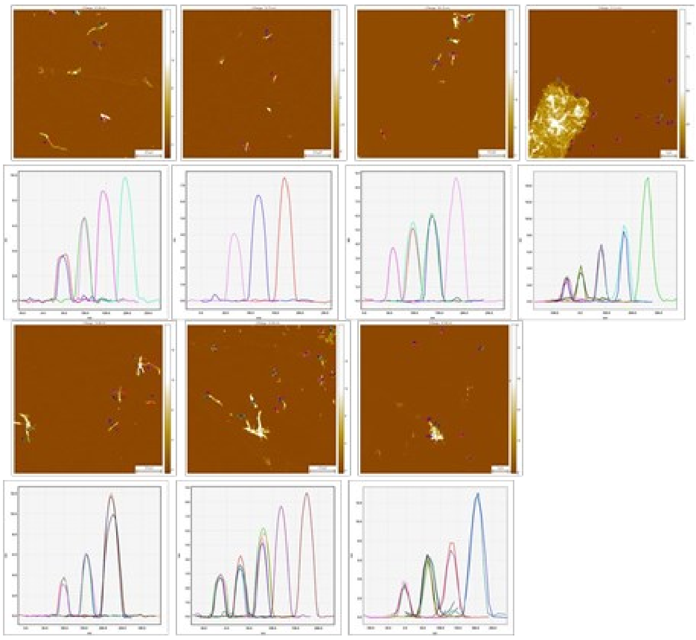

SAP^{5c}

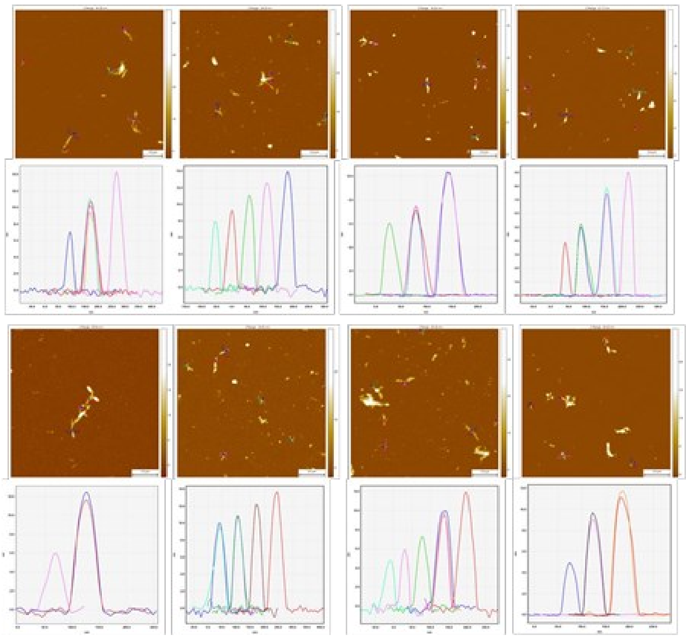

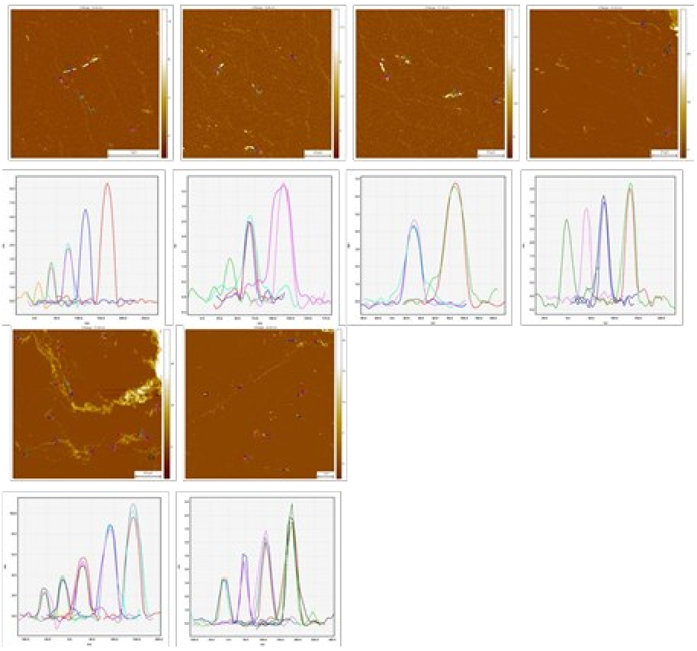

SAP^{6a}

Figure S11

Measurement of cross-sectional height of several fibers in detail for SAP^{2b}, SAP^{2e}, SAP^{5c} and SAP^{6a}.

SAP^{1a}

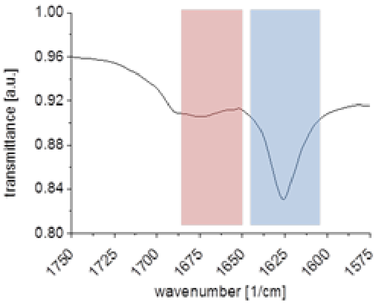

SAP^{1b}

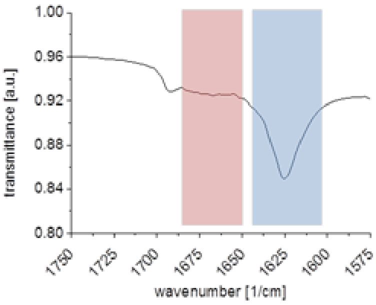

SAP^{1c}

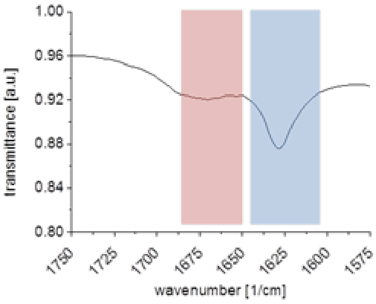

SAP^{1d}

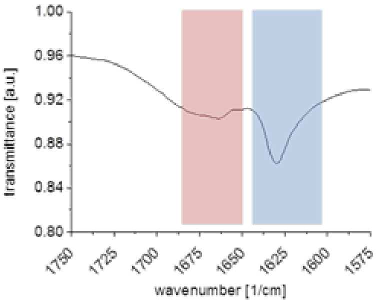

SAP^{1e} (PBS)

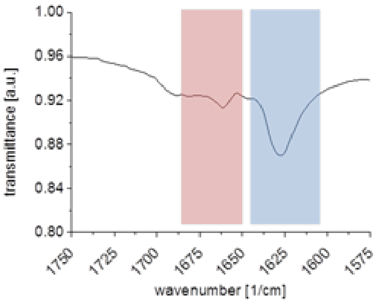

SAP^{1e} (H$_2$O)

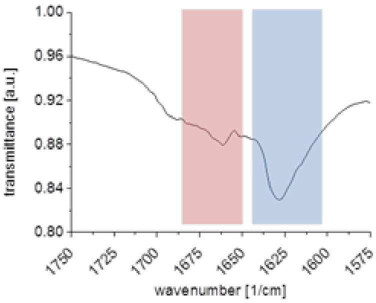

SAP^{2a}

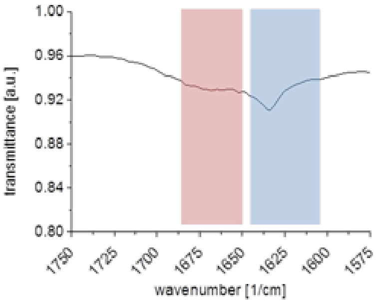

SAP^{2b}

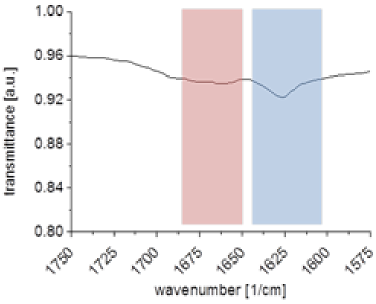

SAP^{2c}

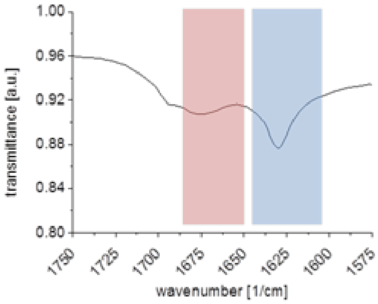

SAP^{2d}

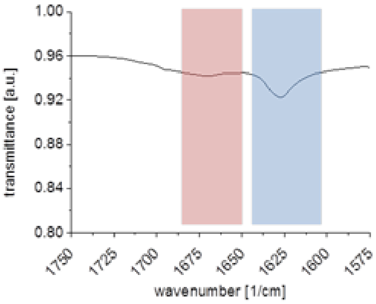

SAP^{2e}

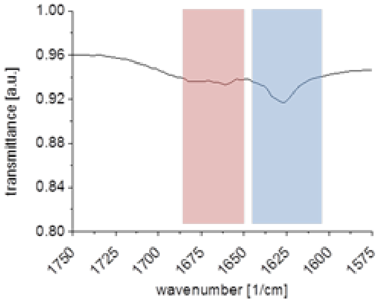

SAP^{3a}

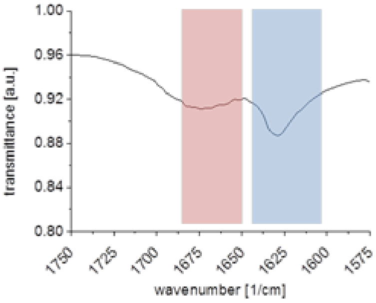

SAP^{3b}

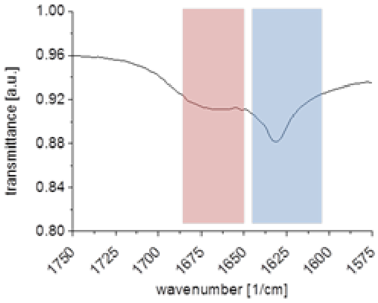

SAP^{3c}

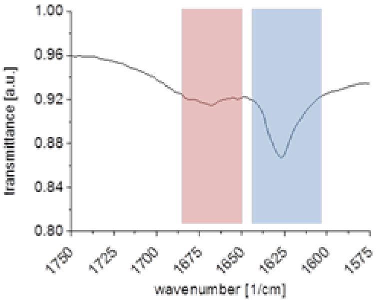

SAP^{4a}

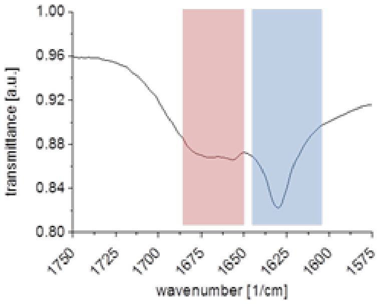

SAP^{4b}

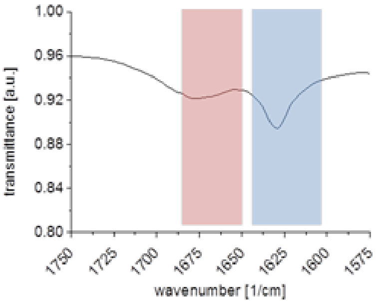

SAP^{4c}

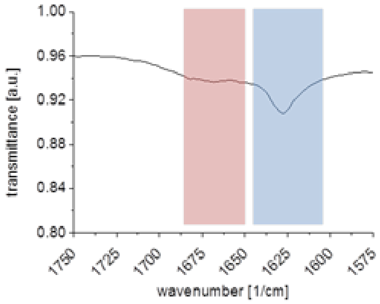

SAP^{4d}

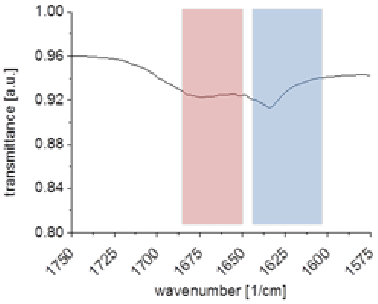

SAP^{4e}

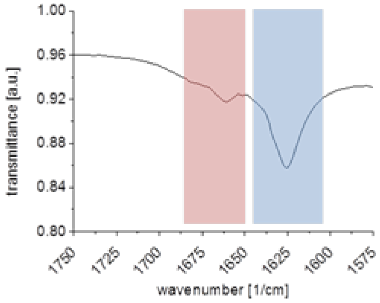

SAP^{4f}

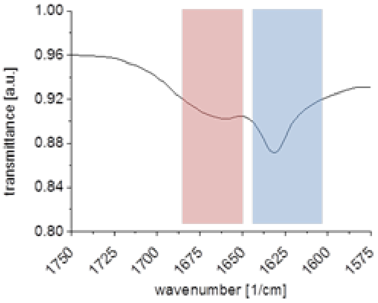

SAP^{5a}

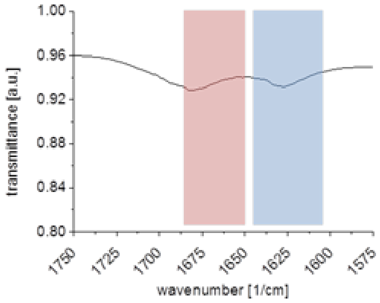

SAP^{5b}

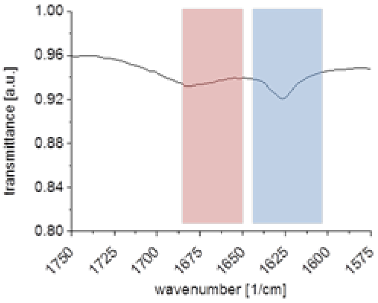

SAP^{5c}

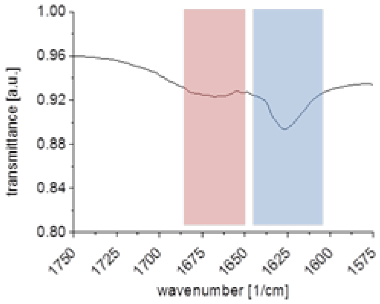

SAP^{5d}

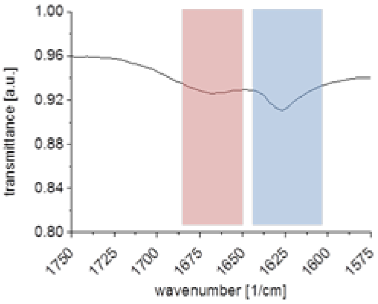

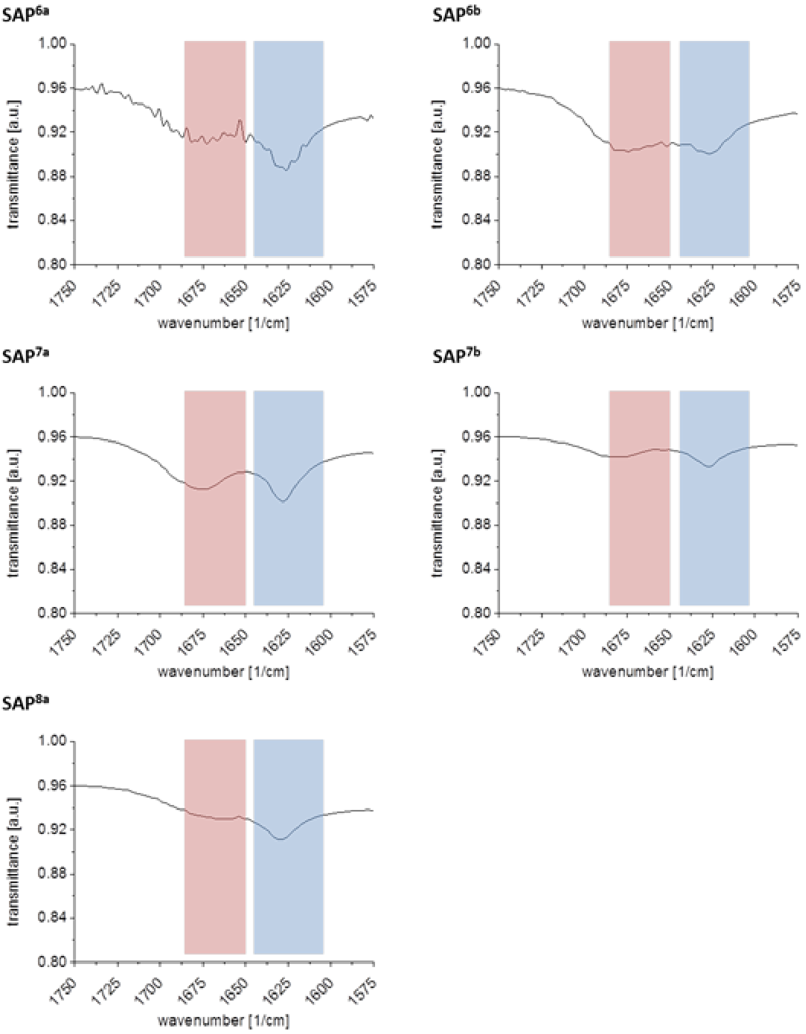

Figure S12

FTIR of all peptides after 1 day incubation in PBS (or ddH_2O) in the amide I region for secondary structure analysis. The blue color represents intermolecular parallel β-sheet peak area and the red color represents α-helix + β-turn peak area.

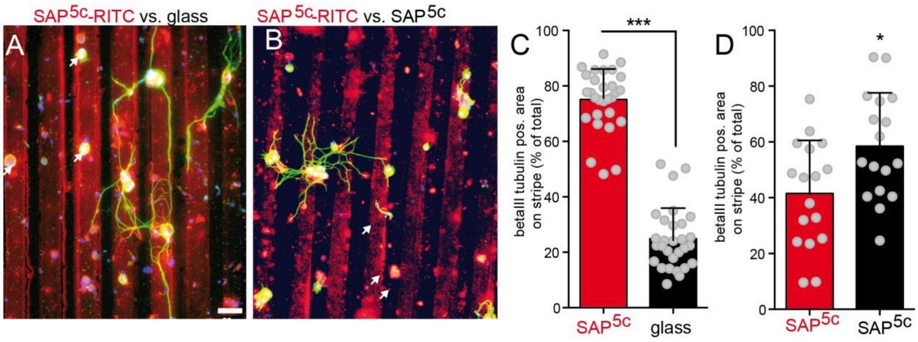

Figure S13

Neurons adhere to SAP5c containing substrates in the stripe assay

(A) Stripe assay with alternating lanes consisting of SAP^{5c}-RITC (red lanes) and glass only (dark lanes). DRG neuronal cell bodies (arrows) and outgrowing neurites preferred to grow on SAP^{5c}.

(B) Stripe assay with both lanes consisting of SAP^{5c}. Here, random outgrowth and localization of neuronal structures was observed.

(C) Quantification of experiments consisting of SAP^{5c}-positive stripes vs. glass only stripes. The majority of neurons was localized on SAP5c. Each dot represents one picture taken from independent stripe assays.

(D) Quantification of stripe assays with both lanes containing SAP^{5c}. Here, neurons grew almost equally well on both stripes. Each dot represents one picture taken from independent stripe assays.

Scale-bar (A, B) = 50 µm

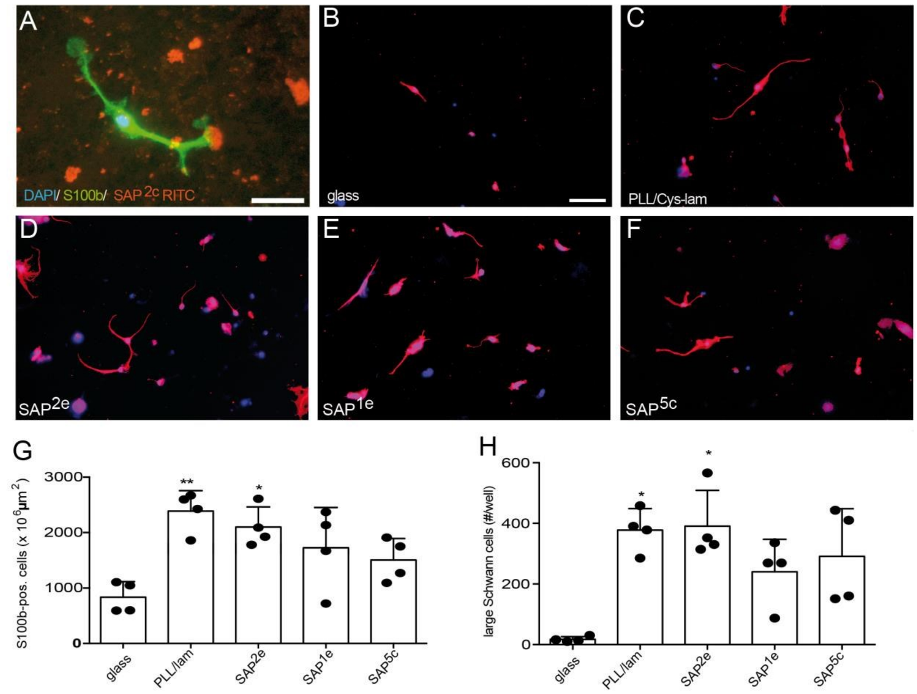

Figure S14

Schwann cell adhesion and growth is enhanced on SAP nanofibers

(A) Mouse Schwann cell stained with S100b (in green) contacts SAP positive plaques (SAP^{2e} conjugated with RITC; in red). DAPI labels the cell nucleus.

(B-F) Glass coverslips were left uncoated (B) or were coated with PLL/Cys-lam (C), SAP^{2e} (D), SAP^{1e} (E) or SAP^{5c} (F). Schwann cells (stained for S100b in red) did not adhere on glass (B) but grew on all three SAPs (D-F) equally well as on PLL/Cys-lam (C). Blue signals are DAPI-positive cell nuclei.

(G, H) Quantification of adhesion (G) and size (H) of Schwann cells on the different substrates. Each circle represents one culture derived from one mouse. Statistical significance was calculated in relation to glass.

Scale-bar (A) = 25 µm; (B-F) = 50 µm

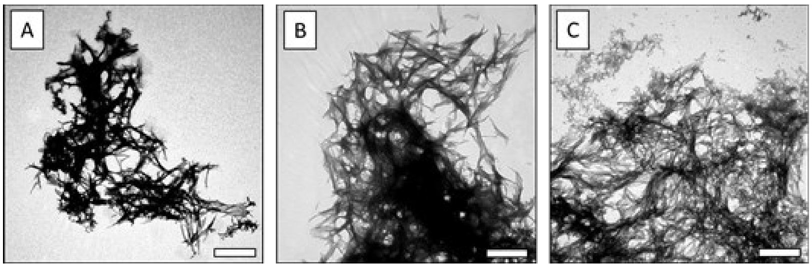

Figure S15

(A) SAP^{5c} fibrils after 1 day incubation in PBS at a final incubation concentration of 1 mg/mL, (B) after 3 more days at 37 °C and (C) after 3 more days in presence of proteinase K (fibril:proteinase K = 20:1 w%) at 37 °C. Scale-bar = 500 nm.

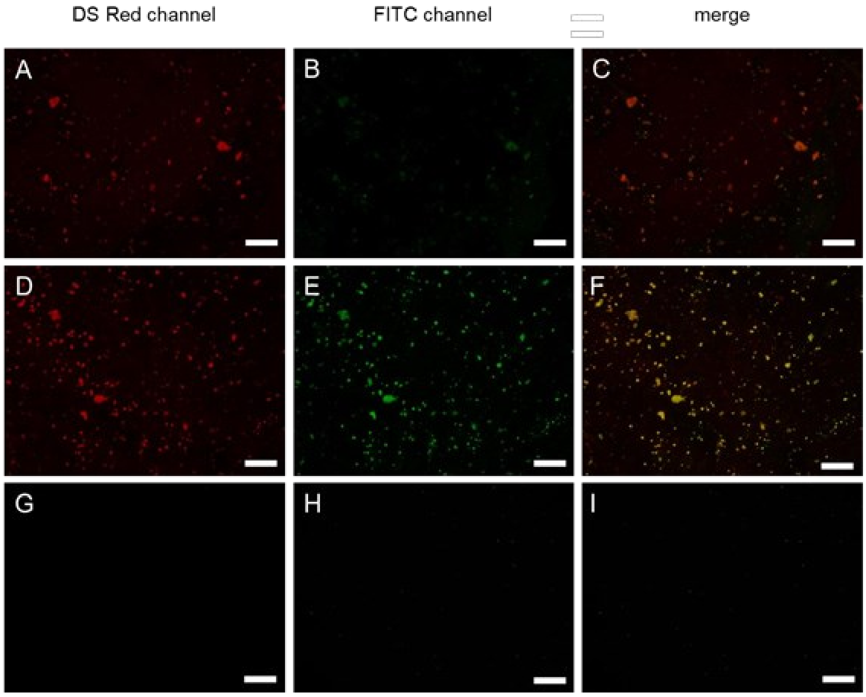

Figure S16

(A-C) Glass coverslips coated with SAP^{5c}-RITC fibrils (fluorescence visible in DS Red channel).

(D-F) Glass coverslips coated with SAP^{5c}-RITC fibrils and incubated with fluorescein labelled human serum album (HSA, fluorescence visible in FITC channel) indicating HSA attachment to SAP^{5c}-RITC fibrils.

(G-I) Glass coverslips were uncoated and incubated with fluorescein labelled HSA.

Scale-bar = 100 µm.

Supporting references

Angeloni, N.L., Bond, C.W., Tang, Y., Harrington, D.A., Zhang, S.M., Stupp, S.I., Mckenna, K.E., and Podlasek, C.A. (2011). Regeneration of the cavernous nerve by Sonic hedgehog using aligned peptide amphiphile nanofibers. *Biomaterials* 32**,** 1091-1101.

Berns, E.J., Alvarez, Z., Goldberger, J.E., Boekhoven, J., Kessler, J.A., Kuhn, H.G., and Stupp, S.I. (2016). A tenascin-C mimetic peptide amphiphile nanofiber gel promotes neurite outgrowth and cell migration of neurosphere-derived cells. *Acta Biomaterialia* 37**,** 50-58.

Berns, E.J., Sur, S., Pan, L., Goldberger, J.E., Suresh, S., Zhang, S., Kessler, J.A., and Stupp, S.I. (2014). Aligned neurite outgrowth and directed cell migration in self-assembled monodomain gels. *Biomaterials* 35**,** 185-195.

Choe, S., Bond, C.W., Harrington, D.A., Stupp, S.I., Mcvary, K.T., and Podlasek, C.A. (2017). Peptide amphiphile nanofiber hydrogel delivery of sonic hedgehog protein to the cavernous nerve to promote regeneration and prevent erectile dysfunction. *Nanomedicine-Nanotechnology Biology and Medicine* 13**,** 95-101.

Ellis-Behnke, R.G., Liang, Y.X., You, S.W., Tay, D.K.C., Zhang, S.G., So, K.F., and Schneider, G.E. (2006). Nano neuro knitting: Peptide nanofiber scaffold for brain repair and axon regeneration with functional return of vision. *Proceedings of the National Academy of Sciences of the United States of America* 103**,** 5054-5059.

Ferreira TA, Blackman AV, Oyrer J, Jayabal S, Chung AJ, Watt AJ, Sjostrom PJ, van Meyel DJ (2014) Neuronal morphometry directly from bitmap images. Nature methods 11:982-984.

Francis, N.L., Bennett, N.K., Halikere, A., Pang, Z.P.P., and Moghe, P.V. (2016). Self-Assembling Peptide Nanofiber Scaffolds for 3-D Reprogramming and Transplantation of Human Pluripotent Stem Cell-Derived Neurons. *Acs Biomaterials Science & Engineering* 2**,** 1030-1038.

Greene, J.J., Mcclendon, M.T., Stephanopoulos, N., Alvarez, Z., Stupp, S.I., and Richter, C.P. (2018). Electrophysiological assessment of a peptide amphiphile nanofiber nerve graft for facial nerve repair. *Journal of Tissue Engineering and Regenerative Medicine* 12**,** 1389-1401.

Knoll, B., Weinl, C., Nordheim, A., and Bonhoeffer, F. (2007). Stripe assay to examine axonal guidance and cell migration. *Nat Protoc* 2(5)**,** 1216-1224.

Kim, J.H., Jung, Y., Kim, B.S., and Kim, S.H. (2013). Stem cell recruitment and angiogenesis of neuropeptide substance P coupled with self-assembling peptide nanofiber in a mouse hind limb ischemia model. *Biomaterials* 34**,** 1657-1668.

Kyte, J., and Doolittle, R.F. (1982). A simple method for displaying the hydropathic character of a protein. *J Mol Biol* 157(1)**,** 105-132.

Li, X., Liu, X., Josey, B., Chou, C.J., Tan, Y., Zhang, N., and Wen, X. (2014). Short Laminin Peptide for Improved Neural Stem Cell Growth. *STEM CELLS Translational Medicine* 3**,** 662-670.

Liang, P., Xiong, J.S., Zhao, L.W., Xu, Y., Zhao, J.X., and Liu, Q. (2015). Recombinant self-assembling 16-residue peptide nanofiber scaffolds for neuronal axonal outgrowth. *Engineering in Life Sciences* 15**,** 152-158.

Liu, Y., Ye, H., Satkunendrarajah, K., Yao, G.S., Bayon, Y., and Fehlings, M.G. (2013). A self-assembling peptide reduces glial scarring, attenuates post-traumatic inflammation and promotes neurological recovery following spinal cord injury. *Acta biomaterialia* 9**,** 8075-8088.

Lu, C., Wang, Y., Yang, S., Wang, C., Sun, X., Lu, J., Yin, H., Jiang, W., Meng, H., Rao, F., Wang, X., and Peng, J. (2018). Bioactive Self-Assembling Peptide Hydrogels Functionalized with Brain-Derived Neurotrophic Factor and Nerve Growth Factor Mimicking Peptides Synergistically Promote Peripheral Nerve Regeneration. *ACS Biomaterials Science & Engineering* 4**,** 2994-3005.

Pedregosa, F., Varoquaux, G., Gramfort, A., Michel, V., Thirion, B., Grisel, O., Blondel, M., Prettenhofer, P., Weiss, R., Dubourg, V., Vanderplas, J., Passos, A., Cournapeau, D., Brucher, M., Perrot, M., and Duchesnay, E. (2011). Scikit-learn: Machine Learning in Python. *Journal of Machine Learning Research* 12**,** 2825-2830.

Shi, W., Huang, C.J., Xu, X.D., Jin, G.H., Huang, R.Q., Huang, J.F., Chen, Y.N., Ju, S.Q., Wang, Y., Shi, Y.W., Qin, J.B., Zhang, Y.Q., Liu, Q.Q., Wang, X.B., Zhang, X.H., and Chen, J. (2016). Transplantation of RADA16-BDNF peptide scaffold with human umbilical cord mesenchymal stem cells forced with CXCR4 and activated astrocytes for repair of traumatic brain injury. *Acta Biomaterialia* 45**,** 247-261.

Tavakol, S., Mousavi, S.M.M., Tavakol, B., Hoveizi, E., Ai, J., and Sorkhabadi, S.M.R. (2017). Mechano-Transduction Signals Derived from Self-Assembling Peptide Nanofibers Containing Long Motif of Laminin Influence Neurogenesis in In-Vitro and In-Vivo. *Molecular Neurobiology* 54**,** 2483-2496.

Tavakol, S., Saber, R., Hoveizi, E., Tavakol, B., Aligholi, H., Ai, J., and Rezayat, S.M. (2016). Self-Assembling Peptide Nanofiber Containing Long Motif of Laminin Induces Neural Differentiation, Tubulin Polymerization, and Neurogenesis: In Vitro, Ex Vivo, and In Vivo Studies. *Molecular Neurobiology* 53**,** 5288-5299.

Walther, P., Wang, L., Liessem, S., and Frascaroli, G. (2010). Viral infection of cells in culture--approaches for electron microscopy. *Methods Cell Biol* 96**,** 603-618. doi: 10.1016/S0091-679X(10)96025-1.

Yamagishi S, Hampel F, Hata K, Del Toro D, Schwark M, Kvachnina E, Bastmeyer M, Yamashita T, Tarabykin V, Klein R, Egea J (2011) FLRT2 and FLRT3 act as repulsive guidance cues for Unc5-positive neurons. The EMBO journal 30:2920-2933.

Zou, Z., Zheng, Q., Wu, Y., Song, Y., and Wu, B. (2009). Growth of rat dorsal root ganglion neurons on a novel self-assembling scaffold containing IKVAV sequence. *Materials Science and Engineering: C* 29**,** 2099-2103.

5.2 Water-Dispersible Polydopamine-Coated Nanofibers for Stimulation of Neuronal Growth and Adhesion

Stefanie Sieste, Thomas Mack, Christopher V. Synatschke, Corinna Schilling, Christopher Meyer zu Reckendorf, Laura Pendi, Sean Harvey, Francesco S. Ruggeri, Tuomas P. J. Knowles, Christoph Meier, David Y. W. Ng, Tanja Weil,* and Bernd Knöll*

* corresponding author

Published in Adv. Healthcare Mater. 2018, 7, 1701485. DOI: 10.1002/adhm.201701485

Abstract:

Hybrid nanomaterials have shown great potential in regenerative medicine due to the unique opportunities to customize materials properties for effectively controlling cellular growth. The peptide nanofiber-mediated autooxidative polymerization of dopamine, resulting in stable aqueous dispersions of polydopamine-coated peptide hybrid nanofibers, is demonstrated. The catechol residues of the polydopamine coating on the hybrid nanofibers are accessible and provide a platform for introducing functionalities in a pH-responsive polymer analogous reaction, which is demonstrated using a boronic acid modified fluorophore. The resulting hybrid nanofibers exhibit attractive properties in their cellular interactions: they enhance neuronal cell adhesion, nerve fiber growth, and growth cone area, thus providing great potential in regenerative medicine. Furthermore, the facile modification by pH-responsive supramolecular polymer analog reactions allows tailoring the functional properties of the hybrid nanofibers in a reversible fashion.

Contribution of the respective authors:

Stefanie Sieste: Design, synthesis and characterization of peptide fibers and polydopamine-peptide hybrids, writing of the manuscript.

Thomas Mack: Synthesis of peptide fibers. Conduction and characterization of polydopamine polymerization on peptide fibers. TEM imaging.

Christopher V. Synatschke: Writing and correcting the manuscript.

Corinna Schilling: Conduction of biological relevant assays in mice.

Christopher Meyer zu Reckendorf: Conduction of biological relevant assays in mice.

Laura Pendi: Conduction of polymerization of polydopamine of peptide fibers. Conduction and study of polydopamine formation by absorbance spectroscopy.

Sean Harvey: Discussion of FTIR results. AFM imaging of polydopamine particles.

Francesco S. Ruggeri: AFM imaging and analysis of polydopamine coated peptide fiber.
Tuomas P.J. Knowles: Acquiring funding for the project, design and discussion of the concept and results, writing and correcting the manuscript.
Christoph Meier: Discussion on the concept and results.
David Y. W. Ng: Discussion on the concept and results, writing and correcting the manuscript.
Tanja Weil: Acquiring funding for the project, design and discussion of the concept and results, writing and correcting the manuscript.
Bernd Knöll: Acquiring funding for the project, design and discussion of the concept and results, writing and correcting the manuscript.

FULL PAPER
ADVANCED HEALTHCARE MATERIALS
Self Assembling Peptides
www.advhealthmat.de

Water-Dispersible Polydopamine-Coated Nanofibers for Stimulation of Neuronal Growth and Adhesion

Stefanie Sieste, Thomas Mack, Christopher V. Synatschke, Corinna Schilling, Christopher Meyer zu Reckendorf, Laura Pendi, Sean Harvey, Francesco S. Ruggeri, Tuomas P. J. Knowles, Christoph Meier, David Y. W. Ng, Tanja Weil, and Bernd Knöll**

Hybrid nanomaterials have shown great potential in regenerative medicine due to the unique opportunities to customize materials properties for effectively controlling cellular growth. The peptide nanofiber-mediated auto-oxidative polymerization of dopamine, resulting in stable aqueous dispersions of polydopamine-coated peptide hybrid nanofibers, is demonstrated. The catechol residues of the polydopamine coating on the hybrid nanofibers are accessible and provide a platform for introducing functionalities in a pH-responsive polymer analogous reaction, which is demonstrated using a boronic acid modified fluorophore. The resulting hybrid nanofibers exhibit attractive properties in their cellular interactions: they enhance neuronal cell adhesion, nerve fiber growth, and growth cone area, thus providing great potential in regenerative medicine. Furthermore, the facile modification by pH-responsive supramolecular polymer analog reactions allows tailoring the functional properties of the hybrid nanofibers in a reversible fashion.

1. Introduction

Amyloid fibers, formed from the self-assembly of oligopeptides into highly stable intermolecular beta-sheet structures, have conventionally been negatively associated ever since they were implicated to be the causative agent for the neuronal plaques found in Parkinson's and Alzheimer's diseases.[1] However, it has been recently shown that these fibers also serve a functional role in many native biological processes (i.e., melanin synthesis[2] and peptide hormone storage[3]) and that those neurodegenerative disease implications have rather become a question of upstream mechanisms that trigger erratically. While Nature uses amyloid fibers as a synthetic template or as efficient storage modules, chemists have exploited the excellent strength and stability to create a broad spectrum of nanomaterials[4] ranging from nanowires for optoelectronic devices[5] to hydrogel matrices,[6] drug transporters for biomedical applications[7] or as synthetic biomaterials mimicking the extracellular matrix.[8] Recently, detailed and comprehensive studies have also shown beneficial effects of bioactive amyloid fibers on neuronal cell attachment, proliferation, or neurite outgrowth.[9]

While a large number of studies have established amyloid fibers as an excellent scaffold material, the implementation of synthetic chemistry to alter the innate functionality and interactions of such fibers with cells by retaining their unique bioactivities have been much less investigated. Conceptually, by providing a very thin surface coating in a single chemical step that retains bioactivity of the amyloid fibers but also introduces functionalities for facile and reversible functionalization, one could envision a fundamental understanding of amyloid biochemistry as well as expand the range of bioapplications. Such a strategy has been recently suggested by Maji and co-workers by applying biotechnological methods.[10] Here, peptide fragments derived from the amyloidogenic and infectious α-Synuclein protein interestingly revealed biocompatibility and even promoted the differentiation of stem cells. In this regard, chemical modification techniques would provide many advantages over, e.g., biotechnological methods due to the variety of functionalities that could be incorporated into the scaffold to increase the versatility of such a self-assembling platform.

Inspired by Nature's synthesis of melanin,[11] an insoluble polymer, whose polymerization is catalyzed by amyloid fibers, we hypothesize that an increase in versatility can be achieved by modifying the surface of peptide nanostructures through the facile polymerization of dopamine (DA) onto the surface of the amyloid fiber thus imparting higher degree of chemical functions. We have recently demonstrated the spatially controlled formation of polydopamine (pDA) on nanoscopic

S. Sieste, T. Mack, Dr. L. Pendi, S. Harvey, Dr. C. Meier,
Dr. D. Y. W. Ng, Prof. T. Weil
Institute of Organic Chemistry III/Macromolecular Chemistry
Ulm University
Albert-Einstein-Allee 11, 89081 Ulm, Germany
E-mail: weil@mpip-mainz.mpg.de
S. Sieste, T. Mack, Dr. C. V. Synatschke, S. Harvey,
Dr. D. Y. W. Ng, Prof. T. Weil
Department Synthesis of Macromolecules
Max Planck Institute for Polymer Research
Ackermannweg 10, 55128 Mainz, Germany
C. Schilling, Dr. C. Meyer zu Reckendorf, Prof. B. Knöll
Institute of Physiological Chemistry
Ulm University
Albert-Einstein-Allee 11, 89081 Ulm, Germany
E-mail: bernd.knoell@uni-ulm.de
Dr. F. S. Ruggeri, Prof. T. P. J. Knowles
Department of Chemistry
University of Cambridge
Lensfield Road, CB2 1EW Cambridge, UK

DOI: 10.1002/adhm.201701485

DNA origami templates using a localized redox catalyst on the nanostructure and the formation of distinct DNA origami structures due to the pDA self-adhesion.[12] pDA is a versatile biomaterial and has earned great acclaim as a multifunctional coating with applications ranging from energy, environmental to biomedical sciences due to its simplicity in formation and ability to adhere to virtually any surface.[13] Although the exact molecular structure of pDA is still under investigation,[13b,14] the type of chemical functional groups that are present within the polymer are well known. Hence, the aforementioned applications can be achieved by using reactive groups such as amines/thiols (Schiff-base, conjugate addition) as well as the metal binding and pH-responsive capabilities of the catechols with boronic acids.[15] In combination with the mechanical and physical properties of the tightly crosslinked structure, a variety of hybrid materials that extend beyond individual components, i.e., vascular devices and stents have been developed recently.[16]

Herein, we report the synthesis of hybrid peptide-polydopamine nanofibers (pDA-PNFs) that combine the nanofibrous morphology derived from PNFs (peptide nanofibers) with the versatile chemical function of pDA coatings. In this aspect, the PNFs serve both as a bioactive scaffold which promotes adhesion and growth of primary mouse neurons as well as a preorganized template for DA polymerization on the fiber surface. Furthermore, taking advantage of pDA as a very thin, functional biocoating, we demonstrate that bioactivity of the fibrils is retained even after coating and that the catechol groups presented on the hybrid fiber surface facilitate pH-responsive and pDA-selective conjugation of cargo molecules to showcase the potential for chemical modifications of the developed platform. Next to PNFs, also pDA is known to facilitate neuronal adhesion[17] and allows for neural cell growth and proliferation,[18] and we anticipate the pDA-coating to be well tolerated by neural cells. Hence, we envision that the fusion of amyloid and synthetic superstructures enables a multifunctional platform that allows customizing physiological and chemical properties of PNFs for regenerative medicine applications.

2. Results and Discussion

2.1. DA Polymerization in the Presence of PNFs

2.1.1. Formation and Characterization of PNFs

To study the polymerization of DA in the presence of self-assembled PNFs, we chose the 8-mer *KIKIQIII* as the nanofiber forming peptide (**Figure 1**a) which was discovered by us recently. This amphiphilic peptide consists of the basic amino acid lysine (K) alternating with isoleucine (I) and a hydrophobic *C*-terminus, thus providing the necessary structural features to readily form self-assembled nanofibers in aqueous solutions.[19] Glutamine (Q) in the center of the sequence is further capable of stabilizing the nano-assemblies through hydrogen bonding. *KIKIQIII* was synthesized according to standard protocols based on Fmoc-protected solid phase peptide synthesis. Purification of the crude product was conducted by reversed phase high performance liquid chromatography and confirmed by matrix-assisted laser desorption/ionization mass spectrometry (Figure S1, Supporting Information).

The peptide readily forms aggregates in aqueous solution when a dimethyl sulfoxide (DMSO) stock solution is diluted into a 100×10^{-3} M KCl solution. After an incubation period of 18 h to ensure complete formation of PNFs and subsequent dilution into Tris-buffer at pH 8.5, the final peptide concentration was 0.5×10^{-3} M. The obtained solution exhibits a significant increase in fluorescence intensity at 610 nm upon addition of the molecular rotor dye ProteoStat, which allows for the detection of aggregate formation in peptide and protein solutions upon excitation at 550 nm (**Figure 2**a).[20]

The morphology of the peptide aggregates was investigated by transmission electron microscopy (TEM, Figure 1b) as well as high resolution atomic force microscopy (AFM, Figure S2a, Supporting Information). The resulting images reveal well-defined nanofibers, which exceed several micrometers in length.

Secondary structure analysis obtained by Fourier-transform infrared (FT-IR) spectroscopy of a freeze-dried sample of *KIKIQIII* PNFs reveals signals in the amide I band region between 1600 and 1700 cm^{-1} (Figure S2b, Supporting Information). Using peak analysis (2nd derivative) and fitting four Gauss curves, two peaks at 1631 and 1692 cm^{-1} were identified, indicating the formation of an antiparallel beta-sheet structure.[21] Furthermore, the two peaks identified at 1662 and 1606 cm^{-1} indicate formation of intermolecular hydrogen bonding of the glutamine side chains.[22]

2.1.2. PNFs Catalyze DA Polymerization

After confirming the successful fiber formation from *KIKIQIII*, we proceeded with the preparation of pDA-PNF hybrids. In the literature, several reports for the functionalization of nanofibrous structures exist; however, these mostly describe the coating of electrospun polymers rather than self-assembled peptides.[23] Notable exceptions are the coating of fibrils from tobacco mosaic virus[24] and surface grown diphenylalanine nanowires.[25]

For the formation of pDA-PNF hybrids, the polymerization of DA occurred by auto-oxidation with oxygen from air, as previously described.[13a] In the presence of PNFs, a stable aqueous solution of brown color was obtained (Figure 1c) indicating pDA formation. Using absorbance spectroscopy, polymerization in the presence and absence of PNFs for 24 h revealed a significant increase in pDA formation in the presence of PNFs (Figure 1d). The polymerization of DA is known to proceed through several intermediates beginning with the oxidation of DA to dopamine-o-quinone and subsequent cyclization to dopaminochrome followed by further oxidative and oligomerization steps until pDA is formed. The final form of pDA consists of a complex mixture of intermediates and oligomers held together by supramolecular interactions.[14] Previous studies using absorbance spectroscopy have revealed the initial presence of dopamine-o-quinone and dopaminochrome through their characteristic absorption at around 300 nm.[12] The reaction continues with the critical oligomerization step and formation of pDA, which absorbs at higher wavelengths,[12,13,26] ultimately yielding a material with a broad absorbance across the UV and

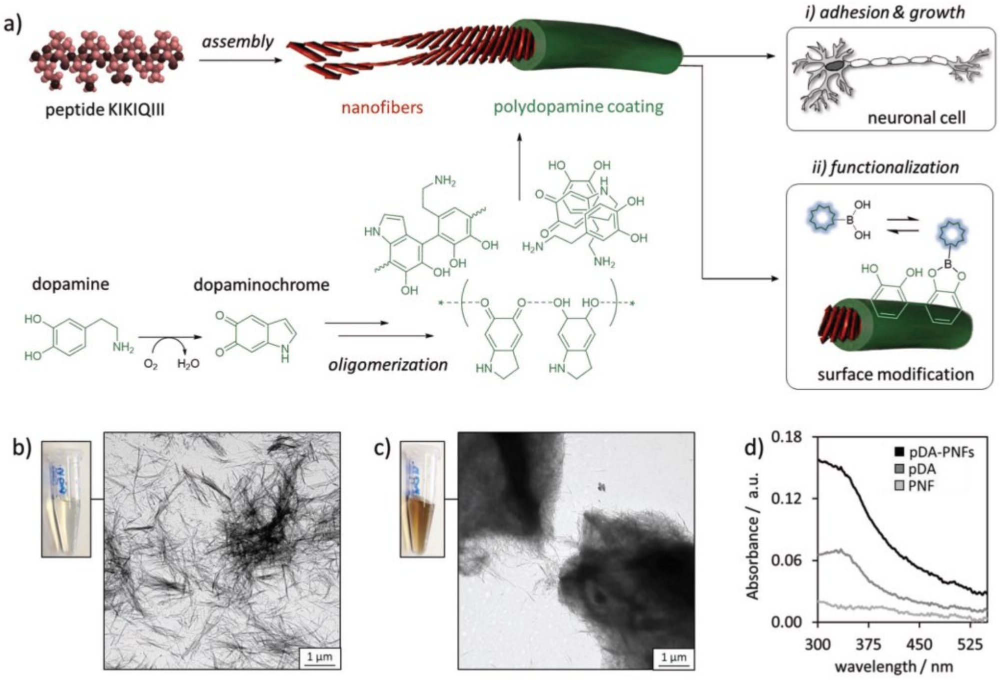

Figure 1. a) Schematic representation of the formation of polydopamine-coated peptide nanofiber hybrids (pDA-PNFs). Following the self-assembly of PNFs from *KIKIQIII* (red), pDA is formed on the PNF surface by auto-oxidation of DA (green). The nanostructures stimulate nerve fiber growth and the pDA-coating allows for additional functionalization. pDA intermediate structures were adapted from Tokura et al.[12] TEM images of PNFs b) before and c) after coating with pDA. Scale bars represent 1 µm. The photographs show the respective PNF containing solutions. d) Absorption spectra of PNF, pDA, and pDA-PNF hybrid solutions. PNF and DA concentrations were 0.5×10^{-3} and 0.08×10^{-3} M, respectively. pDA polymerization was carried out in Tris-buffer at pH 8.5 for 24 h at ambient temperature.

visible spectrum as depicted in Figure 1d. We speculate that the formed reactive dopaminochrome intermediate subsequently reacted to DA oligomers at the surface of the PNFs due to hydrophobic interactions, mimicking the biosynthetic pathway of eumelanin formation in mammals.[2]

Detection at 320 nm was selected to determine significant differences in DA polymerization in the presence and absence of PNFs. For more accurate sample comparisons, the absorption characteristics from the early oxidation products (e.g., dopaminochrome) and pDA were recorded. As the intermediate oligomeric DA species are transitory and after very short time become indistinguishable from pDA,[14,26] pDA will herein be used to refer to all auto-oxidation products of DA.

To further investigate the role of the PNFs on the auto-oxidative polymerization of DA, we determined the initial rate of polymerization v_0 for increasing PNF and DA concentrations. We calculated v_0 from the linear regression of the time resolved absorption spectroscopy during the first 60 min of polymerization by means of absorbance measured at 320 nm (Figure S3, Supporting Information). When studying the effect of PNF concentration on the polymerization kinetics, we used a fixed DA concentration of 0.08×10^{-3} M to avoid precipitation, which occurred at higher concentrations. We found that v_0 increases with higher PNF concentrations up to 0.3×10^{-3} M (Figure 2b) and at this concentration, the corresponding v_0 value is sixfold higher than in the absence of PNFs. Interestingly, a further increase in PNF concentration leads to a decrease of v_0, which we attribute to diffusion limitation as a result of increased solution viscosity (compare PNF hydrogel formation in Figure S2d, Supporting Information). Next, we varied the DA concentration, while keeping the PNF concentration at 0.5×10^{-3} M. As expected, v_0 initially increases with increasing DA concentrations up to 0.13×10^{-3} M (Figure 2c). At DA concentrations above 0.13×10^{-3} M, no further increase of v_0 was observed. However, a black precipitate, most likely pDA, formed in the reaction vessel. To obtain colloidally stable pDA-PNF hybrids, a concentration of 0.08×10^{-3} M DA solution was used for all further experiments.

To additionally substantiate the plausible catalytic effect of the PNFs, we polymerized 0.08×10^{-3} M DA in the presence of different PNF concentrations (0.0, 0.1, 0.3, and 0.5×10^{-3} M, respectively) in Tris-buffer at pH 8.5. After 5 h, the formed

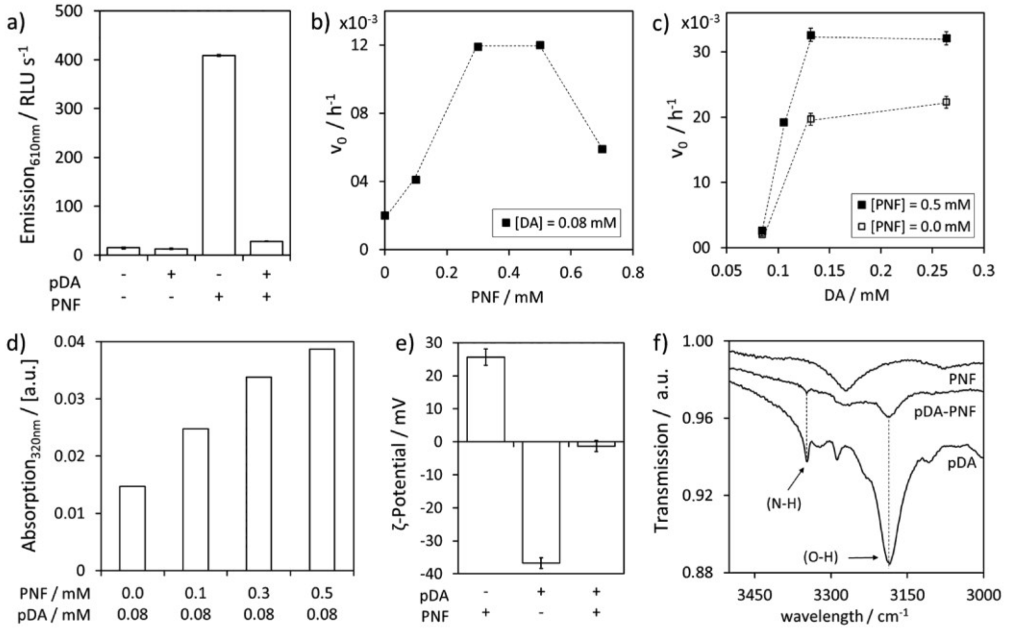

Figure 2. a) Increased fluorescence of the amyloid-specific dye ProteoStat at 610 nm ($\lambda_{ex.} = 550$ nm) upon interaction with free binding sites on PNFs. b) Initial polymerization rate v_0 of DA in the presence of different amounts of *KIKIQIII* PNFs. Dopamine concentration [DA] = 0.08×10^{-3} M. c) Initial polymerization rate v_0 as a function of dopamine concentration [DA] in the presence or absence of PNFs. d) The absorption at 320 nm indicates the total amount of pDA formed after 5 h from 0.08×10^{-3} M DA in the presence of increasing PNF concentrations. For consistent measurements, the samples were centrifuged, and the pellet was washed and dissolved in 1 M NaOH prior to the measurements. e) Zeta potential measurements of PNFs, pDA, and pDA-PNF in 1×10^{-3} M KCl buffer solution. f) Excerpt of FTIR spectra of lyophilized powders of PNFs, pDA, and pDA-PNFs. The peaks at 3346 and 3185 cm^{-1} are assigned to the N—H and O—H stretching bonds of pDA indicating successful polymerization in both pDA and pDA-PNF solutions. Full spectra and assignments are available in Figure S4 of the Supporting Information. Data shown in (a), (e), and (f) were obtained with sample concentrations as stated in Table S1 of the Supporting Information.

polymer was centrifuged, washed, dissolved in 1 M NaOH and the absorption at 320 nm was measured. We found that the amount of formed pDA increases with increasing PNF concentrations. At a PNF concentration of 0.5×10^{-3} M, the total amount of pDA was increased 2.6-fold compared to the sample without PNFs (Figure 2d). If the initiation of polymerization was to proceed by an auto-polymerization mechanism of DA, one would expect similar amounts of pDA formed in absence and presence of PNFs. However, the occurrence of higher amounts of pDA formed in presence of PNFs clearly indicates a catalytic contribution of the PNFs to the polymerization rate.

2.1.3. Characterization of pDA-PNF Hybrid Architectures

To confirm the successful formation of pDA-PNF hybrids, we performed a detailed characterization of the obtained material. Zeta potential measurements, depicted in Figure 2e, showed a distinct change from positive surface charges of unmodified PNFs to almost neutral in pDA-PNF hybrids, further indicating successful surface modification with pDA.

FT-IR spectra were acquired in attenuated total reflectance (ATR) mode, for the PNFs before and after DA polymerization and compared to pure pDA to verify coating (Figure 2f; Figure S4, Supporting Information). IR bands were assigned based on the work of Zangmeister et al. on pDA films[27] and reference tables.[28] Observed features of pDA at 3346 and 3185 cm^{-1} were assigned to the N—H and O—H stretching, respectively; stretching modes of aromatic C=C bonds at 1588 and 1460 cm^{-1}; bending of N—H at 1552 cm^{-1} and stretching of C—O bonds at 1295 cm^{-1}. Amide I and II bands were assigned to peaks at 1670 and 1540 cm^{-1} of the PNF. The spectrum of pDA-PNF exhibits signals from both PNF and pDA, indicating successful polymerization of DA in the presence of fibers.

Further spectroscopic experiments were conducted with the beta-sheet prone fluorescent dye Proteostat to investigate whether a core–shell architecture is formed upon incubation of DA in the presence of PNFs. The increase of fluorescence emission at 610 nm ($\lambda_{ex.} = 550$ nm) of untreated PNF solutions indicated the accessibility of binding-pockets along the fibrillar scaffold for the benzothiazole dye Proteostat. The same experiment was also performed with PNFs, which were incubated with DA in Tris-buffer for one day at ambient temperature. The addition of ProteoStat promoted significantly decreased emission intensities similar to the control samples containing no PNFs (Figure 2a). These findings suggest that the binding pockets for ProteoStat could be blocked by pDA after polymerization further supporting that pDA-PNF hybrid material was successfully prepared.

Microscopic techniques were employed to investigate the PNF hybrid morphology in comparison to PNFs. In TEM images, the unmodified PNFs were visible as fibrous aggregates, which exhibited a minor degree of bundling (Figure 1b; Figure S5a, Supporting Information). However, the solution obtained after DA polymerization revealed dense mats of bundled fibers, with only very few fibers being present individually (Figure 1c; Figure S5b, Supporting Information). pDA is known to be a strong bioadhesive.[13] A coating of pDA along the PNF surface could thus explain the stronger tendency for bundling in comparison to untreated PNFs.

To further substantiate the occurrence of a pDA-coating on PNFs, detailed morphological analysis was conducted by AFM (**Figure 3**a–c; Figure S6, Supporting Information). Samples were deposited on mica substrates for 1 min, avoiding clustering and allowing characterization of individual fibrils. Statistical analysis of the cross-sectional diameter of single fibers was performed by measuring the average height along the maximum height profile of the fiber, referred to as height for simplicity (Figure 3b). The analysis was conducted by measuring the height of all the fibrils present in each sample per unit of area on the surface of deposition (Figure 3a, inset). The unmodified PNFs exhibited an average cross-sectional diameter of 2.54 ± 0.12 nm. This corresponded well to the estimated length of the peptide in a beta-sheet conformation of ≈2.7 nm (Figure S2c, Supporting Information). The data furthermore revealed that pDA-PNF hybrids were characterized by increased average heights of 2.89 ± 0.16 nm, consistent with pDA deposition on the PNFs. Furthermore, no spherical particles corresponding to free pDA (Figure S7, Supporting Information) polymerized in solution were visible in the AFM images indicating that the polymerization mainly proceeded on the PNF surface.[29] The difference between the average of the

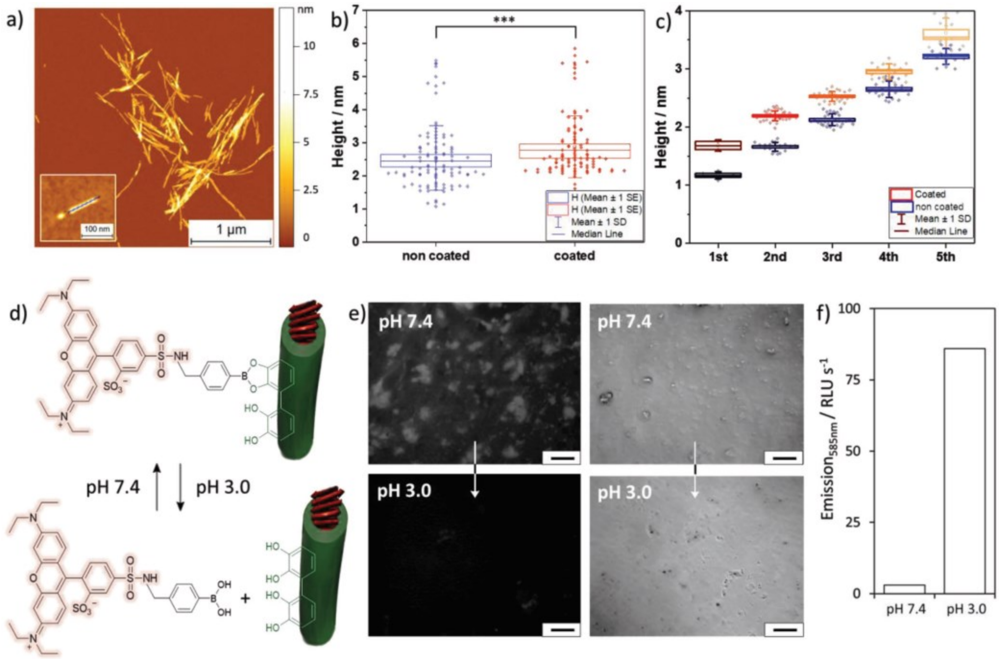

Figure 3. a) AFM 3D morphology maps of PNFs after DA polymerization for 24 h using 0.5 × 10^{-3} M PNF and 0.08 × 10^{-3} M DA (Z scale is in nm). b) Scatter plot of the cross-sectional height of individual PNFs (n = 102) and pDA-PNFs (n = 100). The distributions have statistically significant differences ($p < 0.001$) showing an increase in PNF diameter from 2.54 ± 0.12 nm (blue) to 2.89 ± 0.16 nm (red) after DA polymerization. c) The statistical distributions of height for PNF and pDA-PNFs show the occurrence of several peaks corresponding to different polymorphs of the fibrils. In particular, each PNF polymorph corresponds to a group of pDA-PNFs with increased cross-sectional diameter ($p < 0.001$), enabling to measure an average coating thickness of 0.41 ± 0.08 nm. d) Sketch of the pH-responsive modification of pDA-PNFs with fluorescent dye by reversible boronic acid–catechol interactions and e) fluorescence microscopy images of pDA-PNFs on 13 mm coverslips after incubation with boronic acid modified Rhodamine in PBS buffer at pH 7.4 and pH 3. Scale bars represent 100 µm. f) Fluorescence emission at 585 nm ($\lambda_{ex.}$ = 565 nm) of washing buffer solutions after incubation at different pH values.

distributions was statistically significant ($p < 0.001$). However, the PNFs did not show a narrow distribution of their height and we could observe that they occurred in several polymorphs presenting different cross-sectional diameter (AFM height, Figure S6e–g, Supporting Information). This was most likely due to a hierarchical assembly process of the PNFs where a different number of protofilament units make up their cross-section. The polymorphism is reflected in the statistical distribution of the cross-sectional height, which showed several peaks indicating that PNFs were therefore grouped in different polymorphs as independent distributions according to their heights (Figure 3c; Figure S6, Supporting Information). A similar presence of multiple peaks in the statistical distribution of the cross-sectional height occurred for the pDA-PNFs, indicating again the presence of the several polymorphs. In particular, each population of the uncoated fibrils had a smaller height than the corresponding one for the coated fibrils. The comparison and averaging of the difference in cross-sectional height between individual populations of the PNFs and pDA-PNFs lead to a more accurate determination of the increase of the PNF height and the corresponding thickness upon coating. Our results therefore suggest the presence of an ultrathin pDA coating, which appears in the order of 0.41 ± 0.08 nm. The obtained results indicate a thickness of 0.2 nm for the pDA layer, which roughly corresponds to a single layer of pDA decorating the PNFs.

2.2. Chemical Modification of the Functionalized PNF Hybrid Surface

In macromolecular chemistry, polymer analog reactions are widely used to obtain polymeric materials with physical and chemical properties that are not available using the corresponding monomers directly.[30] In that sense, supramolecular polymer analog reactions allow modifying and adjusting the properties of polymeric materials in a stimuli-responsive fashion. Here, the polymerization of DA on the PNFs decorated the PNF surface with catechol residues. Catechol moieties undergo a specific and pH-responsive reversible covalent reaction with boronic acids which, for instance, enables a pH-controlled release of proteins.[31] To show that the catechol groups were accessible and could be modified in a pH-responsive polymer analog reaction, we synthesized a boronic acid modified Rhodamine dye (BA-Rho, Figure 3d and Supporting Information) as a model compound and investigated its dynamic covalent interaction with the catechol groups on the pDA-PNF surface.

The pDA-PNFs were deposited on glass by drop casting. The strong adhesiveness of the pDA coating ensured a strong adsorption of the nanofibers to the surface. The dye BA-Rho was added in a PBS buffer at pH 7.4 and incubated for 30 min. After washing with PBS buffer at pH 7.4 and pH 3.0, the fluorescence of BA-Rho was measured using fluorescence microscopy. At pH 7.4, the images featured highly fluorescent deposits on the glass surface indicating successful binding of the dye to the catechol residues of pDA (Figure 3e). After subsequent washing with the pH 3.0 buffer, the sample did not show any fluorescent deposits (Figure 3e,f), indicating that the fluorescent dye had been completely removed from the pDA-PNF surface after acid treatment. Bright field microscopy images showed remaining material on glass after treatment with the washing buffers, which we presume to be pDA-PNFs (Figure 3e). The washing solutions were collected and measured for Rhodamine fluorescence. The pH 7.4, the washing buffer showed no fluorescence, whereas the pH 3.0, the buffer revealed high fluorescence intensity, indicating the release of the BA-Rho from the pDA-coated PNFs (Figure 3f). The same reaction was also conducted with untreated PNFs, which were not coated with pDA as a control. No fluorescent aggregates were detected (Figure S8, Supporting Information) under the same reaction conditions indicating that the fluorescent dye was exclusively bound to pDA-modified PNFs in the proposed reversible polymer analog reaction. This finding was confirmed by quantifying the fluorescence intensity of aggregates of PNF and pDA-PNF treated samples (Figure S8b, Supporting Information). In agreement with the qualitative analysis, aggregates with significant fluorescence intensity are only observed in the case of pDA-PNF coated substrates at pH 7.4, and very little signal is detected at all other conditions.

We have demonstrated the opportunity of introducing functional groups containing boronic acid moieties selectively to the hybrid pDA-PNF, which can be exploited in the future for introducing a variety of bioactive groups. Examples of such bioactive groups are short peptide sequences,[32] DNA aptamers, reporter molecules, or proteins[31,33] featuring boronic acid moieties.

2.3. pDA-PNF Enhance Cell Attachment and Neurite Growth of Primary Mouse Neurons

Both pDA coatings and surface deposited PNFs were previously tested for their suitability in neural cell growth, proliferation and adhesion before.[9,17a,18,34] Based on these findings, we investigated the effect of pDA-PNF hybrid coatings on adhesion and nerve fiber growth of primary postnatal mouse cerebellar neurons (**Figure** 4c,f). As a positive control, we included coverslips coated with poly-L-lysine (pll) and the extracellular matrix component laminin (lam), an established nerve fiber growth promoting substrate (Figure 4b,e).[35] pDA-PNFs obtained by polymerization of 0.08×10^{-3} M DA in the presence of 0.5×10^{-3} M PNFs were coated onto glass coverslips. Different concentrations of the coating solution were prepared by diluting the obtained pDA-PNFs, added to the cell culture substrate and dried in air to ensure reproducible coatings. Freshly prepared mouse primary neurons were spread on the modified surfaces and cultured for 72 h. The total cell number including neuronal as well as non-neuronal cells, number of neurons and average neurite length was measured via fluorescence microscopy and automated image analysis (Figure 4).

Compared to pDA alone or glass without any coating (Figure 4a,d), the pDA-PNF hybrids show an increased total number of attached cells (Figure 4g) as well as increased numbers of neurons (Figure 4h) and neurite lengths (Figure 4i) in a dose dependent manner. The average neurite length is comparable to pll/lam, indicating a strong promotion of neuronal attachment and nerve fiber growth of the pDA-PNF hybrids (Figure 4i). The total number of all cells (including

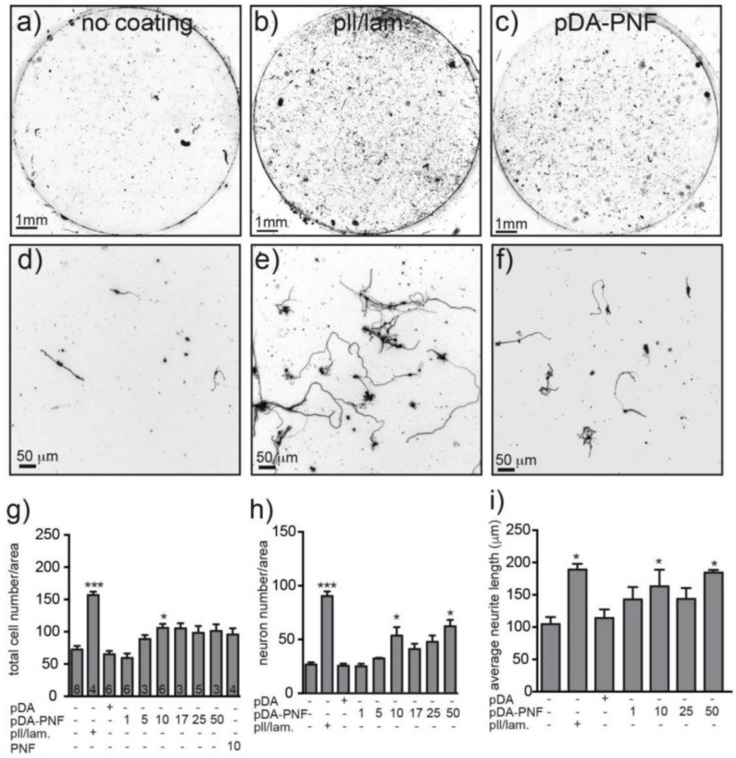

Figure 4. Mouse primary neuron attachment and nerve fiber growth on pDA-PNF. Neurons were cultured on unmodified glass coverslips, pll/lam-coated substrates, pDA-coated substrates, PNF alone or pDA-PNF-coated substrates. a–c) Optical microscopy images of the entire coverslips after incubation. d–f) Magnification showing individual neuronal cells stained with the neuron-specific antibody class III β-tubulin. g–i) Quantification of total cell number (g), number of neurons per area (h) or average neurite length (i) obtained from the optical microscopy images. pDA concentration used for coating is 0.08×10^{-3} M. pDA-PNF was obtained with 0.08×10^{-3} M DA and PNF (0.5×10^{-3} M peptide) and diluted to the indicated peptide concentration in μg mL^{-1}. *: $p \leq 0.05$ and ***: $p \leq 0.001$. Two-way ANOVA was performed. *N*-numbers in bars (g) indicate the number of independent neuronal cultures from different mice analyzed.

non-neuronal cells) per area is significantly increased compared to the uncoated glass coverslips and pDA controls (Figure 4g). Above a concentration of 10 μg mL^{-1} peptide equivalents, no further increase in cell number was detected. The number of neurons per area increases with increasing pDA-PNF concentration, indicating a beneficial effect of the pDA-PNFs on neuronal differentiation (Figure 4h). The average neurite length increases with increasing pDA-PNF concentration up to a length similar to that found for the pll/lam coating (Figure 4i).

We observed a similar impact of PNFs before and after coating with pDA on cell adhesion (Figure 4g) as well as comparable activity with respect to the number of attached neurons and average neurite growth (Figure S9, Supporting Information). Thus, nanofibers significantly enhance adhesion of neuronal cells as well as induced neurite growth compared to uncoated surface or surfaces coated with pDA alone.

In addition to nerve fiber growth, we tested the impact of pDA-PNFs on neuronal growth cones of hippocampal neurons (**Figure 5**). Growth cones are the motile and sensory tips of nerve fibers involved in regulation of neurite extension, growth direction, and axonal regeneration.[36] These structures typically consist of finger-like filopodia, which are rich in polymerized filamentous actin. We measured the growth cone area to analyze whether pDA-PNFs have an impact on growth cone morphology. Growth cones derived from primary mouse hippocampal neurons grown on glass coverslips with no coating (Figure 5a,d) or pll/lam (Figure 5b,e) coating had a decreased number of filopodia and total growth cone area (quantified in Figure 5g) compared to growth cones derived from neurons plated on pDA-PNFs (Figure 5c,f). This suggests a stimulatory function of pDA-PNFs on growth cone morphology. Of note, the results on pDA-PNFs (Figure 5) are comparable to effects achieved with brain derived neurotrophic factor, a well-established growth factor enhancing growth cone area.[37]

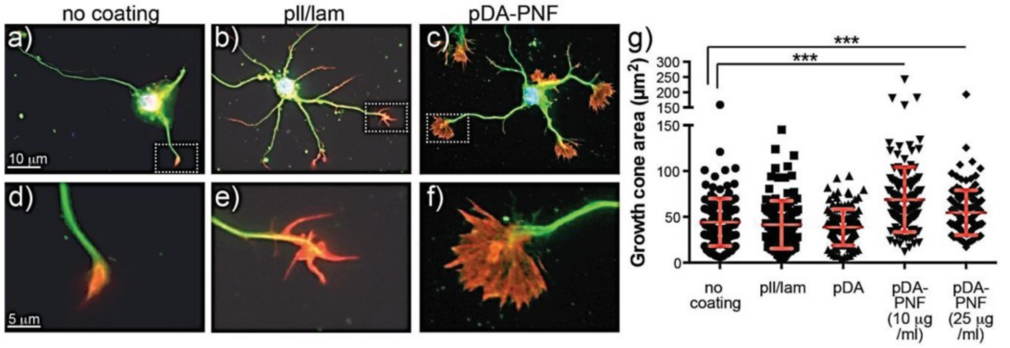

Figure 5. Mouse primary hippocampal neurons were plated on indicated substrates, followed by labeling for microtubules (green) and F-actin (red); the latter is used to label growth cones. a,d) Growth cone area of neurons plated on glass only (no coating) was comparable to b,e) neurons grown on coverslips coated with pll/lam. c,f) By contrast, the growth cone area of neurons cultured on pDA-PNF was enhanced as was the number of finger-like filopodia. (d–f) are higher magnifications of dashed areas in (a–c). g) The growth cone area was quantified for the indicated conditions in at least three independent experiments. Two-way ANOVA was performed. Each circle, square, or triangle reflects a single growth cone. **: $p \leq 0.01$; ***: $p \leq 0.001$.

Thus, our results show that the beneficial effects of PNFs were retained after pDA coating yielding bioactive pDA-PNF hybrid nanostructures with clear beneficial effects on cellular attachment, nerve fiber growth, and growth cone morphology of primary mouse neurons and thus provide attractive potential for neural tissue engineering and repair.

3. Conclusions

We have demonstrated that PNFs obtained from the 8-mer peptide sequence *KIKIQIII* enhance the auto-oxidative polymerization of DA, resulting in catalyzed pDA formation in the presence of PNFs. Our results from concentration dependent measurements of the initial polymerization rate and the inhibited binding of an amyloid-specific dye indicate that binding sites on the PNF surface play a significant role in the formation of pDA-PNFs that are dispersible in aqueous solutions. Most likely, pDA monolayers were formed on the PNF surface and introduced catechol moieties that are accessible and could be modified in a pH-responsive polymer analog reaction. In a proof-of-concept study, we have demonstrated the selective chemical modification of pDA-coated PNF nanostructures with a boronic acid functionalized reporter chromophore. In addition to fluorescent reporter molecules, the approach may also allow for the modulation of material–cell interaction through the dynamic display of bioactive groups on the surface of the hybrid fibers. Furthermore, the pDA-coatings did not affect the biological properties of the nanostructures most likely due to the formation of an ultrathin pDA layer.

The water-dispersible pDA-PNF hybrids were easily coated onto substrates and provide many attractive features such as the attachment and nerve fiber growth of mouse primary cerebellar and hippocampal neurons, which were comparable to the PNF backbone. Due to the unique opportunities for functionalization, we envision further optimizing pDA-PNFs application as potent nerve growth stimulating factors in neural tissue engineering or as coatings of neural implants, for example, during repair strategies in the injured nervous system.

4. Experimental Section

Preparation of KIKIQIII Fibers and pDA-coated PNFs: Purified *KIKIQIII* peptide was dissolved in DMSO to yield a 10.3×10^{-3} M stock solution ($c = 10$ mg mL^{-1}) which was stored at −20 °C prior to usage. To initiate fiber formation, the stock solution was diluted tenfold in 100×10^{-3} M KCl. The dispersed peptide was incubated for at least 18 h to ensure complete fiber formation.

For DA coating experiments, the preformed PNFs were further diluted with 10×10^{-3} M Tris buffer (pH 8.5) to the concentrations as indicated in the main text. A 5.3×10^{-3} M dopamine hydrochloride stock solution in demineralized water was added to the PNFs and incubated for several hours as indicated in the main text. Aliquots were taken and supplemented with 10 vol% 1 N HCl to stop the polymerization process in time dependent measurements.

The preformed PNFs and the DA stock solution were freshly prepared prior to all experiments. A dilution scheme also including the control samples is shown in Scheme S2 of the Supporting Information.

FT-IR Spectroscopy: ATR-FT-IR spectra were recorded of lyophilized sample powders of PNF, pDA, and pDA-PNF at ambient temperature using a Bruker Tensor 27 spectrometer equipped with a diamond crystal as ATR element (PIKE Miracle) with a spectral resolution of 2 cm^{-1}. An FT-IR spectrum of PNFs was furthermore obtained of lyophilized sample which was used to form a KBr pellet. The spectrum was recorded on an IFS 113v FT-IR spectrometer (Bruker) with a spectral resolution of 2 cm^{-1}. The exact compositions for all samples are given in Table S1 of the Supporting Information.

Zetasizer Measurements: The electrophoretic mobility of pDA-PNFs, *KIKIQIII* PNFs, and pDA was measured to enable comparisons of surface charge changes upon coating of the material. 50 µL of sample solutions (prepared according to Table S1, Supporting Information) were diluted in 950 µL of 1×10^{-3} M KCl-solution. The buffer was freshly prepared and filtered (pore size 0.22 µm, Merck) prior to the experiment. The sample dispersions were introduced into separate 1 mL disposable folded capillary cells (Zetasizer Nano series, Malvern) to avoid cross contamination between samples and their electrophoretic mobility was recorded on a Zetasizer Nano ZS (Malvern Instruments) at ambient temperature. The mobility was converted to corresponding ζ-potential values by processing the data with the Zetasizer Nano ZS Software (V7.12). The ζ-potential was calculated by the mean value achieved of three independent measurements à 20 runs.

TEM: TEM images were taken from aliquots of PNF and pDA-PNF-hybrid samples (prepared as described in Table S1, Supporting Information). 5 µL of each sample were deposited on copper grids which were coated with a thin electron-transparent Formvar-layer and were freshly etched with oxygen plasma. After 5 min incubation time, excess sample solution was removed with filter paper and the copper grid was further incubated for 5 min in 2% uranyl acetate solution to enhance sample contrast. After staining, the samples were washed three times in MilliQ-water, dried in air, and images were taken in high vacuum with an EM 109 transmission electron microscope (Zeiss) at an acceleration voltage of 80 kV. Pictures were processed with the EM109 microscope software ImageSP V1.2.6.22.

AFM: AFM measurements were conducted with aliquots of pDA, PNF, and pDA-PNF samples (Table S1, Supporting Information) deposited on freshly etched bare mica substrates. The preparation of the mica AFM samples was realized at ambient temperature by deposition of a 10 µL aliquot of the fully concentrated solution for 1 min. Then the sample was rinsed with ultrapure water and dried with a gentle flow of nitrogen.

In amplitude modulation AFM (AM-AFM), the tip is excited with a fixed amplitude by an external force. The tip's interaction with the sample changes its motion and causes a difference between the initial and the final tip amplitude, which results in a phase shift. Such phase changes reflect the dissipated energy during sample–tip interaction. By recording the phase difference, AM-AFM phase images were created simultaneously to morphology maps. High phase changes represent a strong tip–sample interaction and strong interaction force can lead to sample deformation by the tip, while low phase change represent weak tip–sample interaction.

AFM measurements of PNF (Figures S2a and S6a, Supporting Information) and pDA-PNF sample (Figure 3a; Figure S6c, Supporting Information) were performed in air and high-resolution images (1024×1024 pixels) were collected using an NX10 atomic force microscopy (Park Systems, South Korea) in ambient conditions and in noncontact AM mode. Square areas of 3×3 µm^2 and 6×6 µm^2 were imaged. All measurements were performed using cantilevers (PPP-NCHR, Park Systems, South Korea) with a resonance frequency of 330 kHz and a typical radius of curvature of 8 nm. In order to compare the height of different samples consistently, standardized experimental scanning conditions were established and a regime of phase change was maintained in the order of ≈Δ20°. Raw images were flattened with the XEI software (Park System, South Korea). For consistent comparison of the samples in further statistical analysis, all images were processed with the same parameters. First, images were flattened by a plane and then line by line at a 1st regression order. Then, the maximum height profile of single fibrillar structures was traced using SPIP software (Image Metrology, Denmark). The total experimental error was calculated on the cross-sectional diameter as the sum of the standard deviation, the average roughness of the sample (≈0.05 nm) and the electrical noise of the AFM (≈0.03 nm). The data were analyzed and histograms were created by means of OriginPro (OriginLab) software.

The pDA sample (Figure S7, Supporting Information) was examined in air in tapping mode with a Multimode-AFM NanoScope (R) IV from Digital Instruments (Veeco Instruments Inc.) using cantilevers (Bruker OLTESPA-R3) with a resonance frequency of 70 kHz cantilever (2 N m^{-1}). High-resolution images (1024×1024 pixels) were processed using Gwyddion software V.2.47.

Fluorescence and Absorption Measurements: Fluorescence spectra were recorded on an Infinite M1000 PRO microplate reader (Tecan). Sample solutions were prepared with pDA-PNFs, *KIKIQIII* PNFs, pDA, and solvent only (Table S1, Supporting Information), respectively. 9 µL of sample aliquots were placed in black UV Star 384 microtiter well-plates (Greiner bio-one). A ProteoStat solution was prepared according to manufacturers' protocol and diluted tenfold in PBS. After addition of 1 µL of ProteoStat solution to all samples and 10 min incubation time, the fluorescence emission was recorded at 610 nm upon excitation at 550 nm. Absorption measurements were performed on the same instrument using transparent 384 microtiter well-plates (Greiner bio-one).

Modification of pDA-PNFs with Boronic Acid Dye BA-Rho: Glass coverslips (13 mm) were placed in 24-well plates (Falcon Tissue Culture Plate, flat bottom) and 75 µL of tenfold diluted pDA-PNFs, pDA, or PNFs (prepared according to Table S1, Supporting Information) were immobilized on glass via drop casting. After drying overnight, 150 µL of 4×10^{-9} M BA-Rho in PBS buffer at pH 7.4 were added to each well. Glass without any deposited material served as reference. The solution was incubated for 30 min, thereafter the surface was washed three times with PBS buffer. 75 µL of PBS solution at pH 7.4 was incubated for 10 min and the supernatant was removed and analyzed via fluorescence spectroscopy and microscopy. Absorbance and emission spectra were recorded on an Infinite M1000 PRO microplate reader (Tecan) between 575 and 650 nm. The fluorescence was detected upon excitation at 565 nm. For the release of the dye, the coated glass was treated 30 min with 75 µL of a PBS buffer at pH 3.0. The supernatant solution and the glass were analyzed likewise with fluorescence spectroscopy. Microscopy images were collected after each step for all samples with a 10× objective on a Zeiss fluorescence microscope (Axiovert 200M) with bright field and Texas Red filter settings on an AxioCam MRm camera (Zeiss). All images were recorded with 500 ms exposure time and for comparisons all brightness and contrast settings were adjusted to the same values.

Mouse Primary Neurons: Mouse primary cerebellar neurons were prepared from 5 d old (P3–P5) C57/Bl6 wild type mice as described in the literature.[35] Hippocampal neurons were derived from P1–P3 old pups. Coverslips for the positive control were coated with 100 µg mL^{-1} poly-L-lysine for 1 h at 37 °C and thereafter with 20 µg mL^{-1} laminin overnight at 37 °C. Coverslips (13 mm in diameter) were coated by evenly distributing 50 µL of pDA-PNFs or pDA as control (concentrations given in Figure 4) on the cover slip and air-dried at room temperature overnight under sterile conditions. Before seeding cells, all coverslips were incubated in DMEM/10%HS for 30 min at 37 °C. DMEM/10%HS was then replaced by NMEM/B27 cell culture medium (with Gentamycin at 1:2000) and 8×10^3 primary cerebellar or hippocampal neurons plated on each cover slip. Cells were fixed after 72 h in culture for 15 min in 4% PFA/5% Sucrose/PBS, permeabilized for 5 min in 0.1% Triton-X-100/PBS, and blocked for 30 min in 2% BSA/PBS. The primary antibody against class III β-tubulin (1:1000; Covance) was incubated overnight at 4 °C. The primary antibody was detected with an Alexa488 conjugated secondary antibody (1:1500; Molecular Probes). Cell nuclei were labeled with DAPI and F-actin was stained with phalloidin conjugated to TexasRed.

All experiments were in accordance with institutional regulations by the local animal ethical committee (Regierungspräsidium Tübingen, Germany).

Statistical Analysis: For neuronal growth assays, entire coverslips were recorded with a 4× objective on a Keyence fluorescence microscope (BZ-X700). Quantification of numbers of attached cells, nerve fiber length, and growth cone area was performed with Image-Pro Plus (Media Cybernatics; version 6.0.0260) or the NeuriteTracer plug-in of the ImageJ software.[38] The plug-in analyzes fluorescence microscopy images of neurites and nuclei of primary neurons. Employing user-defined thresholds, the plug-in counts neuronal nuclei, and traces and measures neurite length. The average neurite length was calculated automatically as a ratio of the entire neurite length of all neurons on a coverslip and the total number of DAPI-positive cells present on the coverslip. Neurons were identified by class III β-tubulin immunoreactivity. Growth cones were identified by F-actin localization by ImagePro Plus software. Statistical significance was calculated using Prism6 software with two-way ANOVA multiple comparison tests with *, **, *** indicating $p \leq 0.05$, 0.01, and 0.001, respectively. Data are displayed as mean ± SD. *N* numbers are indicated in the figure legends to Figures 4 and 5 and at least ≥3 independent cultures were performed for each condition.

Statistical analysis of the height data obtained from AFM measurements was performed with OriginPro Software using an unpaired two samples Student's *t*-test; $^{*}p < 0.05$, $^{**}p < 0.01$, $^{***}p < 0.001$; ($n \leq 100$).

Supporting Information

Supporting Information is available from the Wiley Online Library or from the author.

Acknowledgements

The authors acknowledge the funding through the BMBF project "Selekomm" within the Biotechologie 2020+ initiative, the Carl-Zeiss foundation (CM), the Volkswagen foundation 91965 (T.W., C.M., S.S., and L.P.), and the Marie Curie International Training Network Protein Conjugates (T.W. and T.P.J.K.). B.K. was supported by the DFG (Deutsche Forschungsgemeinschaft) through SFB1149, the Schram, the Paul und Marlene Hepp-Stiftung, the Gemeinnützige Hertie Foundation, and by a research grant from an Uni Ulm – Bundeswehrkrankenhaus Ulm research initiative (Zivil-Militärischen Verbund Regenerative Medizin). C.V.S. gratefully acknowledges support from the Humboldt Foundation through a Feodor-Lynen Return Fellowship. T.P.J.K. and F.S.R. thank SNF (Swiss National Foundation for Science) for the financial support (Grant Nos. P2ELP2_162116 and P300P2_171219).

Conflict of Interest

The authors declare no conflict of interest.

Keywords

amyloid fibers, hybrid nanomaterial, neuronal growth, peptide nanofibers, polydopamine coating

Received: December 21, 2017
Revised: February 14, 2018

[1] D. J. Selkoe, J. Hardy, *EMBO Mol. Med.* **2016**, *8*, 595.
[2] D. M. Fowler, A. V. Koulov, C. Alory-Jost, M. S. Marks, W. E. Balch, J. W. Kelly, *PLoS Biol.* **2005**, *4*, e6.
[3] S. K. Maji, M. H. Perrin, M. R. Sawaya, S. Jessberger, K. Vadodaria, R. A. Rissman, P. S. Singru, K. P. R. Nilsson, R. Simon, D. Schubert, D. Eisenberg, J. Rivier, P. Sawchenko, W. Vale, R. Riek, *Science* **2009**, *325*, 328.
[4] a) I. W. Hamley, *Angew. Chem. Int. Ed.* **2007**, *46*, 8128; b) G. Wei, Z. Su, N. P. Reynolds, P. Arosio, I. W. Hamley, E. Gazit, R. Mezzenga, *Chem. Soc. Rev.* **2017**, *46*, 4661.
[5] C. Meier, I. Lifincev, M. E. Welland, *Biomacromolecules* **2015**, *16*, 558.
[6] a) J. Boekhoven, S. I. Stupp, *Adv. Mater.* **2014**, *26*, 1642; b) R. S. Jacob, D. Ghosh, P. K. Singh, S. K. Basu, N. N. Jha, S. Das, P. K. Sukul, S. Patil, S. Sathaye, A. Kumar, A. Chowdhury, S. Malik, S. Sen, S. K. Maji, *Biomaterials* **2015**, *54*, 97; c) G. A. Silva, C. Czeisler, K. L. Niece, E. Beniash, D. A. Harrington, J. A. Kessler, S. I. Stupp, *Science* **2004**, *303*, 1352.
[7] U. Shimanovich, I. Efimov, T. O. Mason, P. Flagmeier, A. K. Buell, A. Gedanken, S. Linse, K. S. Åkerfeldt, C. M. Dobson, D. A. Weitz, T. P. J. Knowles, *ACS Nano* **2015**, *9*, 43.
[8] R. Langer, D. A. Tirrell, *Nature* **2004**, *428*, 487.
[9] R. Pugliese, F. Gelain, *Trends Biotechnol.* **2017**, *35*, 145.
[10] S. Das, K. Zhou, D. Ghosh, N. N. Jha, P. K. Singh, R. S. Jacob, C. C. Bernard, D. I. Finkelstein, J. S. Forsythe, S. K. Maji, *NPG Asia Mater.* **2016**, *8*, e304.
[11] J. M. Pawelek, A. M. Körner, *Am. Sci.* **1982**, *70*, 136.
[12] Y. Tokura, S. Harvey, C. Chen, Y. Wu, D. Y. W. Ng, T. Weil, *Angew. Chem., Int. Ed.* **2018**, *57*, 1587.
[13] a) H. Lee, S. M. Dellatore, W. M. Miller, P. B. Messersmith, *Science* **2007**, *318*, 426; b) Y. Liu, K. Ai, L. Lu, *Chem. Rev.* **2014**, *114*, 5057.
[14] a) N. F. Della Vecchia, R. Avolio, M. Alfè, M. E. Errico, A. Napolitano, M. d'Ischia, *Adv. Funct. Mater.* **2013**, *23*, 1331; b) D. R. Dreyer, D. J. Miller, B. D. Freeman, D. R. Paul, C. W. Bielawski, *Langmuir* **2012**, *28*, 6428; c) S. Hong, Y. S. Na, S. Choi, I. T. Song, W. Y. Kim, H. Lee, *Adv. Funct. Mater.* **2012**, *22*, 4711; d) J. Liebscher, R. Mrówczyński, H. A. Scheidt, C. Filip, N. D. Hădade, R. Turcu, A. Bende, S. Beck, *Langmuir* **2013**, *29*, 10539.
[15] a) H. Lee, J. Rho, P. B. Messersmith, *Adv. Mater.* **2009**, *21*, 431; b) L. He, D. E. Fullenkamp, J. G. Rivera, P. B. Messersmith, *Chem. Commun.* **2011**, *47*, 7497; c) M. Krogsgaard, V. Nue, H. Birkedal, *Chem. - Eur. J.* **2016**, *22*, 844.
[16] a) Z. Yang, Q. Tu, Y. Zhu, R. Luo, X. Li, Y. Xie, M. F. Maitz, J. Wang, N. Huang, *Adv. Healthcare Mater.* **2012**, *1*, 548; b) J. Sobocinski, W. Laure, M. Taha, E. Courcot, F. Chai, N. Simon, A. Addad, B. Martel, S. Haulon, P. Woisel, N. Blanchemain, J. Lyskawa, *ACS Appl. Mater. Interfaces* **2014**, *6*, 3575.
[17] a) K. Kang, I. S. Choi, Y. Nam, *Biomaterials* **2011**, *32*, 6374; b) K. Kang, S. Lee, R. Kim, I. S. Choi, Y. Nam, *Angew. Chem., Int. Ed.* **2012**, *51*, 13101; c) W. C. Low, P.-O. Rujitanaroj, D.-K. Lee, P. B. Messersmith, L. W. Stanton, E. Goh, S. Y. Chew, *Biomaterials* **2013**, *34*, 3581.
[18] K. Yang, J. S. Lee, J. Kim, Y. B. Lee, H. Shin, S. H. Um, J. B. Kim, K. I. Park, H. Lee, S.-W. Cho, *Biomaterials* **2012**, *33*, 6952.
[19] N. R. Lee, C. J. Bowerman, B. L. Nilsson, *Biomacromolecules* **2013**, *14*, 3267.
[20] D. Shen, J. Coleman, E. Chan, T. P. Nicholson, L. Dai, P. W. Sheppard, W. F. Patton, *Cell Biochem. Biophys.* **2011**, *60*, 173.
[21] E. Cerf, R. Sarroukh, S. Tamamizu-Kato, L. Breydo, S. Derclaye, Yves F. Dufrêne, V. Narayanaswami, E. Goormaghtigh, J.-M. Ruysschaert, V. Raussens, *Biochem. J.* **2009**, *421*, 415.
[22] A. Natalello, A. M. Frana, A. Relini, A. Apicella, G. Invernizzi, C. Casari, A. Gliozzi, S. M. Doglia, P. Tortora, M. E. Regonesi, *PLoS One* **2011**, *6*, 1.
[23] a) H.-j. Cho, S. K. Madhurakkat Perikamana, J.-h. Lee, J. Lee, K.-M. Lee, C. S. Shin, H. Shin, *ACS Appl. Mater. Interfaces* **2014**, *6*, 11225; b) J. Jiang, J. Xie, B. Ma, D. E. Bartlett, A. Xu, C. H. Wang, *Acta Biomater.* **2014**, *10*, 1324; c) N. G. Rim, S. J. Kim, Y. M. Shin, I. Jun, D. W. Lim, J. H. Park, H. Shin, *Colloids Surf., B* **2012**, *91*, 189; d) J. Xie, P. L. Michael, S. Zhong, B. Ma, M. R. MacEwan, C. T. Lim, *J. Biomed. Mater. Res., Part A* **2012**, *100A*, 929; e) H. Yang, Y. Lan, W. Zhu, W. Li, D. Xu, J. Cui, D. Shen, G. Li, *J. Mater. Chem.* **2012**, *22*, 16994.
[24] Q. Zhou, X. Liu, Y. Tian, M. Wu, Z. Niu, *Langmuir* **2017**, *33*, 9866.
[25] J. Ryu, S. H. Ku, M. Lee, C. B. Park, *Soft Matter* **2011**, *7*, 7201.
[26] M. Bisaglia, S. Mammi, L. Bubacco, *J. Biol. Chem.* **2007**, *282*, 15597.
[27] R. A. Zangmeister, T. A. Morris, M. J. Tarlov, *Langmuir* **2013**, *29*, 8619.
[28] R. Silverstein, F. Webster, D. Kiemle, *Spectrometric Identification of Organic Compounds*, John Wiley & Sons, New York **1981**.
[29] A. Chassepot, V. Ball, *J. Colloid Interface Sci.* **2014**, *414*, 97.
[30] K. A. Günay, P. Theato, H.-A. Klok, *J. Polym. Sci., Part A: Polym. Chem.* **2013**, *51*, 1.
[31] D. Y. W. Ng, M. Arzt, Y. Wu, S. L. Kuan, M. Lamla, T. Weil, *Angew. Chem., Int. Ed.* **2014**, *53*, 324.
[32] a) J. Adams, M. Behnke, S. Chen, A. A. Cruickshank, L. R. Dick, L. Grenier, J. M. Klunder, Y.-T. Ma, L. Plamondon, R. L. Stein, *Bioorg.*

Med. Chem. Lett. **1998**, *8*, 333; b) K. Knott, J. Fishovitz, S. B. Thorpe, I. Lee, W. L. Santos, *Org. Biomol. Chem.* **2010**, *8*, 3451.

[33] C. Seidler, D. Y. W. Ng, T. Weil, *Tetrahedron* **2017**, *73*, 4979.

[34] a) C. J. Bettinger, J. P. Bruggeman, A. Misra, J. T. Borenstein, R. Langer, *Biomaterials* **2009**, *30*, 3050; b) S. H. Bhang, S.-H. Kwon, S. Lee, G. C. Kim, A. M. Han, Y. H. K. Kwon, B.-S. Kim, *Biochem. Biophys. Res. Commun.* **2013**, *430*, 1294.

[35] B. Knöll, O. Kretz, C. Fiedler, S. Alberti, G. Schütz, M. Frotscher, A. Nordheim, *Nat. Neurosci.* **2006**, *9*, 195.

[36] F. Bradke, J. W. Fawcett, M. E. Spira, *Nat. Rev. Neurosci.* **2012**, *13*, 183.

[37] C. Meier, S. Anastasiadou, B. Knöll, *PLoS One* **2011**, *6*, 1.

[38] M. Pool, J. Thiemann, A. Bar-Or, A. E. Fournier, *J. Neurosci. Methods* **2008**, *168*, 134.

ADVANCED HEALTHCARE MATERIALS

Supporting Information

for *Adv. Healthcare Mater.,* DOI: 10.1002/adhm.201701485

Water-Dispersible Polydopamine-Coated Nanofibers for Stimulation of Neuronal Growth and Adhesion

Stefanie Sieste, Thomas Mack, Christopher V. Synatschke, Corinna Schilling, Christopher Meyer zu Reckendorf, Laura Pendi, Sean Harvey, Francesco S. Ruggeri, Tuomas P. J. Knowles, Christoph Meier, David Y. W. Ng, Tanja Weil, and Bernd Knöll**

Supporting Information

Water-Dispersible Polydopamine-Coated Nanofibers for Stimulation of Neuronal Growth and Adhesion

Stefanie Sieste,[a,c] Thomas Mack,[a,c] Christopher V. Synatschke,[c] Corinna Schilling,[b] Christopher Meyer zu Reckendorf,[b] Laura Pendi,[a] Sean Harvey,[a,c] Francesco Simone Ruggeri,[d] Tuomas P. J. Knowles,[d] Christoph Meier,[a] David Y. W. Ng,[a,c] Tanja Weil,[a,c,] Bernd Knöll [b,*]*

[a] Institute of Organic Chemistry III/Macromolecular Chemistry,
Ulm University,
Albert-Einstein-Allee 11,
89081 Ulm,
Germany

[b] Institute of Physiological Chemistry,
Ulm University,
Albert-Einstein-Allee 11,
89081 Ulm,
Germany

[c] Department Synthesis of Macromolecules,
Max Planck Institute for Polymer Research,
Mainz,
Ackermannweg 10,
55128 Mainz,
Germany

[d] Department of Chemistry,
University of Cambridge,
Cambridge,
Lensfield Road,
CB2 1EW Cambridge,
United Kingdom

* Correspondence should be addressed to
Prof. Dr. Bernd Knöll (bernd.knoell@uni-ulm.de)
or Prof. Dr. Tanja Weil (weil@mpip-mainz.mpg.de)

Synthesis

a) Chemicals

Protected amino acids, *O*-(1H-benzotriazole-1-yl)-*N*,*N*,*N*',*N*'-tetramethyluronium-hexafluorophosphate (HBTU), and preloaded Wang resin were purchased from Merck Novabiochem (Darmstadt, Germany) and used as received. *N*,*N*-dimethylformamide (DMF, peptide synthesis grade), *N*,*N*'-diisopropylethylamine (DIEA), Triisopropylsilane (TIS), acetonitrile (ACN, HPLC grade) and Methanol (MeOH) were purchased from VWR Prolabo (Darmstadt, Germany). Piperidine and trifluoracetic acid (TFA) were purchased from Merck Suchardt (Darmstadt, Germany). The Proteostat® Protein Aggregation Assay kit was received from Enzo Life Sciences (Lörrach, Germany). Dichloromethane (DCM) and all other chemicals were purchased from Sigma-Aldrich and used as received. Water was processed by a Millipore purification system.

b) Synthesis of KIKIQIII

The peptide was synthesized according to standard Fmoc solid-phase peptide synthesis on a microwave-assisted peptide synthesizer (Liberty I, CEM) on a 0.1 mM scale. The *C* to *N* terminal coupling was achieved by using a Wang resin preloaded with Fmoc-Isoleucin. Fmoc-deprotection reactions were carried out with DMF solutions containing 20% v/v piperidine. Coupling reactions with 5 eq. Fmoc-protected amino acid solutions in DMF were catalyzed by addition of 5 eq. HBTU and 10 eq. DIEA. Cleavage off the resin and final deprotection of the side chains were carried out by addition of a mixture of TFA, TIS and H_2O at a ratio of 95:2.5:2.5 by shaking at RT for 2 h. The cleaved peptide was precipitated in cold diethyl ether, lyophilized and purified via HPLC (Shimadzu) on a reversed phase C18 column (LiChrospher, Merck) with a binary gradient of ACN and H_2O supplemented with 0.1% TFA. The final product was analyzed with MALDI ToF mass spectrometry (Bruker Reflex III, **Figure S1**).

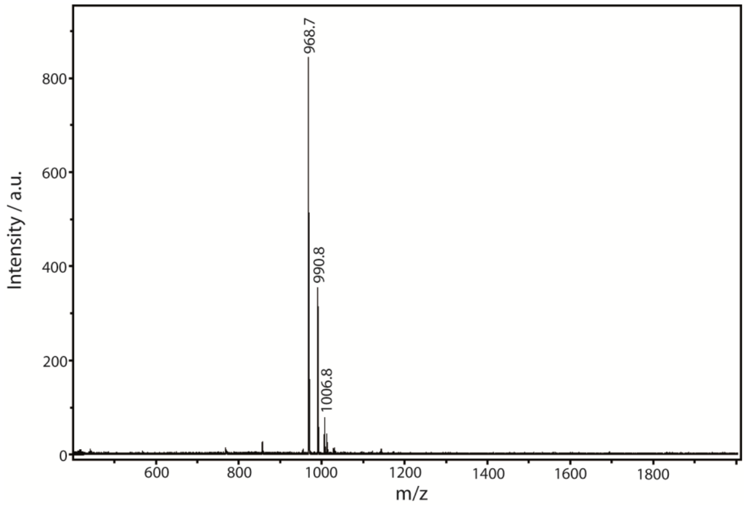

Figure S1. MALDI-ToF mass spectrum of *KIKIQIII* peptide. Measurements were carried out on a Bruker Reflex III matrix assisted laser desorption/ionization time of flight (MALDI-ToF) mass spectrometer. 4-Hydroxy-α-cyano-cinnaminic acid was used as matrix. *m/z*: calculated for *KIKIQIII* $[M+H]^+ = 968.3$, $[M+Na]^+ = 990.3$, $[M+K]^+ = 1006.3$; found 968.7 $[M+H]^+$, 990.8 $[M+Na]^+$, 1006.8 $[M+K]^+$.

c) *Synthesis of boronic acid modified sulforhodamine (BA-Rho)*

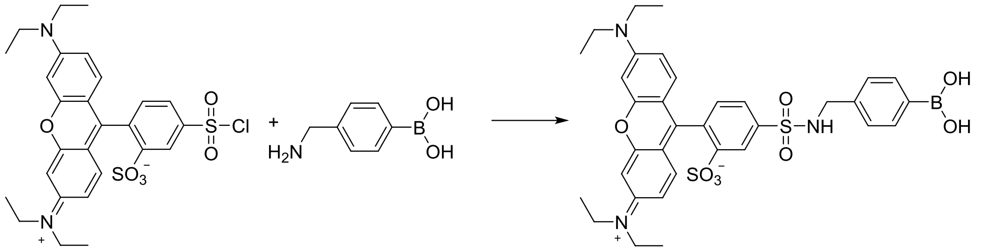

Scheme S1. Synthesis scheme of boronic acid modified sulforhodamine B (BA-Rho).

DIEA (31.7 µL, 0.182 mmol) was added to a solution of 4-aminomethylphenyl boronic acid hydrochloride (17.9 mg, 0.095 mmol) in 4 mL anhydrous DMF. Subsequently, Lissamine Rhodamine B sulfonylchloride (50 mg, 0.087 mmol) was added and stirred overnight at room temperature. The solvent was evaporated under reduced pressure and the crude product was purified using column chromatography (15% MeOH/DCM) to obtain violet BA-Rho in 61% yield.

^{1}H NMR (400 MHz, Bruker Avance 400, $CDCl_3$, δ): 8.55 (t, 1 H, ^3J = 6.0 Hz), 8.44 (m, 1 H, H_{Aryl}), 8.06 (br s, 2 H), 7.87 (m, 1 H, H_{Aryl}), 7.71 (m, 2 H), 7.38 (d, 1 H, ^3J = 8.0 Hz, H_{Aryl}), 7.20 (m, 2 H), 7.04 (m, 2 H, H_{Aryl}), 6.92 (m, 4 H, H_{Aryl}), 4.16 (d, 2 H, ^3J = 6.0 Hz), 3.64 (m, 8 H), 1.21 (t, 12 H, J = 7.2 Hz).

LC-MS (ESI) *m/z*: [$M+H^+$] calculated. for $C_{34}H_{38}BN_3O_8S_2$: 691; found 674 $[M-OH]^+$.

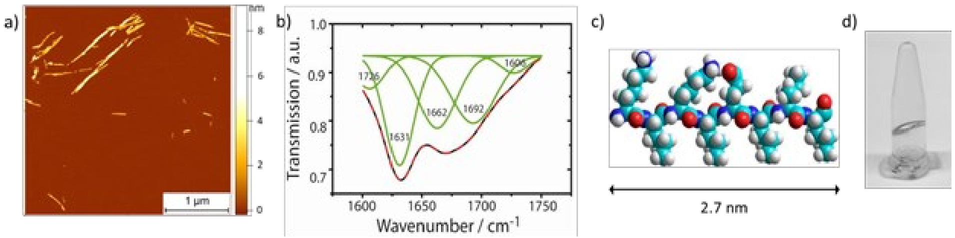

Figure S2. a) AFM measurements of 0.5 mM PNFs performed in air at ambient conditions and in non-contact AM mode. Scalebar represents 1 µm and Z scale is in nm. b) FT-IR spectrum of *KIKIQIII* PNFs and five Gauss functions (green) fitted to identify hidden peaks. The reconstructed spectrum from the fit (red dashed) corresponds to the measured spectrum (black dash). The PNFs were lyophilized, and the resulting solid was used to form a KBr pellet. The spectrum was recorded on a Bruker IFS 113v FT-IR spectrometer. c) Geometry optimized model of the *KIKIQIII* peptide in the beta-sheet conformation, Molecular Mechanics with Bio+(CHARMM) model as implemented in the HyperChem7 software, steepest gradient algorithm and an RMS gradient of 0.1 kcal Å-1 mol-1 in vacuo, E = 115 kcal/mol. The length of the peptide in the beta-sheet conformation was measured to 2.7 nm. d) A photograph of 1000 µL inverted PNF sample tube indicates significant viscosity increase at 2 mg/mL peptide concentration causing the sample to gelate.

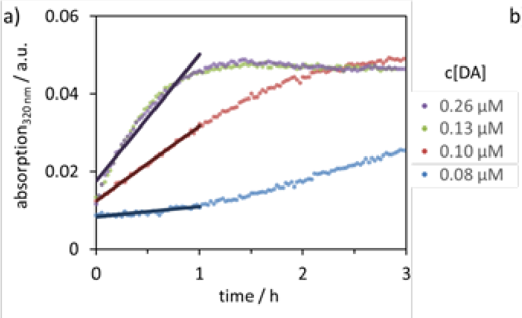

b) v_0 as a function of c[DA] with 0.5 mM PNFs.

c[DA]		linear regression$^{(t = 0 - 1h)}$	
µg/mL	µM	v_0 = slope [h^{-1}]	R²
16	0.08	0.0026 ± 0.0003	0.76
20	0.10	0.0192 ± 0.0002	0.99
25	0.13	0.0326 ± 0.0014	0.95
50	0.26	0.0321 ± 0.0012	0.96

Figure S3. Initial polymerization rates v_0 of DA in the presence and absence of *KIKIQIII* PNFs: a) pDA formation as a function of various [DA] concentrations in the presence of 0.5 mM PNFs in Tris-buffer at pH = 8.5. The absorbance at 320 nm was recorded every 100 seconds during three hours of incubation using an Infinite® M1000 PRO microplate reader (Tecan). The bold lines indicate linear regressions within the first hour of polymerization. b) The initial polymerization rate v_0 was calculated from the slope of the linear regression as a function of dopamine concentration [DA] in the presence of 0.5 mM PNFs.

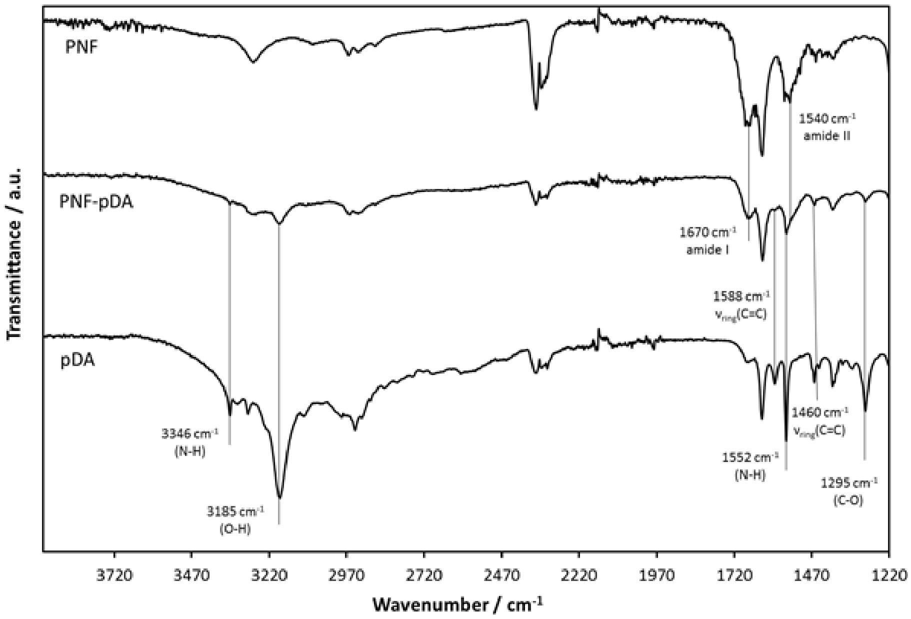

Figure S4. Attenuated Total Reflectance FT-IR spectra of PNFs, pDA-PNFs and pDA measured at ambient temperature using a Bruker Tensor 27 spectrometer equipped with a diamond crystal as ATR element (PIKE Miracle™) with a spectral resolution of 2 cm^{-1}. Selected IR bands are labeled with respective band assignments.

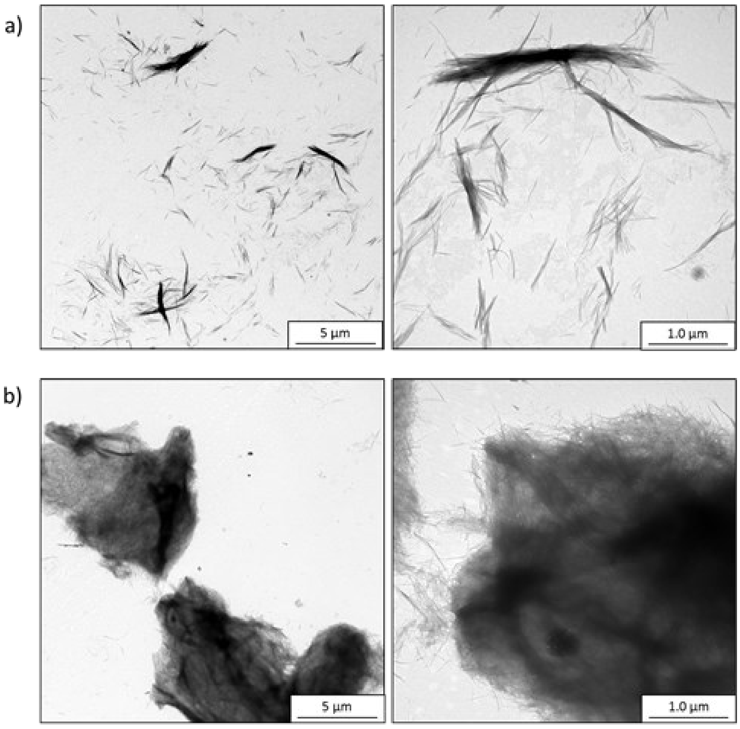

Figure S5. Representative TEM micrographs of a) 0.5 mM PNFs and b) pDA-PNF hybrid material resulting from the polymerization of 0.08 mM DA in the presence of 0.5 mM PNFs. The bundling tendency of the fibers significantly increases upon coating with DA. 5 µL of samples were deposited and freshly etched Formvar-coated copper grids and were stained 1 min with 2% uranyl acetate solution. Scale bars are 5 µm (left) and 1 µm (right), respectively.

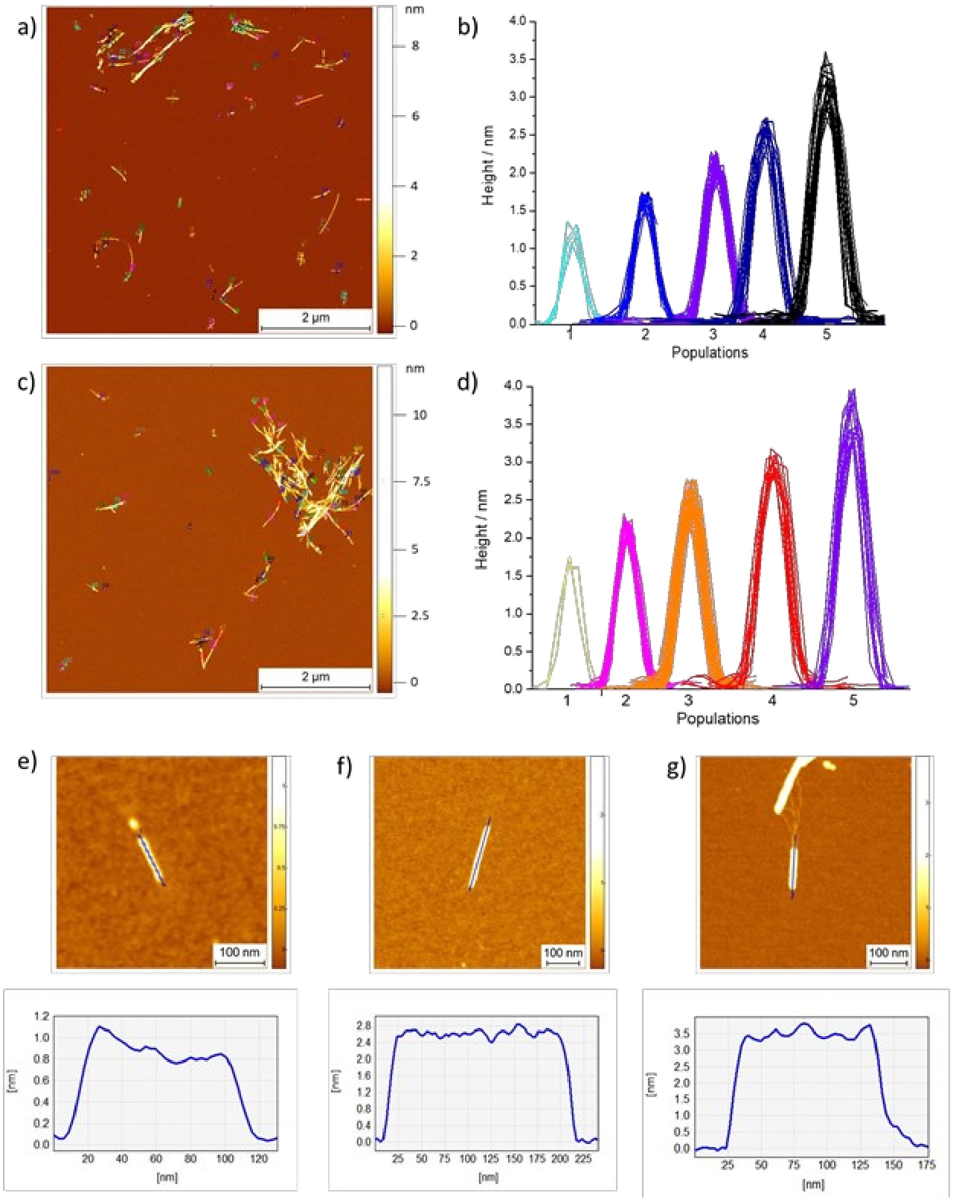

Figure S6. Single fibril statistical analysis of polymorphic fibrils. AFM 3-D morphology maps of a) PNFs and c) pDA-PNF. Measurement of the cross-sectional diameter of all b) PNF and d) pDA-PNFs present in a map show that they occur in populations with different cross-sectional diameter. The distinct differences in height between different polymorphs are illustrated by the longitudinal cross-section of selected PNF fibers e-g).

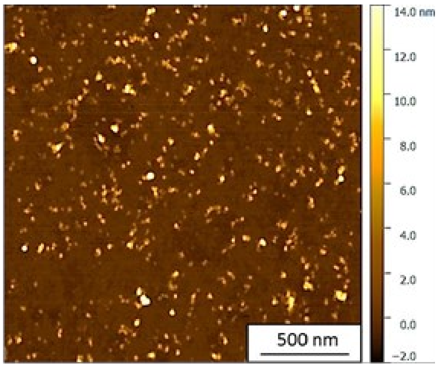

Figure S7. Representative AFM image of 0.08 mM pDA sample synthesized according to **Table S1**. The sample was examined in air in tapping mode with a Multimode-AFM NanoScope (R) IV from Digital Instruments (Veeco Instruments Inc.) using cantilevers with a resonance frequency of 70 kHz cantilever (2 N/m). The image was processed using Gwyddion software V.2.47.

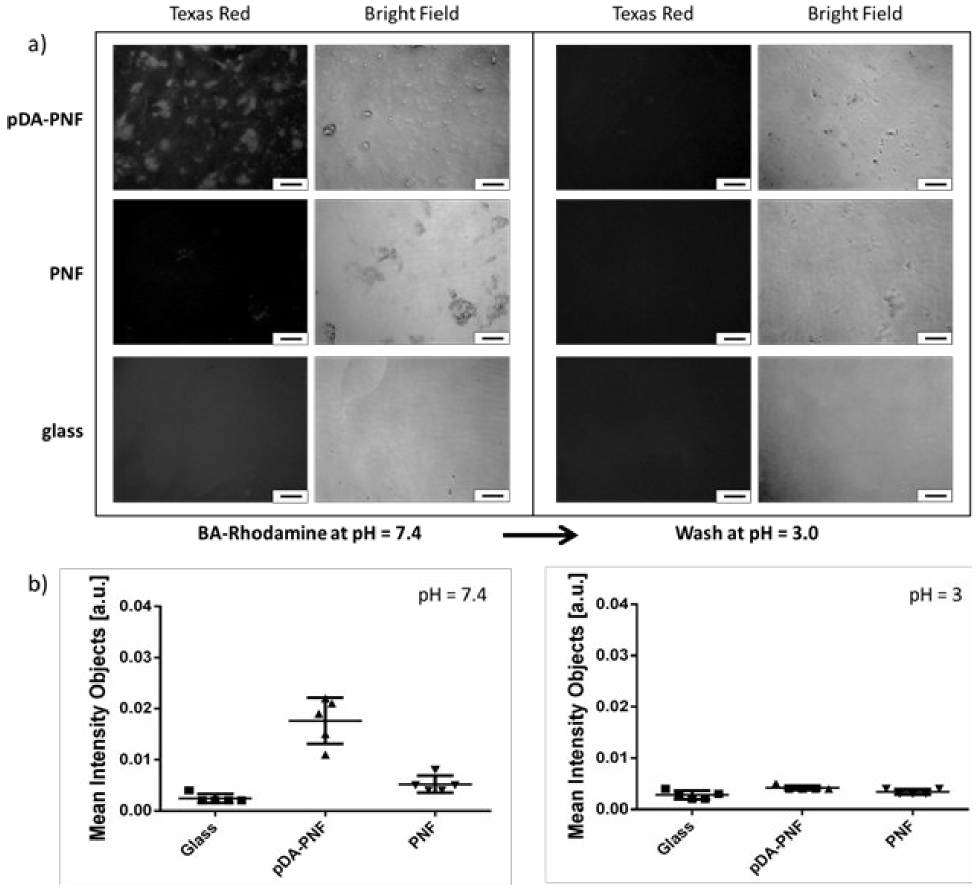

Figure S8. a) Optical and fluorescence microscopy images of the pH-responsive supramolecular polymer analogous reaction after incubation of the PNFs and pDA-PNFs with BA-Rho coated on 13 mm coverslips at pH 7.4 (left) and after incubation at pH 3.0 (right). The absence of fluorescence at pH 3.0 indicates release of the BA-Rho dye. The scalebars represent 100 µm, respectively. b) Quantification of the amount of bound fluorescent dye was obtained from five representative pictures (labeled with triangles or squares) for each condition at pH 7.4 (left) or pH 3.0 (right) for pDA-PNF, PNF and glass which were treated with BA-Rho. The shown evaluation depicts the mean fluorescence intensity of all objects in the size range of 0.001 µm^2 to 0.4 µm^2. The range was set between 17-255 for all objects and calculation was processed with ImageJ.

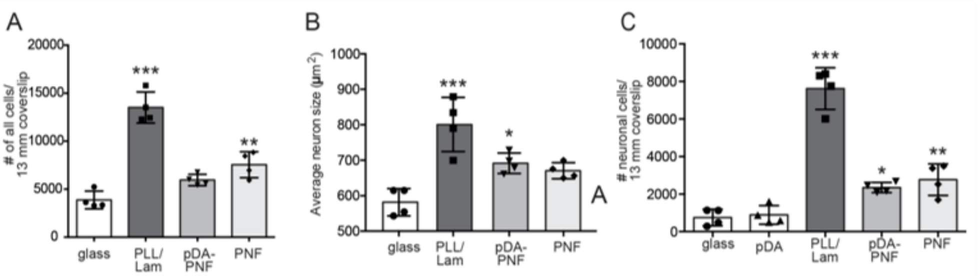

Figure S9. Primary mouse cerebellar neurons were cultured for one day on 13 mm coverslips coated with poly-L-lysine/laminin (PLL/Lam), pDA alone, pDA-PNF (10 µg/ml) or PNF (10 µg/ml). As control we also included no coating ("glass"). Each square, circle or triangle reflects one independent culture derived from one mouse. Statistical significance was calculated with a one-way ANOVA in relation to "glass". No statistical significance was observed between pDA-PNF and PNF. (A) number of all cells (neuronal and non-neuronal) on the entire coverslip is depicted. (B) the average neuron size was calculated by measuring the area (in µm^2) of individual neurons. (C) the number of neurons/coverslip (labeled with the neuron-specific marker βIII tubulin) is depicted.

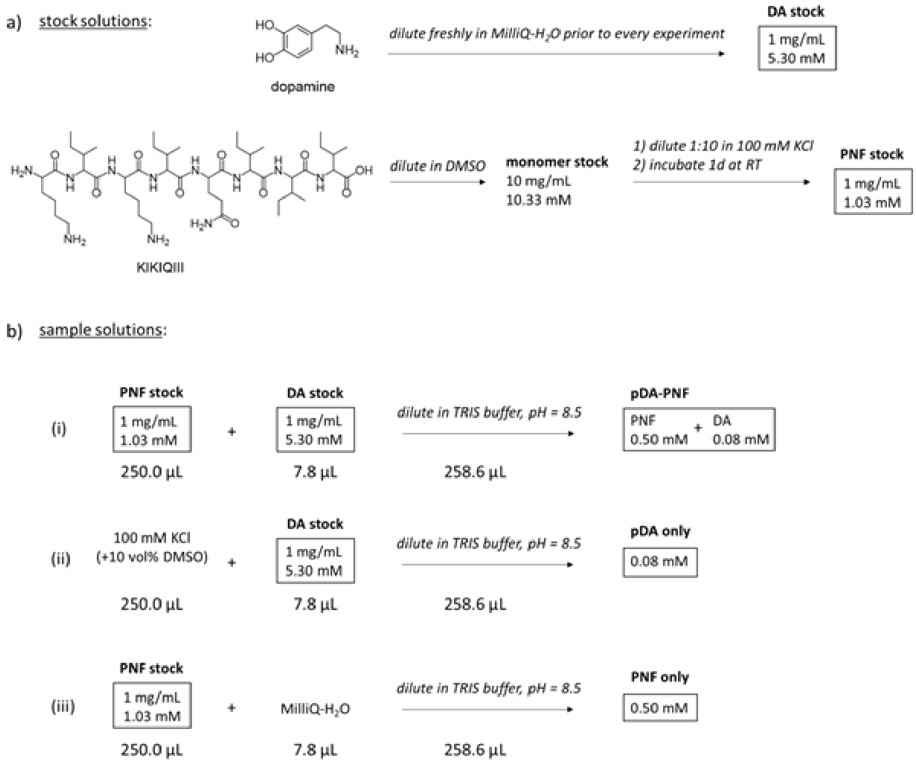

Scheme S2: Dilution scheme to obtain a) stock solutions of DA and PNF which were further used to prepare b) sample solutions of pDA-PNF, pDA and PNF, respectively.

Table S1: Final composition of samples according to **Scheme S2** for FT-IR and fluorescence spectroscopy measurements, TEM and AFM micrographs and analysis of the electrophoretic mobility.

Sample	PNF [mM]	pDA [mM]	Supplements
PNF	0.5	0	3 vol% water in Tris buffer
pDA	0	0.08	10 vol% DMSO in KCl buffer
pDA-PNF	0.5	0.08	-

5.3 Supramolecular Peptide Nanofibrils with Optimized Sequences and Molecular Structures for Efficient Retroviral Transduction

Stefanie Sieste[#], Thomas Mack[#], Edina Lump, Manuel Hayn, Desiree Schütz, Annika Röcker, Christoph Meier, Kübra Kaygisiz, Frank Kirchhoff, Tuomas P. J. Knowles, Francesco S. Ruggeri*, Christopher V. Synatschke*, Jan Münch*, and Tanja Weil*

[#] shared first authorship * corresponding author

Published in Adv. Funct. Mater. 2021, 2009382. DOI: 10.1002/adfm.202009382

Abstract:

Amyloid-like peptide nanofibrils (PNFs) are abundant in nature providing rich bioactivities and playing both functional and pathological roles. The structural features responsible for their unique bioactivities are, however, still elusive. Supramolecular nanostructures are notoriously challenging to optimize, as sequence changes affect self-assembly, fibril morphologies, and biorecognition. Herein, the first sequence optimization of PNFs, derived from the peptide enhancing factor-C (EF-C, QCKIKQIINMWQ), for enhanced retroviral gene transduction via a multiparameter and a multiscale approach is reported. Retroviral gene transfer is the method of choice for the stable delivery of genetic information into cells offering great perspectives for the treatment of genetic disorders. Single fibril imaging, zeta potential, vibrational spectroscopy, and quantitative retroviral transduction assays provide the structure parameters responsible for PNF assembly, fibrils morphology, secondary and quaternary structure, and PNF-virus-cell interactions. Optimized peptide sequences such as the 7-mer, CKFKFQF, have been obtained quantitatively forming supramolecular nanofibrils with high intermolecular β-sheet content that efficiently bind virions and attach to cellular membranes revealing efficient retroviral gene transfer.

Contribution of the respective authors:

Stefanie Sieste: Design, synthesis and characterization of peptide nanofibrils. Writing and correcting of the manuscript. Conduction of laser scanning microscope studies.

Thomas Mack: Design, synthesis and characterization of peptide nanofibrils. Writing and correcting of the manuscript.

Edina Lump: Conduction of infection assays.

Manuel Hayn: Conduction of infection assays.

Desiree Schütz: Conduction of laser scanning microscope studies.

Annika Röcker: Conduction of cell viability studies.

Christoph Meier: Discussion on the concept and results.

Kübra Kaygisiz: Conduction of time-dependent zeta potential measurement. Correcting the manuscript

Frank Kirchhoff: Acquiring funding for the project, design and discussion of the concept and results, correcting the manuscript.

Tuomas P. J. Knowles: Writing and correcting the manuscript.

Francesco S. Ruggeri: Design and discussion of the concept and results, writing and correcting the manuscript. Discussion of the FT-IR studies.

Christopher V. Synatschke: Design and discussion of the concept and results, writing and correcting the manuscript.

Jan Münch: Acquiring funding for the project, design and discussion of the concept and results, writing and correcting the manuscript.

Tanja Weil: Acquiring funding for the project, discussion of the concept and results, writing and correcting the manuscript.

FULL PAPER

ADVANCED FUNCTIONAL MATERIALS
www.afm-journal.de

Supramolecular Peptide Nanofibrils with Optimized Sequences and Molecular Structures for Efficient Retroviral Transduction

Stefanie Sieste, Thomas Mack, Edina Lump, Manuel Hayn, Desiree Schütz, Annika Röcker, Christoph Meier, Kübra Kaygisiz, Frank Kirchhoff, Tuomas P. J. Knowles, Francesco S. Ruggeri, Christopher V. Synatschke,* Jan Münch,* and Tanja Weil**

Amyloid-like peptide nanofibrils (PNFs) are abundant in nature providing rich bioactivities and playing both functional and pathological roles. The structural features responsible for their unique bioactivities are, however, still elusive. Supramolecular nanostructures are notoriously challenging to optimize, as sequence changes affect self-assembly, fibril morphologies, and biorecognition. Herein, the first sequence optimization of PNFs, derived from the peptide enhancing factor-C (EF-C, QCKIKQIINMWQ), for enhanced retroviral gene transduction via a multiparameter and a multiscale approach is reported. Retroviral gene transfer is the method of choice for the stable delivery of genetic information into cells offering great perspectives for the treatment of genetic disorders. Single fibril imaging, zeta potential, vibrational spectroscopy, and quantitative retroviral transduction assays provide the structure parameters responsible for PNF assembly, fibrils morphology, secondary and quaternary structure, and PNF-virus-cell interactions. Optimized peptide sequences such as the 7-mer, CKFKFQF, have been obtained quantitatively forming supramolecular nanofibrils with high intermolecular β-sheet content that efficiently bind virions and attach to cellular membranes revealing efficient retroviral gene transfer.

1. Introduction

Peptide nanofibrils (PNFs) are ubiquitous in nature. They are formed by spontaneous self-assembly and exert many vital functions in living organisms. Peptide nanofibrils consisting of regular cross-β sheet structures, often termed amyloid-like structures,[1–4] feature many outstanding properties such as high rigidity, tensile strength, and enhanced resistance towards biodegradation.[5,6] They play both functional and pathological roles in many living organisms: Serving as templates for melanin biosynthesis,[7] for hormone storage,[8] participating in spermatozoa selection and clearance,[9] or constituting the fibrillar curli structures of *Escherichia coli* promoting their surface adhesion.[10] Their formation has also been associated with numerous human diseases (around 50), such as Alzheimer's disease or Diabetes

---

S. Sieste, T. Mack, K. Kaygisiz, Dr. C. V. Synatschke, Prof. T. Weil
Department Synthesis of Macromolecules
Max Planck Institute for Polymer Research
Ackermannweg 10, 55128 Mainz, Germany
E-mail: synatschke@mpip-mainz.mpg.de; weil@mpip-mainz.mpg.de

S. Sieste, T. Mack, Prof. T. Weil
Institute of Inorganic Chemistry I
Ulm University
Albert-Einstein-Allee 11, 89081 Ulm, Germany

Dr. E. Lump, M. Hayn, D. Schütz, Dr. A. Röcker,
Prof. F. Kirchhoff, Prof. J. Münch
Institute of Molecular Virology
Ulm University Medical Center
Meyerhofstraße 1, Ulm 89081, Germany
E-mail: jan.muench@uni-ulm.de

The ORCID identification number(s) for the author(s) of this article can be found under https://doi.org/10.1002/adfm.202009382.

DOI: 10.1002/adfm.202009382

Dr. C. Meier
Institute of Organic Chemistry III/Macromolecular Chemistry
Ulm University
Albert-Einstein-Allee 11, 89081 Ulm, Germany

Prof. T. P. J. Knowles, Prof. F. S. Ruggeri
Department of Chemistry
University of Cambridge
Cambridge CB2 1EW, UK
E-mail: simone.ruggeri@wur.nl

Prof. T. P. J. Knowles
Cavendish Laboratory
University of Cambridge
Cambridge CB3 0HE, UK

Prof. F. S. Ruggeri
Laboratory of Organic and Physical Chemistry
Wageningen University
Stippeneng 4, Wageningen 6703 WE, The Netherlands

Prof. J. Münch
Core Facility of Functional Peptidomics
Ulm University Medical Center
Albert-Einstein-Allee 47, 89081 Ulm, Germany

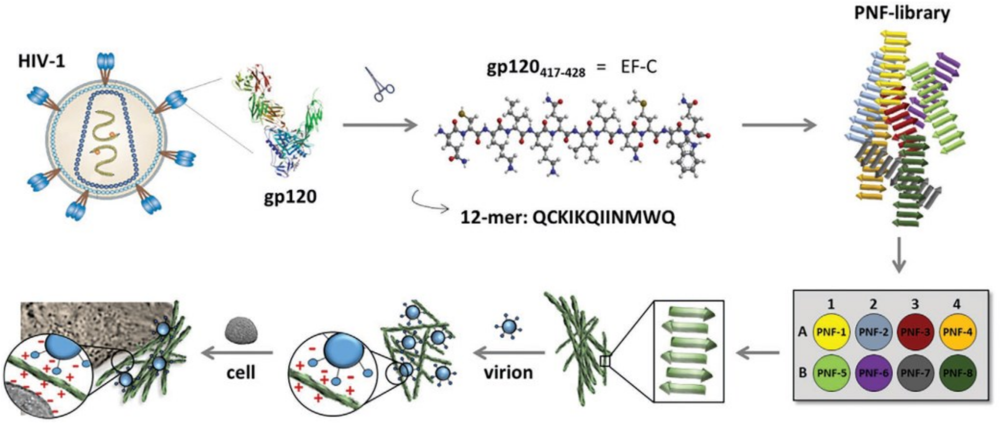

Figure 1. Schematic illustration of the structure–activity study of transduction enhancing PNFs. EF-C is a bioactive fragment of the HIV-1 glycoprotein gp120 that forms PNFs and enhances viral transduction. Through multiparameter and multiscale optimization, a library of EF-C derived peptides was synthesized. The library was evaluated for fibril formation, structural parameters, virion-PNF-cell interactions, and viral transduction enhancement.

mellitus type 2.[11] We have previously shown that PNF formation is also common in semen from healthy human individuals because semen contains an abundance of amyloidogenic fragments of prostate acidic phosphatase and the semenogelins 1 and 2.[12,13] PNFs likely play important roles in innate immunity and in eliminating poor-quality sperm upon deposition in the female reproductive tract.[9] In addition, semen PNFs enhance the infectivity of human immunodeficiency virus-1 (HIV-1), herpesviruses 1 and 2 and Ebola virus, and may increase the transmission potential of these sexually transmitted pathogens.[14,15]

The rich bioactivity of endogenous amyloids has inspired scientists to elucidate structural features crucial for their broad functions. Moreover, understanding their specific interactions of PNF with cellular membranes and viruses is not only of great fundamental interest but also essential to design new nanomaterials for medicine, for example, to enhance retroviral gene transfer.[16–18] Retroviral gene transfer is the method of choice for the delivery of genetic material into cells offering great perspectives for the treatment of genetic disorders, malignancies, and infectious diseases.[19,20] Until now, γ-retroviral and lentiviral vectors (herein both referred to as retroviral vectors) have been used in more than 478 gene therapy clinical trials[21] allowing stable, long-lasting gene expression. HIV-1 based lentiviral vectors even allow transduction of non-dividing cells,[22,23] which is essential to treat, that is, metachromatic leukodystrophy or inherited primary immunodeficiencies with a significant clinical benefit.[24,25] However, major challenges in retroviral gene delivery need to be overcome such as low transduction efficiencies due to: i) low concentrations of transducing particles in the viral vector stock; and ii) low efficiency of virion attachment to the target cell. Nowadays, retroviral gene delivery is often promoted by a combination of spin-infection and utilization of RetroNectin, a long polypeptide, consisting of 574 amino acid and a fibronectin derivative that colocalizes with virions and cells.[26–29] The large scale use of RetroNectin is limited by its high costs and even more importantly, it has to be coated onto plates or the inner surface of culture bags to capture virions, requiring several washing steps[30–32] which impedes in vivo applications.[33]

PNFs have been reported as powerful alternatives to RetroNectin as they enhance retroviral gene transfer with a similar efficiency but do not require coating.[18,34,35] We discovered the self-assembling 12-mer peptide EF-C (QCKIKQIINMWQ) corresponding to residues 417–428 of the HIV envelope protein gp120 (**Figure 1**).[18] EF-C PNFs efficiently concentrate virus stock solutions and increase cell attachment as well as retroviral gene transfer into hematopoietic stem cells and T cells by different types of vectors in vitro and ex vivo, which holds various opportunities for gene therapy approaches, in particular chimeric antigen receptor T cell (CAR-T) immunotherapy.[18,34–36] Compared to other PNFs and known transduction enhancers, EF-C reveals one of the highest enhancing effects on retroviral gene transfer and has been commercialized under the brand name Protransduzin.[34]

Very little is known about the structural features of bioactive PNFs such as EF-C, which severely limits rational approaches to further optimize their bioactivity. To the best of our knowledge, no structure–activity study of supramolecular nanofibrils has been reported yet. This limitation is due to the fact that supramolecular nanostructures are notoriously challenging to optimize as multiple parameters affect self-assembly, fibril morphologies, and biorecognition and the involved structures cover several length scales from the molecular to the mesoscopic regime. A limited number of studies have investigated small sequence variations in amyloid PNFs on transduction enhancement.[37–40] However, rational approaches that unravel structure–morphology–bioactivity relationships of PNF are still elusive. Herein, we report the first sequence optimization of PNFs for enhanced retroviral gene transduction via a rational multiparameter-based approach. The amino acids and peptide motifs within PNFs responsible for self-assembly, fibrils

ADVANCED SCIENCE NEWS
www.advancedsciencenews.com
ADVANCED FUNCTIONAL MATERIALS
www.afm-journal.de

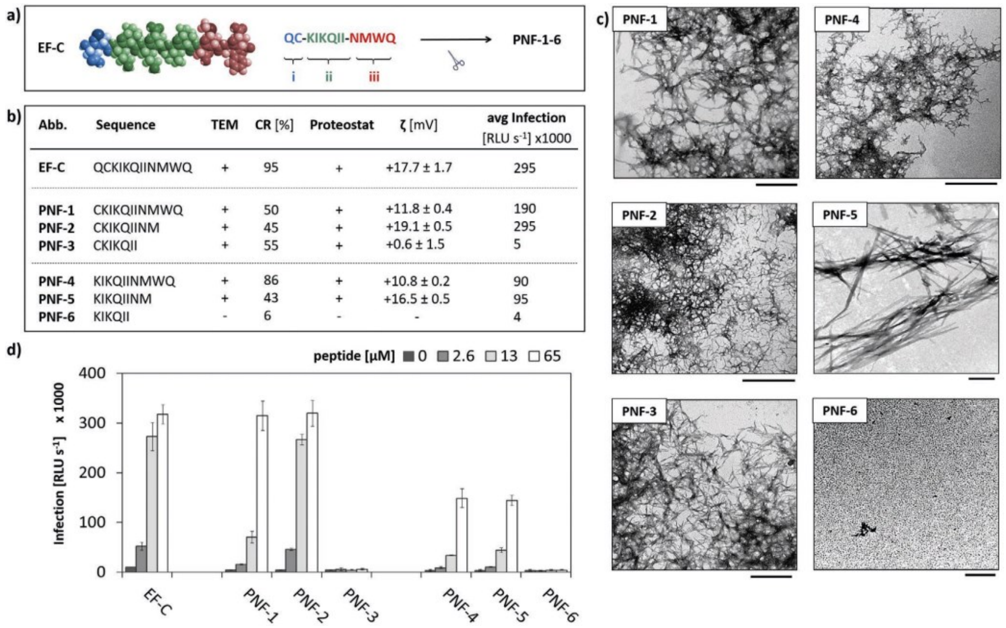

b)

Abb.	Sequence	TEM	CR [%]	Proteostat	ζ [mV]	avg Infection [RLU s-1] x1000
EF-C	QCKIKQIINMWQ	+	95	+	+17.7 ± 1.7	295
PNF-1	CKIKQIINMWQ	+	50	+	+11.8 ± 0.4	190
PNF-2	CKIKQIINM	+	45	+	+19.1 ± 0.5	295
PNF-3	CKIKQII	+	55	+	+0.6 ± 1.5	5
PNF-4	KIKQIINMWQ	+	86	+	+10.8 ± 0.2	90
PNF-5	KIKQIINM	+	43	+	+16.5 ± 0.5	95
PNF-6	KIKQII	-	6	-	-	4

Figure 2. PNF library generation upon sequence truncation of EF-C. a) EF-C was subdivided into three domains: i) QC; ii) KIKQII; and iii) NMWQ. b) Impact of sequence variations on peptide self-assembly (with + = fibrils and − = no aggregate formation detected), monomer-to-fibril conversion rates (CR) and transduction enhancement. Proteostat emission indicates accessible cross β-sheet binding pockets in the fibril core and indicated PNFs with + = Proteostat activity and − = no Proteostat fluorescence observed. ζ-potential values for PNF solutions. Average (avg) RLU s^{-1} in infectivity assay for 13–65 μm. c) Representative TEM micrographs of PNF-1 to PNF-5 reveal the formation of fibrillar aggregates. No aggregates were observed for PNF-6. The scale bars represent 500 nm. d) HIV-1 infection rates of TZM-bl cells observed in the presence of increasing concentrations of PNF. Shown are mean values derived from triplicate infections ± standard deviation. RLU s^{-1}; relative light units per second.

morphology, secondary and quaternary structure, and virus and/or cell binding were identified. We believe that unravelling the structural parameters of PNFs responsible for their unique bioactivities paves the way to a fundamental understanding of the rich bioactivity of PNFs and ultimately addresses the great need for improved nanomaterials for clinical applications, for example, in gene therapy.

EF-C served as a starting point for multiparameter optimization. Its sequence was first divided into smaller fragments to identify amino acids and amino acid patterns responsible for assembly and interaction with virions or cellular membranes. Subsequently, several focused peptide libraries were synthesized as depicted in **Figure 2**a. EF-C features: i) a short N-terminal *QC* fragment; ii) an amphiphilic *KIKQII* domain; and iii) a C-terminal *NMWQ* sequence. The C-terminal *NMWQ* domain represents a fragment of the β20/21 strand in the gp120 HIV-1 envelope protein region that has been proposed to constitute the primary HIV binding site for the CD4 receptors of immune cells[41] and to play a crucial role for the transduction enhancement of PNFs. The hexameric *KIKQII* fragment features an amphiphilic pattern with three hydrophobic isoleucine (I) and two positively charged lysine (K) residues. The lipophilic (I) residues could promote self-assembly, whereas the hydrophilic and positively charged (K) residues provide solubility for stabilizing the superstructures in aqueous media.[15,17]

PNF formation was achieved by dilution from a dimethyl sulfoxide stock solution to PBS buffer and aggregation was confirmed by transmission electron microscopy (TEM). Conversion rates (CR) from the soluble peptide monomers to supramolecular PNFs were quantified as published previously.[42] ζ-potential measurements were performed to determine the charge of PNF assemblies; secondary and quaternary structures of PNFs were characterized by infrared spectroscopy and intermolecular β-sheet structures and were confirmed by the blue-shifted emission of Proteostat[43] (Figure S1, Table S1, Supporting Information). The transduction enhancing properties of the PNFs were evaluated in infection experiments using HIV-1 particles as prototype retroviral vectors. Virions were exposed to increasing concentrations of PNFs and the mixtures were used to infect TZM-bl reporter cells,[44] which are widely used to study HIV infection rates. These cells are genetically engineered to express the HIV receptors CD4 and CXCR4/CCR5 and contain a stably integrated β-galactosidase gene under the control of the viral long terminal repeat promotor region. Upon successful infection, the HIV-1 transactivator Tat protein is expressed and turns on the viral promotor resulting in β-galactosidase production, which was quantified in a chemiluminescence-based assay performed 72 h post infection. None of the peptides tested in this study affected cell viability within the concentrations used for transduction studies (Figure S2, Supporting Information).

2. Results

2.1. PNF Library Generation upon Sequence Truncation

EF-C instantaneously forms positively charged PNFs (ζ = +17.7 mV) with high conversion rates (CR: 95%) and it is used as an internal standard to compare the infectivity enhancement of the peptide nanofibrils in different sets of experiments, that is, on different days. Several studies have shown that even short peptide sequences can exhibit robust fibril formation.[45,46] We therefore envisioned the identification of EF-C derived peptides with fewer than 13 amino acids that retain high transduction enhancement. After deleting the N-terminal glutamine (Q) and stepwise truncation of the C-terminal residues, PNF-1 (CKIKQIINMWQ), PNF-2 (CKIKQIINM), and PNF-3 (CKIKQII) still formed fibrils but with moderate CRs (45–55%) independent of the length of the C-terminal NMWQ fragment (Figure 2b,c). The transduction efficiencies of PNF-1 and PNF-2 with positive ζ-potentials were comparable to EF-C (at 65 µM, corresponding to 200 µg mL^{-1} EF-C, Figure 2d), whereas the almost neutral (ζ = + 0.6 mV) PNF-3 without the NMWQ fragment was inactive.

After deletion of the (QC) sequence, PNF-4 (KIKQIINMWQ) still assembled with high CR (86%) and PNF-5 (KIKQIINM) with moderate CR (43%, Figure 2b,c). A time-dependent measurement of the ζ-potential of PNF-4 and PNF-16 over 30 days revealed no significant changes in the respective ζ-potential values (Figure S3, Supporting Information). Interestingly, positively charged PNF-4 and PNF-5, which lack the cysteine residue, were considerably less active than PNF-1 and PNF-2 despite their positive ζ-potentials and comparable CRs. PNF-6 (KIKQII) did not form fibrils and showed no activity. These data gave a first indication that significant transduction enhancement requires: i) PNF formation; ii) positive ζ-potentials; and iii) an N-terminal cysteine residue.

2.2. Optimized Amphiphilic Pattern Improves Fibril Formation

In polar solvents, the morphology of intermolecular β-sheet rich aggregates is driven by the formation of a bilayer structure, where hydrophobic domains form the fibril core and the hydrophilic side chains arrange at the surface of the fibrillar backbone.[18] In order to improve the packing of the peptides in the PNFs, we altered: i) the arrangement of the hydrophilic and lipophilic amino-acids within the peptide sequences; ii) replaced the lipophilic (I) residues by other hydrophobic amino acids; and iii) identified minimal sequences with high CRs and transduction enhancement.[47,48] The central amphiphilic PNF-6 (KIKQII) fragment of the EF-C sequence reveals two structural defects in its sequence as the second (I) residue of KIKQII faces an opposite direction to the other two (I)-residues and the polar (Q) is located adjacent to the unpolar (I) and also opposite to the polar (K) residues (**Figure 3**a, blue model). By switching the positions of (Q) and its neighboring (I) in the QII fragment to an IQI sequence, a strictly alternating spatial arrangement of hydrophilic and lipophilic residues was obtained (Figure 3a, red model). In contrast to the PNF-1-6 series consisting of the KIKQII fragment, PNF-7 (CKIKIQINMWQ), PNF-8 (CKIKIQINM), and PNF-9 (CKIKIQI) now provide a facial amphiphilic character, where the positively charged and nonpolar residues are oriented not only in parallel but also perpendicular to the fibril axis. PNF-7 to PNF-9 with positive ζ-potentials (ζ = + 10.7–22.3 mV) were formed with moderate to high CRs (54–87%) and showed the ability to enhance retroviral infection at 65 μM, comparable to EF-C (Figure 3b–d; Figure S4, Supporting Information).

The corresponding (C)-free derivatives PNF-10 (KIKIQINMWQ) and PNF-11 (KIKIQINM) with the optimized KIKIQI patterns also assembled with high CRs (64–93%) into PNFs with positive ζ-potentials (ζ = + 17.2–41.9 mV) that were however less active than EF-C in promoting retroviral infection. Interestingly, PNF-9 with only seven amino acids assembled into bioactive and positively charged PNFs (ζ = +17.4 mV, CR = 54%), whereas neutral PNF-3 (ζ = +0.6 mV) was inactive and PNF-6 and PNF-12 lacking the N-terminal (C) did not form fibrils (Figures 2c and 3c). These results indicate that the optimized amphiphilic *CKIKIQI* pattern of PNF-9 with N-terminal (C) represents the shortest sequence for forming positively charged PNFs displaying transduction enhancement in the range of EF-C.

Next, the (I) residues in PNF-9 were replaced by the less bulky and less hydrophobic alanine (A) and the sterically more demanding aromatic phenylalanine (F) residues. PNF-13 (CKAKAQANMWQ), PNF-14 (CKAKAQANM), and PNF-15 (CKAKAQA) assembled into negatively charged PNFs (ζ = −3.7 to −9.1 mV) with high (PNF-13, 92%) to moderate CRs (PNF-14, PNF-15, 38–44%) that did not enhance viral transduction (Figure 3b–d). It has been reported that the aggregates of peptides with similar sequences can significantly vary in their ζ-potential, often preventing a direct correlation between the peptide sequence and ζ-potential.[49–51] The analogous lack in enhancing transduction was found after removing the N-terminal (C) of all three alanine derivatives resulting in PNF-S1 (KAKAQANMWQ), PNF-S2 (KAKAQANM), and PNF-S3 (KAKAQA) (Figure S5, Supporting Information). In contrast, the (F)-containing derivatives PNF-16 (CKFKFQFNMWQ), PNF-17 (CKFKFQFNM), and PNF-18 (CKFKFQF) formed positively charged PNFs (ζ = + 14.1–22.3 mV) with high CRs (88–96%) (Figure 3b–d) that all showed significant transduction enhancement. Removal of the N-terminal (C) afforded PNF-S4 (KFKFQFNMWQ) and PNF-S5 (KFKFQFNM) displaying high transduction enhancement, whereas PNF-S6 (KFKFQF) was inactive (Figure S5, Supporting Information).

2.3. An N-Terminal Cysteine Improves Fibril Formation and Enhances Transduction

The impact of the N-terminal accessible thiol-residues was furthermore investigated by substitution of (C) in PNF-9 by the sulfur-containing amino acid methionine (M) in PNF-S7 (MKIKIQI). Both PNF-9 and PNF-S7 formed positively charged

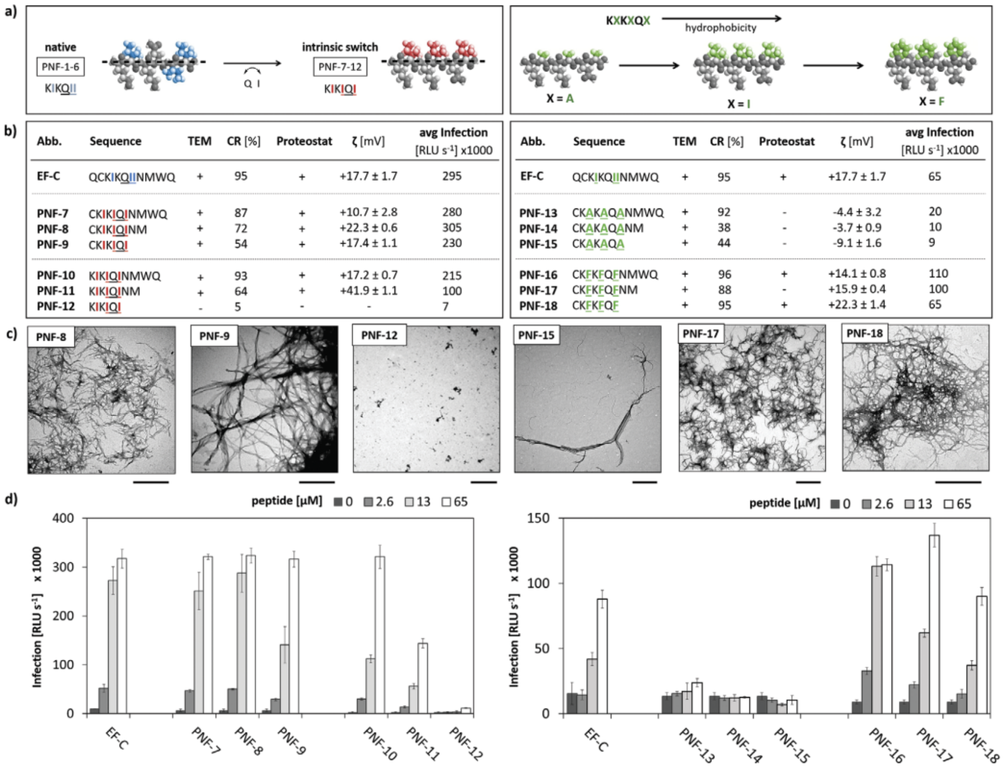

Abb.	Sequence	TEM	CR [%]	Proteostat	ζ [mV]	avg Infection [RLU s^{-1}] x1000
EF-C	QCKIKQIINMWQ	+	95	+	+17.7 ± 1.7	295
PNF-7	CKIKIQINMWQ	+	87	+	+10.7 ± 2.8	280
PNF-8	CKIKIQINM	+	72	+	+22.3 ± 0.6	305
PNF-9	CKIKIQI	+	54	+	+17.4 ± 1.1	230
PNF-10	KIKIQINMWQ	+	93	+	+17.2 ± 0.7	215
PNF-11	KIKIQINM	+	64	+	+41.9 ± 1.1	100
PNF-12	KIKIQI	-	5	-	-	7

Abb.	Sequence	TEM	CR [%]	Proteostat	ζ [mV]	avg Infection [RLU s^{-1}] x1000
EF-C	QCKIKQIINMWQ	+	95	+	+17.7 ± 1.7	65
PNF-13	CKAKAQANMWQ	+	92	-	-4.4 ± 3.2	20
PNF-14	CKAKAQANM	+	38	-	-3.7 ± 0.9	10
PNF-15	CKAKAQA	+	44	-	-9.1 ± 1.6	9
PNF-16	CKFKFQFNMWQ	+	96	+	+14.1 ± 0.8	110
PNF-17	CKFKFQFNM	+	88	-	+15.9 ± 0.4	100
PNF-18	CKFKFQF	+	95	+	+22.3 ± 1.4	65

Figure 3. Improving PNF aggregating and transduction enhancement. a) Optimization of the amphiphilic fragment (II) of EF-C. Hydrophilic amino acids are given in grey and hydrophobic in color. b) Tabular summary of the features of PNF-7 to PNF-18 including PNF formation as observed in TEM measurements with + = fibrils and − = no aggregate formation detected. Monomer-to-fibril conversion rates (CR) were determined in a fluorescence-based assay. Proteostat emission indicates accessible cross β-sheet binding pockets in the fibril core and was assessed for PNFs with + = Proteostat activity and − = no Proteostat fluorescence observed. ζ-potential values for PNF solutions. Average (avg) RLU s^{-1} in infectivity assay for 13–65 µm. c) Representative TEM micrographs of PNF-8,-9,-15,-17,-18 reveal fibrillar aggregate morphologies. No aggregates were observed for PNF-12. Scale bars: 500 nm. d) Transduction enhancement assay showing HIV-1 infection rates of TZM-bl cells observed in the presence of increasing concentrations of PNF given as mean values from triplicate infections ± standard deviation. RLU s^{-1}; relative light units per second.

nanofibrils of comparable morphology as confirmed by TEM measurements and both derivatives assembled with similar CRs (PNF-9, 54% and PNF-S7, 51%) (Figure S6, Supporting Information). However, PNF-S7 was significantly less bioactive than PNF-9 at all tested concentrations. The substitution of (C) by (M) in the shortest bioactive sequence PNF-18 afforded PNF-S8 (MKFKFQF), which was inactive (Figure S6, Supporting Information). The cysteine groups in the bioactive peptides could in principle undergo oxidation reactions under air, which could enhance the formation of disulfide bridges.[52] Therefore, we have studied bioactivity of PNF-8 in the presence of the reducing agent TCEP. Our data shows that the application of TCEP has no significant influence on bioactivity (Figure S7, Supporting Information). We conclude that in our study, N-terminal (C) leads to robust fibril formation and enhances infectivity also in case of short peptide sequences.

2.4. Unraveling the Structure–Activity Relationship

We have shown that the formation of bioactive PNFs required moderate to high CR as well as an overall positive ζ-potential. However, PNFs with similar positive charges and CRs, such as PNF-2 and PNF-5 could still reveal significantly different transduction enhancing activities (Figures 2 and 3). Therefore, CR and positive ζ-potential represent critical features, but additional, yet unknown parameters exist that account for the observed variability in the biological activity of PNFs. To identify these parameters, we first correlated the sequence and transduction enhancement of PNFs with their secondary and quaternary structure that was obtained by FTIR spectroscopy (**Figure 4**) from freeze-dried PNF solutions. It has been shown that the properties of amyloid structures in a liquid and dried environment remain highly conserved.[53–55] In proteins, the IR spectra

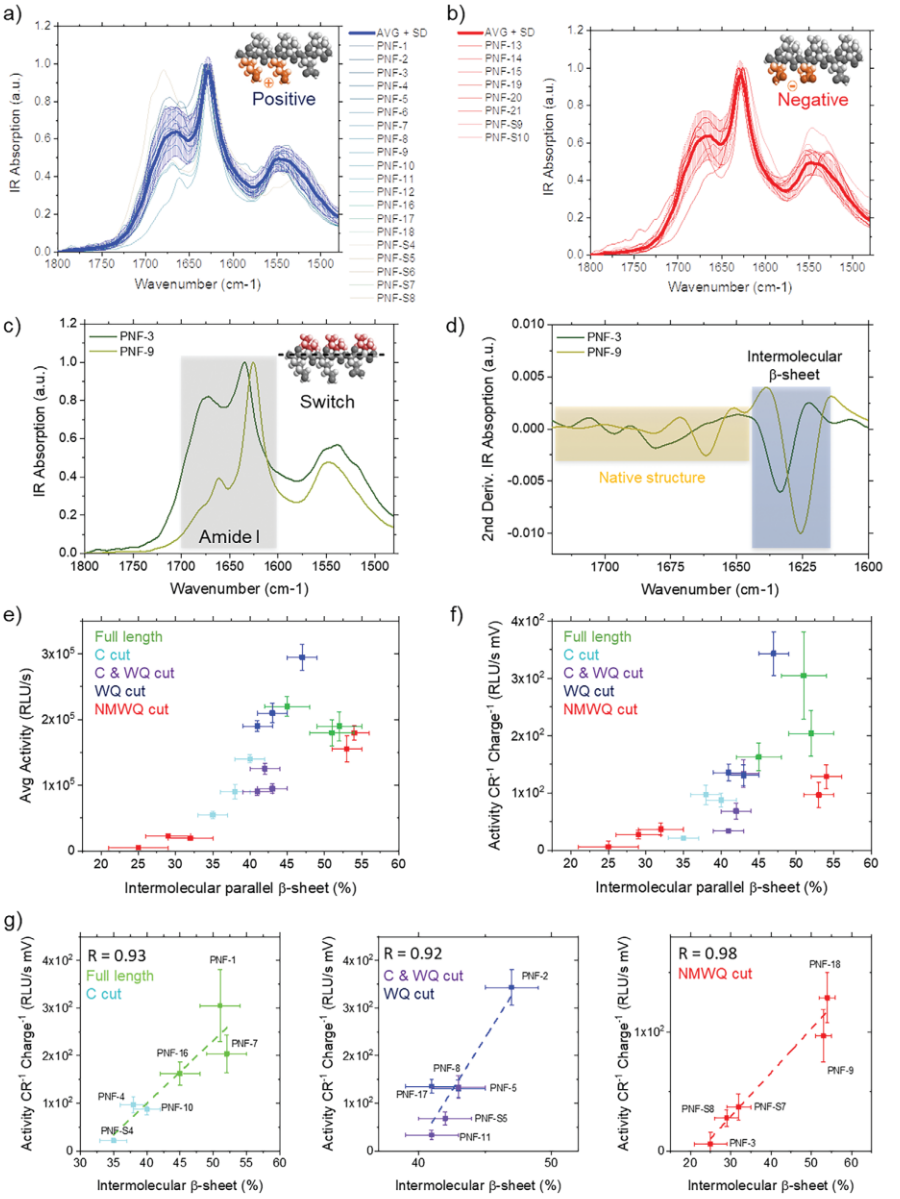

Figure 4. FTIR secondary structure evaluation and infectivity enhancement as a function of intermolecular *β*-sheet for all PNFs. FTIR spectra of a) positively and b) negatively charged PNFs. c) Modification of the amide band I upon intrinsic switch. d) Method of quantification of intramolecular native versus intermolecular aggregated *β*-sheet structure. Secondary structure versus e) average infection enhancing activity and f) average infection enhancing activity normalized by charge and conversion rate. g) Linear fit of activity versus intermolecular *β*-sheet for the groups of peptides with chemical similarity. Full length: PNF-1,-7,-16; C cut: PNF-4,-10,-S4; C and WQ cut: PNF-5,-11,-S5; WQ cut: PNF-2,-8,-17; NMWQ cut: PNF-3,-9,-18,-S7,-S8.

are dominated by the amide band I, whose shape is intimately related to the secondary and quaternary structure of the protein backbone. A first qualitative view of the spectra shows that the amide band I of almost all PNFs exhibited a maximum in the range between 1615–1630 cm^{-1} (Figure 4a,b). The high absorption in this spectroscopic range demonstrates the presence of a high content of intermolecular β-sheet structures, stabilized by a tight network of hydrogen bonds, similar to amyloidogenic aggregates.[56–58] Then, the integration of the deconvolved amide band I by a second derivative analysis allowed robust quantification of each structural contribution (α-helix, random coil, native and aggregated β-sheet) (Figure 4c,d).[59,60] The percentage of native intramolecular secondary structural elements (1635–1700 cm^{-1}) was quantified and correlated versus the percentage of intermolecular hydrogen bonded β-sheet (1610–1635 cm^{-1}) for each PNF (Figure 4d).

The PNF library showed a wide variation of secondary structures as indicated by the heterogeneity of shapes of the amide band I of the PNFs (Figure 4a,b). The amide I band of the different negatively charged PNFs varied significantly (Figure 4b), and with similar standard deviation to the one of the positive PNFs (Figure 4a). However, there were no major differences in the secondary and quaternary structures of negatively charged PNFs that would explain the observed significant differences in their transduction enhancement compared to positively charged PNFs and the EF-C sequence. This observation is in line with previous reports indicating that the ζ-potential of the PNFs is the first factor determining their transduction enhancing features.[17,18,61] However, positively charged PNFs revealed high variations in their structure and ability to boost transduction. An initial qualitative investigation of the spectra of these PNFs indicated that sequence modifications altered their secondary and quaternary structure, which also had an impact on their transduction enhancing features. For instance, the intrinsic switch of the core (Q) and (I) of PNF-3 (CKIKQII) leads to the formation of PNF-9 (CKIKIQI) with a higher content of intermolecular β-sheet structures that displayed improved transduction enhancing features (Figure 4c,d). The corresponding spectra showed that both in the presence and absence of the N-terminal cysteine (C), the intrinsic switch KIKQII → KIKIQI allowed us to modulate with a higher degree of freedom the secondary structure of the PNFs upon the stepwise removal of WQ and NM amino acids (Figure S8, Supporting Information).

2.5. The Intermolecular β-Sheet Content of PNFs Modulates their Transduction Efficiency

Next, we assessed how the molecular structure of the positively charged PNFs affects their impact on transduction efficiency. To reduce the intrinsic variability in the biological assay, the average transduction enhancement was calculated (Table S2, Supporting Information) and plotted as average biological activity against the content of the measured intermolecular β-sheet structures (Figure 4e). These data showed an unexpected and significant correlation as the biological activity increased steadily as a function of the intermolecular β-sheet content of the PNFs. As both charges and the CR are important parameters contributing to transduction enhancement, we normalized our results against CR and ζ-potential. Normalization for CR considers only the fraction of peptide monomers participating in PNF formation, whereas normalization for charge recognizes that only positively charged PNFs facilitate virus transport into cells (Figure 4f; Figure S9, Supporting Information). Interestingly, even after CR and charge normalization, a direct correlation between infectivity enhancement and the presence of intermolecular β-sheet content of the PNFs was observed.

To unravel the functional relationship between secondary structure and bioactivity, we also considered that the side chain absorption of the amino acids W, Q, and N can significantly contribute to the amide band I of a short peptide (≈5–15%). Thus, we grouped the peptides into three groups that are either chemically identical, that is, in case of structural isomers, or consist of amino acids, whose side chains do not affect the amide band I absorption. The plot of the β-sheet content versus infectivity for each of these groups revealed that these physical quantities are correlated by a statistically significant linear relationship (Figure 4g, $R = 0.92$–0.98). These data clearly demonstrate that the content of the intermolecular β-sheet structures in the PNFs is a fundamental parameter modulating their infectivity (Figure 4g).

We observed above that (C) promotes enhanced transduction rates (Figure 2). The structural analysis revealed that deletion of C-terminal cysteine leads to a net average reduction of the intermolecular β-sheets content (≈15%) in the PNFs (Figure 4g, light blue PNF-4,-10,-S4 versus green PNF-1,-7,-16). Interestingly, the influence of the N-terminal (C) is not of a hydrophobic nature, as an exchange of (C) with the chemically similar (M) decreased the intermolecular β-sheets content and reduced infectivity in the corresponding peptides libraries (Figure 4g, red PNF-9, 18 to PNF-S7/-S8). Therefore, we found that the main role of the N-terminal (C) is to generate amyloid-like PNFs with a higher content of hydrogen bonded β-sheets and thus more stable PNFs with a higher degree of order,[45,62] which obviously enhances their infectivity.

Deletion of both the N-terminal (C) and the C-terminus had an impact on the content of intermolecular β-sheet, which also affected transduction. We observed that the N-terminal (C) or part of the C-terminus (NMWQ) is a necessary prerequisite for high infectivity of the EF-C sequence. Truncation of the C-terminal (WQ) sequence only slightly affected PNF infectivity (Figure 4f, green versus blue), and this minor difference in secondary structure was attributed to the absorption of the (WQ) side chains that were removed in the corresponding series PNF-2,-5,-8,-17,-S5. The removal of both (C) and C-terminal (WQ) sequence slightly reduced the intermolecular β-sheet content (≈5%), which also diminished infectivity enhancement (Figure 4g, blue PNF-4,-10,-S4 versus violet PNF-1,-7,-16), whereas deletion of (C) and the full C-terminus significantly reduced the intermolecular β-sheet content (≈20%), which resulted in an almost complete loss of the transduction enhancing features (Figure S10, Supporting Information).

As mentioned previously, the optimization of the amphiphilic pattern also resulted in significant changes in the secondary structure (Figure 4c,d). This effect was smaller for the sequences

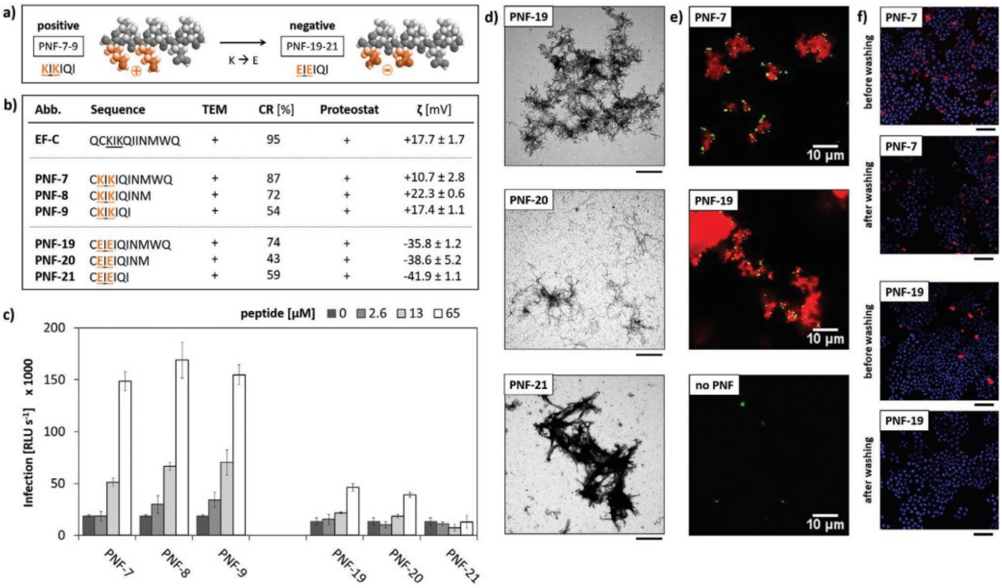

Abb.	Sequence	TEM	CR [%]	Proteostat	ζ [mV]
EF-C	QCKIKQIINMWQ	+	95	+	+17.7 ± 1.7
PNF-7	CKIKIQINMWQ	+	87	+	+10.7 ± 2.8
PNF-8	CKIKIQINM	+	72	+	+22.3 ± 0.6
PNF-9	CKIKIQI	+	54	+	+17.4 ± 1.1
PNF-19	CEIEIQINMWQ	+	74	+	-35.8 ± 1.2
PNF-20	CEIEIQINM	+	43	+	-38.6 ± 5.2
PNF-21	CEIEIQI	+	59	+	-41.9 ± 1.1

Figure 5. Variation of PNF charge from positive (bioactive) to negative (inactive). Both (K)-and (E)-rich fibrils bind virions, but the latter did not increase infectivity. a) Substitution of positively charged Lysine (K) residues by negatively charged glutamic acid (E) in the peptide sequences (PNF-7 to PNF-9) yielded corresponding negatively charged derivatives (PNF-19 to PNF-21) to elucidate the impact of PNF charge on self-assembly and infectivity enhancement. b) Tabular list of peptide derivatives PNF-19 to PNF-21 with glutamic acid residues and a positively charged lysine derivative set PNF-7 to PNF-9 including the ability to form PNFs as observed in TEM measurements with + = fibrils detected. Monomer-to-fibril conversion rates (CR) were determined in a fluorescence-based assay. High values indicate a large percentage of peptides participating in fibril formation. Proteostat emission indicates accessible cross β-sheet binding pockets in the fibril core and was assessed for PNFs with + = Proteostat activity and − = no Proteostat fluorescence observed. ζ-potential values for PNF solutions confirm the negative charge of fibrillar aggregates with glutamic acid residues. c) Infectivity assay showing HIV-1 infection rates of TZM-bl cells observed in the presence of increasing concentrations of PNF. Values above the columns depict the change from baseline (0 µm). Shown are mean values derived from triplicate infections ± standard deviation. RLU s^{-1}; relative light units per second. d) Representative TEM micrographs of PNF-19 to PNF-21 reveal fibrillar aggregate morphologies. The scale bars represent 500 nm. e) Representative LSM micrographs of Proteostat-labelled PNFs (red) incubated with YFP-labelled viral particles (green) revealed formation of mesoscale virus-PNF clusters for PNF-7 and PNF-19. f) Representative LSM micrographs of Proteostat-labelled PNFs (red) and TZM-bl cells (nucleus in blue). PNFs were added to cells for 30 min and analyzed. After 1 h, cells were washed and again analyzed. PNF-7 revealed association with cellular membranes while PNF-19 did not associate with cells. The scale bars represent 100 µm.

close in length to EF-C and it became more pronounced for the highly truncated sequences, that is, those lacking the NMWQ fragment (Figure 4g, red). In these (C)-containing peptides, the intrinsic switch enabled the modulation of the secondary structure and their transduction enhancing features (Figure 4g, red). By optimizing the internal amphiphilic pattern of PNF-3, which afforded PNF-9, both β-sheet content and transduction efficiency received a significant boost (Figure 4g), which is in good agreement with an optimized packing of the molecules due to the elimination of a polarity "defect" in the structure. The effects delivered by the intrinsic switch were of similar importance, when considering the (F)-derivative peptides (PNF-18). This structure–activity relationship represents the first result clearly indicating that the molecular structure, and in particular the content of intermolecular β-sheet content, is a fundamental parameter determining the infectivity enhancing properties of peptide nanofibrils.

2.6. Negatively Charged PNFs Bind Virions but Not Cells

The positively charged (K) residues could be involved in interactions with negatively charged viral membranes and/or the negatively charged lipid bilayers of cellular membranes. In this way, positively charged PNFs could enhance virus transduction by reducing the electrostatic repulsion forces between viral and cellular membranes.[15,17] In order to elucidate the interaction partner of PNFs, negatively charged peptide sequences based on bioactive PNF-7 to PNF-9 were prepared in which the hydrophilic, polar (K) residue was replaced by glutamic acid (E). The corresponding derivatives PNF-19 (CEIEIQINMWQ), PNF-20 (CEIEIQINM), and PNF-21 (CEIEIQI) formed PNFs with negative zeta potentials with good CRs (43–79%), almost comparable to their corresponding positive (K)-derivatives PNF-7 to PNF-9. The CR of the negative (E)-peptides PNF-19 to PNF-21, but their biological activity was an order of magnitude smaller (**Figure 5**).

Next, we studied the formation of mesoscale virus-PNF clusters by applying fluorescent laser scanning microscopy (LSM). PNFs were stained by the red-emitting fluorophore Proteostat and yellow fluorescent protein (YFP)-labelled retroviral particles (green) were used. Colocalization of PNFs and virions was observed for all investigated PNFs as depicted in Figure 5e and Figure S11, Supporting Information, indicating that despite their negative charge, PNF-19 and PNF-21 were still able to bind virions, although to a lower extent as their positively charged analogues. The interaction of PNFs with cellular membranes was then assessed by incubating Proteostat-labelled PNFs with TZM-bl cells for 30 min. The samples were analyzed by confocal microscopy before washing confirming the presence of PNF. After 1 h, cells were washed with PBS and examined again. PNF clusters were removed that did not significantly interact with the cellular surface. In contrast to (*K*)-containing PNFs, negatively charged PNFs based on optimized peptide sequences interacted with virions but they did not associate with the cellular membrane (Figure S12, Supporting Information), which most likely explains their lack of activity in the transduction assay (Figure 5c). The (K) residues in the bioactive PNFs reveal enhanced virus binding and facilitate colocalization of the virus-PNF complexes at cellular membranes. Interestingly, a set of peptides PNF-S9 and PNF-S10, where the charged residues were replaced with serine (S) (Figure S13, Supporting Information), show intermediate activity roughly between that of the highly active (K)-containing PNFs and the non-active (E)-containing PNFs. Colocalization of these PNFs and viral particles indicated poor attachment to cellular membranes confirming the overall importance of positively charged residues to enhance viral transduction efficacy. We conclude that a positive ζ-potential is crucial for the transduction enhancing properties of PNFs but it is not essential for PNF assembly and interaction with virions.

2.7. The Shortest Transduction Enhancing Sequence PNF-18 is a Potent Enhancer of Lenti- and γ-Retroviral Transduction

The peptide PNF-18 is a highly efficient transduction enhancer providing a short sequence of only seven amino acids. We selected this hit peptide for a comparative analysis with the EF-C 12-mer using multiple viral vectors and cell lines (**Figure 6**a). A lentiviral vector encoding a luciferase gene and carrying the G-protein of the vesicular stomatitis virus (VSV-G), a viral fusion protein often used in gene transfer approaches, was generated. p24 antigen of the viral pseudotype preparation (2 or 14 ng) were exposed to EF-C and PNF-18, and used to inoculate HEK 293T cells. Transduction efficiencies were determined 3 days later by quantifying luciferase activities in cellular lysates. Both PNFs substantially increased transduction (Figure 6b). At 100 µg mL^{-1}, PNF-18 is more active than EF-C, with maximal transduction enhancement of 32-fold (2 ng p24) and 17× (14 ng p24), as compared to 23× (2 ng p24) and 10× (14 ng p24), respectively, for EF-C. We also generated a lentiviral vector, SEW LUC2, by co-transfection of a crippled lentiviral genome encoding luciferase, a gag-pol and a VSV-G expression plasmid. The resulting vector was treated with EF-C and PNF-18, and mixtures were added to HeLA (TZM-bl) cells and murine fibroblast 3T3 cells. Again, transduction rates were determined by quantifying luciferase 3 days later. As shown in Figure 6c, both PNF dose-dependently increased transduction of both cell lines analyzed. PNF-18 revealed maximal enhancement of 121-fold in TZM-bl cells and 66-fold in 3T3 cells. Since one of the most advanced clinical applications of PNF is to increase retroviral transduction of T cells in CAR T cell therapy,[34,63] we finally evaluated PNF-18 in this setting. For this, a GFP encoding retroviral vector carrying the Env protein of the Gibbon ape leukemia virus (GALV-Env) which is commonly used in CAR T cell therapy was generated, without applying any optimization protocols or virion concentration by ultracentrifugation. Next, the vector was exposed to PNF-18 and added to primary T cells isolated from two independent blood donors. Transduction rates were analyzed 3 days later by determining the percentage of GFP + cells by flow cytometry (Figure 6d,e). In the absence of PNFs, hardly any transduced GFP+ cells were detected. However, with an increasing concentration of PNF-18, the number of transduced cells gradually increased to 9.5% for donor A, and 7.2% for donor B (Figure 6d), corresponding to 63 or 48-fold increased transduction rates as compared to the control containing no PNFs (Figure 6e). These results show, that fibrils derived from the 7-mer peptide PNF-18 substantially improved lentiviral gene transfer rates into adherent and primary suspension cells, independently of the viral fusion protein and the vector types used, rendering PNF-18 as a novel highly versatile and easy to produce transduction enhancer.

3. Conclusions

Supramolecular nanostructures are notoriously challenging to optimize as rational approaches face multiparameter and multiscale challenges. Herein, we have reported the first sequence optimization of peptides forming bioactive amyloid-like PNFs that enhance retroviral gene transduction based on single fibril analysis and quantitative infection data. The impact of different amino acid patterns and sequences responsible for assembly, fibril morphologies, virus and cell membrane binding were resolved. We found that the motif NMWQ in QCKIKQIINMWQ was not essential for their transduction enhancing properties. Optimizing the amphiphilic six amino acid sequence (KIKQII) afforded (CKFKFQF) with quantitative peptide-to-fibril CRs. The N-terminal (C) also affected fibril morphology by further increasing the intermolecular β-sheet content, which also contributed to high transduction efficacy in particular in short sequences. The structure–activity relationship showed a linear correlation of the content of intermolecular β-sheet structures and transduction enhancement of the PNFs. The (*K*)-residues were found important for binding both virions and cell surface structures by reducing the electrostatic repulsion forces between viral and cellular membranes to colocalize virions at the cellular membrane, which is required for transduction enhancement. Interestingly, negatively charged PNFs with optimized sequence patterns could still bind virions but the formed negative PNF-virion complexes did not co-localize with cellular membranes.

The nine-mers PNF-8 and PNF-17 as well as the seven-mer PNF-18 (CKFKFQF) represent a minimum sequence

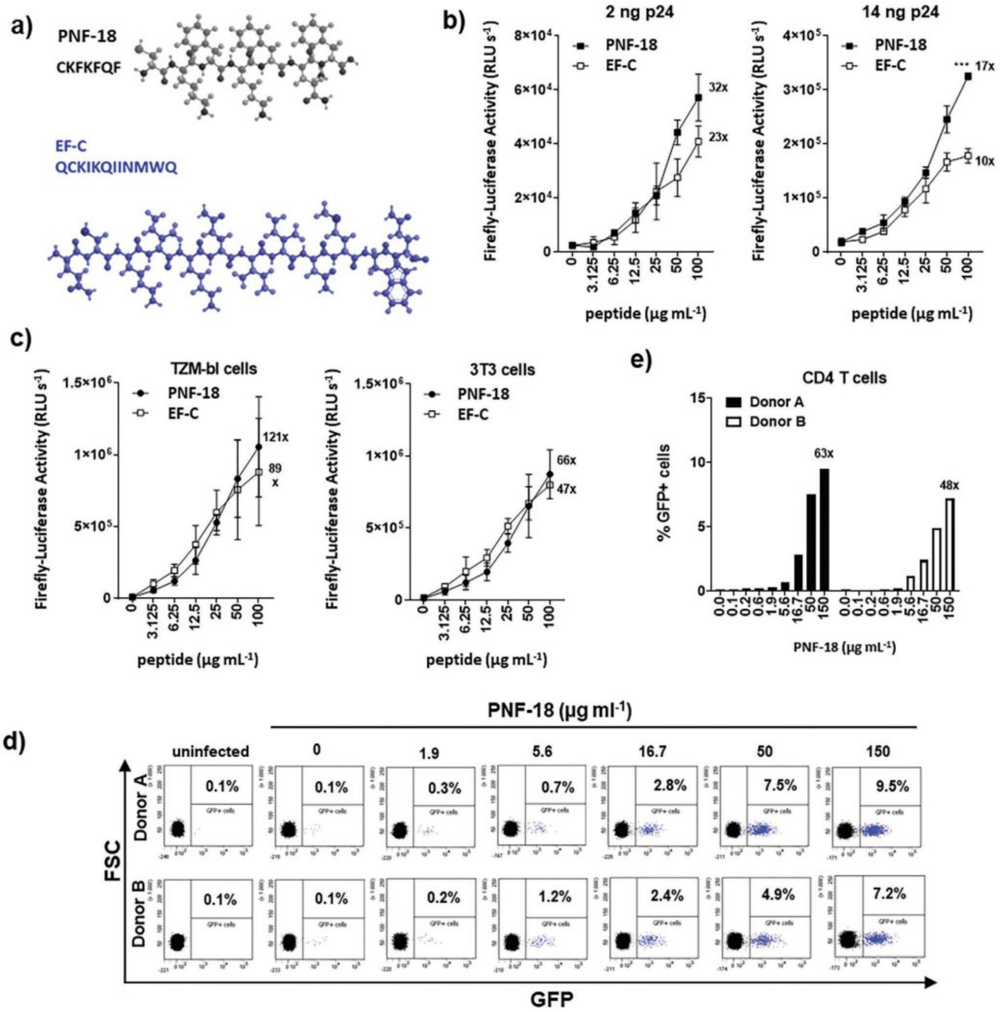

Figure 6. Fibrils derived from the shortened peptide PNF-18 are potent enhancer of lenti- and γ-retroviral transduction. a) Structure of PNF-18 and the parental EF-C peptide. b) Transduction efficiencies of a low (left) or median (right) dose of VSV-G pseudotyped HIV-1 NL4-3 particles encoding a luciferase. Viral particles were exposed to the indicated concentrations of EF-C and PNF-18 and used to inoculate HEK 293T cells. Luciferase activities were determined three days later, shown are mean values derived from triplicate infection ± standard deviation (SD). c) Transduction efficiencies of a VSV-G pseudotyped lentiviral vector (SEW LUC2) in TZM-bl or 3T3 cells. The SEW LUC2 vector preparation was incubated with the PNF and used to infect TZM-bl and 3T3 cells. Luciferases activities were determined 3 days later, shown are mean values derived from triplicate infections ± SD. d) Dot plots showing GFP+ CD4 T cells obtained from two independent donors after transduction with GALV pseudotyped γ-retrovirus at indicated concentrations of PNF-18 at three days post transduction. e) Percentage of GFP positive cells shown in (d). Numbers above data points give the *n*-fold enhancement of transduction as compared to controls containing no PNF.

combining PNF formation with high CRs and high infectivity due to: 1) high content of cross-β-sheet structures; 2) ability to bind virions; and 3) interact with cellular membranes. PNF-18 provides a more than 40% reduced sequence length compared to the original 12-mer EF-C sequence promoting optimized lentiviral HIV infection and enhanced retroviral transduction with high efficiency outperforming the original EF-C sequence. PNF-18 is less expensive to synthesize, it can be purified and produced without batch-to-batch variations and it further provides reactive thiol groups to introduce further chemical modifications, that is, via maleimide chemistry. We envision that negatively charged (E)-based PNFs capable of binding viral particles without interacting with cellular membranes could offer exciting opportunities to develop antiviral nanomaterials as well as PNFs targeting specific cell types as positive charges usually mediate unspecific electrostatic interactions with cellular membranes.

Supporting Information

Supporting Information is available from the Wiley Online Library or from the author.

Acknowledgements

S.S. and T.M. contributed equally to this work. The project was funded by the German Research Foundation (DFG) – project number 316249678 – CRC 1279 (A03, A05, C01). T.W., J.M., and F.K. acknowledge funding by the Volkswagen Foundation (project 89943) and J.M. by the Leibniz Association (SAW project). The authors thank Jasmina Gačanin for assisting in peptide synthesis and Nicole Kirsch-Pietz in proofreading.

Open access funding enabled and organized by Projekt DEAL.

Conflict of Interest

The authors declare no conflict of interest.

Data Availability Statement

Data available on request from the authors.

Keywords

peptide nanofibrils, retroviral gene transfer, self-assembly, structure–activity relationship

Received: November 3, 2020
Revised: January 20, 2021

[1] T. P. J. Knowles, J. F. Smith, G. L. Devlin, C. M. Dobson, M. E. Welland, *Nanotechnology* **2007**, *18*, 044031.
[2] T. Lührs, C. Ritter, M. Adrian, D. Riek-loher, B. Bohrmann, H. Do, D. Schubert, R. Riek, *Proc. Natl. Acad. Sci. USA* **2005**, *102*, 17342.
[3] L. C. Serpell, *Biochim. Biophys. Acta, Mol. Basis Dis.* **2000**, *1502*, 16.
[4] G. Wei, Z. Su, N. P. Reynolds, P. Arosio, I. W. Hamley, E. Gazit, R. Mezzenga, *Chem. Soc. Rev.* **2017**, *46*, 4661.
[5] I. Cherny, E. Gazit, *Angew. Chem., Int. Ed.* **2008**, *47*, 4062.
[6] Z. Xu, R. Paparcone, M. J. Buehler, *Biophys. J.* **2010**, *98*, 2053.
[7] D. M. Fowler, A. V. Koulov, C. Alory-Jost, M. S. Marks, W. E. Balch, J. W. Kelly, *PLoS Biol.* **2006**, *4*, 0100.
[8] S. K. Maji, D. Schubert, C. Rivier, S. Lee, J. E. Rivier, R. Riek, *PLoS Biol.* **2008**, *6*, e17.
[9] N. R. Roan, N. Sandi-Monroy, N. Kohgadai, S. M. Usmani, K. G. Hamil, J. Neidleman, M. Montano, L. Ständker, A. Röcker, M. Cavrois, J. Rosen, K. Marson, J. F. Smith, C. D. Pilcher, F. Gagsteiger, O. Sakk, M. O'Rand, P. V. Lishko, F. Kirchhoff, J. Münch, W. C. Greene, *Elife* **2017**, *6*, e24888.
[10] M. R. Chapman, L. S. Robinson, J. S. Pinkner, R. Roth, J. Heuser, M. Hammar, S. Normark, S. J. Hultgren, *Science* **2002**, *295*, 851.
[11] T. P. J. Knowles, M. Vendruscolo, C. M. Dobson, *Nat. Rev. Mol. Cell Biol.* **2014**, *15*, 384.
[12] N. R. Roan, H. Liu, S. M. Usmani, J. Neidleman, J. A. Muller, A. Avila-Herrera, A. Gawanbacht, O. Zirafi, S. Chu, M. Dong, S. T. Kumar, J. F. Smith, K. S. Pollard, M. Fandrich, F. Kirchhoff, J. Munch, H. E. Witkowska, W. C. Greene, *J. Virol.* **2014**, *88*, 7221.
[13] S. M. Usmani, O. Zirafi, J. A. Müller, N. L. Sandi-Monroy, J. K. Yadav, C. Meier, T. Weil, N. R. Roan, W. C. Greene, P. Walther, K. P. R. Nilsson, P. Hammarström, R. Wetzel, C. D. Pilcher, F. Gagsteiger, M. Fändrich, F. Kirchhoff, J. Münch, *Nat. Commun.* **2014**, *5*, 3508.
[14] J. Münch, E. Rücker, L. Ständker, K. Adermann, C. Goffinet, M. Schindler, S. Wildum, R. Chinnadurai, D. Rajan, A. Specht, G. Giménez-Gallego, P. C. Sánchez, D. M. Fowler, A. Koulov, J. W. Kelly, W. Mothes, J. C. Grivel, L. Margolis, O. T. Keppler, W. G. Forssmann, F. Kirchhoff, *Cell* **2007**, *131*, 1059.
[15] A. Röcker, N. R. Roan, J. K. Yadav, M. Fändrich, J. Münch, *Chem. Commun.* **2018**, *54*, 7557.
[16] K. Kaygisiz, C. V. Synatschke, *Biomater. Sci.* **2020**, *8*, 6113.
[17] C. Meier, T. Weil, F. Kirchhoff, J. Münch, *Wiley Interdiscip. Rev.: Nanomed. Nanobiotechnol.* **2014**, *6*, 438.
[18] M. Yolamanova, C. Meier, A. K. Shaytan, V. Vas, C. W. Bertoncini, F. Arnold, O. Zirafi, S. M. Usmani, J. A. Müller, D. Sauter, C. Goffinet, D. Palesch, P. Walther, N. R. Roan, H. Geiger, O. Lunov, T. Simmet, J. Bohne, H. Schrezenmeier, K. Schwarz, L. Ständker, W.-G. Forssmann, X. Salvatella, P. G. Khalatur, A. R. Khokhlov, T. P. J. Knowles, T. Weil, F. Kirchhoff, J. Münch, *Nat. Nanotechnol.* **2013**, *8*, 130.
[19] E. Montini, D. Cesana, M. Schmidt, F. Sanvito, M. Ponzoni, C. Bartholomae, L. S. Sergi, F. Benedicenti, A. Ambrosi, C. Di Serio, C. Doglioni, C. Von Kalle, L. Naldini, *Nat. Biotechnol.* **2006**, *24*, 687.
[20] L. Naldini, U. Blömer, P. Gallay, D. Ory, R. Mulligan, F. H. Gage, I. M. Verma, D. Trono, *Science* **1996**, *272*, 263.
[21] S. L. Ginn, A. K. Amaya, I. E. Alexander, M. Edelstein, M. R. Abedi, *J. Gene Med.* **2018**, *20*, e3015.
[22] P. Kumar, C. Woon-Khiong, *Curr. Gene Ther.* **2011**, *11*, 144.
[23] T. Sakuma, M. A. Barry, Y. Ikeda, *Biochem. J.* **2012**, *443*, 603.
[24] A. Biffi, E. Montini, L. Lorioli, M. Cesani, F. Fumagalli, T. Plati, C. Baldoli, S. Martino, A. Calabria, S. Canale, F. Benedicenti, G. Vallanti, L. Biasco, S. Leo, N. Kabbara, G. Zanetti, W. B. Rizzo, N. A. L. Mehta, M. P. Cicalese, M. Casiraghi, J. J. Boelens, U. Del Carro, D. J. Dow, M. Schmidt, A. Assanelli, V. Neduva, C. Di Serio, E. Stupka, J. Gardner, C. Von Kalle, C. Bordignon, F. Ciceri, A. Rovelli, M. G. Roncarolo, A. Aiuti, M. Sessa, L. Naldini, *Science* **2013**, *341*, 1233158.
[25] L. W. Seymour, A. J. Thrasher, *Nat. Biotechnol.* **2012**, *30*, 588.
[26] H. Hanenberg, K. Hashino, H. Konishi, A. R. Hock, I. Kato, D. A. Williams, *Hum. Gene Ther.* **1997**, *2206*, 2193.
[27] T. Moritz, P. Dutt, X. Xiao, D. Carstanjen, T. Vik, H. Hanenberg, D. A. Williams, *Blood* **1996**, *88*, 855.
[28] A. Quintás-Cardama, R. K. Yeh, D. Hollyman, J. Stefanski, C. Taylor, Y. Nikhamin, G. Imperato, M. Sadelain, I. Rivière, R. J. Brentjens, *Hum. Gene Ther.* **2007**, *18*, 1253.
[29] P. Zhou, J. Lee, P. Moore, K. M. Brasky, *Hum. Gene Ther.* **2001**, *12*, 1843.
[30] K. Dodo, H. Chono, N. Saito, Y. Tanaka, K. Tahara, I. Nukaya, J. Mineno, *PLoS One* **2014**, *9*, e86275.
[31] C. H. J. Lamers, P. van Elzakker, S. C. L. van Steenbergen, S. Sleijfer, R. Debets, J. W. Gratama, *Cytotherapy* **2008**, *10*, 406.
[32] T. Tsukamoto, S. Okada, *J. Virol. Methods* **2017**, *248*, 234.

[33] H. J. Lee, Y. S. Lee, H. S. Kim, Y. K. Kim, J. H. Kim, S. H. Jeon, H. W. Lee, S. Kim, H. Miyoshi, H. M. Chung, D. K. Kim, *Biologicals* **2009**, *37*, 203.

[34] A. Castro, M. Drosch, M. Liesenfeld, T. Kaan, A. Schilz, H. Wenschuh, W. Forsmann, K. Kuhlke, *Cytotherapy* **2019**, *21*, e14.

[35] D. Fenard, D. Ingrao, A. Seye, J. Buisset, S. Genries, S. Martin, A. Kichler, A. Galy, *Mol. Ther.–Nucleic Acids* **2013**, *2*, e90.

[36] D. Schuetz, S. Rode, C. Read, J. Mueller, B. Glocker, K. Sparrer, O. Fackler, P. Walther, J. Muench, bioRxiv https://doi.org/10.1101/2020.10.01.321810.

[37] J. Chen, R. Ren, S. Tan, W. Zhang, X. Zhang, F. Yu, T. Xun, S. Jiang, S. Liu, L. Li, *PLoS One* **2015**, *10*, e0144522.

[38] J. Chen, R. Ren, F. Yu, C. Wang, X. Zhang, W. Li, S. Tan, S. Jiang, S. Liu, L. Li, *Biophys. J.* **2017**, *113*, 1425.

[39] S. Tan, L. Li, L. Lu, C. Pan, H. Lu, Y. Oksov, X. Tang, S. Jiang, S. Liu, *FEBS Lett.* **2014**, *588*, 1515.

[40] H. Zhang, X. He, Y. Shi, Y. Yu, S. Guan, X. Gong, H. Yin, Z. Kuai, Y. Shan, *RSC Adv.* **2016**, *6*, 82082.

[41] R. Franke, T. Hirsch, J. Eichler, *J. Recept. Signal Transduction* **2006**, *26*, 453.

[42] C. Schilling, T. Mack, S. Lickfett, S. Sieste, F. S. Ruggeri, T. Sneideris, A. Dutta, T. Bereau, R. Naraghi, D. Sinske, T. P. J. Knowles, C. V. Synatschke, T. Weil, B. Knöll, *Adv. Funct. Mater.* **2019**, *29*, 1809112.

[43] S. Navarro, S. Ventura, *Biotechnol. J.* **2014**, *9*, 1259.

[44] E. J. Platt, K. Wehrly, S. E. Kuhmann, B. Chesebro, D. Kabat, *J. Virol.* **1998**, *72*, 2855.

[45] J. Adamcik, F. S. Ruggeri, J. T. Berryman, A. Zhang, T. P. J. Knowles, R. Mezzenga, *Adv. Sci.* **2020**, *8*, 2002182.

[46] V. Castelletto, P. Ryumin, R. Cramer, I. W. Hamley, M. Taylor, D. Allsop, M. Reza, J. Ruokolainen, T. Arnold, D. Hermida-Merino, C. I. Garcia, M. C. Leal, E. Castaño, *Sci. Rep.* **2017**, *7*, 43637.

[47] R. J. Betush, J. M. Urban, B. L. Nilsson, *Pept. Sci.* **2018**, *110*, e23099.

[48] F. T. Senguen, N. R. Lee, X. Gu, D. M. Ryan, T. M. Doran, E. A. Anderson, B. L. Nilsson, *Mol. BioSyst.* **2011**, *7*, 486.

[49] Y. Chen, H. X. Gan, Y. W. Tong, *Macromolecules* **2015**, *48*, 2647.

[50] S. Toksoz, R. Mammadov, A. B. Tekinay, M. O. Guler, *J. Colloid Interface Sci.* **2011**, *356*, 131.

[51] T. A. Martinek, A. Hetényi, L. Fülöp, I. M. Mándity, G. K. Tóth, I. Dékány, F. Fülöp, *Angew. Chem.* **2006**, *118*, 2456.

[52] R. Honda, *Biophys. J.* **2018**, *114*, 885.

[53] F. S. Ruggeri, P. Flagmeier, J. R. Kumita, G. Meisl, D. Y. Chirgadze, M. N. Bongiovanni, T. P. J. Knowles, C. M. Dobson, *ACS Nano* **2020**, *14*, 5213.

[54] K. Baginska, J. Makowska, W. Wiczk, F. Kasprzykowski, L. Chmurzynski, *J. Pept. Sci.* **2008**, *14*, 283.

[55] A. Adochitei, G. Drochioiu, *Rev. Roum. Chim.* **2011**, *56*, 783.

[56] V. Cabiaux, R. Brasseur, R. Wattiez, P. Falmagne, J. M. Ruysschaert, E. Goormaghtigh, *J. Biol. Chem.* **1989**, *264*, 4928.

[57] E. Goormaghtigh, V. Cabiaux, J. Ruysschaert, *Eur. J. Biochem.* **1990**, *193*, 409.

[58] D. M. Byler, H. Susi, *Biopolymers* **1986**, *25*, 469.

[59] F. S. Ruggeri, B. Mannini, R. Schmid, M. Vendruscolo, T. P. J. Knowles, *Nat. Commun.* **2020**, *11*, 2945.

[60] F. S. Ruggeri, G. Longo, S. Faggiano, E. Lipiec, A. Pastore, G. Dietler, *Nat. Commun.* **2015**, *6*, 7831.

[61] N. R. Roan, J. Münch, N. Arhel, W. Mothes, J. Neidleman, A. Kobayashi, K. Smith-McCune, F. Kirchhoff, W. C. Greene, *J. Virol.* **2009**, *83*, 73.

[62] F. S. Ruggeri, J. Adamcik, J. S. Jeong, H. A. Lashuel, R. Mezzenga, G. Dietler, *Angew. Chem., Int. Ed.* **2015**, *54*, 2462.

[63] A. Jamali, L. Kapitza, T. Schaser, I. C. D. Johnston, C. J. Buchholz, J. Hartmann, *Mol. Ther.–Methods Clin. Dev.* **2019**, *13*, 371.

ADVANCED FUNCTIONAL MATERIALS

Supporting Information

for *Adv. Funct. Mater.,* DOI: 10.1002/adfm.202009382

Supramolecular Peptide Nanofibrils with Optimized Sequences and Molecular Structures for Efficient Retroviral Transduction

Stefanie Sieste, Thomas Mack, Edina Lump, Manuel Hayn, Desiree Schütz, Annika Röcker, Christoph Meier, Kübra Kaygisiz, Frank Kirchhoff, Tuomas P. J. Knowles, Francesco S. Ruggeri, Christopher V. Synatschke,* Jan Münch,* and Tanja Weil**

Supplementary Information for

Supramolecular Peptide Nanofibrils with Optimized Sequences and Molecular Structures for Efficient Retroviral Transduction

Stefanie Sieste, Thomas Mack, Edina Lump, Manuel Hayn, Desiree Schütz, Annika Röcker, Christoph Meier, Kübra Kaygisiz, Frank Kirchhoff, Tuomas P. J. Knowles, Francesco S. Ruggeri, Christopher V. Synatschke,* Jan Münch,* and Tanja Weil**

S. Sieste, T. Mack, K. Kaygisiz, Dr. C. V. Synatschke, Prof. T. Weil
Department Synthesis of Macromolecules
Max Planck Institute for Polymer Research
Ackermannweg 10, 55128 Mainz, Germany
Email: weil@mpip-mainz.mpg.de, synatschke@mpip-mainz.mpg.de

S. Sieste, T. Mack, Dr. C. Meier, Prof. T. Weil
Institute of Inorganic Chemistry I
Ulm University
Albert-Einstein-Allee 11, 89081 Ulm, Germany

Dr. E. Lump, M. Hayn, D. Schütz, Dr. A. Röcker, Prof. F. Kirchhoff, Prof. J. Münch
Institute of Molecular Virology
Ulm University Medical Center
Meyerhofstraße 1, 89081 Ulm, Germany
Email: jan.muench@uni-ulm.de

Prof. T. P. J. Knowles, Prof. F. S. Ruggeri
Department of Chemistry
University of Cambridge
Cambridge CB2 1EW, UK
Email: fsr26@cam.ac.uk

Prof. T. P. J. Knowles
Cavendish Laboratory
University of Cambridge
Cambridge CB3 0HE, UK

Prof. F. S. Ruggeri
Laboratory of Physical Chemistry, Stippeneng 4, 6703 WE, Wageningen University, the Netherlands
Email: simone.ruggeri@wur.nl

Prof. J. Münch
Core Facility of Functional Peptidomics
Ulm University Medical Center
Albert-Einstein-Allee 47, 89081 Ulm, Germany

Methods

Materials for peptide synthesis and characterization

PyBOP, HBTU, Fmoc-Lys(Boc)-OH, Fmoc-Phe-OH, Fmoc-Gln(Trt)-OH, Fmoc-Ile-OH, Fmoc-Cys(Trt)-OH, Fmoc-Trp(Boc)-OH, Fmoc-Asn(Trt)-OH, Fmoc-Met-OH, Fmoc-Glu(OtBu)-OH, Fmoc-Ala-OH, Fmoc-Phe-Wang resin, Fmoc-Ile-Wang resin, Fmoc-Gln(Trt)-Wang resin and Fmoc-Met-Wang resin were purchased from Novabiochem®. *N*-ethyldiisopropylamine for synthesis (DIPEA) and potassium chloride (KCl) were obtained from Merck. Piperidine (≥ 99.5% for peptide synthesis) and trifluoroacetic acid (TFA, ≥ 99.9%) were obtained from Carl Roth. Dimethylformamide (DMF, peptide synthesis), diethyl ether and acetonitrile (HiPerSolv Chromanorm for HPLC-gradient grade) were purchased from VWR Chemicals Prolabo. Dimethylsulfoxid (DMSO, ACS reagent, ≥ 99.9%) was purchased from Honeywell, Riedel-de Haën®. Vivaspin 500 tubes (3 kDa MWCO) were purchased from Sartorius. Syringe filters Chromafil®Xtra RC-20/13 (0.20 µm) were obtained from Machery-Nagel. Uranyl acetate was purchased from Merck. Fluorescamine was purchased from PanReac AppliChem. PBS and α-Cyano-4-hydroxycinnamic acid were purchased from Sigma Aldrich. Proteostat® was purchased from Enzo Life Sciences. All chemicals were used as received unless explicitly stated otherwise. Some PNF sequences were purchased from Phtd Peptides industrial Co. limited with purity of ≥ 95% (marked with ** in Supporting Table S3).

1. Synthesis of PNF derivatives

The peptides were synthesised according to standard Fmoc solid phase peptide synthesis on a microwave assisted peptide synthesizer (Liberty I by CEM or a Biotage Initiator+) in a 0.1 mmol scale. The C- to N-terminal coupling was achieved by using Wang resins preloaded with the first Fmoc-protected amino acid. Fmoc-deprotections were carried out with DMF solutions containing 20% or 25% v/v piperidine. Coupling reactions with 5 equiv. Fmoc-protected amino acid solutions in DMF at 75 °C for 5 or 10 min were catalysed by addition of 5 equiv. HBTU or PyBOP and 10 equiv. DIEA. Cleavage of the resin and final deprotection of the side chains were performed with a mixture of TFA, TIS and H_2O at a ratio of 95:2.5:2.5 by shaking at RT for 2h. The cleaved peptides were precipitated in cold diethyl ether and lyophilized. The final products were analysed with mass spectrometry measured on a Bruker Reflex III matrix assisted laser desorption/ionization time of flight (MALDI-TOF) MS device. 4-Hydroxy-α-cyanocinnaminic acid served as matrix.

2. Purification of PNF derivatives

All peptides were purified via HPLC using an optimized binary gradient (0.1% TFA water-acetonitrile as mobile phase). For preparative scale a Shimadzu system was used (LC-20AP, CBM-20A, SPD-20A) with a reversed phase C18 column (LiChrospher, Merck). Purity was verified by MALDI-TOF-MS (Bruker Reflex III) and analytical HPLC using a 1260 Infinity Quarternary LC System (Agilent Technologies) with an analytical ChroCART® 125-4 column (LiChrospher, Merck). All data can be found in Figurer S12 and Table S3 (Supporting Information).

3. Preparation of PNF fibrils

The peptides were dissolved in DMSO (c = 10 mg/mL, stored at 4°C before usage) and added dropwise to PBS buffer to a final incubation concentration of 650 µM or 1 mg/mL as indicated in the text. Other concentrations described in the text were achieved by further dilution of preformed PNFs.

4. TEM characterization of PNFs

5 µL of pre-assembled PNF fibrils (1 mg/mL) were placed on copper grids which were coated with a thin electron-transparent Formvar-layer and freshly etched with oxygen plasma before use. After 5 min incubation time, the grids were washed three times with ddH_2O (double-distilled water) followed by sample staining with 2% uranyl acetate solution for 5 min. After additional three washing steps excess solvent was removed by filter paper. Measurements were performed on a Jeol 1400 electron microscope with 100 kV acceleration voltage or with an EM 109 transmission electron microscope (Zeiss) at an acceleration voltage of 80 kV.

5. ATR FT-IR

For ATR FT-IR spectroscopy measurements, 50 µL of the respective 1 mg/mL PNF solution was lyophilized and the resulting powder used for measurement. All spectra were recorded on a Bruker Tensor 27 spectrometer with a diamond crystal as ATR element (PIKE MiracleTM, spectral resolution 4 cm^{-1}). Every sample was measured with 20 scans. Data were analyzed with OriginPro (OriginLab) software.

6. Zeta potential

50 µL of preformed PNF fibrils (1 mg mL^{-1}) were diluted to 1 mL in an aqueous solution of 1 mM KCl. The dilution ratio was adjusted, if the count rate was not sufficient. The zeta potential was derived from the electrophoretic mobility of the peptides and measured using a Zeta Nanosizer ZS (Malvern Instruments) with 1 mL disposable folded capillary cells (Zetasizer Nano series, Malvern). Each measurement was performed in triplicates.

7. Laser scanning microscopy

For cell-binding studies 60 000 TZM-bl cells were seeded in 8-well IBIDI slides and stained the following day with Hoechst for 5 min at 37°C. 180 µL preformed PNF fibrils were stained with 20 µL diluted Proteostat Amyloid plaque detection kit solution according to suppliers' protocols (Enzo Life Science) to get a final concentration of 5 µg/ml. After 5 min, fibril mixtures were transferred to TZM-bl cells. The interaction of fibril clusters with cells was monitored after 30 min incubation time on a Leica confocal microscope with laser excitation wavelengths of 405 nm (Hoechst) and 561 nm (Proteostat). After 1h incubation, samples were washed three times with PBS and analysed again. For MLV-binding studies 180 µl preformed and Proteostat stained fibrils were mixed with 20 µl MLV-YFP and incubated for 10 min. to get a final concentration of 50 µg/ml. Then the mixture was added to an 8-well IBIDI slide and analysed after sedimentation with laser excitation of 488 nm (YFP) and 561 nm (Proteostat).

8. Conversion rate

For the determination of the amount of peptide monomer converting into fibrils, we established a fluorescence-based assay using amine reactive dye fluorescamine.[1] Each PNF was incubated in PBS for 1 d with a concentration of 1 mg/mL (200 µL). 100 µL sample was centrifuged using a Vivaspin 500 tube (3kDa MWCO) to separate free monomers from fibrils (16.06 g, 4°C, 45 min). The other 100 uL of the sample served as a reference (original sample). Both the filtrate and the original sample were lyophilized and then dissolved in 25 µL DMSO. In a black 384-well-plate (Greiner Bio-one) 10 µL of DMSO sample (original sample and filtrate) was added and mixed with 3 uL of fluorescamine solution (3 mg/mL, DMSO). Fluorescence enhancement was measured with an excitation wavelength of λ_{ex}= 365 nm and an emission wavelength of λ_{em}= 470 nm with multiple reads 3x3 (Infinite® M1000 PRO microplate reader) after 20 mins of incubation. All values were calculated as n-fold fluorescence enhancement (DMSO-only as a reference was set to 1). The conversion rate CR was defined according to the following equation:

$$CR = 100 - \frac{100 \times Fluorescence\ Intensity\ (Filtrate)}{Fluorescence\ Intensity\ (Original)}\ [\%]$$

9. Proteostat® assay

Fluorescence spectra were recorded on an Infinite® M1000 PRO microplate reader (Tecan). 9 µL of sample aliquots (incubated for 1d in PBS at 1 mg/mL) were placed in black UV Star® 384 microliter well-plates (Greiner bio-one). A ProteoStat® solution was prepared according to manufacturers' protocol and diluted hundred-fold in PBS. After addition of 1 µL of Proteostat® solution to every sample and 10 mins of incubation time, the fluorescence emission was recorded at 603 nm upon excitation at 550 nm with multiple reads per well (3x3).

10. Effect of PNF on HIV-1 infection

HIV-1 NL4-3 (R5) virus stocks were generated by calcium phosphate transfection as described before.[2] 10000 TZM-bl cells (a HeLa cell line derivative that expresses high amounts of human CD4, CCR5 and CXCR4 and contain a ß-galactosidase gene under the control of the HIV-1 long terminal repeat (LTR) promotor) were seeded into 96-well plates in 100 µL DMEM. On the next day, 80 µL fresh medium was added to the cells. 40 µL dilutions of EF-C or PNF solutions were prepared in PBS and mixed 1:1 (v/v) with 40 µL virus (pre-diluted 1:30 (v/v) in cell culture medium) by resuspending. After 10 min incubation to allow binding of virus particles to fibrils, 20 µL of virus-fibril mixture was added to 180 µL of cells. 3 days post infection, viral infectivity was determined using a galactosidase screen kit from Tropix as recommended by the manufacturer. β-Galactosidase activities were quantified as relative light units (RLU) per second with an Orion Microplate luminometer (Berthold).

11. CellTiter-Glo assay

TZM-bl cells were seeded in 96 well plates (~6000 cells/well). On the following day, 50 µL of fibril samples (130 µM) were added and serial diluted to the final concentrations of 65, 13, 2.6 and 0 µM. 50 µL of CellTiter-Glo mix was added and shaken for 2 mins. After 10 mins

50 µL were transferred to white plates and luminescence was recorded using an Orion microplate luminometer (Berthold).

12. Generation of lenti- and γ-retroviral vectors

800 000 HEK293T cells were seeded in 2 ml DMEM one day prior to the transfection. Cells were cotransfected with 250 µl OptiMEM containing 2.5 µg DNA and 7.5µl TransIT-LT1. For GALV pseudotyped γ-retrovirus, plasmids were used in a ratio 3:1:2.5 (pcmE26-gfp : GALV : pCsGPpA-ed). For VSV-G pseudotyped pSEW LUC2, plasmids were used in a ratio 2:2:1 (pSEW-luc: VSV-G : delta8.9). 64 h after transfection, virus was harvested, centrifuged for 3 min at 1300 rpm and stored at -80°C. VSV-G pseudotyped HIV-1 NL4-3 Firefly-Luciferase reporter virus stocks were generated using the calcium phosphate transfection method. For this, env-deficient proviral NL4-3 plasmid DNA and VSV-G env plasmid DNA were inoculated with $CaCl_2$ and ultrapure water before being mixed with 1x HBS. After incubation for 10 min at room temperature, the 200 µL of the transfection mix were added to 650,000 HEK293T cells/well seeded one day prior to the transfection in 6W plates. 16 hours post transfection, transfection mix was removed from the cells and cell culture medium was replaced with fresh medium. 48 hours post transfection, virus stocks were harvested, characterized by p24 ELISA and frozen at -80°C. HIV-1 NL4-3 (R5) virus stocks were generated by calcium phosphate transfection as described before.[3]

13. Effect of PNF on VSV-G pseudotyped lentiviral transduction

To determine the effect of PNF on VSV-G pseudotyped HIV-1 or VSV-G pseudotyped pSEW LUC2 transduction, 10 000 cells were seeded in 96W microtiter plates. The next day, virus stocks were inoculated for 10 minutes with either EF-C or PNF-13 to allow binding of virus particles to fibrils. Indicated fibril concentrations were achieved during this inoculation step.

180 µL cells were subsequently infected with 20 µL of these PNF/VS mixtures in triplicates to achieve the indicated final concentrations of p24/mL on the cells. Three days post infection, infection rates were determined using the Firefly luciferase reporter assay (Promega). Firefly-Luciferase activities were quantified as relative light units (RLU) per second with an Orion Microplate luminometer (Berthold).

14. Effect of PNF on GALV pseudotyped γ-retroviral transduction

PBMCs were isolated using lymphocyte separation medium (Biocoll separating solution; Biochrom, Berlin, Germany). CD4 +T cells were isolated using the RosetteSep Human CD4 +T Cell Enrichment Cocktail (Stem Cell Technologies, Vancouver, Canada). Primary cells were cultured in RPMI-1640 containing 10% fetal calf serum (FCS), 2 mM glutamine, streptomycin (100 µg ml^{-1}), penicillin (100 U ml^{-1}), and 66 IU ml^{-1} = 10 ng ml^{-1} interleukin 2 (IL-2). Before infection, primary cells were stimulated for three days with phytohemagglutinin (PHA) (1 µg ml^{-1}). 20 000 CD4 +T cells were seeded into 96-well plates in 100 µl RPMI. Next day, 80 µl fresh medium was added to the cells. Dilutions of EF-C or PNF-13 were prepared in 80µl volume and mixed with 80µl virus (virus was diluted 1:8 in RPMI without FCS). After 10 min incubation to allow binding of virus particles to fibrils, 20µl of virus-fibril mixture was added to 180 µl cells. 3 days post infection percentage of GFP+ cells were determined by flow cytometry.

Supporting Tables

Table S1. Qualitative fibril formation determined via transmission electron microscopy ("+" for fibrils, and "-" for no fibrils/aggregates). Ability to bind Proteostat ("Prot bind.," "+" for ≥10 n-fold fluorescence enhancement and "-" for ≤10 n-fold fluorescence enhancement). Zeta potential calculated by electrophoretic mobility. Conversion rate ("CR") as the percentage of monomers converting into a fibril. Entries marked with * have previously been published.[1]

PNF name	sequence	TEM	Prot bind.	Zeta potential [mV]	CR [%]
PNF-1	CKIKQIINMWQ	+	+	+11.8 ± 0.4	50
PNF-2	CKIKQIINM	+	+	+19.1 ± 0.5	45*
PNF-3	CKIKQII	+	+	+0.6 ± 1.5	55*
PNF-4	KIKQIINMWQ	+	+	+10.8 ± 0.2	86
PNF-5	KIKQIINM	+	+	+16.5 ± 0.5	43
PNF-6	KIKQII	-	-	-	6
PNF-7	CKIKIQINMWQ	+	+	+10.7 ± 2.8*	87*
PNF-8	CKIKIQINM	+	+	+22.3 ± 0.6*	72*
PNF-9	CKIKIQI	+	+	+17.4 ± 1.1*	54*
PNF-10	KIKIQINMWQ	+	+	+17.2 ± 0.7	93*
PNF-11	KIKIQINM	+	+	+41.9 ± 1.1*	64*
PNF-12	KIKIQI	-	-	-	5*
PNF-13	CKAKAQANMWQ	+	-	-4.4 ± 3.2	92
PNF-14	CKAKAQANM	+	-	-3.7 ± 0.9	38
PNF-15	CKAKAQA	+	-	-9.1 ± 1.6	44
PNF-16	CKFKFQFNMWQ	+	+	+14.1 ± 0.8	96
PNF-17	CKFKFQFNM	+	-	+15.9 ± 0.4	88
PNF-18	CKFKFQF	+	+	+22.3 ± 1.4*	95*
PNF-19	CEIEIQINMWQ	+	+	-35.8 ± 1.2	74
PNF-20	CEIEIQINM	+	+	-38.6 ± 5.2	43
PNF-21	CEIEIQI	+	+	-41.9 ± 1.1	59
PNF-S1	KAKAQANMWQ	+	+	-19.6 ± 1.7	65
PNF-S2	KAKAQANM	+	n.d.	n.d.	n.d.
PNF-S3	KAKAQA	+	n.d.	n.d.	n.d.
PNF-S4	KFKFQFNMWQ	+	-	+27.4 ± 0.3	94

PNF-S5	KFKFQFNM	+	-	+20.1 ± 1.9*	91
PNF-S6	KFKFQF	+	-	-	83*
PNF-S7	MKIKIQI	+	-	10.1 ± 0.9	51
PNF-S8	MKFKFQF	+	-	+8.8 ± 0.5	75
PNF-S9	CSISIQINM	+	+	-31.7 ± 2.8	86
PNF-S10	CSISIQI	+	+	-31.8 ± 1.5	82

Table S2. Average RLU/s in infectivity assays of the peptides over multiple experiments at 13 and 65 µM.

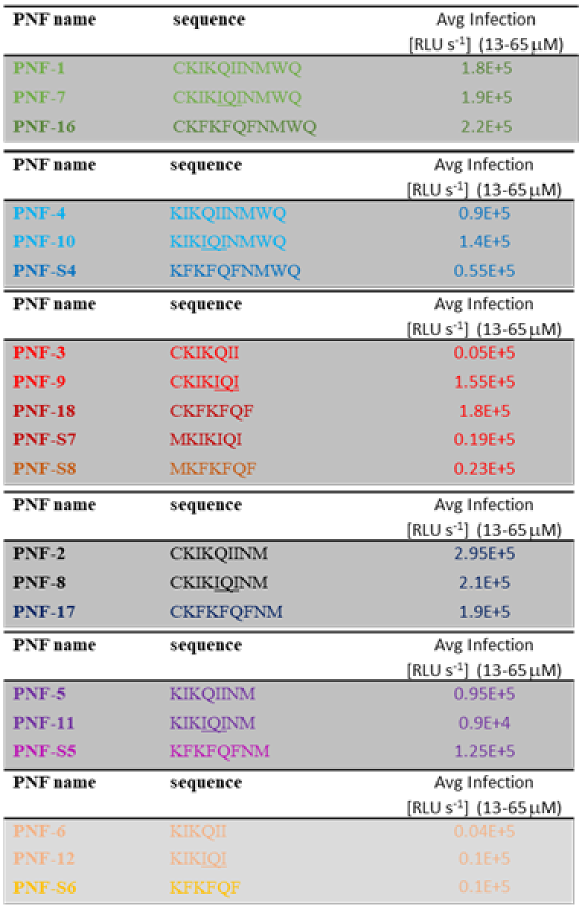

PNF name	**sequence**	Avg Infection [RLU s⁻¹] (13-65 µM)
PNF-1	CKIKQIINMWQ	1.8E+5
PNF-7	CKIKIQINMWQ	1.9E+5
PNF-16	CKFKFQFNMWQ	2.2E+5

PNF name	**sequence**	Avg Infection [RLU s⁻¹] (13-65 µM)
PNF-4	KIKQIINMWQ	0.9E+5
PNF-10	KIKIQINMWQ	1.4E+5
PNF-S4	KFKFQFNMWQ	0.55E+5

PNF name	**sequence**	Avg Infection [RLU s⁻¹] (13-65 µM)
PNF-3	CKIKQII	0.05E+5
PNF-9	CKIKIQI	1.55E+5
PNF-18	CKFKFQF	1.8E+5
PNF-S7	MKIKIQI	0.19E+5
PNF-S8	MKFKFQF	0.23E+5

PNF name	**sequence**	Avg Infection [RLU s⁻¹] (13-65 µM)
PNF-2	CKIKQIINM	2.95E+5
PNF-8	CKIKIQINM	2.1E+5
PNF-17	CKFKFQFNM	1.9E+5

PNF name	**sequence**	Avg Infection [RLU s⁻¹] (13-65 µM)
PNF-5	KIKQIINM	0.95E+5
PNF-11	KIKIQINM	0.9E+4
PNF-S5	KFKFQFNM	1.25E+5

PNF name	**sequence**	Avg Infection [RLU s⁻¹] (13-65 µM)
PNF-6	KIKQII	0.04E+5
PNF-12	KIKIQI	0.1E+5
PNF-S6	KFKFQF	0.1E+5

Table S3. Collected fractions for all peptides after purification with HPLC, see Supplementary Fig. 12. Calculated mass and assignments for all signals found in mass spectra with an intensity of at least 10 % in relation to the main peak. Entries marked with * have previously been published.[1] PNF marked with ** have been purchased from Phtd Peptides industrial Co. limited with purit ≥ 95%.

SAP name	fraction collected [min]	calc. exact mass [g mol^{-1}]	m/z found
PNF-1	10.90 to 11.89	1403.74	1404.75 [M+H]$^{+}$, 1416.75 [unknown], 1420.75 [M+O+H]$^{+}$, 2807.48 [2M-2H+H]$^{+}$, 2823.48 [2M-2H+O+H]$^{+}$
PNF-2*	9.81 to 10.79	1089.60	976.57 [M-ASN+H]$^{+}$, 1090.61 [M+H]$^{+}$, 1112.59 [M+Na]$^{+}$, 1196.65 [M+Anisyl+H]$^{+}$, 2065.15 [unknown], 2179.20 [2M-2H+H]$^{+}$, 2201.18 [2M-2H+Na]$^{+}$
PNF-3*	9.63 to 10.05	844.52	845.53 [M+H]$^{+}$, 867.51 [M+Na]$^{+}$, 1034.57 [M+CHCA+H]$^{+}$, 1688.03 [2M-2H+H]$^{+}$, 1710.01 [2M-2H+Na]$^{+}$
PNF-4	10.42 to 11.02	1300.73	1301.74 [M+H]$^{+}$
PNF-5	9.55 to 10.12	986.59	987.60 [M+H]$^{+}$, 1003.60 [M+O+H]$^{+}$
PNF-6	9.09 to 9.65	741.51	742.52 [M+H]$^{+}$, 764.50 [M+Na]$^{+}$
PNF-7*	10.29 to 11.28	1403.74	1404.75 [M+H]$^{+}$, 1420.74 [M+O+H]$^{+}$, 1426.73 [M+Na]$^{+}$, 1436.74 [unknown], 1452.73 [unknown], 2807.47 [2M-2H+H]$^{+}$
PNF-8*	10.25 to 10.67	1089.60	976.57 [M-ASN+H]$^{+}$, 1090.61 [M+H]$^{+}$, 1003.60 [M+O+H]$^{+}$, 2065.16 [unknown], 2179.20 [2M-2H+H]$^{+}$
PNF-9	9.96 to 10.48	844.52	845.53 [M+H]$^{+}$, 857.53 [unknown], 867.51 [M+Na]$^{+}$, 1688.03 [2M-2H+H]$^{+}$, 1710.02 [2M-2H+Na]$^{+}$, 1725.99 [unknown]
PNF-10*	10.65 to 11.29	1300.73	1301.74 [M+H]$^{+}$, 1317.74 [M+O+H]$^{+}$, 1323.55 [M+Na]$^{+}$, 1349.73 [unknown]
PNF-11*	9.96 to 10.49	986.59	987.60 [M+H]$^{+}$, 1003.60 [M+O+H]$^{+}$

PNF-12*	9.82 to 10.29	741.51	742.52 $[M+H]^+$, 764.50 $[M+Na]^+$
PNF-13	8.95 to 9.68	1277.60	1278.61 $[M+H]^+$
PNF-14**	n.d.	963.46	n.d.
PNF-15**	n.d.	718.38	n.d.
PNF-16	10.99 to 11.98	1505.69	1506.70 $[M+H]^+$, 1522.70 $[M+O+H]^+$, 1528.69 $[M+Na]^+$
PNF-17	10.84 to 11.48	1191.56	1192.56 $[M+H]^+$, 1204.56 [unknown]
PNF-18*	10.78 to 11.38	946.47	947.48 $[M+H]^+$, 1136.52 $[M+CHCA+H]^+$, 1892.94 $[2M-2H+H]^+$
PNF-19**	n.d.	1405.64	n.d.
PNF-20**	n.d.	1091.50	n.d.
PNF-21**	n.d.	846.42	n.d.
PNF-S1	8.16 to 9.15	1174.59	1175.60 $[M+H]^+$, 1191.60 $[M+O+H]^+$, 1223.59 [unknown]
PNF-S2**	n.d.	860.45	n.d.
PNF-S3**	n.d.	615.37	n.d.
PNF-S4	11.16 to 11.80	1402.69	1403.69 $[M+H]^+$, 1419.69 $[M+O+H]^+$, 1435.69 [unknown], 1451.68 [unknown]
PNF-S5*	10.09 to 11.08	1088.55	1089.55 [M+H]+, 1105.55 [M+O+H]+, 1111.54 $[M+Na]^+$
PNF-S6*	10.64 to 11.41	843.46	844.47 [M+H]+, 866.45 [M+Na]+
PNF-S7	10.25 to 10.79	872.55	873.56 $[M+H]^+$, 889.55 $[M+O+H]^+$, 895.54 $[M+Na]^+$, 911.52 $[M+K]^+$
PNF-S8	9.99 to 10.98	974.50	975.51 $[M+H]^+$, 991.51 $[M+O+H]^+$
PNF-S9**	n.d.	1007.48	n.d.
PNF-S10**	n.d.	762.39	n.d.

Supporting Figures

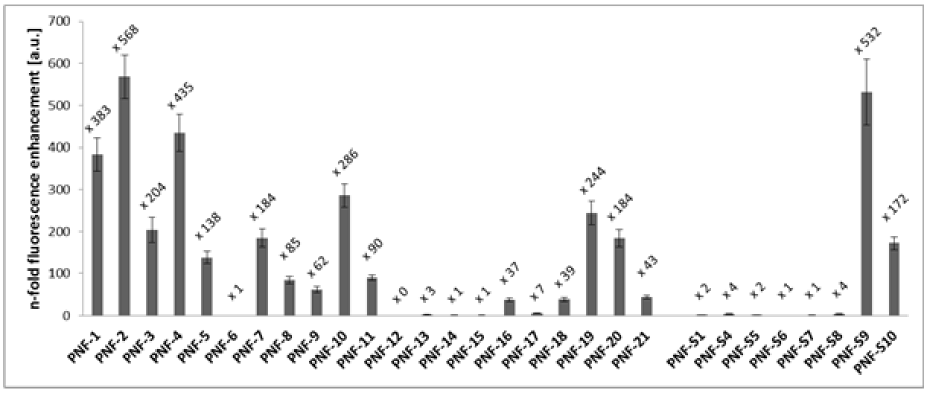

Figure S1: Proteostat® assay showing n-fold fluorescence enhancement of preformed PNF samples at 1 mg mL^{-1}.

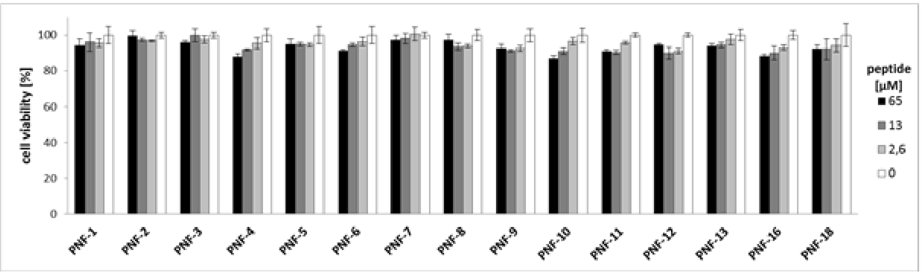

Figure S2: CellTiter-Glo cell viability assay of TZM-bl cells treated with increasing concentrations of PNFs. Values shown indicate mean values derived from biological triplicate ± standard deviation.

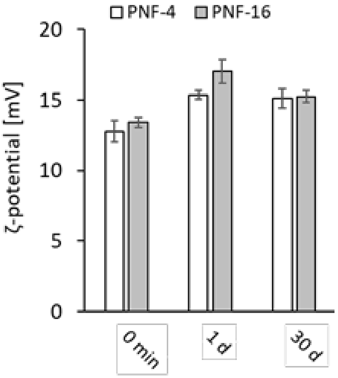

Figure S3: Time-dependent ζ-potential measurements of PNF-4 and PNF-16.

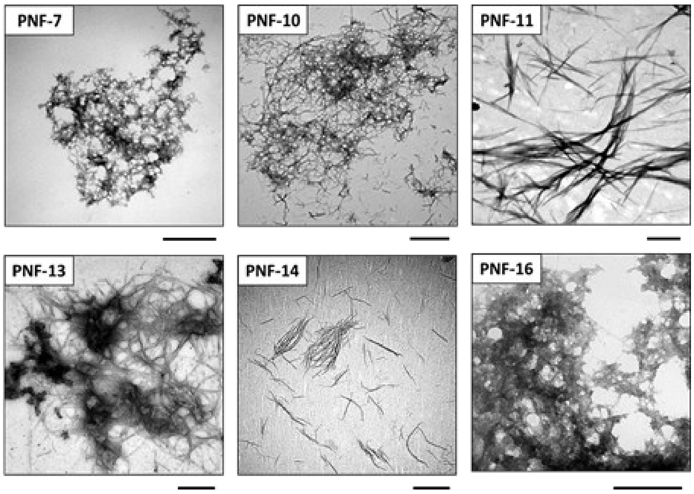

Figure S4: Representative TEM micrographs of PNF assemblies. Scale bars represent 500 nm.

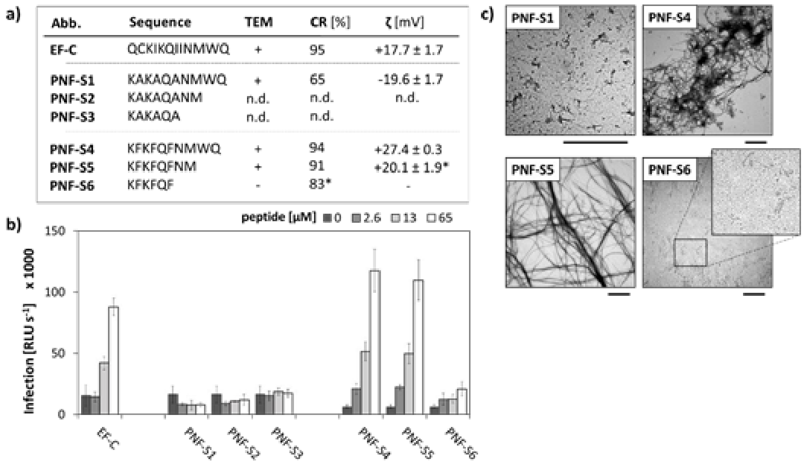

a)

Abb.	Sequence	TEM	CR [%]	ζ [mV]
EF-C	QCKIKQIINMWQ	+	95	+17.7 ± 1.7
PNF-S1	KAKAQANMWQ	+	65	-19.6 ± 1.7
PNF-S2	KAKAQANM	n.d.	n.d.	n.d.
PNF-S3	KAKAQA	n.d.	n.d.	
PNF-S4	KFKFQFNMWQ	+	94	+27.4 ± 0.3
PNF-S5	KFKFQFNM	+	91	+20.1 ± 1.9*
PNF-S6	KFKFQF	-	83*	-

Figure S5: a) Tabular list of alanine and phenylalanine containing peptide derivatives, including the ability to form PNFs for PNF-S1, PNF-S4 and PNF-S5 as observed in TEM measurements with + = fibrils and - = no aggregate formation detected. Monomer-to-fibril conversion rates (CR) were determined in a fluorescence-based assay. High values indicate a large percentage of peptides participating in fibril formation. Zeta potential values for PNF solutions. b) Transduction enhancement assay showing HIV-1 infection rates of TZM-bl cells observed in the presence of increasing concentrations of PNF. Shown are mean values derived from triplicate infections ± standard deviation. RLU/s; relative light units per second. c) Representative TEM micrographs of PNF assemblies. Scale bars represent 500 nm. Entries marked with * have previously been published.[1]

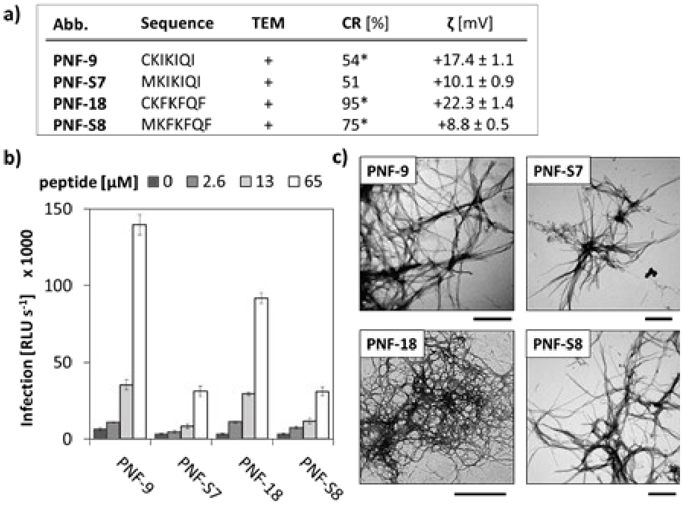

a)

Abb.	Sequence	TEM	CR [%]	ζ [mV]
PNF-9	CKIKIQI	+	54*	+17.4 ± 1.1
PNF-S7	MKIKIQI	+	51	+10.1 ± 0.9
PNF-18	CKFKFQF	+	95*	+22.3 ± 1.4
PNF-S8	MKFKFQF	+	75*	+8.8 ± 0.5

Figure S6: a) Tabular list of cysteine and methionine containing peptide derivatives, including the ability to form PNFs as observed in TEM measurements with + = fibrils and - = no aggregate formation detected. Monomer-to-fibril conversion rates (CR) were determined in a fluorescence-based assay. High values indicate a large percentage of peptides participating in fibril formation. Zeta potential values for PNF solutions. b) Transduction enhancement assay showing HIV-1 infection rates of TZM-bl cells observed in the presence of increasing concentrations of PNF. Shown are mean values derived from triplicate infections ± standard deviation. RLU/s; relative light units per second. c) Representative TEM micrographs of PNF assemblies. Scale bars represent 500 nm. Entries marked with * have previously been published.[1]

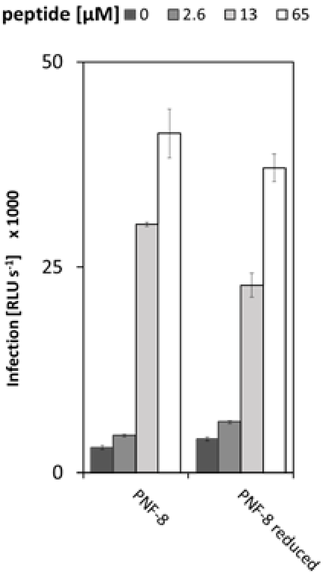

Figure S7: Transduction enhancement assay showing HIV-1 infection rates of TZM-bl cells observed in the presence of increasing concentrations of PNF. Shown are mean values derived from triplicate infections ± standard deviation. RLU/s; relative light units per second. PNF-8 and PNF-8 treated with 1 eq TCEP before inducing self-assembly.

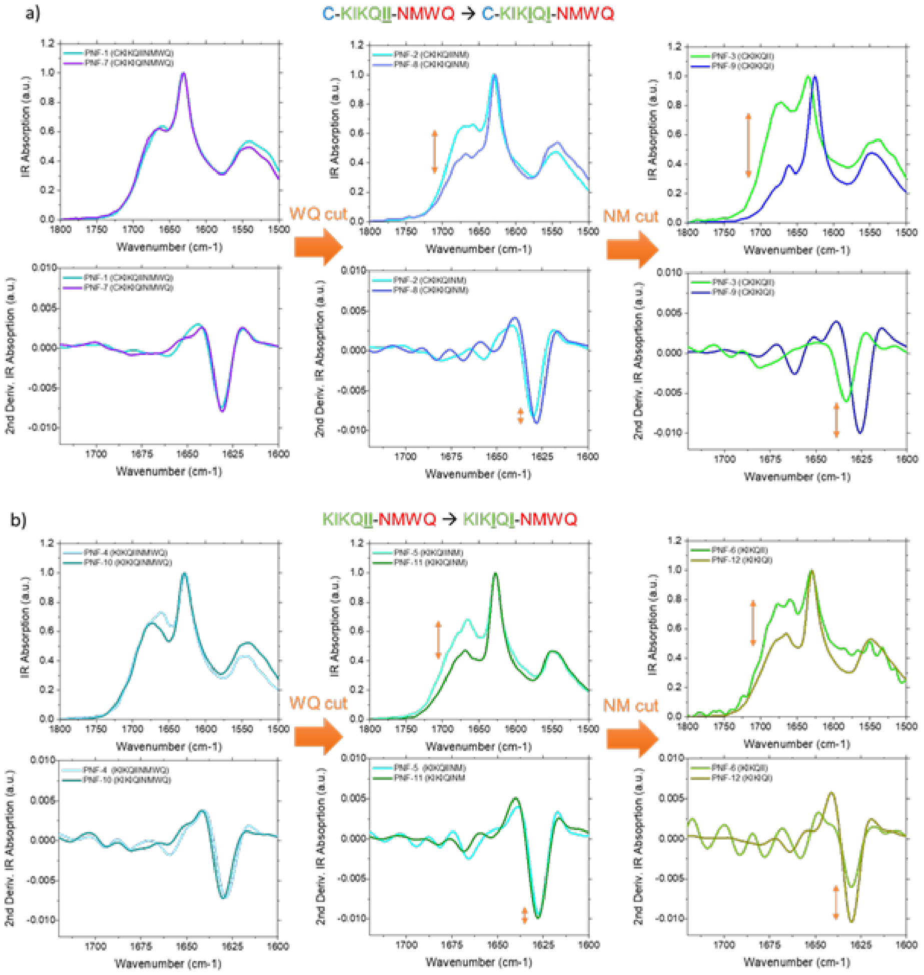

Figure S8: Structural variability upon intrinsic switch in a) presence and b) absence of the N-terminal cysteine.

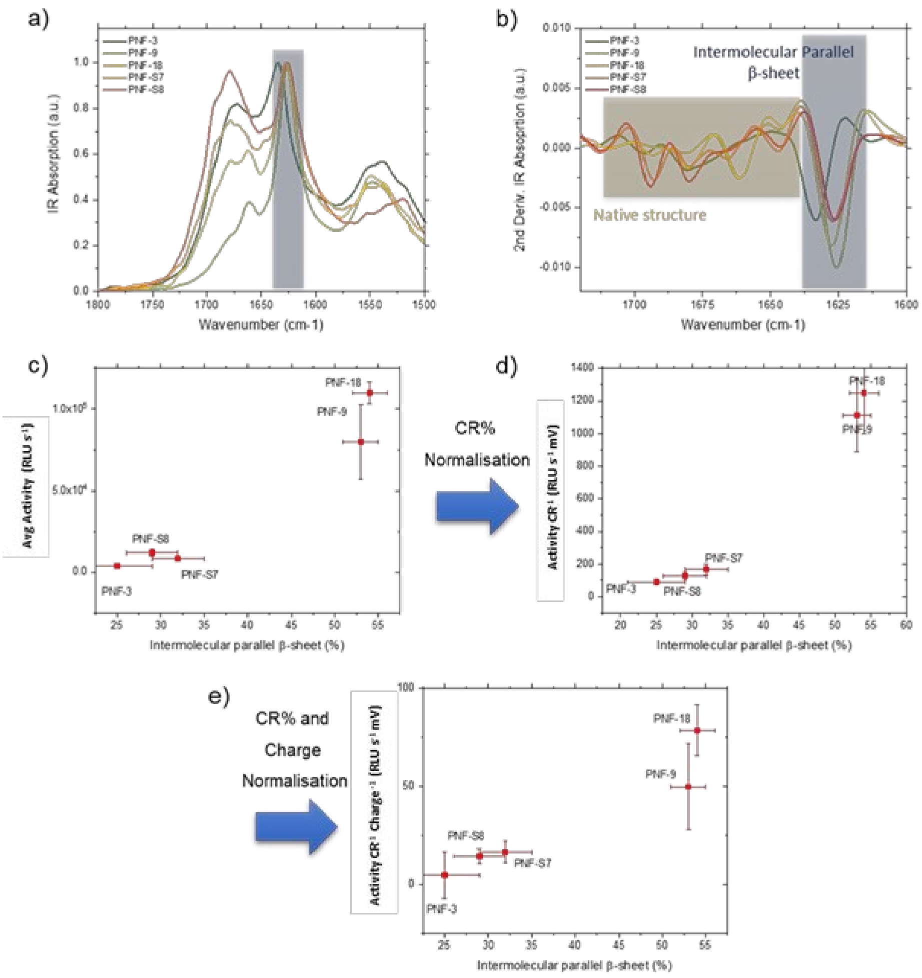

Figure S9: Structural variability upon intrinsic switch in a) presence and b) absence of the N-terminal cysteine.

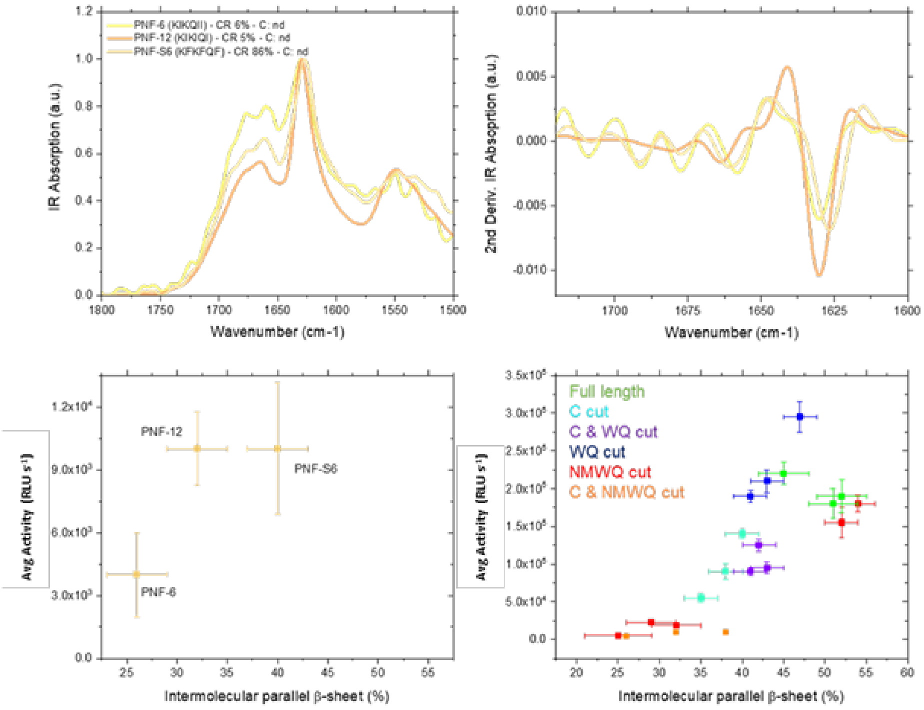

Figure S10: Structural variability vs. activity for PNF-6, -12, S6.

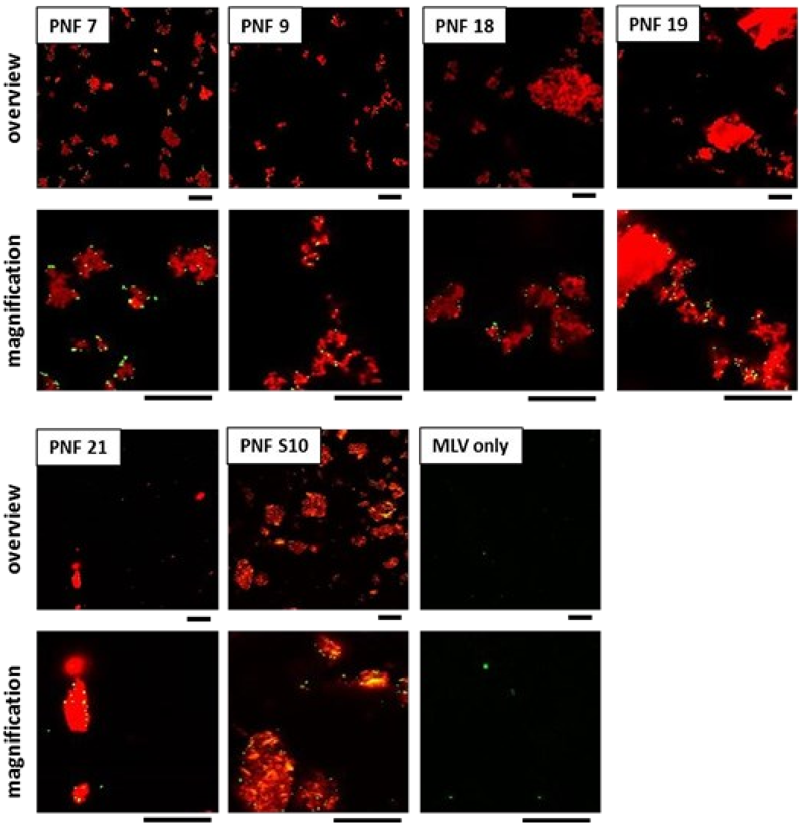

Figure S11: Laser scanning micrographs of different Proteostat® stained PNFs (red) incubated with MLV-YFP (green) to investigate attractions between fibrils and viral particles. Scale bars represent 20 µm.

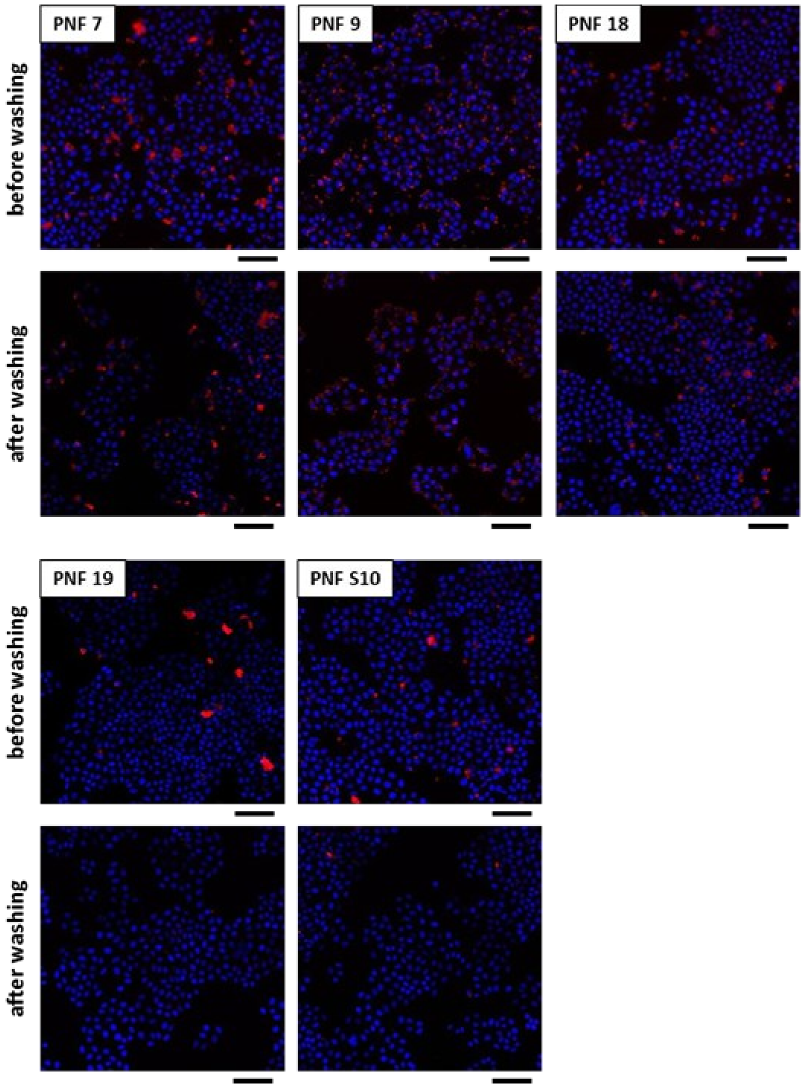

Figure S12: Laser scanning micrographs of Proteostat® stained PNFs (red) incubated on Hoechst stained TZM-bl cells (blue) for determination of PNF cell attachment before and after washing with PBS. Scale bars represent 100 µm.

a)

Abb.	Sequence	TEM	CR [%]	ζ [mV]
PNF-S9	CSISIQINM	+	86	-31.7 ± 2.8
PNF-S10	CSISIQI	+	82	-31.8 ± 1.5

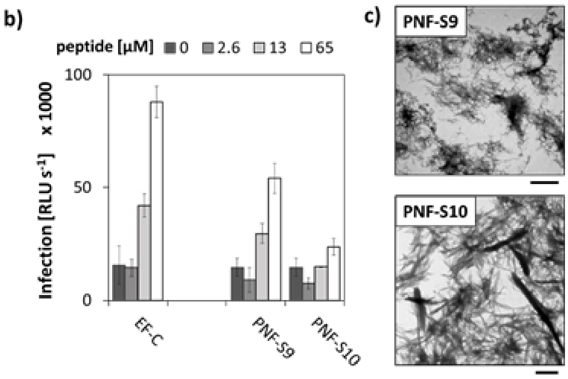

Figure S13: a) Tabular list of serine containing peptide derivatives, including the ability to form PNFs as observed in TEM measurements with + = fibrils and - = no aggregate formation detected. Monomer-to-fibril conversion rates (CR) were determined in a fluorescence-based assay. High values indicate a large percentage of peptides participating in fibril formation. Zeta potential values for PNF solutions. b) Transduction enhancement assay showing HIV-1 infection rates of TZM-bl cells observed in the presence of increasing concentrations of PNF. Shown are mean values derived from triplicate infections ± standard deviation. RLU/s; relative light units per second. c) Representative TEM micrographs of PNF assemblies. Scale bars represent 500 nm.

PNF-1

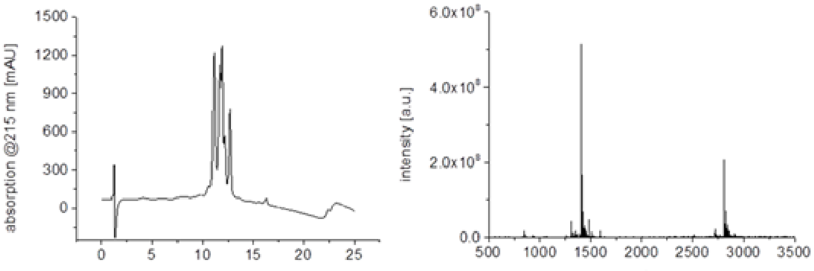

PNF-2*

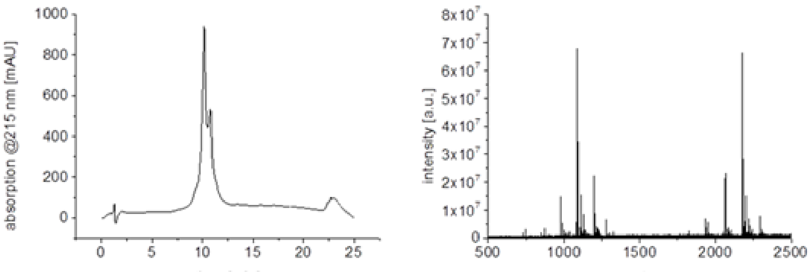

PNF-3*

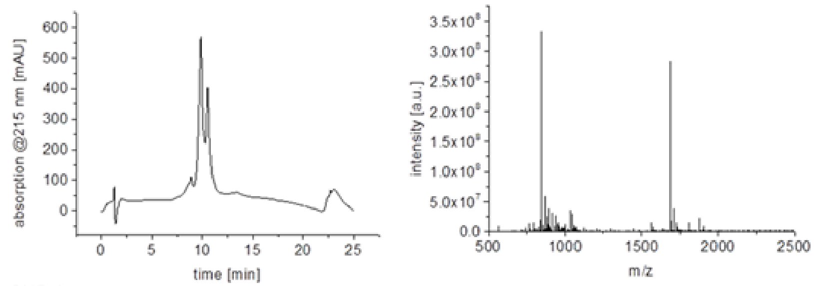

PNF-4

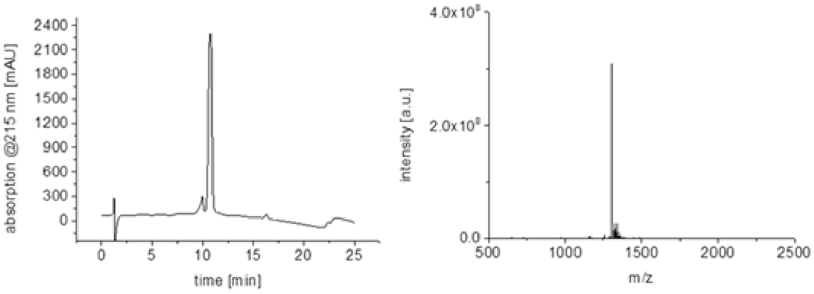

Figure S14: ctnd.

PNF-5

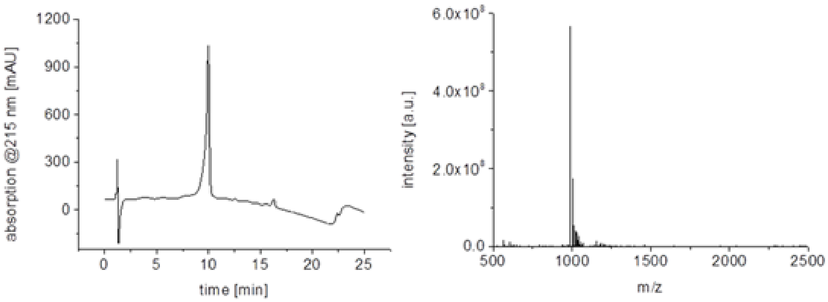

PNF-6

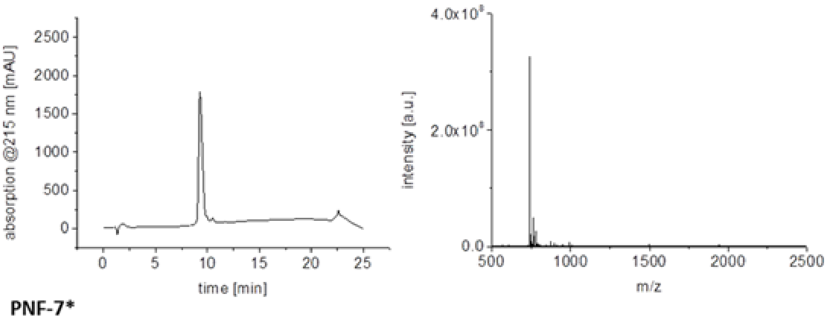

PNF-7*

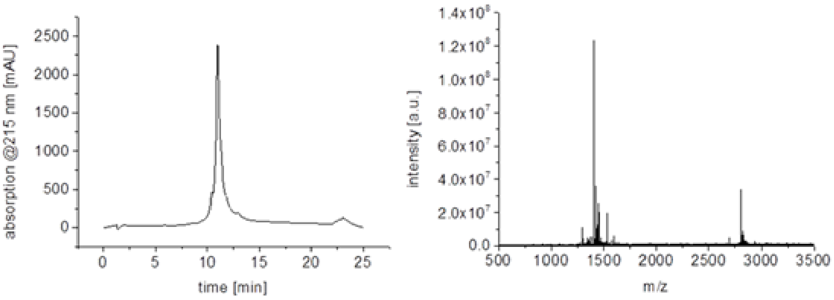

PNF-8*

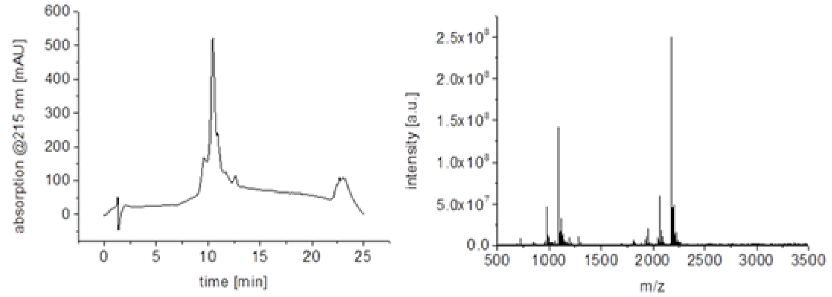

Figure S14: ctnd.

PNF-9

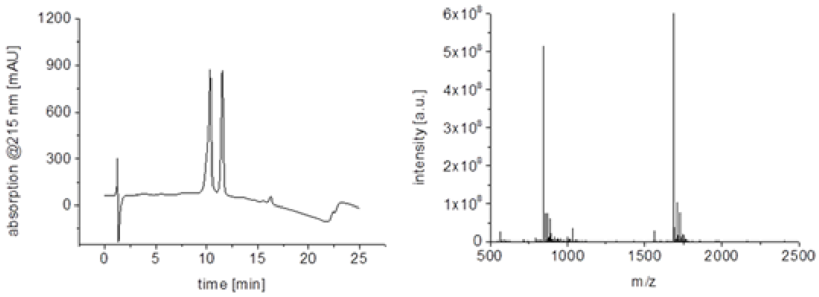

PNF-10*

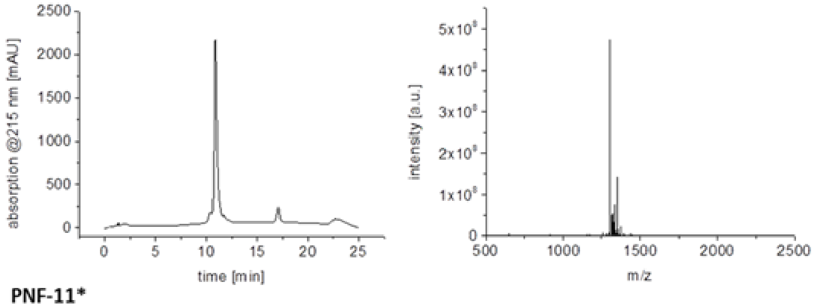

PNF-11*

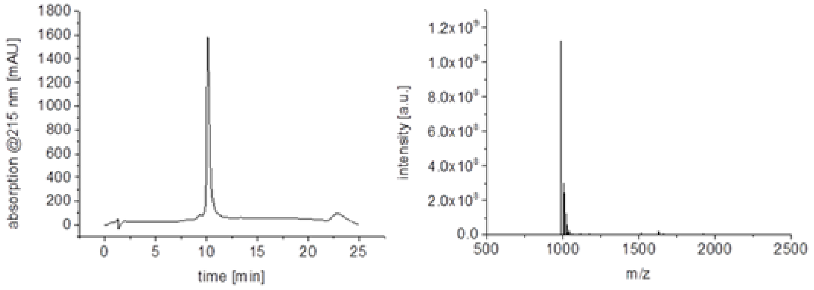

PNF-12*

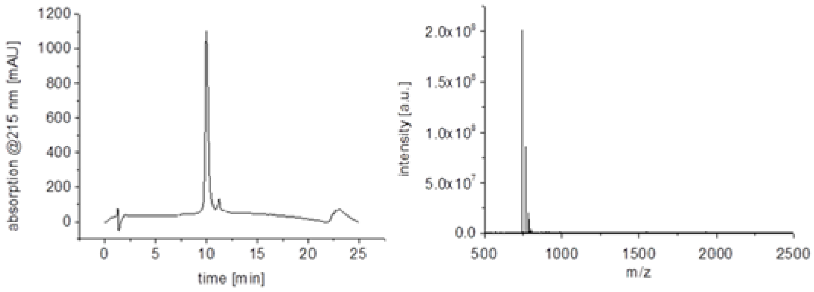

Figure S14: ctnd.

PNF-13

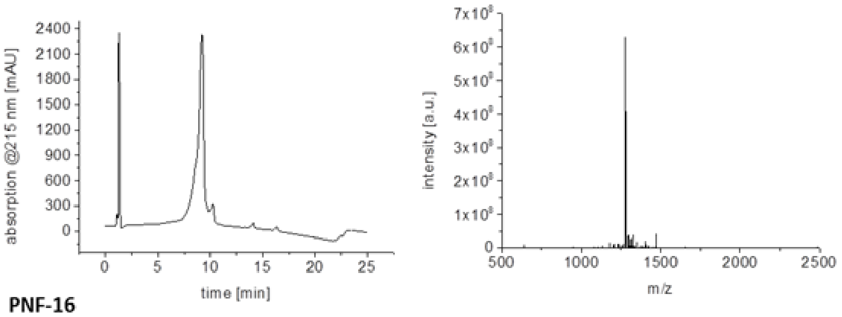

PNF-16

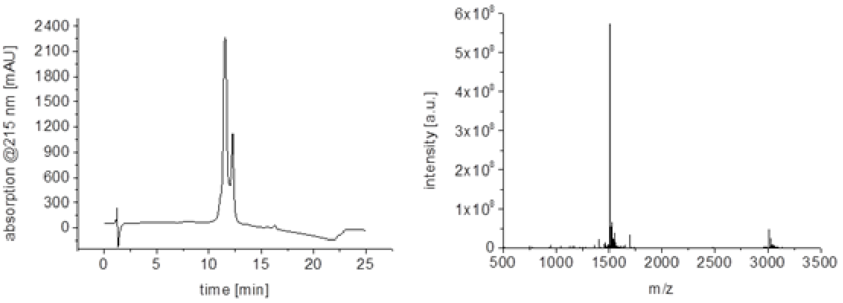

PNF-17

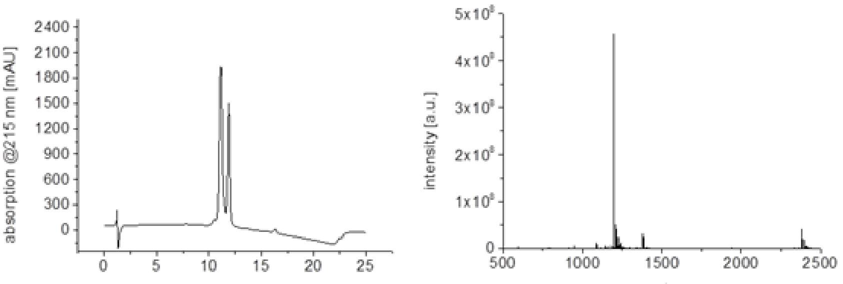

PNF-18*

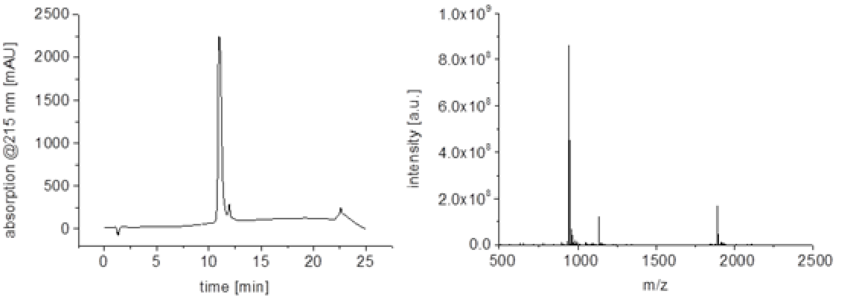

Figure S14: ctnd.

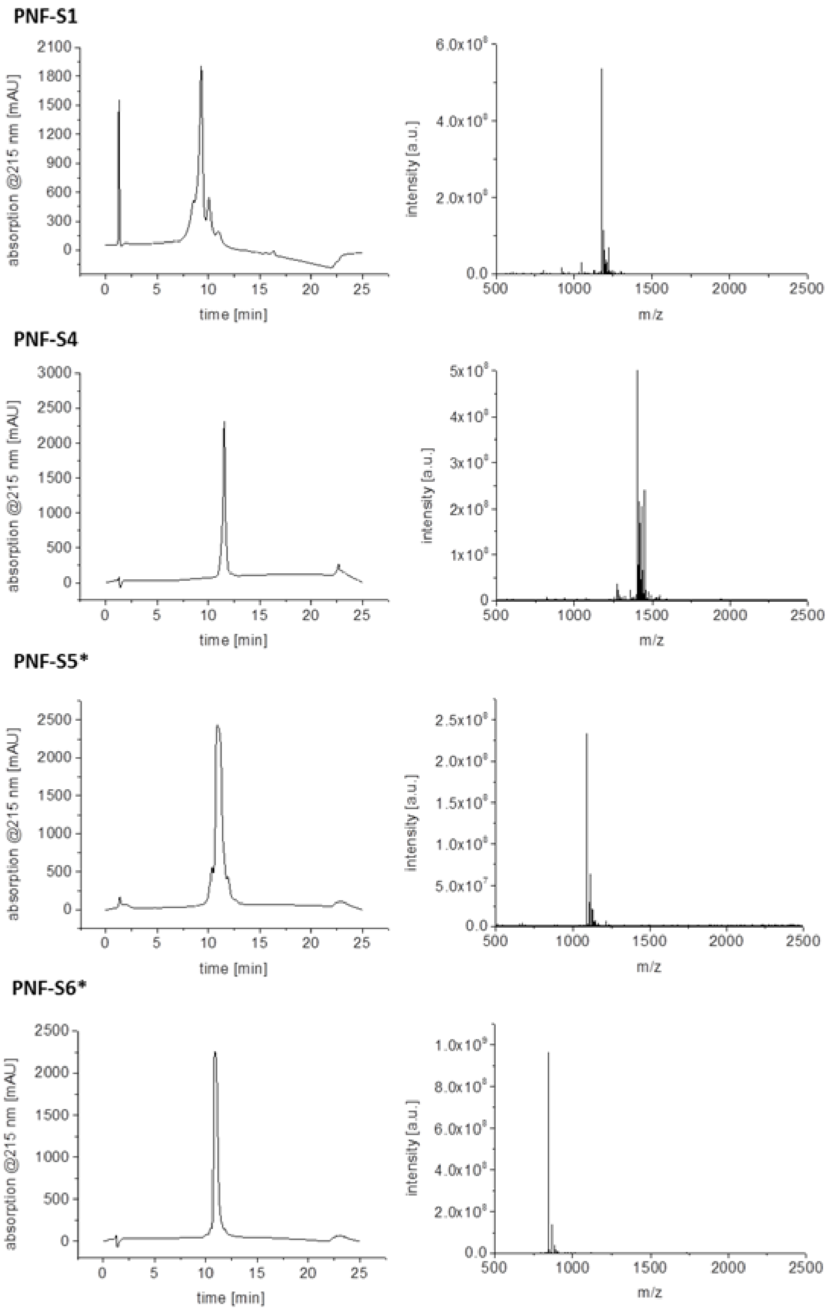

Figure S14: ctnd.

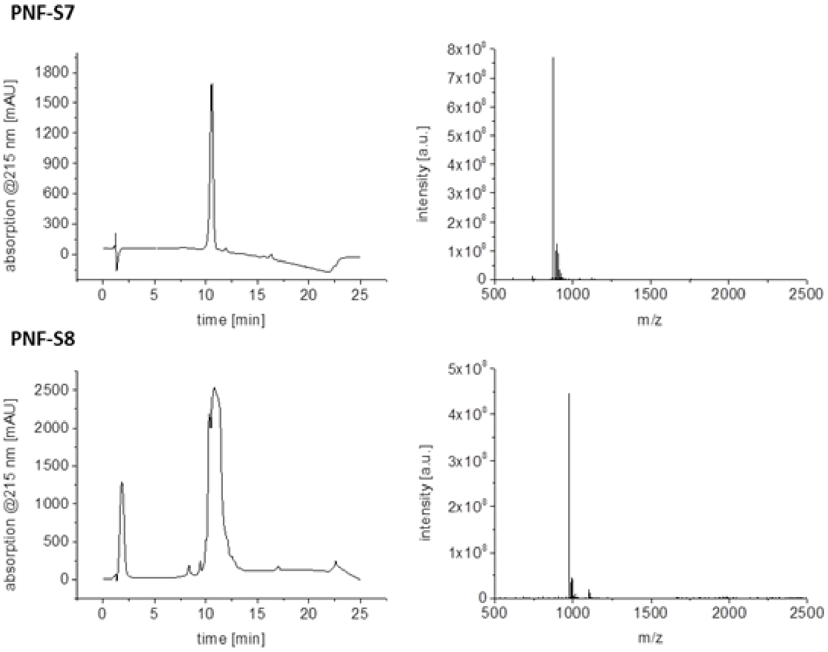

Figure S14: High performance liquid chromatograms of PNFs and corresponding MALDI spectra of purified fractions. Entries marked with * have previously been published.[1]

References

[1] C. Schilling, T. Mack, S. Lickfett, S. Sieste, F. S. Ruggeri, T. Sneideris, A. Dutta, T. Bereau, R. Naraghi, D. Sinske, T. P. J. Knowles, C. V. Synatschke, T. Weil, B. Knöll, *Adv. Funct. Mater.* **2019**, *29*, 1809122.

[2] M. Yolamanova, *Ph.D. Thesis*, Univeristy Ulm, **2016**.

[3] A. Papkalla, J. Münch, C. Otto, F. Kirchhoff, *J. Virol.* **2002**, *76*, 8455.

References

1. Tasciotti, E., Sakamoto, J. & Ferrari, M. 12th Annual International Conference on the Industrial and Medical Applications of Nanotechnology. *Nanomedicine* **4**, 619–621 (2009).
2. Feynman, R. P. There's Plenty of Room at the Bottom. *Talk* (1960).
3. Iqbal, P., Preece, J. A. & Mendes, P. M. Nanotechnology : The " Top-Down " and " Bottom-Up " Approaches. *Supramol. Chem. From Mol. to Nanomater. John Wiley Sons, Ltd* **Volume 8**, 1–14 (2012).
4. Majumder, D. D., Banerjee, R., Ulrichs, C., Mewis, I. & Goswami, A. Nano-materials: Science of bottom-up and top-down. *IETE Tech. Rev. (Institution Electron. Telecommun. Eng. India)* **24**, 9–25 (2007).
5. Ronse, K. Optical lithography-a historical perspective. *Comptes Rendus Phys.* **7**, 844–857 (2006).
6. Mendes, A. C., Baran, E. T., Reis, R. L. & Azevedo, H. S. Self-assembly in nature: Using the principles of nature to create complex nanobiomaterials. *Wiley Interdiscip. Rev.: Nanomed. Nanobiotechnol* **5**, 582–612 (2013).
7. Li, H., LaBean, T. H. & Leong, K. W. Nucleic acid-based nanoengineering: Novel structures for biomedical applications. *Interface Focus* **1**, 702–724 (2011).
8. Liu, Z., Qiao, J., Niu, Z. & Wang, Q. Natural supramolecular building blocks: From virus coat proteins to viral nanoparticles. *Chem. Soc. Rev.* **41**, 6178–6194 (2012).
9. Kargozar, S. & Mozafari, M. Nanotechnology and Nanomedicine: Start small, think big. *Mater. Today Proc.* **5**, 15492–15500 (2018).
10. Liu, L., Klausen, L. H. & Dong, M. Two-dimensional peptide based functional nanomaterials. *Nano Today* **23**, 40–58 (2018).
11. Merrifield, R. B. Solid Phase Peptide Synthesis. I. Synthesis of a Tetrapeptide. *J. Am. Chem. Soc.* **85**, 2149–2154 (1963).
12. Reches, M. & Gazit, E. Designed aromatic homo-dipeptides: Formation of ordered nanostructures and potential nanotechnological applications. *Phys. Biol.* **3**, 10–19 (2006).
13. Narancic, T., Almahboub, S. A. & O'Connor, K. E. Unnatural amino acids: production and biotechnological potential. *World J. Microbiol. Biotechnol.* **35**, 1–11 (2019).
14. Yan, X., Zhu, P. & Li, J. Self-assembly and application of diphenylalanine-based nanostructures. *Chem. Soc. Rev.* **39**, 1877–1890 (2010).
15. Midtgaard, S. R. *et al.* Self-assembling peptides form nanodiscs that stabilize membrane proteins. *Soft Matter* **10**, 738–752 (2014).
16. Wang, M. *et al.* Nanoribbons self-assembled from short peptides demonstrate the formation of polar zippers between β-sheets. *Nat. Commun.* **9**, 1–11 (2018).
17. Ulijn, R. V. & Smith, A. M. Designing peptide based nanomaterials. *Chem. Soc. Rev.* **37**, 664–675 (2008).

18. Ramachandran, G. N., Ramakrishnan, C. & Sasisekharan, V. Stereochemistry of polypeptide chain configurations. *J. Mol. Biol.* **7**, 95–99 (1963).
19. Kühn, K. Struktur und Biochemie des Kollagens. *Chemie unserer Zeit* **8**, 97–103 (1974).
20. Knowles, T. P. J., Vendruscolo, M. & Dobson, C. M. The amyloid state and its association with protein misfolding diseases. *Nat. Rev. Mol. Cell Biol.* **15**, 384–396 (2014).
21. Jiang, T. *et al.* Structurally defined nanoscale sheets from self-assembly of collagen-mimetic peptides. *J. Am. Chem. Soc.* **136**, 4300–4308 (2014).
22. Mannige, R. V. *et al.* Peptoid nanosheets exhibit a new secondary-structure motif. *Nature* **526**, 415–420 (2015).
23. Zaccai, N. R. *et al.* A de novo peptide hexamer with a mutable channel. *Nat. Chem. Biol.* **7**, 935–941 (2011).
24. Wu, Y. *et al.* A Supramolecular Vaccine Platform Based on α-Helical Peptide Nanofibers. *ACS Biomater. Sci. Eng.* **3**, 3128–3132 (2017).
25. Faragallah, W. H. Amyloidosis: A Convoluted Story. *Br. J. Haematol.* **114**, 529–538 (2001).
26. Sipe, J. D. & Cohen, A. S. Review: History of the amyloid fibril. *J. Struct. Biol.* **130**, 88–98 (2000).
27. Friedrich, N. & Kekule, A. Zur Amyloidfrage. *Virchows Arch. Pathol. Anat. Physiol.* **16**, 50–65 (1859).
28. Westermark, P. *et al.* Amyloid: Toward terminology clarification: Report from the Nomenclature Committee of the International Society Of Amyloidosis. *Amyloid* **12**, 1–4 (2005).
29. Geddes, A. J., Parker, K. D., Atkins, E. D. T. & Beighton, E. 'Cross-β' conformation in proteins. *J. Mol. Biol.* **32**, 343–358 (1968).
30. Sunde, M. *et al.* Common core structure of amyloid fibrils by synchrotron X-ray diffraction. *J. Mol. Biol.* **273**, 729–739 (1997).
31. Fändrich, M. & Dobson, C. M. The behaviour of polyamino acids reveals an inverse side chain effect in amyloid structure formation. *EMBO J.* **21**, 5682–5690 (2002).
32. Salemme, F. R. Structural properties of protein β-sheets. *Prog. Biophys. Mol. Biol.* **42**, 95–133 (1983).
33. Cantor, E. J. *et al.* Effects of amino acid side-chain volume on chain packing in genetically engineered periodic polypeptides. *J. Biochem.* **122**, 217–225 (1997).
34. Walsh, D. M., Lomakin, A., Benedek, G. B., Condron, M. M. & Teplow, D. B. Amyloid β-Protein Fibrillogenesis. *J. Biol. Chem.* **272**, 22364–22372 (1997).
35. Dearborn, A. D. *et al.* α-Synuclein amyloid fibrils with two entwined, asymmetrically associated protofibrils. *J. Biol. Chem.* **291**, 2310–2318 (2016).
36. Fändrich, M. On the structural definition of amyloid fibrils and other polypeptide aggregates. *Cell. Mol. Life Sci.* **64**, 2066–2078 (2007).
37. Almeida, Z. L. & Brito, R. M. M. Structure and aggregation mechanisms in

amyloids. *Molecules* **25**, 32155822 (2020).

38. Frieden, C. Protein aggregation processes: In search of the mechanism. *Protein Sci.* **16**, 2334–2344 (2007).

39. Morris, A. M., Watzky, M. A. & Finke, R. G. Protein aggregation kinetics, mechanism, and curve-fitting: A review of the literature. *Biochim. Biophys. Acta - Proteins Proteomics* **1794**, 375–397 (2009).

40. Ferrone, F. Analysis of protein aggregation kinetics. *Methods Enzymol.* **309**, 256–274 (1999).

41. Arosio, P., Knowles, T. P. J. & Linse, S. On the lag phase in amyloid fibril formation. *Phys. Chem. Chem. Phys.* **17**, 7606–7618 (2015).

42. JT, J. & Jr, L. P. T. Seeding 'one-dimensional crystallization' of amyloid: A pathogenic mechanism in Alzheimer's disease and scrapie? *Cell* **73**, 1055–1058 (1993).

43. Linse, S. Mechanism of amyloid protein aggregation and the role of inhibitors. *Pure Appl. Chem.* **91**, 211–229 (2019).

44. Törnquist, M. *et al.* Secondary nucleation in amyloid formation. *Chem. Commun.* **54**, 8667–8684 (2018).

45. Stelzmann, R. A., Norman Schnitzlein, H. & Reed Murtagh, F. An english translation of Alzheimer's 1907 Paper, "Über eine eigenartige Erkankung der Hirnrinde". *Clin. Anat.* **8**, 429–431 (1995).

46. Iadanza, M. G., Jackson, M. P., Hewitt, E. W., Ranson, N. A. & Radford, S. E. A new era for understanding amyloid structures and disease. *Nat. Rev. Mol. Cell Biol.* **19**, 755–773 (2018).

47. Westermark, P., Andersson, A. & Westermark, G. T. Islet amyloid polypeptide, islet amyloid, and diabetes mellitus. *Physiol. Rev.* **91**, 795–826 (2011).

48. Sanchorawala, V. Light-chain (AL) amyloidosis: diagnosis and treatment. *Clin. J. Am. Soc. Nephrol.* **1**, 1331–1341 (2006).

49. Evangelisti, E. *et al.* Binding affinity of amyloid oligomers to cellular membranes is a generic indicator of cellular dysfunction in protein misfolding diseases. *Sci. Rep.* **6**, 1–14 (2016).

50. Winner, B. *et al.* In vivo demonstration that α-synuclein oligomers are toxic. *Proc. Natl. Acad. Sci. U. S. A.* **108**, 4194–4199 (2011).

51. Cherny, I. & Gazit, E. Amyloids: Not Only Pathological Agents but Also Ordered Nanomaterials. *Angew. Chemie - Int. Ed.* **47**, 4062–4069 (2008).

52. Knowles, T. P. J. & Buehler, M. J. Nanomechanics of functional and pathological amyloid materials. *Nat. Nanotechnol.* **6**, 469–479 (2011).

53. Fowler, D. M. *et al.* Functional Amyloid Formation within Mammalian Tissue. *PLoS Biol.* **4**, 0100–0107 (2006).

54. Fowler, D. M., Koulov, A. V., Balch, W. E. & Kelly, J. W. Functional amyloid - from bacteria to humans. *Trends Biochem. Sci.* **32**, 217–224 (2007).

55. Vidal, O. *et al.* Isolation of an Escherichia coli K-12 mutant strain able to form biofilms on inert surfaces: Involvement of a new ompR allele that increases curli

expression. *J. Bacteriol.* **180**, 2442–2449 (1998).

56. Chapman, M. R. *et al.* Role of Escherichia coli curli operons in directing amyloid fiber formation. *Science.* **295**, 851–855 (2002).

57. Gophna, U. *et al.* Curli Fibers Mediate Internalization of Escherichia coli by Eukaryotic Cells. *Infect. Immun.* **69**, 2659–2665 (2001).

58. Romero, D., Aguilar, C., Losick, R. & Kolter, R. Amyloid fibers provide structural integrity to Bacillus subtilis biofilms. *Proc. Natl. Acad. Sci. U. S. A.* **107**, 2230–2234 (2010).

59. Claessen, D. *et al.* A novel class of secreted hydrophobic proteins is involved in aerial hyphae formation in Streptomyces coelicolor by forming amyloid-like fibrils. *Genes Dev.* **17**, 1714–1726 (2003).

60. Garcia-Sherman, M. C. *et al.* Peptide detection of fungal functional amyloids in infected tissue. *PLoS One* **9**, 19326203 (2014).

61. Macindoe, I. *et al.* Self-assembly of functional, amphipathic amyloid monolayers by the fungal hydrophobin EAS. *Proc. Natl. Acad. Sci. U. S. A.* **109**, 804–811 (2012).

62. Mackay, J. P. *et al.* The hydrophobin EAS is largely unstructured in solution and functions by forming amyloid-like structures. *Structure* **9**, 83–91 (2001).

63. Riek, R. & Saupe, S. J. The HET-s/s prion motif in the control of programmed cell death. *Cold Spring Harb. Perspect. Biol.* **8**, 27352624 (2016).

64. Shewmaker, F., Mull, L., Nakayashiki, T., Masison, D. C. & Wickner, R. B. Ure2p function is enhanced by its prion domain in Saccharomyces cerevisiae. *Genetics* **176**, 1557–1565 (2007).

65. Iconomidou, V. A., Vriend, G. & Hamodrakas, S. J. Amyloids protect the silkmoth oocyte and embryo. *FEBS Lett.* **479**, 141–145 (2000).

66. Bissig, C., Rochin, L. & van Niel, G. PMEL amyloid fibril formation: The bright steps of pigmentation. *Int. J. Mol. Sci.* **17**, 14220067 (2016).

67. Ito, S. & Wakamatsu, K. Chemistry of mixed melanogenesis - Pivotal roles of dopaquinone. *Photochem. Photobiol.* **84**, 582–592 (2008).

68. Maji, S. K. *et al.* Functional amyloids as natural storage of peptide hormones in pituitary secretory granules. *Science.* **325**, 328–332 (2009).

69. Münch, J. *et al.* Semen-Derived Amyloid Fibrils Drastically Enhance HIV Infection. *Cell* **131**, 1059–1071 (2007).

70. Roan, N. R. *et al.* The Cationic Properties of SEVI Underlie Its Ability To Enhance Human Immunodeficiency Virus Infection. *J. Virol.* **83**, 73–80 (2009).

71. Roan, N. R. *et al.* Semen amyloids participate in spermatozoa selection and clearance. *Elife* **6**, 2050084X (2017).

72. Hartgerink, J. D., Beniash, E. & Stupp, S. I. Self-Assembly and Mineralization of Peptide-Amphiphile Nanofibers. *Science.* **294**, 1684–1689 (2001).

73. Webber, M. J., Berns, E. J. & Stupp, S. I. Supramolecular nanofibers of peptide amphiphiles for medicine. *Isr. J. Chem.* **53**, 530–554 (2013).

74. Hendricks, M. P., Sato, K., Palmer, L. C. & Stupp, S. I. Supramolecular Assembly

of Peptide Amphiphiles. *Acc. Chem. Res.* **50**, 2440–2448 (2017). *https://pubs.acs.org/doi/10.1021/acs.accounts.7b00297*

75. Jiang, H., Guler, M. O. & Stupp, S. I. The internal structure of self-assembled peptide amphiphiles nanofibers. *Soft Matter* **3**, 454–462 (2007).

76. Behanna, H. A., Donners, J. J. J. M., Gordon, A. C. & Stupp, S. I. Coassembly of amphiphiles with opposite peptide polarities into nanofibers. *J. Am. Chem. Soc.* **127**, 1193–1200 (2005).

77. Niece, K. L., Hartgerink, J. D., Donners, J. J. J. M. & Stupp, S. I. Self-assembly combining two bioactive peptide-amphiphile molecules into nanofibers by electrostatic attraction. *J. Am. Chem. Soc.* **125**, 7146–7147 (2003).

78. Da Silva, R. M. P. *et al.* Super-resolution microscopy reveals structural diversity in molecular exchange among peptide amphiphile nanofibres. *Nat. Commun.* **7**, 1–10 (2016).

79. Beniash, E., Hartgerink, J. D., Storrie, H., Stendahl, J. C. & Stupp, S. I. Self-assembling peptide amphiphile nanofiber matrices for cell entrapment. *Acta Biomater.* **1**, 387–397 (2005).

80. Niece, K. L. *et al.* Modification of gelation kinetics in bioactive peptide amphiphiles. *Biomaterials* **29**, 4501–4509 (2008).

81. Zhang, S. *et al.* A self-assembly pathway to aligned monodomain gels. *Nat. Mater.* **9**, 594–601 (2010).

82. Sone, E. D. & Stupp, S. I. Semiconductor-encapsulated peptide-amphiphile nanofibers. *J. Am. Chem. Soc.* **126**, 12756–12757 (2004).

83. Spoerke, E. D., Anthony, S. G. & Stupp, S. I. Enzyme directed templating of artificial bone mineral. *Adv. Mater.* **21**, 425–430 (2009).

84. Greenwald, R. B., Choe, Y. H., McGuire, J. & Conover, C. D. Effective drug delivery by PEGylated drug conjugates. *Adv. Drug Deliv. Rev.* **55**, 217–250 (2003).

85. Soukasene, S. *et al.* Antitumor activity of peptide amphiphile nanofiber-encapsulated camptothecin. *ACS Nano* **5**, 9113–9121 (2011).

86. Matson, J. B. & Stupp, S. I. Drug release from hydrazone-containing peptide amphiphiles. *Chem. Commun.* **47**, 7962–7964 (2011).

87. Webber, M. J., Matson, J. B., Tamboli, V. K. & Stupp, S. I. Controlled Release of Dexamethasone from Peptide Nanofiber Gels to Modulate Inflammatory Response. *Biomaterials* **33**, 6823–6832 (2013).

88. Matson, J. B., Webber, M. J., Tamboli, V. K., Weber, B. & Stupp, S. I. A peptide-based material for therapeutic carbon monoxide delivery. *Soft Matter* **8**, 6689–6692 (2012).

89. Sur, S., Newcomb, C. J., Webber, M. J. & Stupp, S. I. Tuning supramolecular mechanics to guide neuron development. *Biomaterials* **34**, 4749–4757 (2013).

90. Tysseling, V. M. *et al.* Self-assembling peptide amphiphile promotes plasticity of serotonergic fibers following spinal cord injury. *J. Neurosci. Res.* **88**, 3161–3170 (2010).

91. Jiao, Y. *et al.* BDNF Increases Survival and Neuronal Differentiation of Human

Neural Precursor Cells Cotransplanted with a Nanofiber Gel to the Auditory Nerve in a Rat Model of Neuronal Damage. *Biomed Res. Int.* **2014**, (2014).

92. Angeloni, N. L. *et al.* Regeneration of the cavernous nerve by Sonic hedgehog using aligned peptide amphiphile nanofibers. *Biomaterials* **32**, 1091–1101 (2011).

93. Bull, S. R., Guler, M. O., Bras, R. E., Meade, T. J. & Stupp, S. I. Self-assembled peptide amphiphile nanofibers conjugated to MRI contrast agents. *Nano Lett.* **5**, 1–4 (2005).

94. Sargeant, T. D. *et al.* Hybrid bone implants: Self-assembly of peptide amphiphile nanofibers within porous titanium. *Biomaterials* **29**, 161–171 (2008).

95. Fomby, P. *et al.* Stem cells and cell therapies in lung biology and diseases: Conference report. *Ann. Am. Thorac. Soc.* **12**, 181–204 (2010).

96. ZHANG, S. Spontaneous assembly of a self-complementary oligopeptide to form a stable macroscopic membrane. *Proc. Natl. Acad. Sci.* **90**, 3334–3338 (1993).

97. Cormier, A. R., Pang, X., Zimmerman, M. I., Zhou, H. X. & Paravastu, A. K. Molecular structure of RADA16-I designer self-assembling peptide nanofibers. *ACS Nano* **7**, 7562–7572 (2013).

98. Wang, R., Wang, Z., Guo, Y., Li, H. & Chen, Z. Design of a RADA16-based self-assembling peptide nanofiber scaffold for biomedical applications. *J. Biomater. Sci. Polym. Ed.* **30**, 713–736 (2019).

99. Zhang, Z. X., Zheng, Q. X., Wu, Y. C. & Hao, D. J. Compatibility of neural stem cells with functionalized selfassembling peptide scaffold in vitro. *Biotechnol. Bioprocess Eng.* **15**, 545–551 (2010).

100. Lu, C. *et al.* Bioactive Self-Assembling Peptide Hydrogels Functionalized with Brain-Derived Neurotrophic Factor and Nerve Growth Factor Mimicking Peptides Synergistically Promote Peripheral Nerve Regeneration. *ACS Biomater. Sci. Eng.* **4**, 2994–3005 (2018).

101. Horii, A., Wang, X., Gelain, F. & Zhang, S. Biological designer self-assembling peptide nanofiber scaffolds significantly enhance osteoblast proliferation, differentiation and 3-D migration. *PLoS One* **2**, 19326203 (2007).

102. Yanlian, Y. *et al.* Designer self-assembling peptide nanomaterials. *Nano Today* **4**, 193–210 (2009).

103. Matsuoka, A. J. *et al.* Creating a stem cell niche in the inner ear using self-assembling peptide amphiphiles. *PLoS One* **12**, 19326203 (2017).

104. Wang, X. *et al.* Self-assembling peptide hydrogel scaffolds support stem cell-based hair follicle regeneration. *Nanomedicine Nanotechnology, Biol. Med.* **12**, 2115–2125 (2016).

105. Wu, H., Zhou, T., Tian, L., Xia, Z. & Xu, F. Self-Assembling RADA16-I Peptide Hydrogel Scaffold Loaded with Tamoxifen for Breast Reconstruction. *Biomed Res. Int.* **2017**, 3656193 (2017).

106. Briuglia, M. L., Urquhart, A. J. & Lamprou, D. A. Sustained and controlled release of lipophilic drugs from a self-assembling amphiphilic peptide hydrogel. *Int. J. Pharm.* **474**, 103–111 (2014).

107. Ashwanikumar, N. *et al.* Self-assembling peptide nanofibers containing phenylalanine for the controlled release of 5-fluorouracil. *Int. J. Nanomedicine* 5583–5594 (2016).

108. Paradís-Bas, M., Tulla-Puche, J., Zompra, A. A. & Albericio, F. RADA-16: A Tough Peptide - Strategies for Synthesis and Purification. *Eur. J. Org. Chem.* **2013**, 5871–5878 (2013).

109. Reches, M. & Gazit, E. Casting metal nanowires within discrete self-assembled peptide nanotubes. *Science.* **300**, 625–627 (2003).

110. Sedman, V. L., Adler-Abramovich, L., Allen, S., Gazit, E. & Tendler, S. J. B. Direct observation of the release of phenylalanine from diphenylalanine nanotubes. *J. Am. Chem. Soc.* **128**, 6903–6908 (2006).

111. Kol, N. *et al.* Self-assembled peptide nanotubes are uniquely rigid bioinspired supramolecular structures. *Nano Lett.* **5**, 1343–1346 (2005).

112. de Pablo, P. J., Schaap, I. A. T., MacKintosh, F. C. & Schmidt, C. F. Deformation and Collapse of Microtubules on the Nanometer Scale. *Phys. Rev. Lett.* **91**, 1–4 (2003).

113. Mason, T. O. *et al.* Expanding the solvent chemical space for self-assembly of dipeptide nanostructures. *ACS Nano* **8**, 1243–1253 (2014).

114. Hill, R. J. A. *et al.* Alignment of aromatic peptide tubes in strong magnetic fields. *Adv. Mater.* **19**, 4474–4479 (2007).

115. Hendler, N. *et al.* Formation of well-organized self-assembled films from peptide nanotubes. *Adv. Mater.* **19**, 1485–1488 (2007).

116. Reches, M. & Gazit, E. Controlled patterning of aligned self-assembled peptide nanotubes. *Nat. Nanotechnol.* **1**, 195–200 (2006).

117. Reches, M. & Gazit, E. Self-assembly of peptide nanotubes and amyloid-like structures by charged-termini-capped diphenylalanine peptide analogues. *Isr. J. Chem.* **45**, 363–371 (2005).

118. Jayawarna, V., Smith, A., Gough, J. E. & Ulijn, R. V. Three-dimensional cell culture of chondrocytes on modified di-phenylalanine scaffolds. *Biochem. Soc. Trans.* **35**, 535–537 (2007).

119. Smith, A. M. *et al.* Fmoc-diphenylalanine self assembles to a hydrogel via a novel architecture based on π-π interlocked β-sheets. *Adv. Mater.* **20**, 37–41 (2008).

120. Pellach, M. *et al.* Molecular Engineering of Self-Assembling Diphenylalanine Analogues Results in the Formation of Distinctive Microstructures. *Chem. Mater.* **28**, 4341–4348 (2016).

121. Guo, C. *et al.* Expanding the Nanoarchitectural Diversity Through Aromatic Di- and Tri-Peptide Coassembly: Nanostructures and Molecular Mechanisms. *ACS Nano* **10**, 8316–8324 (2016).

122. Jones, B. H. *et al.* A multi-stimuli responsive, self-assembling, boronic acid dipeptide. *Chem. Commun.* **51**, 14532–14535 (2015).

123. Yan, X. *et al.* Transition of cationic dipeptide nanotubes into vesicles and oligonucleotide delivery. *Angew. Chemie - Int. Ed.* **46**, 2431–2434 (2007).

124. Yan, X., Cui, Y., He, Q., Wang, K. & Li, J. Organogels based on self-assembly

of diphenylalanine peptide and their application to immobilize quantum dots. *Chem. Mater.* **20**, 1522–1526 (2008).

125. Zhou, M. *et al.* Self-assembled peptide-based hydrogels as scaffolds for anchorage-dependent cells. *Biomaterials* **30**, 2523–2530 (2009).
126. Carny, O., Shalev, D. E. & Gazit, E. Fabrication of coaxial metal nanocables using a self-assembled peptide nanotube scaffold. *Nano Lett.* **6**, 1594–1597 (2006).
127. Adler-Abramovich, L., Badihi-Mossberg, M., Gazit, E. & Rishpon, J. Characterization of peptide-nanostructure-modified electrodes and their application for ultrasensitive environmental monitoring. *Small* **6**, 825–831 (2010).
128. Fowler, J. R., Lavasani, M., Huard, J. & Goitz, R. J. Biologic strategies to improve nerve regeneration after peripheral nerve Repair. *J. Reconstr. Microsurg.* **31**, 243–248 (2015).
129. Beris, A., Gkiatas, I., Gelalis, I., Papadopoulos, D. & Kostas-Agnantis, I. Current concepts in peripheral nerve surgery. *Eur. J. Orthop. Surg. Traumatol.* **29**, 263–269 (2019).
130. Hill, C., Riaz, M., Mozzam, A. & Brennen, M. D. A regional audit of hand and wrist injuries: A study of 4873 injuries. *J. Hand Surg. Eur. Vol.* **23**, 196–200 (1998).
131. Rasulic, L. Current Concept in Adult Peripheral Nerve and Brachial Plexus Surgery. *J. Brachial Plex. Peripher. Nerve Inj.* **12**, e7–e14 (2017).
132. Isaacs, J. Treatment of Acute Peripheral Nerve Injuries: Current Concepts. *J. Hand Surg. Am.* **35**, 491–497 (2010).
133. Albert, E. Einige Operationen an Nerven. *Ber. d. Naturwissen. med. Vereins Innsbruck* **9**, 97–106 (1878).
134. Pinho, A. C., Fonseca, A. C., Serra, A. C., Santos, J. D. & Coelho, J. F. J. Peripheral Nerve Regeneration: Current Status and New Strategies Using Polymeric Materials. *Adv. Healthc. Mater.* **5**, 2732–2744 (2016).
135. Ichihara, S., Inada, Y. & Nakamura, T. Artificial nerve tubes and their application for repair of peripheral nerve injury: an update of current concepts. *Injury* **39**, 29–39 (2008).
136. Slutsky, D. J. A practical approach to nerve grafting in the upper extremity. *Atlas Hand Clin.* **10**, 73–92 (2005).
137. Faroni, A., Mobasseri, S. A., Kingham, P. J. & Reid, A. J. Peripheral nerve regeneration: Experimental strategies and future perspectives. *Adv. Drug Deliv. Rev.* **82**, 160–167 (2015).
138. Carvalho, C. R., Oliveira, J. M. & Reis, R. L. Modern Trends for Peripheral Nerve Repair and Regeneration: Beyond the Hollow Nerve Guidance Conduit. *Front. Bioeng. Biotechnol.* **7**, 22964185 (2019).
139. Magaz, A. *et al.* Bioactive Silk-Based Nerve Guidance Conduits for Augmenting Peripheral Nerve Repair. *Adv. Healthc. Mater.* **7**, (2018).
140. IJPMA, F. F. A., Van DE Graaf, R. C. & Meek, M. F. The early history of tubulation in nerve repair. *J. Hand Surg. Eur. Vol.* **33**, 581–586 (2008).

141. Archibald, S. J., Krarup, C., Shefner, J., Li, S. -T & Madison, R. D. A collagen-based nerve guide conduit for peripheral nerve repair: An electrophysiological study of nerve regeneration in rodents and nonhuman primates. *J. Comp. Neurol.* **306**, 685–696 (1991).

142. Tanaka, N. *et al.* Chitosan tubes can restore the function of resected phrenic nerves. *Interact. Cardiovasc. Thorac. Surg.* **21**, 8–13 (2015).

143. Hung, V. & Dellon, A. L. Reconstruction of a 4-cm Human Median Nerve Gap by Including an Autogenous Nerve Slice in a Bioabsorbable Nerve Conduit: Case Report. *J. Hand Surg. Am.* **33**, 313–315 (2008).

144. Ruiter, G. C. De, Moore, M. J. & Ph, D. Accuracy of motor axon regeneration across autograft, single-lumen, and multichannel poly(lactic-co-glycolic acid) nerve tubes. *Neurosurgery* **63**, 144–155 (2008).

145. Reid, A. J. *et al.* Long term peripheral nerve regeneration using a novel PCL nerve conduit. *Neurosci. Lett.* **544**, 125–130 (2013).

146. de Ruiter, G. C. W., Malessy, M. J. A., Yaszemski, M. J., Windebank, A. J. & Spinner, R. J. Designing ideal conduits for peripheral nerve repair. *Neurosurg. Focus* **26**, 1–9 (2009).

147. Yang, Y. *et al.* Nerve conduits based on immobilization of nerve growth factor onto modified chitosan by using genipin as a crosslinking agent. *Eur. J. Pharm. Biopharm.* **79**, 519–525 (2011).

148. Madduri, S., Feldman, K., Tervoort, T., Papaloïzos, M. & Gander, B. Collagen nerve conduits releasing the neurotrophic factors GDNF and NGF. *J. Control. Release* **143**, 168–174 (2010).

149. Yang, Y. *et al.* Neurotrophin releasing single and multiple lumen nerve conduits. *J. Control. Release* **104**, 433–446 (2005).

150. Silva, G. A. *et al.* Selective Differentiation of Neural Progenitor Cells by High-Epitope Density Nanofibers. *Science.* **303**, 1352–1355 (2004).

151. Yolamanova, M. *et al.* Peptide nanofibrils boost retroviral gene transfer and provide a rapid means for concentrating viruses. *Nat. Nanotechnol.* **8**, 130–136 (2013).

152. Naldini, L. *et al.* In vivo gene delivery and stable transduction of nondividing cells by a lentiviral vector. *Science.* **272**, 263–267 (1996).

153. Hbckel, M. & Yuan, F. A. N. Multiply attenuated lentiviral vector achieves efficient gene delivery in vivo. *Nat. Biotechnol.* **3**, 3–8 (1997).

154. Meier, C., Weil, T., Kirchhoff, F. & Münch, J. Peptide nanofibrils as enhancers of retroviral gene transfer. *Wiley Interdiscip. Rev.: Nanomed. Nanobiotechnol* **6**, 438–451 (2014).

155. Coelen, R. J., Jose, D. G. & May, J. T. The effect of hexadimethrine bromide (polybrene) on the infection of the primate retroviruses SSV 1/SSAV 1 and BaEV. *Arch. Virol.* **75**, 307–311 (1983).

156. Davis, H. E., Morgan, J. R. & Yarmush, M. L. Polybrene increases retrovirus gene transfer efficiency by enhancing receptor-independent virus adsorption on target cell membranes. *Biophys. Chem.* **97**, 159–172 (2002).

157. Hodgson, C. P. & Sotaiman, F. Virosotnes: Cationic Liposomes Enhance Retroviral Transduction. *Nat. Biotechnol.* **14**, 339–342 (1996).

158. Cornetta, K. & Anderson, W. F. Protamine sulfate as an effective alternative to polybrene in retroviral-mediated gene-transfer: implications for human gene therapy. *J. Virol. Methods* **23**, 187–194 (1989).

159. Rotonda, J. *et al.* Colocalization of retrovirus and target cells on specific fibronectin fragments increases genetic transduction of mammalian cells. *Nat. Struct. Biol.* **2**, 876–882 (1996).

160. Loo, Y. *et al.* Self-Assembled Proteins and Peptides as Scaffolds for Tissue Regeneration. *Adv. Healthc. Mater.* **4**, 2557–2586 (2015).

161. Gačanin, J. *et al.* Autonomous Ultrafast Self-Healing Hydrogels by pH-Responsive Functional Nanofiber Gelators as Cell Matrices. *Adv. Mater.* **31**, 15214095 (2019).

List of abbreviations

%	percent
Å	Ångström
AFM	atomic force microscope
BDNF	brain-derived neutrophic factor
CNS	central nervous system
cm	centimeter
CO	carbon monoxide
DMSO	dimethyl sulfoxide
DNA	desoxyribonucleic acid
DRG	dorsal root ganglia
EF-C	enhancement factor C
FF	diphenylamine
FT-IR	fourier-transform infrared spectroscopy
GDNF	glial-derived neurotrophic factor
GPa	gigapascal
HIV	human immunodeficiency virus
HPLC	high performance liquid chromatography
MLV	murine leukemia virus
NGC	nerve guidance conduit
NGF	nerve growth factor
Mn	motor neuron
nm	nanometer
PA	peptide amphiphile
PBS	phosphate buffer saline
pDA	polydopamine
pLL	poly-ʟ-lysine
PNF	peptide nanofibrils
PNI	peripheral nerve injury
PNS	peripheral nervous system

RNA	ribonucleic acid
SAR	structure-activity-relationship
SAP	self-assembling peptide
TEM	transmission electron microscopy
µm	micrometer

List of amino acids

amino acid	three letter code	one letter code
alanine	ala	A
arginine	arg	R
asparagine	asn	N
aspartic acid	asp	D
cysteine	cys	C
glutamine	gln	Q
glutamic acid	glu	E
glycine	gly	G
histidine	his	H
isoleucine	ile	I
leucine	leu	L
lysine	lys	K
methionine	met	M
phenylalanine	phe	F
proline	pro	P
serine	ser	S
threonine	thr	T
tryptophan	trp	W
tyrosine	tyr	Y
valine	val	V

List of publications

1.) C. Schilling, T. Mack, S. Lickfett, S. Sieste, F. S. Ruggeri, T. Sneideris, A. Dutta, T. Bereau, R. Naraghi, D. Sinske, T. P. J. Knowles, C. V. Synatschke, T. Weil, B. Knöll, Sequence-Optimized Peptide Nanofibers as Growth Stimulators for Regeneration of Peripheral Neurons, *Adv. Funct. Mater.* **2019**, *29*.

https://doi.org/10.1002/adfm.201809112

2.) S. Sieste, T. Mack, C. V. Synatschke, C. Schilling, C. Meyer zu Reckendorf, L. Pendi, S. Harvey, F. S. Ruggeri, T. P. J. Knowles, C. Meier, D. Y. W. Ng, T. Weil, B. Knöll, Water-Dispersible Polydopamine-Coated Nanofibers for Stimulation of Neuronal Growth and Adhesion, *Adv. Healthc. Mater.* **2018**, *7*.

https://doi.org/10.1002/adhm.201701485

3.) S. Sieste, T. Mack, E. Lump, M. Hayn, D. Schütz, A. Röcker, C. Meier, K. Kaygisiz, F. Kirchhoff, T. P. J. Knowles, F. S. Ruggeri, C. V. Synatschke, J. Münch, and T. Weil, Supramolecular Peptide Nanofibrils with Optimized Sequences and Molecular Structures for Efficient Retroviral Transduction, Adv. Funct. Mater. **2021**, 2009382.

https://doi.org/10.1002/adfm.202009382

Curriculum vitae

The Curriculum vitae has been removed for data protection reasons.

List of conferences

1.) 4th Statussymposium on “Integration of Molecular Components in Functional Macroscopic Systems”, Hannover, Germany, October 2018 (poster presentation).

2.) Sixth International Symposium Frontiers in Polymer Science, Budapest, Hungary, May 2019 (poster presentation).

Statutory declaration

I hereby declare that I wrote the present dissertation with the topic:

“In-depth Investigation of Self-assembling Peptides for Functional Nanomaterials”

independently and used no other aids than those cited. In each individual case, I have clearly identified the source of the passages that are taken word for word or paraphrased from other works.

I also hereby declare that I have carried out my scientific work according to the principles of good scientific practice in accordance with the current „Satzung der Universität Ulm zur Sicherung guter wissenschaftlicher Praxis“ [Rules of the University of Ulm for Assuring Good Scientific Practice].

Ulm,

……………………………………………

Thomas Mack

Acknowledgements

The Acknowledgement has been removed for data protection reasons.